Department of Physics and Astronomy, University of Canterbury,
Private Bag 4800, Christchurch 8140, New Zealand

Analysis of Internal Boundaries and Transition Regions in Geophysical Systems with Advanced Processing Techniques

A thesis
submitted in partial fulfilment
of the requirements for
a
Doctor of Philosophy in Physics
at the
University of Canterbury

by

Nikolai Christian Krützmann

University of Canterbury

2013

Supervisors: Dr. Adrian McDonald

Dr. Wolfgang Rack

Dr. Steve George

Abstract

This thesis examines the utility of the Rényi entropy (RE), a measure of the complexity of probability density functions, as a tool for finding physically meaningful patterns in geophysical data. Initially, the RE is applied to observational data of long-lived atmospheric tracers in order to analyse the dynamics of stratospheric transitions regions associated with barriers to horizontal mixing. Its wider applicability is investigated by testing the RE as a method for highlighting internal boundaries in snow and ice from ground penetrating radar (GPR) recordings. High-resolution 500 MHz GPR soundings of dry snow were acquired at several sites near Scott Base, Antarctica, in 2008 and 2009, with the aim of using the RE to facilitate the identification and tracking of subsurface layers to extrapolate point measurements of accumulation from snow pits and firn cores to larger areas.

The atmospheric analysis focuses on applying the RE to observational tracer data from the EOS-MLS satellite instrument. Nitrous oxide (N_2O) is shown to exhibit subtropical RE maxima in both hemispheres. These peaks are a measure of the tracer gradients that mark the transition between the tropics and the mid-latitudes in the stratosphere, also referred to as the edges of the tropical pipe. The RE maxima are shown to be located closer to the equator in winter than in summer. This agrees well with the expected behaviour of the tropical pipe edges and is similar to results reported by other studies. Compared to other stratospheric mixing metrics, the RE has the advantage that it is easy to calculate as it does not, for example, require conversion to equivalent latitude and does not rely on dynamical information such as wind fields.

The RE analysis also reveals occasional sudden poleward shifts of the southern hemisphere tropical pipe edge during austral winter which are accompanied by increased mid-latitude N_2O levels. These events are investigated in more detail by creating daily high-resolution N_2O maps using a two-dimensional trajectory model and MERRA reanalysis winds to advect N_2O observations forwards and backwards in time on isentropic surfaces. With the aid of this 'domain filling' technique it is illustrated that the increase in southern hemisphere mid-latitude N_2O during austral winter is probably the result of the cumulative effect of several large-scale, episodic leaks of N_2O-rich air from the tropical pipe. A comparison with the global distribution of potential vorticity strongly suggests that irreversible mixing related to planetary wave breaking is the cause of the leak events. Between 2004 and 2011 the large-scale leaks are shown to occur approximately every second year and a connection to the equatorial quasi-biennial oscillation is found to be likely, though this cannot be established conclusively due to the relatively short data set.

Identification and tracking of subsurface boundaries, such as ice layers in snow or the bedrock of a glacier, is the focus of the cryospheric part of this project. The utility of the RE for detecting amplitude gradients associated with reflections in GPR recordings is initially tested on a 25 MHz sounding of an Antarctic glacier. The results show distinct regions of increased RE values that allow identification of the glacial bedrock along large parts of the profile. Due to the low computational requirements, the RE is found to be an effective pseudo gain function for initial analysis of GPR data in the field. While other gain functions often

have to be tuned to give a good contrast between reflections and background noise over the whole vertical range of a profile, the *RE* tends to assign all detectable amplitude gradients a similar (high) value, resulting in a clear contrast between reflections and background scattering. Additionally, theoretical considerations allow the definition of a 'standard' data window size with which the *RE* can be applied to recordings made by most pulsed GPR systems and centre frequencies. This is confirmed by tests with higher frequency recordings (50 and 500 *MHz*) acquired on the McMurdo Ice Shelf. However, these also reveal that the *RE* processing is less reliable for identifying more closely spaced reflections from internal layers in dry snow.

In order to complete the intended high-resolution analysis of accumulation patterns by tracking internal snow layers in the 500 *MHz* data from two test sites, a different processing approach is developed. Using an estimate of the emitted waveform from direct measurement, deterministic deconvolution via the Fourier domain is applied to the high-resolution GPR data. This reveals unambiguous reflection horizons which can be observed in repeat measurements made one year apart. Point measurements of average accumulation from snow pits and firn cores are extrapolated to larger areas by identifying and tracking a dateable dust layer horizon in the radargrams. Furthermore, it is shown that annual compaction rates of snow can be estimated by tracking several internal reflection horizons along the deconvolved radar profiles and calculating the average change in separation of horizon pairs from one year to the next. The technique is complementary to point measurements from other studies and the derived compaction rates agree well with published values and theoretical estimates.

Acknowledgements

First of all, I would like to thank my supervisors Adrian McDonald, Wolfgang Rack, and Steve George for allowing me to undertake this somewhat unconventional project. It has been a pleasure working with all three of you and I greatly appreciate your constant readiness to provide advice, knowledge, or copious amounts of feedback when required, as well as guidance and encouragement, particularly when things were not going so well. Without your continued support, this work and especially its completion would not have been possible.

I also want to thank my long- and short-term office mates: Mita Brierly, Simon Parsons, Jack Coggins, Robert Ward, Madeleine Smith, and Jakob Grahn for their great company, helpful advice, and fun chats that kept me socialised during the more intensive periods of this research, and for not minding to work in an office that is occasionally misused as a bedroom. Thank you also to Karl Howley and Phillippa Dobson for putting up with a flat mate who has never heard of keeping regular hours and starts to bake bread at 2:00 am, and for generally being the best flat mates I could have wished for. Special thanks go to Mette Riger-Kusk for her participation in the Antarctic field work in 2008, her amazing skills with duct tape, and also for the radar data from the Touchdown Glacier (Antarctica) that is used in this thesis.

I am also very grateful to all the institutions who have provided me with financial support along the way, such as the University of Canterbury, the UC Department of Physics & Astronomy, and Gateway Antarctica. The support of the Antarctic measurement campaigns from the Christchurch City Council and by Antarctica New Zealand under the field event K053 'Cryosphere Remote Sensing' is greatly appreciated. Furthermore, I want to thank Nick Key and Justin Harrison from the UC Department of Geography who were of great assistance during the preparations for the field campaigns, the Scott Base staff for great support and an enjoyable time in Antarctica, and Bob Noonan for assisting with some of the preparation and processing of the radar data.

Finally, I thank my family and friends for their continued support by email, telephone, Skype, or whatever other means were necessary to get a hold of me during the last few years. I especially thank my wife Stephanie for managing to pull me out of my thesis-gloom from halfway around the globe whenever I needed it and particularly for her patience and commitment to hang in there with me throughout all these years.

Contents

List of Figures

List of Tables

Abbreviations

CH_3Cl Methyl chloride

CH_4 Methane

CO Carbon monoxide

N_2O Nitrous oxide

ACF Autocorrelation function

AGC Automatic gain control

BDC Brewer-Dobson Circulation

DFT Discrete Fourier transform

DJF December, January, February

DVL Data video logger (pulse EKKO PRO)

EOS Earth Observing Systems

FDTD Finite-difference time-domain (model)

FFT Fast Fourier transform

FT Fourier transform

GMT Greewich Mean Time

GPR Ground penetrating radar

GPS Global Positioning System

HT Hilbert transform

HYSPLIT Hybrid Single Particle Lagrangian Integrated Trajectory Model

IFT Inverse Fourier transform

iHT Inverse Hilbert transform

JJA June, July, August

MAM March, April, May

MERRA Modern Era Retrospective analysis for Research and Applications

MLS Microwave limb sounder

NCAR National Center for Atmospheric Research

NCEP National Centers for Environmental Prediction

PDF Probability distribution function

ppbv Parts per billion by volume

pptv Parts per trillion by volume

PV Potential vorticity

PVU potential vorticity unit ($1 \cdot 10^{-6}\ \frac{m^2 K}{s \cdot kg}$)

QBO Quasi-biennial oscillation

RE Rényi entropy

RMSD Root mean square deviation

SEC Spreading and exponential compensation

SOCOL SOlar Climate Ozone Links (chemistry-climate model)

SON September, October, November

TWT Two-way-travel time

UTC Coordinated Universal Time, same as GMT

UV ultra-violet

Chapter 1

Introduction

1.1 Motivation

Most real world geophysical systems are complex, meaning they are non-linear and often display irregular patterns as a result of the interactions and interdependencies of the numerous physical processes involved in the system. Measures of complexity are a means of analysing such intricate systems. Similar to statistical methods, they are a way of "standing back" and investigating the behaviour of the system as a whole, instead of trying to understand and model all its details with perfect accuracy. By identifying regions where transitions occur, complexity measures can highlight key areas of a geophysical system, thereby giving detailed information about a complex system in a simple way.

The Rényi entropy (RE) is a statistical complexity measure that was established as an efficient tool for identifying tracer gradients associated with stratospheric barriers to horizontal mixing in *Krützmann et al.* (2008) and *Krützmann* (2008). Having successfully applied this measure to tracer data from climate model simulations, one objective of this thesis is to use the RE to study the properties and behaviour of stratospheric mixing barriers in more detail by applying it to satellite observations. Being a statistical measure based on (discrete) probability density functions (PDFs), the RE can be calculated for any kind of numerical data set. Therefore, the second objective is to investigate the applicability of the RE methodology to other geophysical systems. In particular, the RE's utility for detecting amplitude gradients in cryospheric ground penetrating radar (GPR) measurements is examined. To this end, high-frequency GPR profiles of dry snow were recorded at several locations in the vicinity of Scott Base on Ross Island, Antarctica. Identifying and tracking internal layers in this data, in order to extrapolate point measurements of accumulation from snow pits and firn cores to larger areas, is the third objective of the present work.

The main focus of previous atmospheric work with the RE has been on identifying the stratospheric barrier to horizontal mixing at the edge of the Antarctic polar vortex, a strong circumpolar stratospheric wind that occurs every austral winter and spring (e.g. *Waugh and Randel*, 1999). Additionally, the RE measure was able to consistently identify mixing barriers associated with the boundaries of the so-called 'tropical pipe' region or tropical reservoir in the model data. *Trepte and Hitchman* (1992) discovered that this region around the equator is relatively isolated from the rest of the stratosphere. As tropical upwelling into this region is

the main source for many stratospheric trace gases, it constitutes one of the most important links between the troposphere and the stratosphere. *Neu et al.* (2003) and more recently *Palazzi et al.* (2011) investigated the dynamics of these mixing barriers, yet they are still far from being fully understood. A detailed analysis of the (sub-)tropical mixing barriers is performed in the present work by applying the *RE* to stratospheric tracer observations from the Earth Observing System Microwave Limb Sounder (EOS-MLS) satellite instrument, in order to improve the understanding of the evolution of the tropical pipe.

Being fundamentally sensitive to gradients, the *RE* can potentially also detect transition regions in other geophysical data sets. In snow and ice, transition regions are associated with boundaries between internal layers created by changes in the ambient conditions at the time of deposition. By identifying and tracing internal layers using high-frequency, pulsed GPR measurements of the Antarctic snow cover, changes in the depth and spacing of the layers in snow can be used to determine accumulation and compaction over time (e.g. *Arcone et al.*, 2005). This information is important for validation of satellite altimeter observations used for estimating the polar mass balance, since snow accumulation and snow compaction need to be separated in order to quantify imbalances from satellite derived surface elevation change (*Wingham et al.*, 2006). Similarly, low-frequency GPR profiles can be used to determine the subsurface topography and thickness of Antarctic glaciers (e.g. *Bogorodsky et al.*, 1985), information which is also very important for mass balance calculations. In both cases, the contrast between layers with different dielectric properties, e.g. dense snow vs. depth hoar or ice vs. subglacial rock, causes partial reflection of the GPR pulse and thereby a change in received signal amplitude. These amplitude gradients can potentially be detected with the *RE*, similar to the detection of tracer gradients in the stratosphere.

The intensity of the signal recorded with GPR soundings can vary over several orders of magnitude. Accordingly, a considerable number of processing steps are often required to allow identification of subsurface structures. The *RE*, being a relative measure, is independent of the absolute values in a data set and can therefore potentially detect amplitude gradients of varying intensity without requiring additional processing. In an atmospheric context, the *RE* has also been shown to be more efficient when analysing large amounts of data than other, more elaborate processing techniques (*Krützmann*, 2008). This can be advantageous when considering initial data processing of GPR recordings in the field, where the available time and computational power is often limited. Additionally, the statistical nature of the *RE* entails that, while numerous data points are required to calculate one *RE* value, individual outliers or data gaps caused for example, by disturbances of the measuring equipment, can be excluded to improve the results.

Analysing both recent atmospheric and cryospheric data is also highly relevant to the ongoing debate on climate change, as they provide complementary information on the state of the climate system. Accordingly, improving our understanding of complexity measures can, due to their potential versatility, significantly contribute to the understanding of the Earth system as a whole.

1.2 Thesis Outline

This thesis is structured into four main chapters and a final chapter that summarises the results. Chapter 2 introduces the geophysical background material and is split into two parts. The first half starts with an overview of the structure of the atmosphere and the stratosphere in particular, followed by explanations of several relevant concepts, such as potential vorticity (PV), the quasi-biennial oscillation (QBO), and the use of long-lived chemical tracers for understanding stratospheric dynamics. Next, a methodology for using the *RE* to detect mixing barriers in measurements of stratospheric tracer concentrations is introduced. Details are then given regarding the data sets that are used for the atmospheric analyses in Ch. 3, such as the tracer observations from the EOS-MLS satellite instrument and the MERRA reanalysis data. In the second half of Ch. 2 an overview of the applications of GPR for studies of the cryosphere is given and the relevant dielectric properties of snow and ice are discussed. This is followed by a summary of several processing steps often applied to GPR data. Finally, the location and setup of the measurement campaign in Antarctica is described, the methodologies used for data acquisition are introduced, and the setup and specifications of the GPR equipment are detailed. Additionally, the origin of a 25 *MHz* GPR cross-section of an Antarctic glacier used in Ch. 4 is briefly explained.

Chapter 3 begins with the introduction of a 'global binning' method for atmospheric tracer data that is different from the previously used 'optimal binning' procedure for creating the PDFs from which the *RE* is calculated, and its advantages are highlighted. The new approach is applied to EOS-MLS observations of several stratospheric trace gases: nitrous oxide (N_2O), methyl chloride (CH_3Cl), and carbon monoxide (CO). Comparison of the results leads to insights about the effects of noise on the *RE* patterns and the comparability of different trace species. Additionally, a seven-year climatology of the *RE* of N_2O observations is presented, followed by a detailed analysis of the evolution of the mixing barriers at the edges of the tropical pipe in the lower and middle stratosphere as identified by the *RE* of N_2O between 2004 and 2011. The results are compared with previous work and lead to the detection of several periods during which considerable amounts of N_2O-rich air appear to 'leak' from the tropics into the southern hemisphere surf-zone during austral winter. The temporal evolution and vertical extent of these 'leak events' is then investigated and changes in the vertical structure of the tropical pipe when these leaks occur are discussed. The dynamics leading to the tropical leaks are examined by using 'domain filling', a method for artificially enhancing the number of N_2O observations for a particular day by using a trajectory model. The applicability of the *RE* to the high-resolution domain filled maps for investigating longitudinal variability of the tropical pipe edges is also investigated. Finally, the results are summarised and a potential link between the occurrence of tropical leaks and the phase of the QBO is discussed.

Before applying the *RE* to cryospheric GPR observations, a sensitivity study of the *RE* to synthetic gradients of varying extent is performed at the beginning of Ch. 4. From these results, a suitable data window size is selected for using the *RE* to identify amplitude gradients related to internal layers and the bedrock reflection in a 25 *MHz* GPR cross-section of an Antarctic glacier. This is followed by an investigation of the effects of applying several standard GPR processing steps before calculating the *RE*. Additionally, the effects

of varying parameters such as the data window size, the number of bins for the histograms, or the exponent of the RE are tested. The RE patterns are then compared to the results of a more conventional processing methodology and differences are discussed. This leads to guidelines for applying the RE to a wider variety of GPR recordings, which are tested on higher frequency (50 and 500 MHz) profiles of the McMurdo Ice Shelf (Antarctica) in the last part of the chapter. The results are then summarised and conclusions regarding the utility of the RE as an alternative pseudo gain function for initial analysis of GPR data in the field are drawn.

Due to some limitations of the RE methodology when it comes to identifying multiple closely spaced gradients, the RE is not ideal for identifying and tracking relatively weak reflections related to internal layers in dry snow. Consequently, an alternative processing approach, the deterministic Fourier deconvolution is developed in Ch. 5, which is particularly suitable for GPR recordings of relatively low-contrast media. The deterministic Fourier deconvolution is first tested on a simulated radar profile and then applied to 500 MHz GPR data of dry polar snow. The established stake farms as well as information on snow density and internal layering from snow pits and firn cores are used to estimate accumulation rates over several years at the measurements sites. By identifying and tracking internal layers in the deconvolved GPR profiles, the accumulation estimates are then expanded to larger areas. Furthermore, the change in the separation of individual reflection horizons from one year to the next is used to calculate snow compaction rates down to 13 m depth. The derived accumulation and compaction rates are compared to previous studies and differences are discussed, before giving a summary of the results and drawing conclusions regarding the wider applicability of the presented processing technique.

Chapter 6 summarises the findings of the previous chapters and outlines future work that could be pursued as a result of these.

Additionally, this thesis has an electronic supplement containing several animations of domain filled maps of N_2O. The filenames and some details about the individual animations are given in Appendix A.

Chapter 2

Geophysical Background

Some parts of this chapter are derived from the article "Snow accumulation and compaction derived from GPR data near Ross Island, Antarctica" published in the online journal The Cryosphere (Kruetzmann et al., 2011).

This chapter introduces the atmospheric and cryospheric context for the work presented in the following chapters and illustrates a number of basic concepts from the two fields. Additionally, details are given about the different data sets that will be used.

Section 2.1 gives an overview of the atmospheric structure and the stratosphere in particular. The role of chemical tracers in the stratosphere and how these can be used to gain information about stratospheric dynamics is discussed, followed by an explanation of potential vorticity and the quasi-biennial oscillation. Section 2.2 describes how the Rényi entropy (RE) statistical measure can identify tracer gradients associated with mixing barriers in stratospheric tracer data. In Sect. 2.3, various data sets used for the atmosphere-related part of this thesis (Ch. 3) are introduced. The second half of this chapter begins with an overview of the utility of ground penetrating radar (GPR) for glaciological studies and for the detection of internal layers in particular (Sect. 2.4), followed by a discussion of the dielectric properties of snow and ice. Section 2.5 then introduces a number of basic processing steps commonly applied to GPR recordings. Section 2.6 illustrates the location and layout of the sites of the Antarctic measurement campaign and explains how the snow accumulation and density information used in Ch. 5 was acquired from stake farms, snow pits, and firn cores. Furthermore, the specifications of the GPR system are given and the different setups used for 50 and 500 MHz data acquisition are described. Additionally, the origin and acquisition parameters of a 25 MHz GPR cross-section of a glacier in the Trans-Antarctic Mountains, analysed in Ch. 4, is detailed.

2.1 Atmospheric Structure and Stratospheric Dynamics

The Earth's atmosphere can be considered as a succession of layers of continuously decreasing density with alternating negative and positive vertical temperature gradients. From the surface up, the layers are called the troposphere, stratosphere, mesosphere, thermosphere, and exosphere. The intermittent regions in which the temperature gradient reverses are refer-

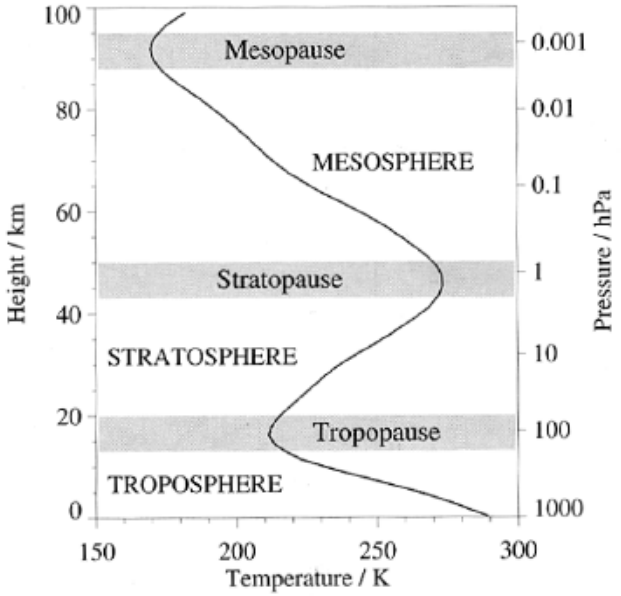

Figure 2.1: The lowest three layers of the atmosphere and the evolution of the (mean) temperature with altitude. The boundaries between layers are characterised by a reversal of the temperature gradient (from *Andrews*, 2000).

red to as the "pauses", i.e. the tropopause, the stratopause, etc. This structure is illustrated in Fig. 2.1 for the three layers closest to the surface.

Figure 2.1 also shows that both height (above sea level) and pressure can be used as a vertical coordinate. The approximate altitude, z, of a particular pressure level, p, can be calculated by:

$$z(p) = \frac{R \cdot T}{g} \cdot \ln\left(\frac{p_o}{p}\right) \tag{2.1}$$

where $R \approx 287.05\ \frac{J}{kg\,K}$ is the specific gas constant for dry air, $p_0 \approx 1013\ hPa$ is the average pressure at sea level, $T = 255\ K$ is the approximate average temperature of the troposphere and stratosphere (*Wallace and Hobbs*, 2006), and $g \approx 9.8\,\frac{m}{s^2}$ is the acceleration due to gravity, taken to be constant in this case. Equation 2.1 can be derived from the hydrostatic equation:

$$\frac{\partial p}{\partial z} = -g \cdot \rho \tag{2.2}$$

where ρ is the density of air, which assumes that the air is in hydrostatic equilibrium, meaning that the pressure at a particular point is determined only by the mass per unit area of the column of air above that point. Using the ideal gas law in its molar form (with R being the specific gas constant for dry air as above):

$$p = \rho R T \tag{2.3}$$

ρ can be eliminated from Eq. 2.2. Rearranging and integrating from the surface ($z = 0$, $p = p_0$) to altitude z and pressure p, assuming an isothermal atmosphere with a temperature equal to the average $T = 255\ K$, then results in Eq. 2.1.

The troposphere is the layer closest to the Earth's surface and is therefore also the region in which "weather" occurs. It is associated with turbulent dynamics and strong vertical and horizontal mixing as the negative temperature gradient (or lapse rate) with altitude makes the troposphere inherently unstable (*Andrews*, 2000). Additionally, the Earth's surface absorbs large amounts of solar radiation which in turn heats up the air close to the surface. This results in strong convective mixing processes, particularly at the equator, and causes the air in the troposphere to be relatively well mixed in the vertical. The transition region above the troposphere, the tropopause, can be defined as "the lowest level at which the lapse rate decreases to $2\,\frac{^\circ C}{km}$ or less, provided that the average lapse rate between this level and all higher levels within $2\,km$ does not exceed $2\,\frac{^\circ C}{km}$." (*World Meteorological Organization*, 1992) The tropopause isolates the troposphere from the stratosphere, as it only allows limited transport between these regions, and its height tends to decrease with latitude (*Shepherd*, 2003).

As the name suggests, the stratosphere is highly stratified in most cases and vertical transport and mixing is limited (*Wallace and Hobbs*, 2006). The positive temperature gradient in the stratosphere implies that the region is much more stable with regards to convective mixing than the troposphere. Combined with the fact that it is close to radiative equilibrium (*Shepherd*, 2003), this results in the stratosphere being stably stratified on potential temperature surfaces. The potential temperature, θ, for an ideal gas at pressure, p, can be calculated as:

$$\theta = T \cdot \left(\frac{p_0}{p}\right)^{\frac{R}{c_p}} \tag{2.4}$$

where p_0 is the surface pressure (often taken as 1000 hPa everywhere for simplicity), $c_p \approx 1.003\,\frac{kJ}{kg\,K}$ is the specific heat capacity of air at constant pressure, and T is the temperature of the air in K. The potential temperature of a volume of air (or air parcel) corresponds to the temperature the air would have if it were compressed until it reaches the (assumed) surface pressure, without adding or removing heat, i.e. adiabatically (*Wallace and Hobbs*, 2006). As the stratosphere is approximately in radiative equilibrium, the heat required for diabatic changes to an air parcel is not readily available, which is why short-term motions (5-10 days) largely occur on potential temperature surfaces (*Holton et al.*, 1995). Therefore, potential temperature is often used as an alternative vertical coordinate to altitude or pressure in studies of the stratosphere. It is particularly useful when the short-term motion of individual air parcels is being considered, since the three-dimensional problem can be reduced to two-dimensional motion on a potential temperature surface by ignoring the (weak) diabatic effects. Figure 2.2 shows the zonal average altitude and pressure of a number of potential temperature levels derived from the monthly zonal[1] mean temperature data for October 2009 (MERRA reanalysis, see also Sect. 2.3.2), illustrating the approximately horizontal nature of potential temperature surfaces. Note that the altitude scale in Fig. 2.2 is derived from an exponential fit to the tabulated values of the U.S. Standard Atmosphere 1976 (*U.S. Government Printing Office*, 1976), which results in a slightly lower altitude for each pressure level than the use of Eq. 2.1.

[1] 'Zonal' means at a constant longitude. Similarly, 'meridional' means at a constant latitude.

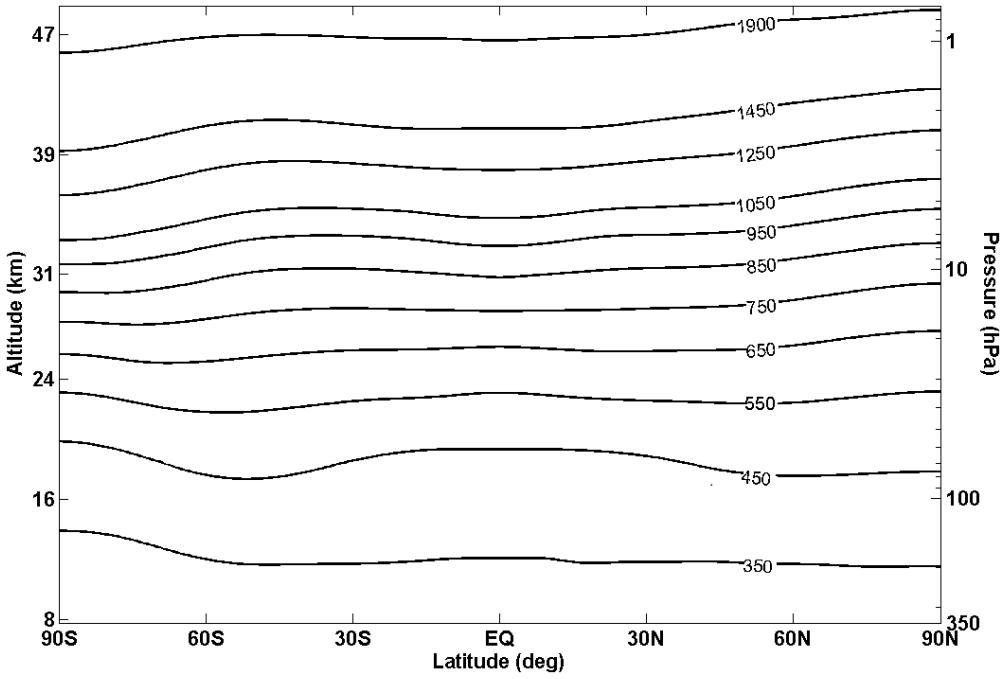

Figure 2.2: Relationship between altitude, pressure, and potential temperature contours (in K) in the stratosphere, derived from monthly zonal mean MERRA temperature data for October 2009.

Figure 2.2 also illustrates that the potential temperature increases with altitude, i.e. that $\frac{\partial\theta}{\partial z} > 0$ throughout the stratosphere. This is important with respect to the stability of the stratosphere: it can be shown that the behaviour of an air parcel that has been displaced adiabatically in the vertical is directly related to the local gradient in potential temperature. If the gradient is positive ($\frac{\partial\theta}{\partial z} > 0$), the air parcel will rebound and begin to oscillate around its equilibrium position with the Brunt-Väisälä frequency (*Wallace and Hobbs*, 2006):

$$N = \sqrt{\frac{g}{\theta} \cdot \frac{\partial\theta}{\partial z}} \tag{2.5}$$

Barring any other external forces, the oscillation will be gradually damped by viscous forces, eventually returning the air parcel to its original altitude. If on the other hand, the potential temperature gradient is negative ($\frac{\partial\theta}{\partial z} < 0$), Eq. 2.5 gives an imaginary Brunt-Väisälä frequency which means that the air parcel will not begin to oscillate but continue to move away from its original position (*Wallace and Hobbs*, 2006). Accordingly, the atmosphere is statically stable when $\frac{\partial\theta}{\partial z} > 0$, and statically unstable if $\frac{\partial\theta}{\partial z} < 0$.

Being close to radiative equilibrium, the net radiative heating in the stratosphere is small and only a limited amount of heat is available for diabatic motion. Combined with the vertical stability of the stratosphere with respect to adiabatic motion, this results in the stratospheric circulation being considerably slower and less variable than the tropospheric one. Global-scale mixing can take up to several years in the stratosphere (*Pendlebury and Shepherd*, 2003) and large-scale circulation patterns can persist over long time periods, allowing distinct regions to form. During most of the year, the stratosphere can be horizontally divided into: the summer hemisphere, the tropics or "tropical pipe" (*Plumb*, 1996), the winter mid-latitudes, and the winter polar vortex region. These are separated by barriers to horizontal mixing, as

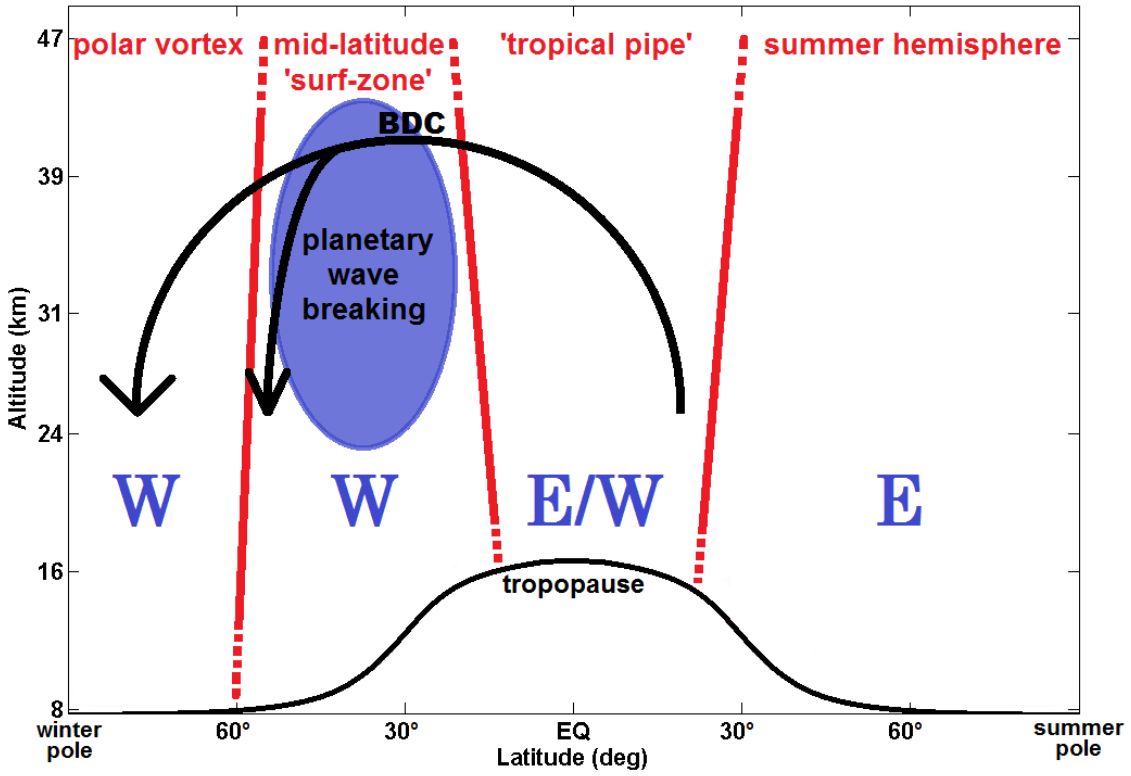

Figure 2.3: Schematic representation of the four regions of the stratosphere. The vertical red lines indicate barriers to horizontal mixing. The large blue letters indicate the dominant zonal mean zonal wind direction. A maximum in westerly winds separates the winter polar vortex and mid-latitude 'surf-zone' near 60°, while weak easterlies persist in the summer hemisphere. Zonal winds in the tropical pipe alternate between easterly and westerly (QBO, see also Fig. 2.6). Planetary wave breaking in the winter surf-zone (blue oval) results in poleward 'pumping' in the middle and upper stratosphere, which drives the Brewer-Dobson Circulation (BDC, black arrows). The diagram is based on Fig. 2 in *Plumb* (2002).

illustrated in Fig. 2.3. The tropical pipe is the only permanent feature, though its edges can shift considerably throughout the year (usually toward the summer hemisphere), while the other three regions depend on the season in their respective hemisphere.

The four regions differ in their dominant zonal wind patterns (Fig. 2.3). The summer hemisphere is usually characterised by relatively calm easterlies and weak horizontal mixing. The tropics show an irregular pattern of alternating easterly and westerly winds which is known as the quasi-biennial oscillation (QBO; see also Sect. 2.1.3). The winter hemisphere is dominated by westerly winds with a maximum near 60°, separating the mid-latitudes from the polar regions. In late autumn and winter time, the lack of solar insolation causes considerable cooling of the polar winter stratosphere. The resulting temperature gradient between the polar night and lower latitudes causes westerly winds throughout most of the hemisphere which increase in strength with altitude (thermal wind shear, *Holton*, 2004). The highest wind speeds tend to occur between 60° and 65° and are also referred to as the polar night jet. Particularly in the southern hemisphere, it can persist well into springtime and the strong winds can act as a barrier to horizontal mixing, isolating the polar winter stratosphere

from warmer, lower latitude air and allowing it to radiatively cool even further.[2] The region between the polar vortex and the tropics is often referred to as the "surf-zone" (*McIntyre and Palmer*, 1984) since planetary wave breaking occurs regularly during winter and spring, causing considerable horizontal mixing in this region.

Planetary waves are planetary-scale disturbances that are created at the Earth's surface by large-scale topography and the contrast in temperature due to differences in radiative heating over land and water. Under the right conditions, they can propagate upwards and transfer their momentum to the mean flow when they break in the stratosphere, making them an important source of momentum for the stratospheric circulation. Given the exponential decrease of density with altitude (Eq. 2.2), wave amplitudes increase as the waves propagate upward (due to energy conservation) and they eventually break, similar to water waves when they reach shallow water.

Rossby waves are a particular type of planetary wave that carry easterly momentum and for which the conservation of angular momentum acts as the restoring force. *Charney and Drazin* (1961) showed that Rossby waves with a zonal phase velocity c can only propagate vertically if the zonal wind, u, adheres to the inequality:

$$0 < u - c < U_c \tag{2.6}$$

where U_c is the Rossby critical velocity, which depends on latitude and the horizontal dimensions of the wave. For typical Rossby wavelengths ($\approx 10,000 - 35,000\,km$) at mid-latitudes, U_c is positive (westerly) with values of several tens of metres per second (*Plumb*, 2010). Since the sources of these waves (large-scale topography and land-water contrasts) are permanent features of the Earth's surface, atmospheric Rossby waves are often stationary with respect to the surface, i.e. their zonal phase velocity is zero. This simplifies Eq. 2.6 to:

$$0 < u < U_c \tag{2.7}$$

which is often referred to as the Charney-Drazin criterion (*Holton*, 2004). While Rossby waves are created throughout the year, Eq. 2.7 implies that they can only propagate into the stratosphere when the zonal winds are westerly (> 0) and not too strong ($< U_c$), e.g. at mid-latitudes during winter and spring (Fig. 2.3). Similarly, the vertical structure of the zonal wind affects the altitude at which wave breaking occurs. As the zonal wind velocities tend to increase with height in the surf-zone, upward propagating waves eventually reach a critical level for which $u = U_c$. As the waves approach this level they begin to break, depositing their momentum at or just below the critical level (*Holton*, 2004). The vertical range where the wavebreaking occurs is referred to as the critical layer.

Rossby wave breaking causes considerable horizontal mixing in the winter stratosphere. In summer, the persistent easterlies do not allow planetary wave propagation and horizontal mixing is relatively weak. The blue shaded region in Fig. 2.3 indicates the area in which most planetary wave breaking takes place. In addition to causing horizontal mixing, the easterly momentum deposited by breaking Rossby waves drives a poleward circulation known as the Brewer-Dobson Circulation (BDC; *Shepherd*, 2003). This circulation effectively sucks up

[2]The cold temperatures are also one of the main prerequisites for the formation of the ozone hole in the southern hemisphere.

air from the tropical regions and pumps it toward the pole where it cools off and sinks. The continuous breaking of planetary waves, and the accompanying deposition of easterly momentum, also affects the springtime deceleration and eventual break-up of the polar night westerly jet. Due to the larger topographical contrasts, planetary wave activity is generally higher in the northern hemisphere, which is the main reason for the earlier break-up of the northern hemisphere polar vortex compared to the Antarctic one.

2.1.1 Stratospheric Tracers

More than 99.9% of the Earth's atmosphere is made up of only three gases: nitrogen (N_2, 78%), oxygen (O_2, 21%), and argon (Ar, 0.93%). All other gaseous components of air occur in much smaller (trace) amounts. Gases that are also relatively chemically inert with respect to a particular timescale will be transported along with the atmospheric flow within that timescale and are therefore often referred to as chemical tracers. Their relative amounts are often given in volume mixing ratio with units of parts-per-million-by-volume (*ppmv*), parts-per-billion-by-volume (*ppbv*), or parts-per-trillion-by-volume (*pptv*), though other measures such as partial pressure or mole fraction are also common. The turbulent dynamics in the troposphere, and particularly in the boundary layer[3], result in the air undergoing thorough vertical and horizontal mixing on relatively short timescales (several weeks for intra-hemispheric mixing). Additionally, many trace species have tropospheric sources all over the globe, limiting the potential for latitudinal gradients. Accordingly, long-lived trace species are almost evenly distributed throughout the troposphere. The average time they spend in the atmosphere before they undergo a chemical reaction is much longer than the mixing timescale.

The considerably slower mixing processes in the stratosphere and the existence of distinct regions separated by mixing barriers, imply that large-scale circulation patterns, such as the BDC, have a significant effect on the distribution of the chemical constituents. Due to the slow large-scale dynamics, most chemical tracers are gradually removed with time. This means that the chemical composition of stratospheric air is dependent on the time the air has spent in the stratosphere.[4] Depending on the lifetime of a particular chemical and the location of its stratospheric sources and sinks, different scales of mixing can be important in the spatial distribution of these tracers. Figure 2.4 shows the average lifetime of a number of atmospheric tracers on the vertical axis and the spatial scale on which their distribution varies on the horizontal axis. The stratospheric distribution of long-lived tracers with an average chemical lifetime of several months or even years, e.g. nitrous oxide (N_2O) or methane (CH_4), are strongly influenced by large-scale, long-term circulation tendencies such as the BDC (which has an overturning time of about three years; *Rosenlof*, 1995). In reverse, this implies that the large-scale distribution of a long-lived tracer can be used to infer details about the underlying dynamics occurring in the stratosphere. This is illustrated by the zonal mean distribution of N_2O for October shown in Fig. 2.5. Figure 2.5 is derived from observational data from the Earth Observing System Microwave Limb Sounder (EOS-MLS) which is discussed in more detail in Sect. 2.3.3. Among other chemicals, the EOS-MLS

[3]The first kilometre above the surface.

[4]This is also known as chemical ageing.

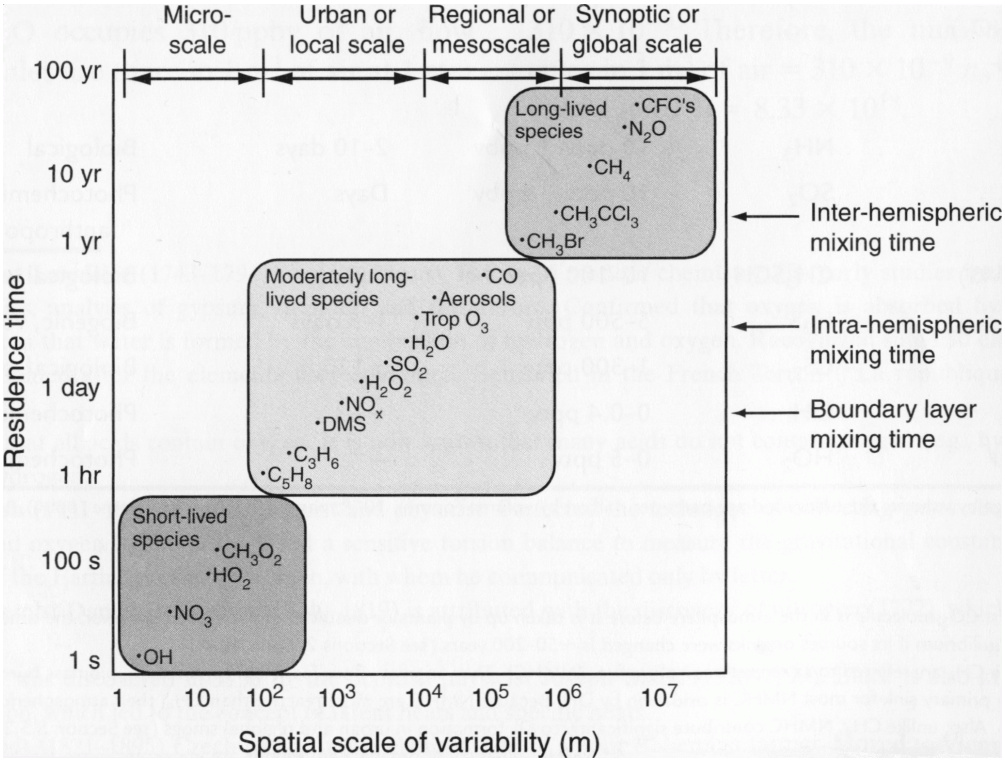

Figure 2.4: Atmospheric trace gas residence times and associated mixing scales (from *Wallace and Hobbs*, 2006).

observes three stratospheric tracers: nitrous oxide (N_2O), methyl chloride (CH_3Cl), and carbon monoxide (CO), which are used in the present work. The main chemical processes that affect the stratospheric abundances of these tracers are detailed in the following.

Nitrous oxide is created at the Earth's surface by biological processes as well as human activities. It is relatively evenly distributed throughout the troposphere with an average mixing ratio of approximately 320 *ppbv* (*Lambert et al.*, 2007). The main source of stratospheric air in general and stratospheric N_2O in particular is in the tropics. The intense surface heating in this region causes deep convection whereby the air rises rapidly and can penetrate through the tropopause. At higher latitudes, mixing from the troposphere into the stratosphere is generally reduced and occurs intermittently (*Stohl et al.*, 2003). Once it has reached the tropical lower stratosphere, the up-welling arm of the BDC causes the air with its (high) tropospheric amounts of N_2O to move upward and eventually poleward, which is why the peak of each contour in Fig. 2.5 is found in the tropics. When the air reaches higher altitudes, the increase in short-wave solar radiation enhances the photodissociation of N_2O according to Eq. 2.8:

$$N_2O + h\nu \longrightarrow N_2 + O \tag{2.8}$$

where $h\nu$ represents a photon of ultra-violet (UV) light ($\lambda < 337$ *nm*; *Bates and Hays*, 1967). The amount of UV light is much higher in the upper regions of the stratosphere than at lower levels, as it gets absorbed by the ozone layer between 20 and 30 *km* altitude. Hence, the chemical lifetime of N_2O is only a few months at 40 *km* (≈ 1400 *K*) compared to 100 years at 20 *km* (≈ 500 *K*) (*Lambert et al.*, 2007). The photochemical destruction of N_2O

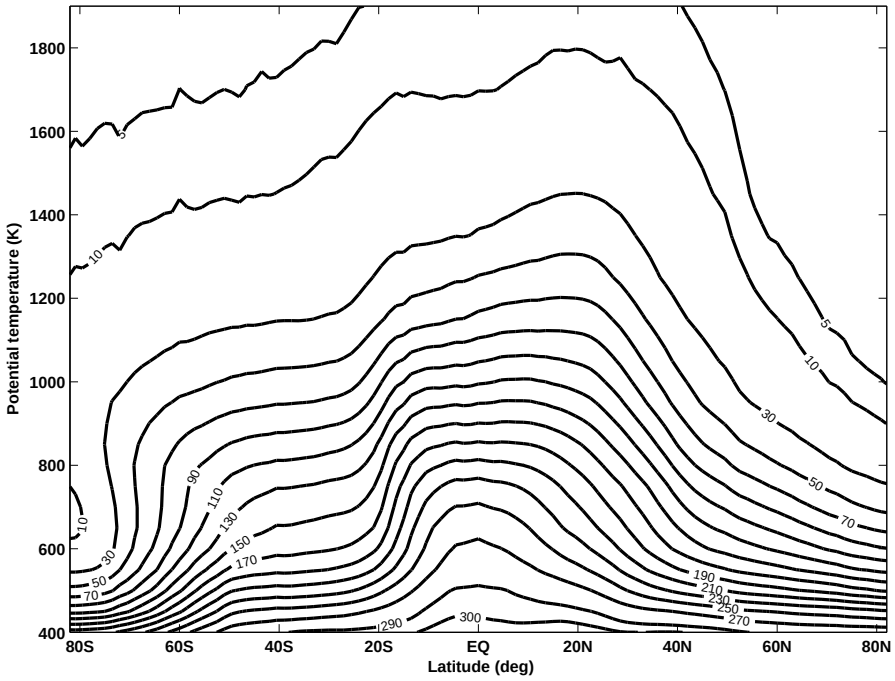

Figure 2.5: Meridional cross-section of zonal mean nitrous oxide (N_2O) mixing ratio (contours in *ppbv*) for October from combined satellite measurements from 2004 to 2011. The strong horizontal gradients near 20°S and 60°S are associated with the transition regions between the tropics, surf-zone, and the polar vortex. The potential temperatures from 400 to 1900 K approximately correspond to a vertical range between 16 and 47 km altitude (compare Fig. 2.2).

(Eq. 2.8) is its main stratospheric sink (*Lambert et al.*, 2007), though the chemical reaction with excited oxygen radicals (O):

$$N_2O + O \longrightarrow 2NO \tag{2.9}$$

also occurs frequently at high altitudes and further reduces the N_2O abundance. Consequently, the mixing ratio of N_2O gradually reduces with time while the air is pumped poleward by the BDC. In the winter mid-latitudes (between approximately 20°S and 60°S in Fig. 2.5), the strong horizontal stirring caused by planetary wave breaking results in a flattening of the N_2O contours. This creates a meridional gradient between the tropics and the surf-zone that can be seen as a step in the zonal mean N_2O distribution (Fig. 2.5). Another meridional gradient is observed between the winter mid-latitudes and the inside of the polar vortex (at approximately 60°S). Air from the surf-zone cannot easily penetrate through the strong winds of the polar night jet. Therefore, a large part of the air within the polar vortex is air that has been moved poleward at high altitudes by the BDC and has subsequently undergone cooling and descent. Accordingly, vortex air contains relatively low amounts of N_2O as most of it has been removed at high altitudes by the processes described in Eqs. 2.8 and 2.9.

Methyl chloride (CH_3Cl) is a tracer similar to N_2O in that it is created at the Earth's surface and is photodissociated in the stratosphere. Its chemical properties, and particularly its average residence time, are similar to that of CH_3Br – approximately one year (see Fig.

2.4) – which is shorter than that of N_2O but still sufficiently long to be useful as a tracer of the dynamics in the lower stratosphere. Its typical volume mixing ratio in the troposphere is 600 *pptv*, almost three orders of magnitude smaller than that of N_2O.

In the stratosphere, Carbon monoxide has an even shorter average residence time than CH_3Cl. However, its chemical lifetime and abundance is highly altitude dependent. In the mesosphere, CO is created through photolysis of carbon dioxide (CO_2):

$$CO_2 + h\nu \longrightarrow CO + O \tag{2.10}$$

by high-energy UV radiation ($h\nu$) and CO's lifetime increases from several months in the lower mesosphere to more than a year at higher levels (*Jin et al.*, 2009). In the stratosphere, CO is created during the photochemical oxidation of CH_4 according to Eq. 2.11 (*Randel et al.*, 1998).

$$CH_4 + 3O_2 + h\nu \longrightarrow 2H_2O + CO + O_3 \tag{2.11}$$

The main sink of CO is oxidation by the hydroxyl radical (OH):

$$CO + OH \longrightarrow CO_2 + H \tag{2.12}$$

As the chain of reactions that lead to the creation of OH requires UV radiation (Eq. 2.13) and OH is very reactive, almost no OH is found in the polar middle atmosphere during winter due to the lack of sunlight.

$$\begin{aligned} O_3 + h\nu &\longrightarrow O_2 + O \\ O + H_2O &\longrightarrow 2OH \end{aligned} \tag{2.13}$$

Therefore, there is little destruction of CO during polar night and CO can accumulate inside the polar vortex during this time. In the presence of sunlight, however, the stratospheric lifetime of CO can be as short as three weeks in the upper stratosphere and as long as six months in the lower stratosphere (*Jin et al.*, 2009). As a tracer, the unusual geometry of sources and sinks makes CO more dependent on local dynamics and seasonal effects than N_2O and therefore can be a complimentary source of information on mixing dynamics, particularly in the polar regions during winter.

2.1.2 Isentropic Potential Vorticity

Another quantity that is frequently used to analyse stratospheric dynamics is Ertel's isentropic potential vorticity, often just referred to as potential vorticity (PV). It has properties very similar to chemical tracers in that it is conserved on potential temperature surfaces under the assumption of adiabatic motion. In isentropic coordinates the potential vorticity is defined as *(Hoskins et al., 1985)*:

$$PV = -\frac{g\,(f + \zeta_\theta)}{\left(\frac{\partial p}{\partial \theta}\right)} \tag{2.14}$$

where g is the acceleration due to gravity[5], p is pressure, θ is the potential temperature, f is the Coriolis parameter, and ζ_θ is the isentropic vorticity. The Coriolis parameter is a function of latitude, φ, and the Earth's angular velocity, $\Omega = 7.2921 \cdot 10^{-5}\ \frac{rad}{s}$, according to Eq. 2.15.

$$f = 2 \cdot \Omega \cdot \sin \varphi \tag{2.15}$$

The isentropic vorticity, ζ_θ, depends on the horizontal wind field on isentropic levels:

$$\zeta_\theta = \vec{k} \cdot \left(\vec{\nabla}_\theta \times \vec{v}\right) = \left(\frac{\partial v}{\partial x}\right)_\theta - \left(\frac{\partial u}{\partial y}\right)_\theta \tag{2.16}$$

where $\vec{k}$ is a vertical unit vector perpendicular to potential temperature levels, and $\vec{v} = (u, v)$ is the horizontal wind vector, with u and v corresponding to the zonal and meridional wind component on isentropic levels, respectively. $\frac{\partial}{\partial x}$ and $\frac{\partial}{\partial y}$ are the derivatives with respect to longitude and latitude, respectively, where the index θ indicates that the derivatives are to be taken on potential temperature levels. The SI units of PV are $\frac{m^2 K}{s\,kg}$, but it is usually given in potential vorticity units or PVU, where $1\ PVU = 1 \cdot 10^{-6}\ \frac{m^2 K}{s\,kg}$.

2.1.3 The Equatorial Quasi-Biennial Oscillation

Figure 2.6 shows a contour plot of the zonal mean zonal wind velocities at the equator from August 2004 through April 2011, derived from MERRA reanalysis data (see also Sect. 2.3.2) on potential temperature levels. Negative wind velocities (blue) correspond to easterly winds, positive velocities (red/yellow) are westerly. The thick black contour indicates the zero wind line. Figure 2.6 illustrates that the zonal mean wind does not follow a strictly seasonal or annual variation, particularly between 400 and 1250 K. In this region the zonal winds oscillate between downward propagating easterly and westerly winds with an approximately two year period. The long-term average period is 28 months, but the actual period can vary between 22 and 34 months (*Baldwin and Dunkerton*, 2001). Hence this zonal wind pattern is known as the (equatorial) quasi-biennial oscillation (QBO). Above 600 K, the QBO's easterly phase tends to last longer and the westerlies descend faster, while the opposite is the case between 600 K and the tropopause.

The QBO is the result of the interaction of different types of atmospheric waves with the zonal mean flow. The waves are similar to Rossby waves (see Sect. 2.1) but can carry either westerly or easterly momentum. Waves that carry westerly momentum can only propagate upwards when the zonal winds are easterly, while those that transport easterly momentum can only propagate upwards when the prevailing winds are westerly (*Baldwin et al.*, 2001). When these waves break in the stratosphere they transfer their momentum to the background flow, thereby decelerating the zonal winds which allow them to propagate in the first place. This feedback effect causes the cyclic behaviour of the QBO. Figure 2.7 illustrates this mechanism. In Fig. 2.7a, the average zonal wind profile in the stratosphere, $\overline{u}$ (thick line), is

[5] $g = 9.8\ \frac{m}{s^2}$ is assumed, independent of altitude. While g can vary by up to 2% between the surface and 50 km altitude (depending on latitude), this error is negligible when considering adiabatic motion of an air parcel on the order of a few days. Additionally, this error is likely to be small compared to the measurement error of other involved quantities, particularly the horizontal wind velocities.

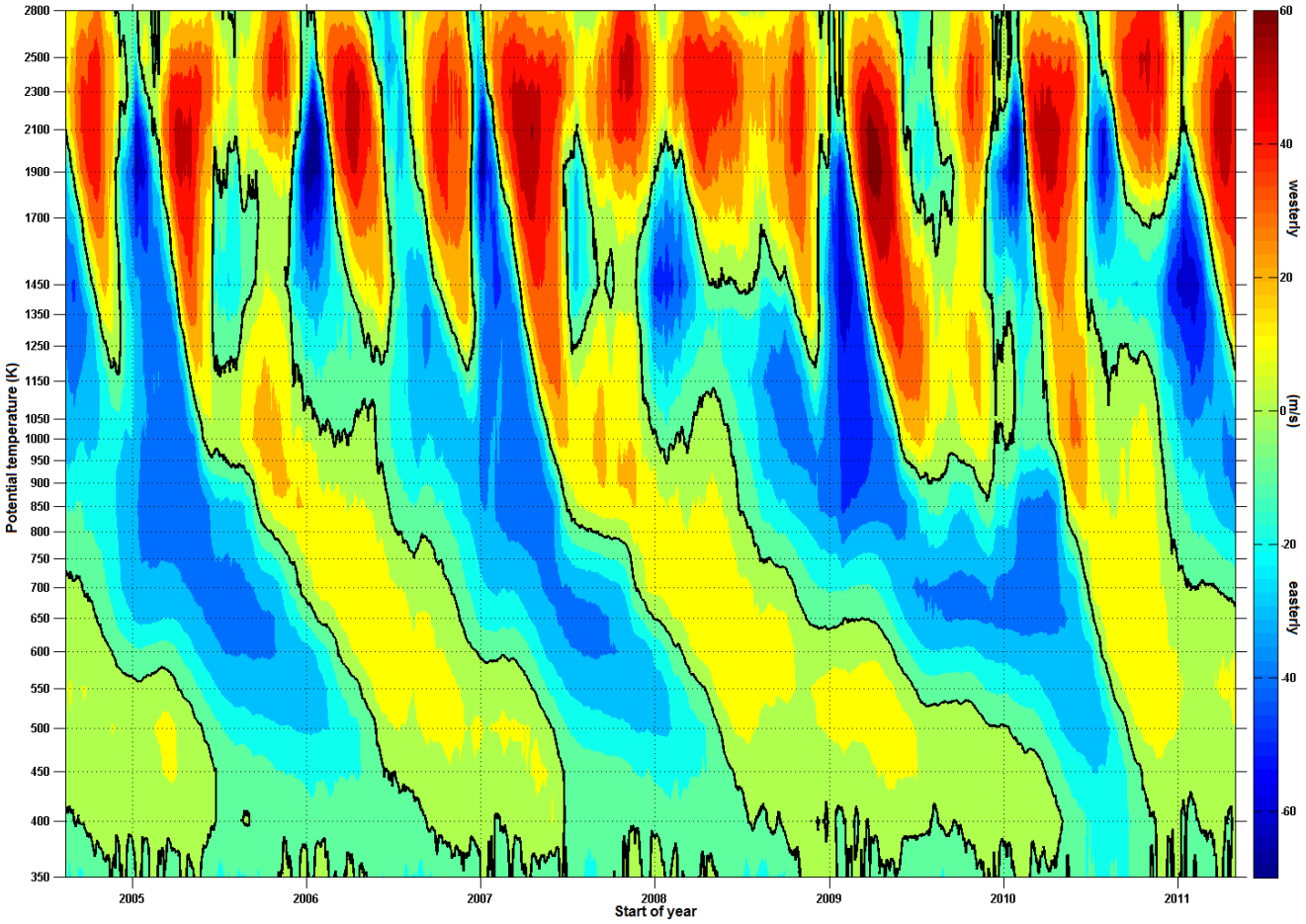

Figure 2.6: Contour plot of the zonal mean zonal winds (in $\frac{m}{s}$) at the equator from August 2004 through April 2011 derived from MERRA reanalysis data. The contour interval is $10\,\frac{m}{s}$. Positive (red/yellow) velocities are westerly (eastward). The thick black contour marks the zero wind line. The potential temperatures from 350 to 2800 K correspond to an approximate altitude range of 13 to 60 km.

westerly at lower levels but changes rapidly to easterly with altitude, z. Waves with a westerly phase velocity ($+c$) cannot propagate far into the stratosphere as they can only propagate upwards when the background winds are easterly. Waves with easterly phase velocity ($-c$) on the other hand, can propagate through the lower part of the stratosphere until they reach a critical layer where the average zonal wind velocity is easterly and similar in magnitude to the phase velocity of the wave (i.e. when $|\overline{u} - c|$ is small), where they break and deposit their easterly momentum (double arrow in the left half of Fig. 2.7a). The critical layer tends to lie below the altitude where c matches $\bar{u}$, which means that the maximum descends with time.[6] Above the maximum there are no further driving forces and viscous diffusion gradually reduces the mean zonal winds (thin horizontal arrows in Fig. 2.7). Similarly, the thinning layer of westerly winds at the lowest levels is eventually destroyed by viscous forces when it becomes too thin (*Gray*, 2010). The resulting purely easterly mean wind profile (Fig. 2.7b) now allows waves with westerly phase velocity to propagate upwards. When these break at higher levels, they speed up the deceleration of the prevailing easterlies. Eventually, this results in increasingly westerly winds at higher levels impeding the vertical propagation of the westerly momentum carrying waves while at the same time the peak in easterly winds moves further down (Fig. 2.7c). Now the westerly wind regime gradually descends, due to the breaking of the westerly momentum carrying waves, resulting in the reverse of the initial situation – thinning, low-level easterlies and westerly winds at higher levels (Fig. 2.7d). From here the cycle continues in reverse.

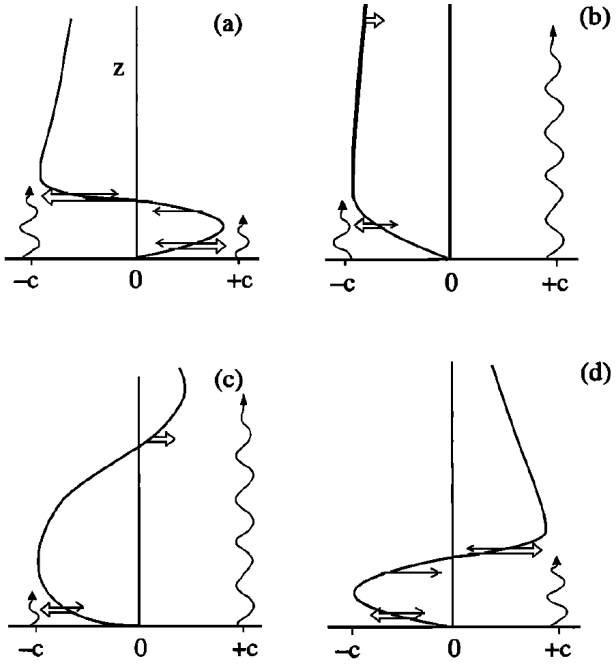

Figure 2.7: Illustration of the mechanism driving the QBO. Zonal wind velocities are shown on the horizontal axis. The thick lines indicate the background zonal wind profiles, the wavy arrows show how high waves with easterly (-) and westerly (+) phase velocity c can propagate. Double arrows correspond to acceleration driven by breaking waves, single arrows indicate the natural diffusive tendency of the atmosphere to slow down strong winds through viscous forces. After *Baldwin et al.* (2001) and *Plumb* (1984).

[6]This also explains how the downward propagation of the phase of the QBO can be driven by upwardly propagating waves.

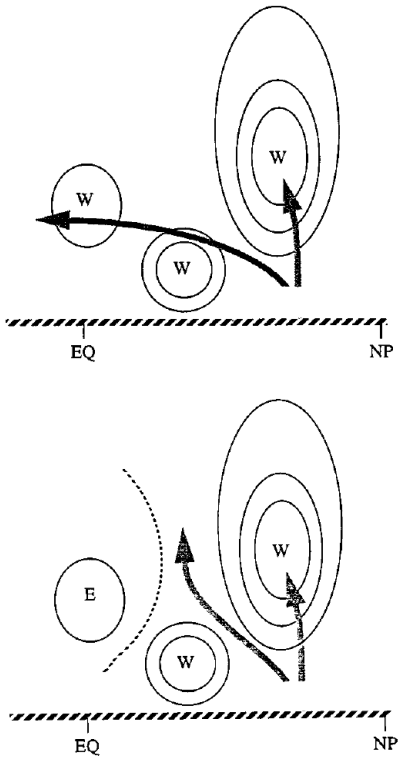

Figure 2.8: *"Schematic diagram showing the zonal wind structure in the winter hemisphere in the westerly phase of the QBO in the lower stratosphere (top) and in the easterly phase (bottom). The dashed line in the bottom panel shows the location of the zero wind line. The thick arrows denote the dominant paths of wave activity propagation for quasi-stationary planetary waves forced near the surface in the extratropics"* (from *Hamilton*, 1998).

Holton and Lindzen (1972) established that the waves in Fig. 2.7 carrying westerly momentum correspond to planetary Kelvin waves, while mixed Rossby-gravity waves provide the easterly momentum. However, the QBO mechanism described here is only a simplified model. For example, the momentum provided by Kelvin and mixed Rossby-gravity waves has to be complemented by a "broad spectrum of gravity waves that account for the remaining accelerations" (*Yang et al.*, 2011), the exact details of which are not yet fully understood. A more complete description of the QBO theory is given in *Baldwin et al.* (2001) and references therein, and a detailed explanation of the properties of the different wave types involved can be found in *Holton* (2004).

While the QBO is primarily an equatorial phenomenon, it also affects higher latitudes. For example, during the easterly phase of the QBO the zero wind line between the winter westerlies and summer easterlies lies in the winter hemisphere. Since $u = 0$ is a critical line for (stationary) Rossby waves, these cannot cross the equator and the effectiveness of wave energy propagation to high altitudes and latitudes in the winter hemisphere is increased. During the westerly phase of the QBO on the other hand, the zero wind line is shifted toward the summer hemisphere, allowing planetary waves to propagate across the equator and effectively reducing the planetary wave activity in the winter hemisphere (*Ruzmaikin et al.*, 2005). This is illustrated in Fig. 2.8. Consequently, the occurrence of Rossby wave breaking in the surf-zone is reduced during the westerly phase of the QBO, leading to a stronger, undisturbed polar vortex and weaker horizontal mixing, while the easterly phase of

the QBO is associated with more vigorous horizontal mixing in the surf-zone and a weaker polar vortex due to an increase in wave activity. This effect was discovered by *Holton and Tan* (1980) and is therefore also known as the Holton-Tan effect.

2.2 Tracer Data Processing with Rényi Entropy (RE)

The Rényi entropy (RE), as used here for atmospheric analysis, is a measure of the chemical information content of the area under consideration. It is similar to the idea suggested by *Sparling* (2000) of characterising hemispheric probability density functions (PDFs) by using the Shannon entropy to define an "effective number of states" (*Sparling*, 2000) analogous to thermodynamics. A highly variable region, with a large number of air parcels containing different concentrations of a particular tracer, has a high entropy, since the tracer distribution has a detailed chemical structure. On the other hand, low entropy is associated with (almost) equal tracer concentrations everywhere, representing a field without any chemical structure (*Sparling*, 2000).

The RE statistical measure was introduced by Alfréd Rényi as a generalised form of the Shannon entropy information metric (*Rényi*, 1961). It can be written as:

$$RE(\alpha, b, N) = \frac{1}{1-\alpha} \cdot \ln\left(\sum_{i=1}^{b} p_i^{\alpha}(b, N)\right) \tag{2.17}$$

where $p_i(b, N)$ represents a discrete probability density function (PDF) derived from a histogram with N data points and b bins, and α is the exponent of the RE. For $\alpha = 1$, Eq. 2.17 converges to the Shannon entropy (*Beck and Schlögl*, 1993).[7] In *Krützmann et al.* (2008) and *Krützmann* (2008) it was shown that the RE can be applied to PDFs derived from chemical tracer fields of a chemistry-climate model, in order to identify tracer gradients that are associated with barriers to horizontal mixing. Specifically, the standardised[8] RE with $\alpha = 2$ was used to identify the mixing barrier at the Antarctic polar vortex edge in ten years of SOCOL model simulations of stratospheric methane (CH_4).[9] This standardised form of the RE is given in Eq. 2.18:

$$RE(2, b, N) = -\frac{1}{\ln(b)} \cdot \ln\left(\sum_{i=1}^{b} p_i^{2}(b, N)\right) \tag{2.18}$$

This form of the RE will also be used in the following, unless explicitly mentioned otherwise. It can be considered as a measure of the homogeneity of a PDF, i.e. how evenly the probabilities are distributed among all possible values. The maximum $RE = 1$ corresponds to a perfectly flat PDF – all values are equally likely.

[7] For $\alpha \to 1$ the RE converges to the Shannon entropy. This can be seen by applying l'Hôpital's rule to Eq. 2.17.

[8] The RE given in Eq. 2.17 can be standardised by dividing it by the maximum possible value, which is the logarithm of the number of bins used, $\ln(b)$.

[9] The RE is a monotonically decreasing function of α and other values of α could be used as well, but $\alpha = 2$ arguably gives the best bin weighting for the stratospheric application (see *Krützmann* (2008) for further details).

The probabilities that make up the PDFs, $p_i(b, N)$, are calculated by binning the chemical tracer mixing ratios within a particular region into a histogram with b equal-width bins and dividing the population of each bin by the total number of points N in the histogram.[10] In order to create a reliable representation of the local tracer distribution, zonal concatenation of data points is often performed, i.e. all data points at a particular latitude are used to create the histogram for that latitude. When considering large-scale dynamics in the stratosphere, daily variations in tracer concentrations at a given altitude can usually be neglected since vertical transport is relatively slow. Therefore, several days of data can be combined to further increase the number of points for creating the PDFs. In the following, the method of creating the PDFs is indicated by a subscript where appropriate. For example, when using 'zonal ten-day PDFs', i.e. including all data points at a particular vertical level and latitude from ten consecutive days, this is abbreviated as RE_{z10}. Other data windows used for creating atmospheric tracer PDFs include combining zonal data from ten days and three latitude bins (RE_{z10la3}), or combining the data from five latitude and nine longitude bins (RE_{la5lo9}).

The basic idea behind using the RE is as follows: a stratospheric barrier that prevents horizontal mixing (or slows it down considerably) will lead to a meridional gradient in the distribution of long-lived (relative to the mixing timescale) chemical trace gases to build up across the barrier (*Miyazaki and Iwasaki*, 2008). On either side of such a barrier, mixing can occur relatively unhindered, and randomly selected parcels of air are likely to contain very similar amounts of the chemical tracers present. Accordingly, a histogram (or PDF) of the concentrations of a particular tracer created from a sample of air parcels in such a well-mixed region can be expected to have a single strong peak close to the average mixing ratio of the tracer in this region, which drops off rapidly. If a histogram is created from data near the mixing barrier, however, air parcels with a range of tracer mixing ratios between the maximum on one side and the minimum on the other side of the barrier are likely to be present. Therefore, such a histogram is likely to be generally flatter and contain a much weaker peak with long tails or have multiple small peaks. As PDFs with strong peaks tend to have relatively low values of RE and flat distributions have high[11] RE, tracer PDFs created from well-mixed air masses have low values of RE while air close to a mixing barrier is likely to result in higher values of RE. This is illustrated in Fig. 2.9 which shows a meridional profile of the RE_{z10} between 550 and 1450 K for 18.10.2008 (i.e. using data from 9^{th} to 18^{th} October) calculated from satellite observations of N_2O volume mixing ratios gridded to a 1.5° latitude grid and interpolated to potential temperature levels (for more details on this data set see Sect. 2.3.3), together with the histograms for six locations marked A through F. The ten-day zonal data window results in most histograms having between 280 and 290 data points, which should be a sufficiently large number to obtain a reliable representation of the local tracer distributions. The blue dotted lines are zonal mean N_2O contours (in $ppbv$) averaged over the same time period.

A broad comparison between the RE pattern and the zonal mean N_2O contours shows

[10] As any histogram can be transformed into a PDF in this manner, the two terms are considered synonymous in the following.

[11] The maximum RE value of one corresponds to a perfectly flat distribution, i.e. a PDF where all values are equally probable.

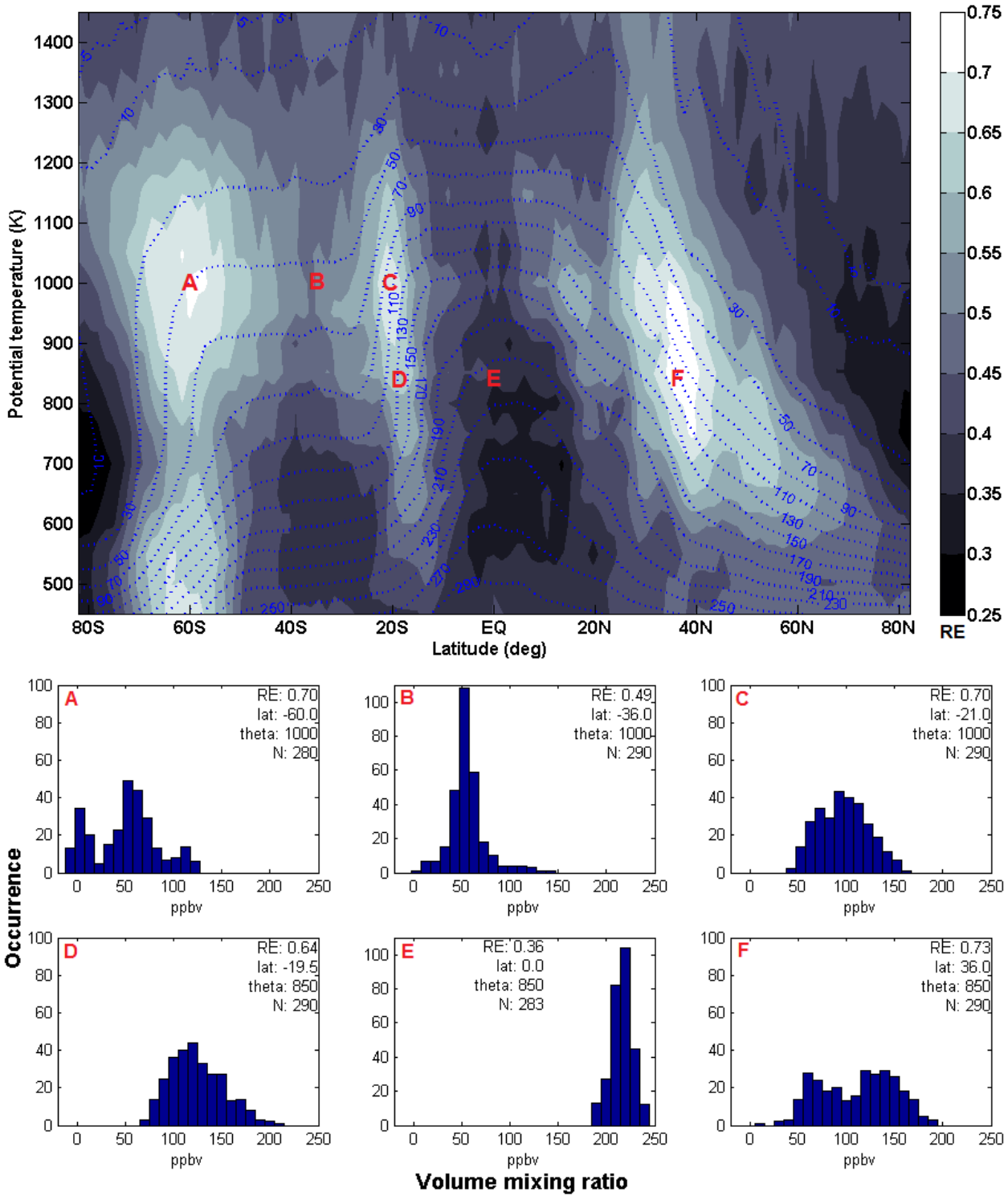

Figure 2.9: Meridional profile of the RE_{z10} for 18.10.2008 (using data from 9^{th} October to 18^{th}) calculated from global satellite observations of N_2O volume mixing ratios gridded to a 1.5° latitude grid and interpolated to potential temperature levels. The blue dotted lines are zonal mean N_2O contours (in $ppbv$) averaged over the same ten days. The histograms A to F show the data used for calculating the RE value at the corresponding locations. The numbers in the top right corner of the histograms are (from top to bottom) the calculated RE_{z10} value, the corresponding latitude, the potential temperature level (in K), and the total number of data points N, respectively.

that the RE_{z10} has its highest values in regions where a meridional N_2O gradient can be seen, i.e. where there are barriers to horizontal mixing. A closer look at the regions marked A through F in Fig. 2.9 and the corresponding histograms illustrates the underlying distributions for different values of RE_{z10}. At 850 K in the tropics (E in Fig. 2.9) the air contains relatively large amounts of N_2O and the tracer distribution has a single strong peak at 220 *ppbv* which drops off rapidly. This represents a rather inhomogeneous PDF and therefore the RE_{z10} value is quite small. Around 20°S, a strong meridional N_2O gradient is evident from the zonal mean contours in Fig. 2.9. As expected, the histograms in this region (C and D in Fig. 2.9) have a flatter appearance with a weak peak and large tails covering a wide range of N_2O mixing ratios, e.g. between 60 and 210 *ppbv* at 19.5°S and 850 K, which in turn leads to high RE_{z10} values. In the surf-zone on the other hand, the air is quite well-mixed by planetary wave breaking and therefore most air parcels contain similar amounts of N_2O. The histogram at 36°S and 1000 K (B in Fig. 2.9) is similar to the tropical distribution, but with the peak shifted to lower mixing ratios, i.e. centred around 50 *ppbv.* As expected, the RE_{z10} generally has lower values in this region, though not as low as in the tropics. At 60°S the mixing barrier and concomitant N_2O gradient between the surf-zone and the polar vortex again results in a flatter distribution of the N_2O histograms (A in Fig. 2.9) and higher values of RE_{z10}. In the northern hemisphere, large-scale mixing processes are still weak at this time of the year and the tropical N_2O mixing ratios drop off more gradually toward higher latitudes, with the strongest change occurring between 20°N and 40°N. The corresponding histogram at 36°N and 850 K (F in Fig. 2.9) displays a particularly wide spread of N_2O mixing ratios, ranging almost from 0 to 200 *ppbv*. Accordingly, the high-RE_{z10} region marking the northen hemisphere mixing barrier between the tropics and the subtropics is somewhat wider than its southern hemisphere counterpart. Figure 2.9 also illustrates that the value of the RE is largely independent of the absolute values of the underlying data and is more sensitive to the shape of the distribution.

This shows how the RE statistical measure can be applied to atmospheric tracer data for identifying gradients associated with mixing barriers. A more comprehensive analysis of the properties of the RE as a complexity measure is given in *Krützmann* (2008) and an investigation of the utility and limitations of the RE when applied to satellite observations of tracer concentrations is performed in Ch. 3. As the RE is a relative measure, it can theoretically be utilised to identify gradients in any kind of numerical data set, provided a sufficiently large data window is used. Therefore, the utility of the RE for identifying amplitude gradients in ground penetrating radar recordings of Antarctic snow and ice is tested in Ch. 4.

2.3 Atmospheric Data Sets

This section gives an overview of the various atmospheric data sets used in Ch. 3.

2.3.1 SOCOL Chemistry-Climate Model

The SOCOL model was the main data source for the initial study of the utility of the Rényi entropy as a mixing measure (*Krützmann et al.*, 2008 and *Krützmann*, 2008). Only a small part of the methane (CH_4) data set is used in Ch. 3 to compare the effect of a new data binning method to that used in previous work. Hence, only a brief summary of the model is given here.

The SOlar Climate Ozone Links (SOCOL) model v1.0, is a combination of the MEZON (Model for the Evaluation of oZONe trends) chemistry-transport model and the MA-ECHAM4 (Middle Atmosphere version of the European Centre Hamburg Atmosphere Model 4) global circulation model and is focused on simulating the chemistry and dynamics of the stratosphere and mesosphere. Control integrations for the years 1980-1999 were performed on the University of Canterbury Super Computer, with the sea surface temperatures and sea ice concentrations forced by corresponding values from the AMIP II (Atmospheric Model Intercomparison Project) database[12], while solar forcings and chemical sources and sinks were taken according to E. Rozanov and T. Egorova, PMODWRC (Physikalisch-Meteorologisches Observatorium Davos / World Radiation Center), Davos, March 2003. With the MEZON component, 41 chemical species with 118 gas phase, 33 photolysis, and 16 heterogeneous reactions are simulated. Due to the MA-ECHAM4 component, the horizontal resolution of SOCOL is 3.75° in latitude and longitude (T30 spectral resolution), and 39 pressure levels from the surface to 0.01 *hPa* are simulated, though the data output is re-gridded to 30 levels between 1000 and 0.01 *hPa*. SOCOL uses a simplified timescale consisting of 12 months with 30 days each. The data used here is output on a daily basis. Further details on the SOCOL model can be found in *Egorova et al.* (2005) and references therein.

2.3.2 MERRA Reanalysis

The Modern Era Retrospective analysis for Research and Applications (MERRA) is a high-resolution reanalysis provided by the NASA GMAO (Global Modelling and Assimilation Office) and is based on the GEOS-5 DAS (Goddard Earth Observing System Data Assimilation System Version 5) assimilation system (version 5.2.0). It is the main source for the horizontal-wind and temperature fields (u, v, and T) between August 2004 and November 2011, which is the main focus of the present study. For each 6-hourly data set throughout this period, the GEOS-5 system assimilates approximately four million observations from various sources (including the EOS satellites) during each analysis cycle (*Rienecker et al.*, 2011).[13]

The GEOS-5 assimilation uses a ½° latitude × ⅔° longitude horizontal grid and 72 pressure levels from the surface to 0.01 *hPa* (*Rienecker et al.*, 2011). The data used for this study is from the "DAS 3d analyzed state on pressure (inst6_3d_ana_Np)" product. This uses the native horizontal grid (½° × ⅔°), but with a reduced vertical resolution of 42 levels from 1000 to 0.1 *hPa*. For each day, four data points are given at each grid point,

[12] http://www-pcmdi.llnl.gov/projects/amip/AMIP2EXPDSN/BCS_OBS/amip2_bcs.htm (last accessed on 24.08.2013)

[13] The MERRA data products are available from: http://disc.sci.gsfc.nasa.gov/daac-bin/DataHoldings.pl (last accessed on 24.08.2013)

corresponding to the instantaneous value of the respective variable at 0:00 GMT, 6:00 GMT, 12:00 GMT, and 18:00 GMT.

In order to work with the data on isentropic levels, the horizontal wind fields were interpolated to potential temperature levels. Using the temperature data and Eq. 2.4, the potential temperature at each grid point and each pressure level was calculated. The wind fields were then interpolated linearly to the following potential temperature levels (in K): 350, 400, 450, 500, 550, 600, 650, 700, 750, 800, 850, 900, 950, 1000, 1050, 1150, 1250, 1350, 1450, 1700, 1900, and 2100.

Between 350 and 1050 K the level separation is 50 K. Above 1050 K the separation gradually increases to approximately match the vertical sampling of the original data. These levels correspond to an altitude range of about 12 to 50 km, covering most of the stratosphere. Figure 2.2 also illustrates the approximate altitude of every second of these levels for October 2009.

2.3.3 EOS-MLS Observations

The Microwave Limb Sounder (MLS) instrument on board the Aura satellite is part of NASA's Earth Observing System (EOS). It is a passive microwave sounder that uses measurements of the natural (thermal) emissions from a number of atmospheric constituents in five spectral bands (between 118 GHz and 2.5 THz) to derive vertical profiles of the atmospheric abundances of 15 chemicals as well as temperature, geopotential height, relative humidity and cloud ice water content (*Waters et al.*, 2006; *Livesey et al.*, 2011). The forward looking instrument's line-of-sight is effectively tangential to the Earth's surface. Each vertical profile consists of a series of measurements with increasing limb tangent heights from 8 to 90 km altitude (*Cofield and Stek*, 2006). The MLS instrument performs one vertical scan approximately every 25 seconds, resulting in over 3400 vertical profiles per day. The Aura satellite is in a near-polar orbit which allows measurements between 82°S and 82°N. It performs approximately 14 orbits per day. The constant frequency of the measurements means that observations are performed on an almost regular latitude grid with a grid-interval of 1.5°, starting at 0°. Only at high latitudes does the sampling become more dense, with eleven measurements between 79° and 82° (N and S) per orbit.

The present work uses the methyl chloride (CH_3Cl), carbon monoxide (CO), nitrous oxide (N_2O), and temperature data from the EOS-MLS Level-2 Version 3.3 Standard Atmospheric Product for 13.8.2004 to 24.11.2011. The data is available on a vertical pressure grid from the Goddard Earth Sciences Data and Information Services Center (GES DISC).[14] Using the temperature data, the examined chemical constituent fields are interpolated from the native pressure levels to the same isentropic levels as those used for the MERRA data set (see Sect. 2.3.2). The interpolation is preceded by a quality screening step. There are several quality flags for each profile and any profiles that do not meet the quality criteria described in the MLS documentation (*Livesey et al.*, 2011) for the respective chemical species are not included in the isentropic data set. In some cases the potential temperature levels lie outside the vertical range that is recommended for scientific use of the chemical data. For example,

[14] http://disc.sci.gsfc.nasa.gov/Aura/data-holdings/MLS (last accessed on 24.08.2013)

Table 2.1: MLS data characteristics. The quoted vertical resolution is for stratospheric levels only, the mesospheric resolution tends to be lower. Values are according to *Livesey et al.* (2011).

	useful levels	vertical resolution	single profile precision
N_2O	100 - 0.46 hPa	4 - 6 km	$\approx$ 13 $ppbv$ above 21 hPa $\approx$ 20 $ppbv$ below 21 hPa
CH_3Cl	147 - 4.6 hPa	4 - 6 km (below 14 hPa)	100 $pptv$
CO	215 - 0.0046 hPa	4 - 6 km	$\approx$ 15 $ppbv$ in stratosphere $>$ 150 $ppbv$ in mesosphere

for N_2O only the measurements between 100 and 0.46 hPa can be considered reliable. While the upper limit (0.46 hPa) lies above the highest potential temperature level used here (2100 K), the lower limit implies that the interpolated data on the lowest three levels (350, 400, and 450 K) could be (partially) based on unreliable data. Additionally, the precision of the data also has to be taken into consideration in some cases, e.g. while the N_2O data can be used up to 0.46 hPa, the precision at this altitude is low relative to the measured values and therefore only large scale averages (such as zonal averages) should be used, rather than individual measurements. Table 2.1 shows a summary of the data characteristics for the three chemical tracers.

Due to the latitudinal regularity of the satellite's sampling pattern, the tracer data is binned to its 'natural' 1.5° latitude grid whenever zonal resolution is not required. Given the higher measurement density, slightly narrower bins are used at the highest latitudes. Specifically, between 79.5°S and 79.5°N the latitude bins are centred at 1.5° intervals (e.g. the bin centred at 78°S includes all measurements acquired between 78.75°S and 77.25°S) and at higher latitudes another two bins are centred at 80.75° and 82° (N and S), giving a total of 111 latitude bins between 82°S and 82°N. The reduced bin widths at high latitudes are selected to approximately match the satellite's sampling pattern and to avoid large temporal fluctuations in the number of observations in each bin. This latitudinal binning results in an average of 29 measurements per day in the 1.5°-wide bins, and an average of 57, 57, and 42 points in the bins centred at 79.5°, 80.75°, and 82°, respectively.

An overview of the zonal mean stratospheric distributions of N_2O, CH_3Cl, and CO on potential temperature levels derived from the EOS-MLS data is given in the following sections. Nitrous oxide distributions are illustrated on the 550 and 850 K. The former is representative of the lower stratosphere, while the latter is typical for the middle stratosphere. Methyl chloride is only examined in the lower stratosphere as its concentrations are very low at higher altitudes. The opposite is the case for CO. It should be noted that slightly negative mixing ratios can occur in the MLS observations and should not in general be discarded (*Livesey et al.*, 2011).

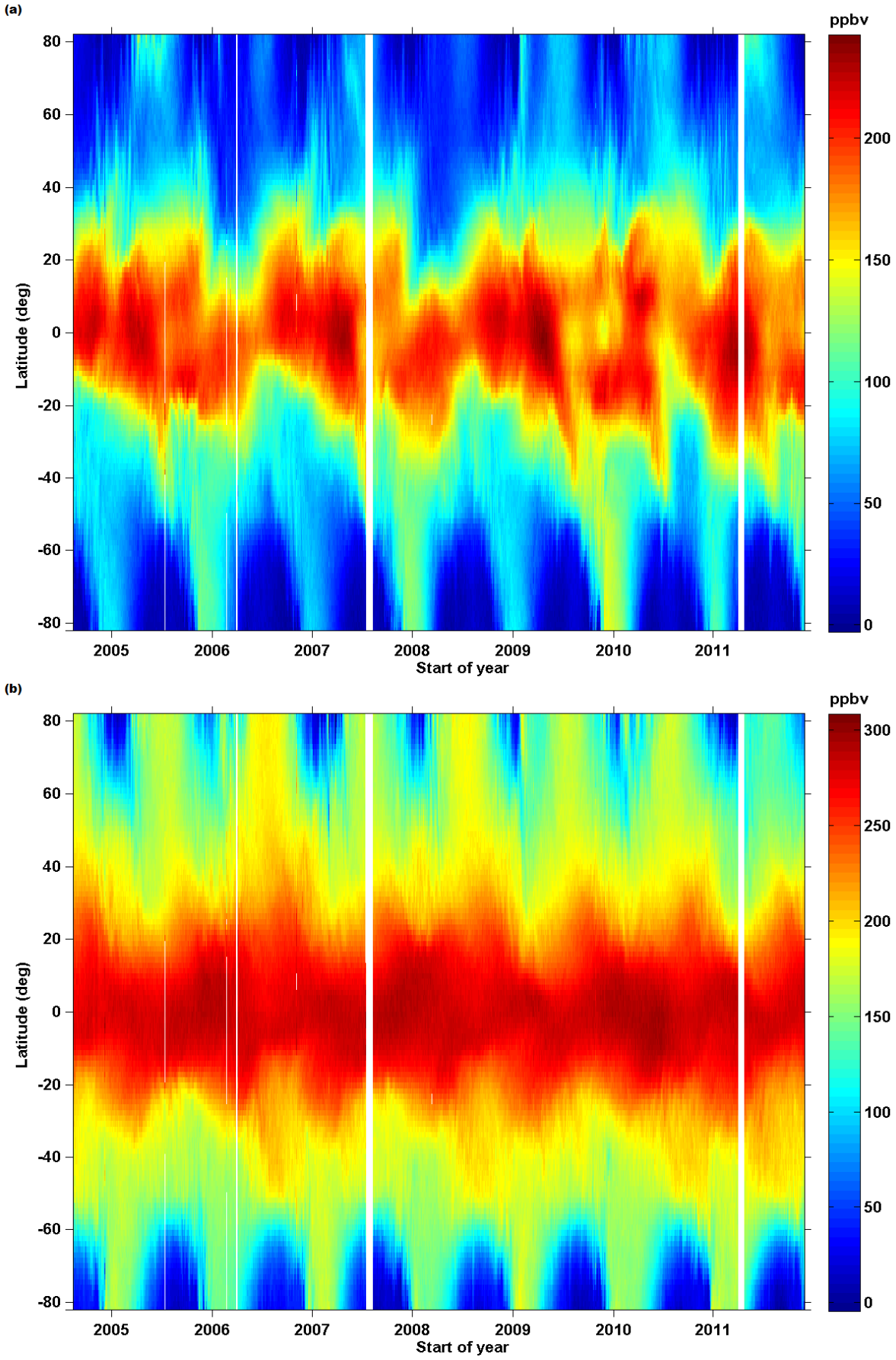

Figure 2.10: Zonal mean of EOS-MLS N_2O observations (in *ppbv*) interpolated to the (a) 850 K and (b) 550 K isentropic surface for August 2004 through November 2011. The observations are binned to 1.5° latitude bins. White lines indicate data gaps.

2.3.3.1 Nitrous Oxide

Figures 2.10a and b show the zonal mean structure of nitrous oxide (N_2O) volume mixing ratio on the 850 K and the 550 K potential temperature level, respectively, derived from EOS-MLS satellite observations from August 2004 through November 2011. White lines indicate data gaps. The general trend of lower mixing ratios at higher latitudes fits the expected structure of a trace species with a tropical source and a polar sink (see also Sect. 2.1.1). At 850 K, the oscillation between very low N_2O values (0-50 *ppbv*, blue in Fig. 2.10a) during the polar vortex periods in winter and intermediate mixing ratios (80-120 *ppbv*, turquoise/green) in summer, is clearly visible in both hemispheres. Figure 2.10a also shows that there is considerable variability in the magnitude and location of the tropical maximum of N_2O at 850 K throughout the observation period. Some of the variability is probably due to changes in the tropospheric source term, but other factors, such as the strength of the BDC, the phase of the QBO, and the meridional extent of planetary wave propagation related to this (Holton-Tan effect, see Fig. 2.8), can also affect the tropical tracer distribution (*Trepte and Hitchman*, 1992). This interannual variability appears to be somewhat reduced at 550 K (Fig. 2.10b).

A closer examination of Fig. 2.10a reveals that, in some years, air containing very high (tropical) N_2O mixing ratios (200-250 *ppbv*), which are usually restricted to latitudes between approximately 25°N and 25°S, appears to reach higher latitudes in the southern hemisphere for several months. For example, around mid-2009, an 'arm' of air with high, tropical mixing ratios (200 *ppbv*) extends from the southern hemisphere tropics to almost 40°S. Such apparent leak events of tropical air into the southern hemisphere surf-zone can be found in several years (i.e. 2005, 2007, 2009, 2010, and 2011) and extend vertically over a number of levels. These leaks are investigated further in Sect. 3.2.

Due to its relatively long stratospheric life-time ($>$ 100 days below 37 *km* / 5 *hPa* / 1200 *K, Andrews et al., 1987*), the large-scale distribution of N_2O on a given stratospheric level is largely determined by dynamics and transport, and is strongly affected by the barriers to horizontal mixing at the tropical pipe and the polar vortex edges. While the latter is only a seasonal barrier, the tropical pipe edge is permanent, though its permeability is higher in summer and also depends on the QBO (*Punge et al.*, 2009). As the source of stratospheric N_2O is in the tropics it can be assumed that changes in the tropical pipe have a stronger impact on the N_2O distributions than variations in the polar vortex. Other trace species, such as carbon monoxide (CO), have different source regions and therefore different horizontal distributions in the stratosphere, and can give complementary information about the presence of mixing barriers.

2.3.3.2 Methyl Chloride

Methyl chloride is a tracer with a similar stratospheric distribution to N_2O. In the stratosphere, it also has a tropical source and is photodissociated at higher altitudes. Its average stratospheric lifetime is somewhat shorter than that of N_2O and its typical volume mixing ratio is almost three orders of magnitude smaller. Figure 2.11 shows the zonal mean mixing ratio of CH_3Cl (in *pptv*) at 550 K for the available observation period. Comparing Fig. 2.11

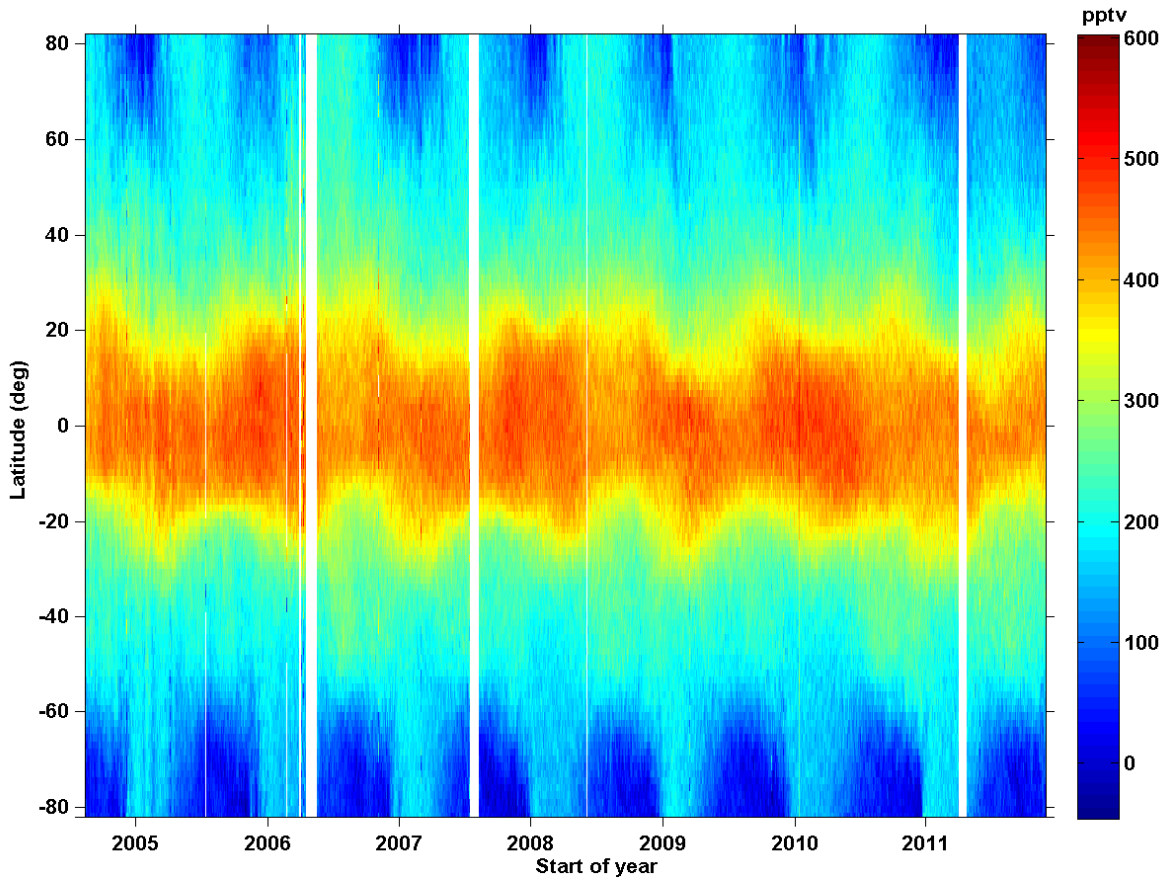

Figure 2.11: Zonal mean of EOS-MLS CH_3Cl observations (in *pptv*) interpolated to the 550 K isentropic surface for August 2004 through November 2011. The observations are binned to 1.5° latitude bins. White lines indicate data gaps.

to Fig. 2.10b shows the similarity between the distribution of CH_3Cl and N_2O. The highest CH_3Cl mixing ratios are found in the tropics, intermediate amounts in the subtropics, and intermediate to low amounts at high latitudes ($> 60°$) with lower values during winter. The interannual variability is relatively low, particularly in the southern hemisphere, though some of it might be concealed by the lower signal-to-noise ratio of the data.

Methyl chloride (CH_3Cl) volume mixing ratio is a recent product of the Aura-MLS instrument and has only been available since version 3. The quality of the retrieval has not yet been thoroughly tested, but is expected to be considerably lower than the quality of the N_2O data. The very low volume mixing ratios present in the stratosphere result in a much lower signal-to-noise ratio of the CH_3Cl measurements compared to N_2O. *Livesey et al.* (2011) report an approximate single profile precision of 100 *pptv*, corresponding to 40% of the average amount of CH_3Cl present at 550 K and to more than 100% above 800 K, though this is improved by zonal averaging in Fig. 2.11. However, the zonal mean distributions at levels above 550 K (not shown) become increasingly featureless as the signal-to-noise ratio deteriorates, and are not used.

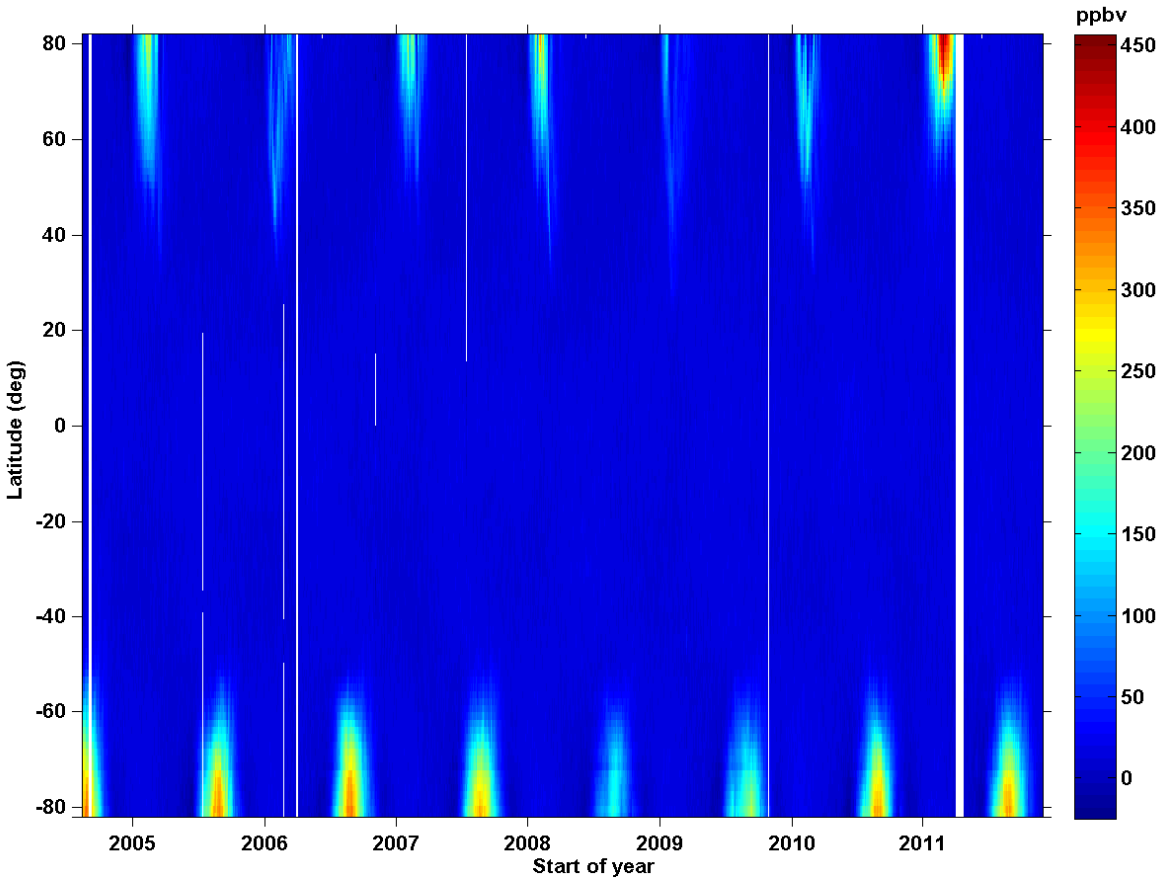

Figure 2.12: Zonal mean of EOS-MLS CO observations (in *ppbv*) interpolated to the 850 K isentropic surface for August 2004 through November 2011. The observations are binned to 1.5° latitude bins. White lines indicate data gaps.

2.3.3.3 Carbon Monoxide

Carbon monoxide (CO) is a stratospheric (and mesospheric) trace species with a different distribution than N_2O or CH_3Cl. This is because the main stratospheric sources of CO are photolysis of CO_2 (Eq. 2.10) and the oxidation of CH_4 (Eq. 2.11), while it is destroyed by the OH radical (Eq. 2.12). Carbon monoxide has a relatively short lifetime in the upper stratosphere (several weeks), which increases to several months in the mesosphere *(Jin et al., 2009)*. Accordingly, the mixing ratio of CO tends to increase with altitude. In the stratosphere, the highest values of CO are generally found in the polar regions during winter. Here, the downwelling arm of the BDC allows high-CO air from the upper stratosphere and lower mesosphere to travel down to lower levels. During this time, the lifetime of CO is also prolonged as no OH molecules are created in the polar darkness (*Jin et al.*, 2009). Figure 2.12 illustrates the general pattern of CO on the 850 K level.

The very low CO mixing ratios outside the winter polar regions in Fig. 2.12 demonstrate the sensitivity of CO's lifetime to the presence of sunlight. This suggests that lower latitude dynamics are not as important for the large-scale distribution of CO as they are for N_2O and CH_3Cl, since most of the CO is destroyed before advection can noticeably affect its distribution. Hence, CO is probably not a good tracer for investigating tropical mixing barriers, but might be more useful when considering the dynamics of the polar vortices,

since N_2O only occurs in small amounts inside these. Due to their different source and sink regions, CO and N_2O could provide complimentary information on the ongoing dynamics. This is discussed further in Sect. 3.1.3.

2.3.4 Trajectory Model

In Sect. 3.3, a two-dimensional trajectory model is used for advecting the MLS measurements over a time period of up to five days. On this timescale, stratospheric motion can be assumed to be adiabatic (*Holton et al.*, 1995), i.e. along potential temperature surfaces. Accordingly, a two-dimensional isentropic model should give a reasonable approximation of the motion of an air parcel in the stratosphere over a period of several days.

The trajectory model used here is based on a standard 4^{th} order Runge-Kutta integration scheme *(Press et al., 1997)* with a one hour integration time step. Between 70°S and 70°N the integration is performed on a latitude-longitude grid. At higher latitudes, a Cartesian coordinate system is used to avoid numerical issues at the poles. The underlying wind data is interpolated to the trajectory location by bilinear horizontal interpolation and linearly in time between the 6-hourly data points.

Figure 2.13 shows a comparison of 72-hour trajectories calculated with the two-dimensional trajectory model and the (three-dimensional) HYSPLIT (Hybrid Single Particle Lagrangian Integrated Trajectory) Model. The HYSPLIT trajectory model is available from NOAA (National Oceanic and Atmospheric Administration).[15] The tests were performed using NCEP/NCAR reanalysis data[16] as HYSPLIT does not currently support the use of MERRA data. A grid of 49 air parcels, with latitudes ranging from 5° to 65° in 10° intervals, and longitudes from 170°W to 120°E in 50° intervals, was initialised on 1.6.2009 at 00:00 UTC, in the northern (Fig. 2.13a and e) and in the southern hemisphere (Fig. 2.13b and f). Each air parcel was advected for 72 hours. With the two-dimensional model all calculations were performed on the 550 K potential temperature level, while HYSPLIT parcels were started at 22.4 km above mean sea level (vertical starting position must be entered in metres for the HYSPLIT model), the approximate equivalent of 550 K (see also Fig. 2.2).

Comparison of Fig. 2.13a with Fig. 2.13e and Fig. 2.13b with Fig. 2.13f shows that the horizontal component of the resulting trajectories from the two models are very similar in both hemispheres. Noticeable differences in the results are mostly limited to relatively short trajectories, i.e. where wind velocities are small. In these cases the small discrepancies in the starting altitudes can be sufficient to lead to different trajectories. Additionally, the shorter time step of the HYSPLIT model (six minutes) also affects the trajectories. In most cases, this effect is likely to be relatively small and therefore again more noticeable in short trajectories.

Figures 2.13c and d show the potential temperature of each HYSPLIT air parcel in Figs. 2.13a and b throughout the simulation period, respectively. The initial potential temperature values of the HYSPLIT air parcels (stars in Figs. 2.13c and d) illustrate that the starting altitude (22.4 km) does indeed correspond to the 550 K potential temperature level to within

[15] http://ready.arl.noaa.gov/HYSPLIT.php (last accessed on 24.08.2013)

[16] Available from http://www.esrl.noaa.gov/psd/data/reanalysis/reanalysis.shtml (last accessed on 24.08.2013)

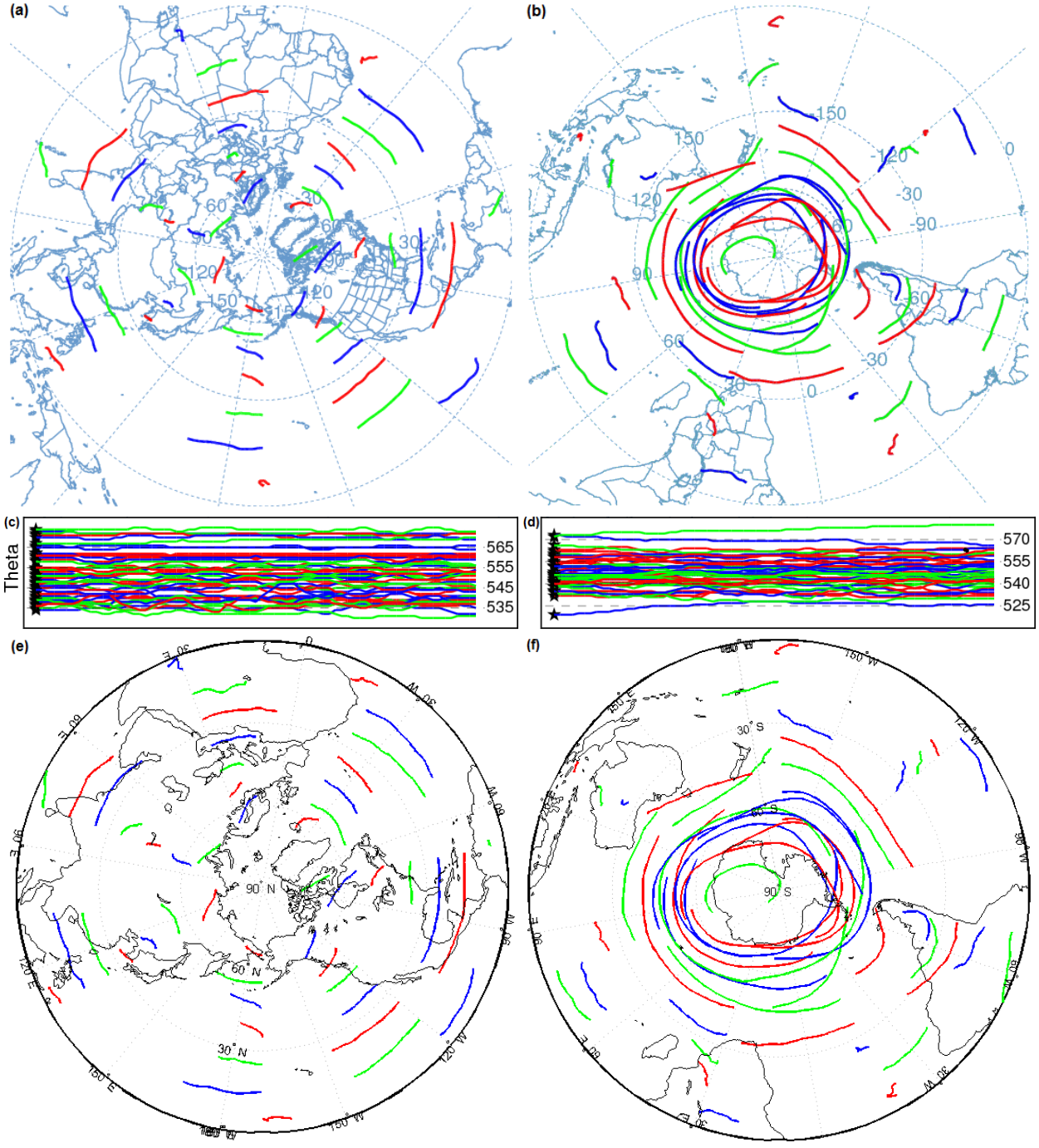

Figure 2.13: Comparison of trajectories calculated with HYSPLIT and a two-dimensional trajectory model using NCEP/NCAR winds for June 2009. Air parcels were initialised at 22.4 *km* altitude in the HYSPLIT model (a and b) and at 550 *K* potential temperature in the 2D-model (e and f), and advected for 72 hours starting on 1.6.2009 at 00:00 UTC. (c) and (d) show the potential temperature of each HYSPLIT air parcel in (a) and (b) throughout the simulation period, respectively.

$\pm 25\,K$. Figures 2.13c and d also demonstrate that the vertical displacement of the air parcels in terms of potential temperature is small over the 72-hour simulation period.

The overall good agreement with the HYSPLIT results shows that the simplified two-dimensional trajectory model can be used with confidence for the domain filling performed in Sect. 3.3.

2.4 Ground Penetrating Radar in Cryospheric Studies

The following sections focus on the cryospheric background for Ch. 4 and Ch. 5, starting with an overview of how ground penetrating radar is used for glaciological studies and followed by an introduction of some standard processing routines for this type of data. Finally, the locations and acquisition details of the radar- and snow-density measurements acquired in Antarctica are described.

Radar has been utilised for glaciological analysis of ice thickness and the detection of internal layers for many years, e.g. *Robin et al. (1969), Bentley et al.* (1979), *Bogorodsky et al.* (1985), *Eisen et al.* (2004), and *Rotschky et al.* (2006). While internal reflections were already observed in the earliest studies (e.g. *Jiracek and Bentley*, 1971; *Oswald and Robin*, 1973), they mostly focused on gathering ice thickness information using airborne systems, which allow covering large areas with relative ease, particularly in the remote regions of the polar ice caps. While airborne studies are still performed today (e.g. *Peters et al.*, 2005; *Hawley et al.*, 2006; *de la Pena et al.*, 2010), they are supplemented by a growing amount of ground-based studies (e.g. *Arcone et al.*, 1995; *Eisen et al.*, 2004; *Dunse et al.*, 2008), which allow a higher resolution of the stratigraphy of internal reflections in ice. This has become increasingly important as internal layer information, combined with ice core records, can be used to measure accumulation over large areas and long time-scales (*Arcone et al.*, 2004). The overall aim of these studies is to gain information about the internal structure and mass balance[17] of individual glaciers (*Bjornsson et al.*, 1996) or large continuous bodies of ice such as the Antarctic Ice Sheet (*Eisen et al.*, 2008) or the Greenland Ice Sheet (*Oswald and Gogineni*, 2008).

Due to the relatively low attenuation of radar signals in dry snow and ice, lower frequency (e.g. 25 *MHz*) ground penetrating radar (GPR) signals can propagate through many hundreds of metres of ice *(Arcone et al., 1995; Plewes and Hubbard, 2001)*. Reflections in GPR recordings can generally be caused by two things: sudden changes in conductivity and/or permittivity. In thick ice bodies, variations of these parameters can have four different reasons. Close to the surface, changes in density are the main cause for dielectric contrasts (see Sect. 2.4.2), while changes in conductivity due to acidic layers associated with large volcanic events are dominant further down (*Fujita et al.*, 1999). Furthermore, regions with a preferred crystal orientation can also form in the deeper parts of an ice sheet and differences in the alignment can create radar reflections (e.g. *Siegert and Hodgkins, 2000*). The deepest reflections are of course caused by the interface between the ice and the underlying bedrock

[17]The mass balance is the sum of all accumulation and ablation processes that influence a particular body of snow and ice. A positive (negative) mass balance implies that its total amount of ice increases (decreases) with time.

or in some cases by subglacial lakes (*Kapitsa et al.*, 1996). Additionally, a region with a noticeable lack of radar reflectors has been observed near the bottom of various parts of the polar ice sheets. The nature of this so-called echo free zone is not yet fully understood but it is probably linked to flow-induced disturbances of the coherent layering in ice (e.g. *Drews et al.*, 2009).

Identifying and tracking the various reflections in GPR soundings can give important glaciological and climatological information. For example, the reflections from the glacial bedrock can be used to estimate the total thickness of a glacier and give information about the subglacial topography (*Bogorodsky et al.*, 1985), which is important as an input for numerical modeling of glacier dynamics. Analysis of internal layers in ice and snow with commercial GPR systems for estimating accumulation has been demonstrated by *Arcone et al.* (2005), *Dunse et al.* (2008), and *Heilig et al.* (2010), amongst others. Internal reflections that can be tracked over long distances, are interpreted as isochronal horizons (*Robin et al.*, 1969) and can be used for synchronising ice core records from different locations (e.g. *Siegert and Hodgkins, 2000*) or for calculating accumulation rates by matching them to dated layers in ice- or firn cores and snow pits (*Eisen et al.*, 2008). Through this kind of stratigraphic analysis, it is possible to acquire long-term accumulation estimates of the Antarctic Ice Sheet (*Arcone et al.*, 2004; *Spikes et al.*, 2004) or to analyse local variability of recent accumulation in Greenland (*Dunse et al.*, 2008). However, reliable identification and tracking of reflections can be very laborious and usually involves considerable data processing, particularly when considering closely spaced and relatively weak reflections in snow (e.g. *Dunse et al.*, 2008; *Heilig et al.*, 2010). This is one motivation for attempting to use the *RE* as a simplified method for identifying amplitude gradients associated with internal reflections in GPR data in Ch. 4.

2.4.1 Accumulation and Compaction of Snow

In dry snow, the number of observed layers close to the surface and their densities largely depend on weather-related factors such as air temperature, humidity, and wind at the time of deposition, as well as pressure from additional snow or solar insolation shortly after it has settled down (*Harper and Bradford*, 2003). With increasing depth the added overburden pressure tends to gradually compress small snow crystals, reducing the pore space and leading to an increase in snow density. This affects the return of the radar signal, since it is the contrast in density between layers that causes the reflections (Sect. 2.4.2). As the snow is compacted by the increasing pressure with depth, neighbouring layers can merge, reducing the number of distinct layers and therefore the number of GPR reflectors. The detailed mechanisms causing this snow metamorphosis are highly complex and are largely influenced by temperature (both at the surface and in the snow), humidity, wind, and the overburden pressure caused by accumulation (e.g. *Bader*, 1954; *Alley et al.*, 1982; *Hoerhold et al.*, 2011).

Associating reflections in GPR recordings with layers from distinct accumulation or melt events, or depth hoar *(Arcone et al., 2004; Eisen et al., 2004; Helm et al., 2007; Dunse et al., 2008)* requires additional information about the density of the snow (and thereby about the velocity at which the radar signal travels, see Eqs. 2.20 and 2.21 below) and the depth and properties of particular internal layers that are likely to cause the observed reflections.

Firn cores and snow pits coincident with the GPR measurements can provide relatively high resolution point measurements of density, stratigraphy, and annual accumulation. By associating a reflection in the radargram with a particular layer found in the snow pit or firn core and estimating the age of that layer, the average annual accumulation since the deposition of that layer can be estimated. Analysing GPR data recorded in the same area and tracking the identified layers along intersecting profiles then allows an extrapolation of the point measurements to accumulation estimates for a larger region. Combined with accurate horizontal and vertical positioning information (e.g. from Global Positioning System (GPS) measurements), the tracked layer data can also be converted to 2D or 3D representations of the large-scale areal snow structure (e.g. *Dunse*, 2006). Snow accumulation can vary considerably even over relatively short temporal and spatial scales (*Eisen et al.*, 2008), and this variability is often represented in the undulations of internal horizons (*Vaughan et al.*, 1999). Therefore, detailed information about differences in accumulation from GPR surveys is essential to complement potentially unrepresentative point measurements from ice cores or snow pits.

Large-scale, long-term accumulation information is particularly relevant for understanding and estimating past and future changes in the extent and volume of the polar ice sheets, i.e. for determining the Arctic and Antarctic mass balances. The variability in the mass of polar ice sheets has important implications for sea-level rise and the global radiation balance (*Davis et al.*, 2005). In recent decades, satellite altimeters have also been used to estimate and monitor the Antarctic mass balance by measuring surface height changes around Antarctica (*Wingham et al.*, 1998; *Davis and Ferguson*, 2004; *Nguyen and Herring*, 2005). Key uncertainties for determining snow accumulation from changes in surface elevation (measured by satellite altimetry) are snow density and compaction (*Arthern and Wingham*, 1998) and the spatial variability thereof (*Drinkwater et al.*, 2001; *Nguyen and Herring*, 2005). The amount of snow compaction near the surface is related to mechanical settling during and immediately after accumulation, the overburden pressure by additional snow deposition, and the complex mechanism of temperature metamorphosis (*van den Broeke*, 2008), while melt metamorphosis is mostly restricted to coastal areas in Antarctica. Densification processes can also change the snow morphology, which affects the height retrieval from reflected radar waveforms such as those from the CryoSat-2 radar altimeter (*Wingham et al.*, 2006). Hence, a change in surface height as measured by satellite altimeters does not necessarily reflect a mass imbalance but may instead be caused by meteorological conditions affecting snow compaction. These uncertainties can only be quantified by means of ground truthing.

For the validation of satellite sensors, information on accumulation and compaction is normally not available over areas comparable to the satellite footprint. During the 2008/09 and 2009/10 field seasons, the author participated in the Antarctica New Zealand Event K053 during which a large amount of snow accumulation and snow morphology data was collected on land ice. Snow pit logs, firn cores, stake measurements, and GPR profiles were obtained from differing snow regimes in the Scott Base region, Ross Island, Antarctica (see Sect. 2.6). The new data set was acquired at three test sites comparable in size to the footprint of the CryoSat-2 radar altimeter and along one satellite track, as the data was intended to be used for validation of the satellite instrument. All radar measurements were repeated along the same tracks during the second season, potentially allowing compaction

rates to be estimated from changes in the separation of internal reflections, similar to the approach detailed in *Jenkins et al.* (2006).

Studies which measure compaction of snow are rare, since accurately measuring snow compaction can be complicated, particularly over larger areas. Recently, *Arthern et al.* (2010) presented an experimental setup for measuring snow compaction down to three distinct depth levels with very high temporal resolution. *Zwally and Li* (2002) developed a compaction model which shows good agreement with point measurements of compaction rates. Their results indicate that compaction of dry snow is a continuous process whose seasonal variability depends largely on temperature, though *Hoerhold et al.* (2011) point out that the real picture is somewhat more complex. Furthermore, compaction can vary considerably even over relatively short distances such as the footprint of radar altimeters (approximately 1.65 *km* in diameter in case of CryoSat-2)[18] and therefore point measurements can give unreliable estimates for the validation of satellite sensors. In Ch. 5, a method for estimating accumulation and compaction rates over large areas from internal reflection horizons in dry snow using high-frequency (500 *MHz*) GPR measurements is presented. The following section discusses the basic dielectric properties of snow and ice relevant for understanding the propagation of radio signals.

2.4.2 Dielectric Properties of Snow and Ice

Generally, the relative dielectric permittivity, ε_r, of a medium can be written as:

$$\varepsilon_r = \varepsilon_r' - i\varepsilon_r'' = \varepsilon_r' - i \cdot \frac{\sigma}{\varepsilon_0 \cdot \omega} \tag{2.19}$$

where ε_0, σ, and ω are the vaccum permittivity ($\approx 8.854 \cdot 10^{-12} \frac{s}{\Omega\, m}$), the conductivity (in $\frac{1}{\Omega\, m}$), and the angular frequency of the electromagnetic field, respectively. As mentioned earlier, the conductivity of dry snow is very small: typical values of σ for dry snow and cold ice are on the order of $1 \cdot 10^{-5} \frac{1}{\Omega\, m}$ (*Eisen et al.*, 2003). Therefore, the imaginary part of the relative permittivity (or dielectric loss factor), ε_r'', is typically on the order of $1 \cdot 10^{-3}$ for radio signals in the 100 *MHz* range. Accordingly, the imaginary part in Eq. 2.19 can usually be neglected for snow and $\varepsilon_r \approx \varepsilon_r'$ is assumed.

In dry snow, the main cause of radar reflections are changes in snow density (*Eisen et al.*, 2008). The real part of the relative dielectric permittivity, ε_r', of dry snow is nearly frequency independent for radio frequencies and can be related to its density, ρ (in $\frac{kg}{m^3}$), using the empirical formula (*Kovacs et al.*, 1995):

$$\varepsilon_r'(\rho) = (1 + 0.000845 \cdot \rho)^2 \tag{2.20}$$

Using density information, e.g. from snow pits or firn cores, to estimate ε_r' with Eq. 2.20, the velocity, v, of the GPR signal in snow can be calculated with Eq. 2.21:

[18] This refers to the single-shot footprint of the altimeter. With synthetic aperture processing the effective footprint of CryoSat-2 can be reduced to an area of approximately 1.65 *km* (across-track) x 0.3 *km* (along-track). (*Scagliola*, 2013)

$$v(d) = \frac{c}{\sqrt{\varepsilon'_r(d)}} \tag{2.21}$$

where $c \approx 3 \cdot 10^8 \frac{m}{s}$ is the speed of light in vacuum. Equation 2.21 can be used to convert the two-way-travel time (TWT) of a GPR signal to an approximate depth, d, of a reflection. However, for this conversion one needs to take into account the different densities of the various snow layers. To get an accurate correspondence between TWT and depth, the TWT through each consecutive snow layer has to be calculated separately, using the measured density and thickness of the snow in each layer. The individual TWTs through the layers then have to be added up down to the depth (or total TWT) of interest. Similarly, (an estimate of) the average density of the snow between two reflections is required to calculate the average velocity of the radar wave between these reflections with Eqs. 2.20 and 2.21. This average velocity can then be used for converting TWT between the reflections to physical separation.

Cold glacier ice has a density of $\rho = 917 \frac{kg}{m^3}$ and the dielectric permittivity is almost independent of depth: $\varepsilon'_r \approx 3.2$, which corresponds to a radar velocity of $v_{ice} = 0.168 \frac{m}{ns}$ *(Jiracek and Bentley, 1971)*.

2.5 Conventional GPR Processing

Most of the standard processing approaches for GPR data have been adapted from the processing of seismic recordings. Several of the basic processing steps are introduced in the following.

2.5.1 Nonstationarity Correction (Dewow)

Probably the most common artefact in GPR signals is nonstationarity. Particularly the initial part of a radar trace often displays a non-zero average which decays with time. This is usually due to initial oversaturation of the receiver by the first (and strongest) signal. The blue line in Fig. 2.14a shows the first 50 *ns* of an unprocessed 500 *MHz* trace. For the first 30 *ns*, the signal clearly does not oscillate around zero but has a strong low-frequency component that slowly decays. This signal saturation effect, sometimes referred to as 'wow', is particularly strong for Sensors & Software pulseEKKO GPR systems (all GPR data used in this thesis was recorded with a Sensors & Software pulseEKKO PRO system, see also Sect. 2.6) and Sensors & Software has designed a special correction filter called 'dewow'. The red line in Fig. 2.14a corresponds to the trace after this filter is applied.

The dewow is basically a running-mean filter, which is commonly used for DC- and low-frequency corrections in data processing of oscillatory signals. The average value within a certain window around each data point is subtracted from the value at the centre of the window. This is done independently for every point of each trace in a recorded line. The width of the window over which the average is calculated is given as "one pulsewidth" (*Sensors and Software Inc.*, 2003). However, it is not clearly defined what the pulsewidth of the 500 *MHz* transmitter for the pulseEKKO PRO system is. Figure 2.14b compares the

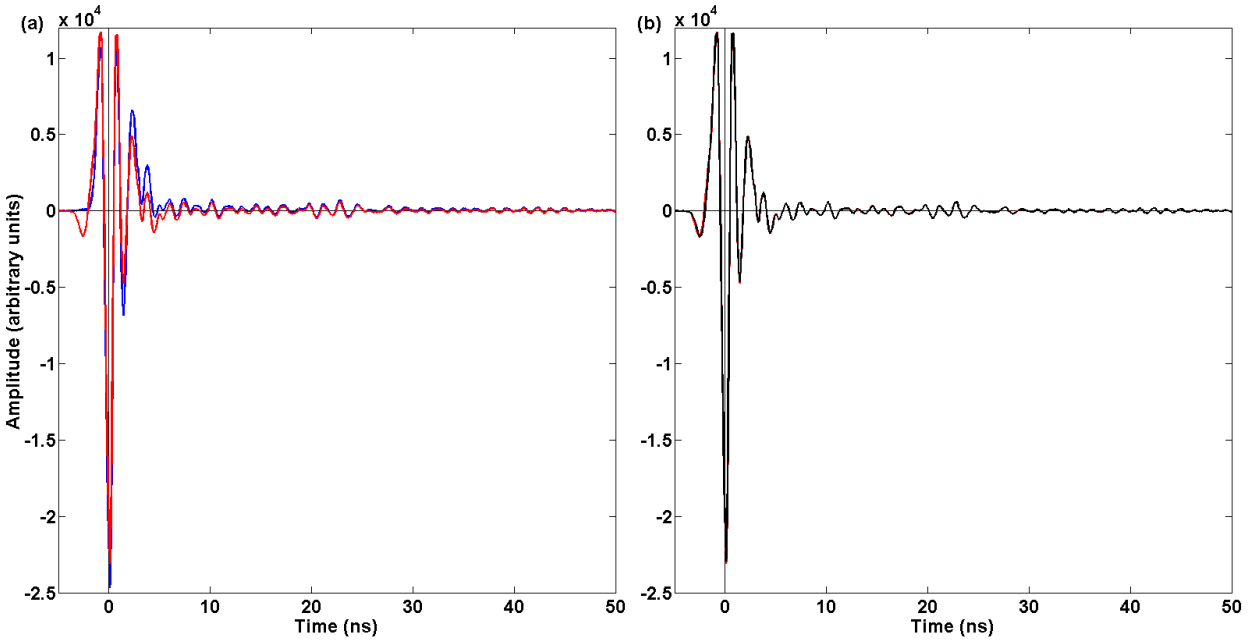

Figure 2.14: (a) Effect of the dewow filter on the first 50 *ns* of a typical 500 *MHz* radar trace in dry snow. The blue and the red line are the same trace before and after dewow filtering, respectively. (b) Using the same trace, subtracting the running average of a two-period (4 *ns*) window from the central point of the window gives a very similar result (black) to applying the dewow filter provided by the EKKO_View Deluxe software (red).

results of the dewow filter (red) and a manually applied running mean filter with a window width of 4 *ns* (black) to the same trace as in Fig. 2.14a. While the results do not match perfectly, they are very similar. This suggests that the pulsewidth (and the length of the dewow filter) is approximately equal to two periods of the nominal centre frequency of the system.[19] Presumably, the dewow filter supplied with the EKKO_View Deluxe software[20] is better at this particular processing step than the manual approach, since "Dewow has been optimized after many experiments over many years" (*Sensors and Software Inc.*, 2003). As this artefact is quite strong and very system specific, the filter should be applied to all data before any further processing. All GPR data used in the present work have undergone dewow filtering, except where explicitly mentioned otherwise.

It should be noted that the removal of the wow-artefact does introduce a different one. Subtraction of the running mean slightly changes the shape of the signal. Figure 2.14a shows that the dewowed data (red) has a small, negative peak that occurs before the onset of the signal in the unprocessed trace (blue). Due to the timing, this effect is sometimes referred to as a 'precursor'. This side-effect of the dewow filter should be kept in mind when applying further processing steps. However, as long as individual reflections are identified by the location of their peak amplitude rather than the onset of the reflection, the precursor does not have a noticeable effect on the results.

[19]For $f = 500\,MHz$ the period, τ, is equal to $\frac{1}{f} = 2\,ns$.

[20]EKKO_View Deluxe is the software package for GPR processing provided by Sensors & Software Inc.

2.5.2 Range Power Loss Compensation (Gain)

Another very common step in GPR processing is the application of a gain function to each trace. Thereby, the recorded value at each point is multiplied by a certain amount which increases with depth. This is to compensate for the power loss of the signal with depth, caused by spherical spreading and attenuation. Automatic gain control (AGC) or spreading and exponential compensation (SEC) are often used to determine the shape of the gain.

The aim of AGC is to create approximately equal amplitude levels along the whole trace. This is achieved by first calculating the average absolute amplitude of the trace and then scaling all amplitudes within a certain time window[21] so that the average within the window equals the overall average of the trace. This type of gain particularly emphasises weak reflections, but information about the relative reflectivity of different layers is lost. To avoid over-amplification of plain noise at the bottom of the trace, a maximum gain factor can be defined. Its value depends on the signal-to-noise ratio at the bottom of the trace. Automatic gain control is often used when taking a first look at recorded data in the field and values between 300 and 1000 are common settings for the maximum gain.

While the AGC is very useful for getting a first impression of the data, the SEC is a more realistic approach to compensating for the losses in a GPR trace. It consists of a linear and an exponential term. The linear term is meant to correct for the power loss in the signal due to the spherical spreading of the emitted wave. When the emitted wave travels a distance d from the source, the power per unit area is reduced by a factor of $\frac{1}{d^2}$. As the power of a wave is proportional to the square of the amplitude, the SEC linearly increases the amplitude with depth, thereby correcting for the loss of power over distance *(Yilmaz, 1987)*. Similarly, the exponential term corrects for power loss through attenuation. The power of the exponential can be adjusted depending on the lossiness of the medium. Additionally, a maximum amplification factor can be determined, for the same reason as for the AGC.

The attenuation loss is proportional to the imaginary part of the dielectric permittivity of the medium, which in turn is proportional to its conductivity (Eq. 2.19). However, as mentioned in Sect. 2.4.2, the conductivity of dry snow (as well as ice), and therefore the imaginary part of its permittivity, is relatively small and can usually be neglected *(Kovacs et al., 1995)*. Hence, the exponential term of an SEC can be expected to be rather small and can be omitted for relatively shallow profiles (*Arcone et al.*, 2004). Accordingly, a simple linear gain function is sufficient to correct for the geometrical spreading of the GPR signal in high-frequency profiles of dry snow.

For most GPR surveys application of a gain function is essential. The $\frac{1}{d^2}$ power loss means that the received signal amplitudes can vary by several orders of magnitude from the start to the end of a long (deep) radar trace, particularly since the radar wave has to cover the distance to any subsurface reflector twice before reaching the receiver. While a suitable gain function can compensate for these losses quite well, deep reflections tend to have a smaller signal-to-noise ratio and can be hard to identify even after gaining of the data. Therefore, frequency filters are often used to remove noise from the data.

[21] Usually the time window is chosen to be a multiple of the period of the nominal centre frequency of the system.

2.5.3 Frequency Filters

Frequency filters can be applied in many different ways to GPR data and for a variety of reasons, most of which have to do with suppressing noise. This can be coherent, low-frequency noise caused by, for example, nearby metal parts when using unshielded antennae, system noise due to the recording equipment, or ambient noise. The latter is usually what causes the deterioration of the signal quality of deeper reflections and has relatively high frequencies. Therefore, applying a simple low-pass filter can often already improve the data quality considerably. The cut-off frequency above which all frequencies are suppressed should be chosen according to the characteristics of the emitted waveform in order to avoid removing frequencies that are actually part of the signal.

Even more common are trapezoidal band-pass filters. These filter out any frequencies that are not within the limited range of frequencies that are considered to be part of the main signal. Two 'outer' and two 'inner' frequency limits are selected. Between the outer and the inner limits the spectrum of the data is gradually damped down to zero, in order to avoid the strong artefacts that sudden cut-offs can cause. *Belina et al.* (2009) for example use a 0/50 - 300/500 trapezoidal filter for a GPR system for which they measured an effective centre frequency of 110 *MHz*. This means that all frequencies between 50 and 300 *MHz* are left unchanged, while the amplitudes of frequencies between 0 and 50 *MHz* are scaled by a function that increases from zero at 0 *MHz* to one at 50 *MHz*. Similarly, the amplitudes of frequencies above 300 *MHz* are gradually scaled down until 500 *MHz*, above which all frequencies are completely removed. In this case the pass-band is relatively wide. *Dunse et al.* (2008) for example, use somewhat narrower limits: for GPR data with a nominal centre frequency of 500 *MHz* they use a 350/430 - 680/820 *MHz* filter, while their 800 *MHz* data is filtered with a 620/720 - 950/1100 *MHz* band-pass. There are no set rules on how to chose the limits of a low- or band-pass: too narrow limits can result in important information being lost, while too wide limits will allow more noise-related frequencies to remain in the data. Accordingly, the actual frequency content of the emitted signal should be taken into account when using frequency filters for noise suppression.

2.5.4 Stacking and Background Subtraction

One of the simplest ways to increase the signal-to-noise ratio of GPR data is to record several traces at the same location and then average them to create a single trace. This is referred to as stacking. Thereby, statistical noise averages out while the signal adds coherently and becomes (relatively) stronger. Ideally, the transmitter and receiver should be at identical locations for all shots that are to be stacked. However, traces that have been recorded very close to each other are likely to be very similar and stacking them can still improve the data quality, if it is reasonable to assume that the composition of the subsurface does not change significantly within the relevant horizontal interval. *Moore and Grinsted* (2006) suggest that, when acquiring GPR data with a moving system, stacking in the field should be avoided – particularly since it can be applied quite easily in the office later. While stacking of multiple neighbouring shots obviously reduces the horizontal resolution of a data set, it can be very useful for emphasising weaker signals in the deeper regions of a transect. Generally, stacking

improves the signal quality of continuous reflectors that are parallel to the surface, such as annual layers in snow, but can be detrimental to signals from dipping- or point reflectors, such as the sides of a glacier bed or an individual rock buried in ice or snow.

System limitations, system geometry, or other external factors can sometimes create relatively strong noise that lies within the system's bandwidth, is coherent throughout many traces, and can therefore not be removed by stacking or frequency filtering. This consistent background noise, often referred to as 'ringing', appears as bright or dark horizontal bands within 2D-plots of a GPR transect. It can be corrected for by subtracting the average trace of the whole transect from each individual trace, which is known as background subtraction. It can also be used for removing similar artefacts that may be caused by deconvolution (see Sect. 5.1).

2.5.5 Envelope Calculation

Another frequently used procedure is to calculate the envelope of radar traces via the Hilbert transform (e.g. *Taner et al.*, 1979). It is a simple way to remove the oscillations of the signal which are largely due to the carrier wave, though it does remove the phase information as well which can sometimes be useful. The Hilbert transform, HT, of the received (real) signal, $s(t)$, is used as an estimate of the imaginary part of the analytical signal, $z(t)$:

$$z(t) = s(t) + i \cdot HT(s) \tag{2.22}$$

The envelope, $Env(s)$, is then calculated by quadratically adding the real and imaginary parts of $z(t)$ (*Moore and Grinsted*, 2006):

$$Env(s) = \sqrt{s(t)^2 + HT(s)^2}. \tag{2.23}$$

The resultant trace gives a picture of the instantaneous amplitude of the received signal.

The Hilbert Transform of a function $g(t)$ is defined by the integral:

$$HT(g) = \frac{1}{\pi} \int_{-\infty}^{\infty} \frac{g(\tau)}{t - \tau} d\tau \tag{2.24}$$

Equation 2.24 can also be written as the convolution of $g(t)$ with the function $\frac{1}{\pi t}$:

$$HT(g) = g(t) \star \frac{1}{\pi t} \tag{2.25}$$

where $\star$ is the convolution operator. The convolution of two functions, $g(t)$ and $f(t)$, is defined as:

$$g\,(t) \star f(t) = \int_{-\infty}^{\infty} g(\tau) \cdot f(t - \tau) d\tau \tag{2.26}$$

Convolution can be pictured as 'scanning' one function, g, with another (filter-) function, f, like, for example, when observing the spectrum of a star with a coloured filter. The colour of the filter determines which part of the spectrum is viewed, i.e. which frequencies are allowed through the filter. Solving a convolution integral like Eq. 2.24 can be quite complicated. It is

therefore often solved by using the Fourier transform and the so-called convolution theorem instead. According to the convolution theorem, the Fourier transform of the convolution of two functions, f and g, is equal to the pointwise multiplication of the Fourier transforms of the individual functions (*Bracewell*, 2003):

$$FT(f \star g) = FT(f) \cdot FT(g) \tag{2.27}$$

The Fourier transform of a function, g, can be defined as:

$$FT(g)(\omega) = \frac{1}{\sqrt{2\pi}} \int_{-\infty}^{\infty} g(t) \cdot e^{i\omega t} dt = G(\omega) \tag{2.28}$$

which takes the function from the time-domain into the frequency-domain. The frequency-domain representation of a function, referred to as the frequency spectrum, is often written in capital letters, i.e. $FT(g(t)) = G(\omega)$. The inverse Fourier transform that returns the function to the time-domain is:

$$IFT(G)(t) = \frac{1}{\sqrt{2\pi}} \int_{-\infty}^{\infty} G(\omega) \cdot e^{-i\omega t} d\omega = f(t) \tag{2.29}$$

Applying the convolution theorem (Eq. 2.27) to the convolution form of the Hilbert transform (Eq. 2.25) for a trace $s(t)$ gives:

$$FT(HT(s)) = FT(s) \cdot FT(\frac{1}{\pi t}) \tag{2.30}$$

Using $FT(\frac{1}{\pi t}) = -i \cdot sgn(\omega)$ and the notation $FT(s) = S(\omega)$, Eq. 2.30 can be written as:

$$FT(HT(s)) = (-i) \cdot sgn(\omega) \cdot S(\omega) \tag{2.31}$$

where $sgn(\omega)$ is the sign function:

$$sgn(\omega) = \begin{cases} -1 & if\ \omega < 0 \\ 0 & if\ \omega = 0 \\ 1 & if\ \omega > 0 \end{cases}$$

The inverse Fourier transform of Eq. 2.31 then returns the Hilbert transform, $HT(s)$, of the input trace, $s(t)$, and can be used to calculate the envelope of the trace with Eq. 2.23.[22]

The Fourier transform in general (Equations 2.28 and 2.29) and the convolution theorem in particular (Equation 2.27) are defined for infinite and stationary time series. However, they can be applied to discreet and finite time series in a similar manner via the discrete Fourier transform (DFT):

$$DFT(g)(\omega_k) = \frac{1}{N} \cdot \sum_{n=0}^{N-1} g(t_n) \cdot e^{-2i\pi(\frac{\omega_k}{N})t_n}. \tag{2.32}$$

[22]Equation 2.31 also shows that the Hilbert transform can be interpreted as the application of a phase shift of $+\frac{\pi}{2}$ to the negative frequencies ($\omega < 0$) and a phase shift of $-\frac{\pi}{2}$ to the positive frequencies ($\omega > 0$) of the input signal.

The DFT implies that the time series, $g(t_n)$, infinitely repeats itself and requires the function to be sampled at a constant rate. The sampling interval, $\Delta t = t_n - t_{n-1}$, with which the data is acquired determines the maximum frequency that can be resolved with the transform, $\omega_{max} = \frac{1}{4 \cdot \pi \cdot \Delta t}$, and the number of data points, N, determines the number of frequency bins in the transform. In the context of GPR trace analysis, this poses certain limits on the resolution of the results. While perfect data at infinite resolution would make it possible to distinguish between layers that are very close together, the discreet nature of any real measurement can lead to interference of several close reflections, making them look like one (possibly distorted) reflection.

Using the DFT, the envelope calculation can be performed particularly quickly for discrete signals, such as those recorded with GPR system, thanks to the fast Fourier transform (FFT) algorithm (e.g. *Bracewell*, 2003). In the present work, the implementation included in the EKKO_View Deluxe software package (*Sensors and Software Inc.*, 2003) is used whenever envelope detection is required. The Fourier transforms required for deconvolution on the other hand (see Sect. 5.1), are performed via FFT algorithms included in the MATLAB™ software package.

2.6 Cryospheric Data Acquisition

This section describes the locations at and methodologies with which the Antarctic GPR and snow data used in Ch. 4 and Ch. 5 were acquired.

2.6.1 Stake farms, Snow Pits, and Firn Cores

Three stake farms were established on the land ice of the McMurdo Ice Shelf and on Ross Island, Antarctica (Figs. 2.15a and b), in November 2008 and revisited in 2009. The measurement sites are located within 30 *km* of New Zealand's Scott Base in different climatic settings and named L1, L2, and L3 (see Fig. 2.15b).

The stake farms were set up to measure snow accumulation over a one year time period and to allow repeat GPR measurements along the same profiles. At L1 and L2, 81 bamboo stakes were installed on a regular 800 m × 800 m grid at 100 m intervals. The distances between stakes and the regularity of the grid were established with centimetre accuracy using a total station (electronic theodolite and distance meter). The stake in the southwest corner of each farm was labelled A1. The stake in the northeast is I9, with numbers increasing from west to east. The layout of a site is illustrated in Fig. 2.15c. As the data acquisition was conducted as part of a validation experiment for the CryoSat-2 satellite, the sites were oriented along anticipated satellite ground tracks.[23] For topographic and safety reasons, site L3 was reduced to a 400 m × 400 m grid of 25 stakes. Only odd numbered labels were used in this case to maintain consistent nomenclature for the corners (see Fig. 2.15d). In addition to the stake farms, a profile of 20 stakes was established between L1 and L2 with a separation of approximately 1.6 *km* between the stakes. These were marked S2 to S20 (the

[23]Originally, the ground measurements were intended to be coincident with satellite overpasses but, due to several major delays, the launch of CryoSat-2 did not occur until April 2010.

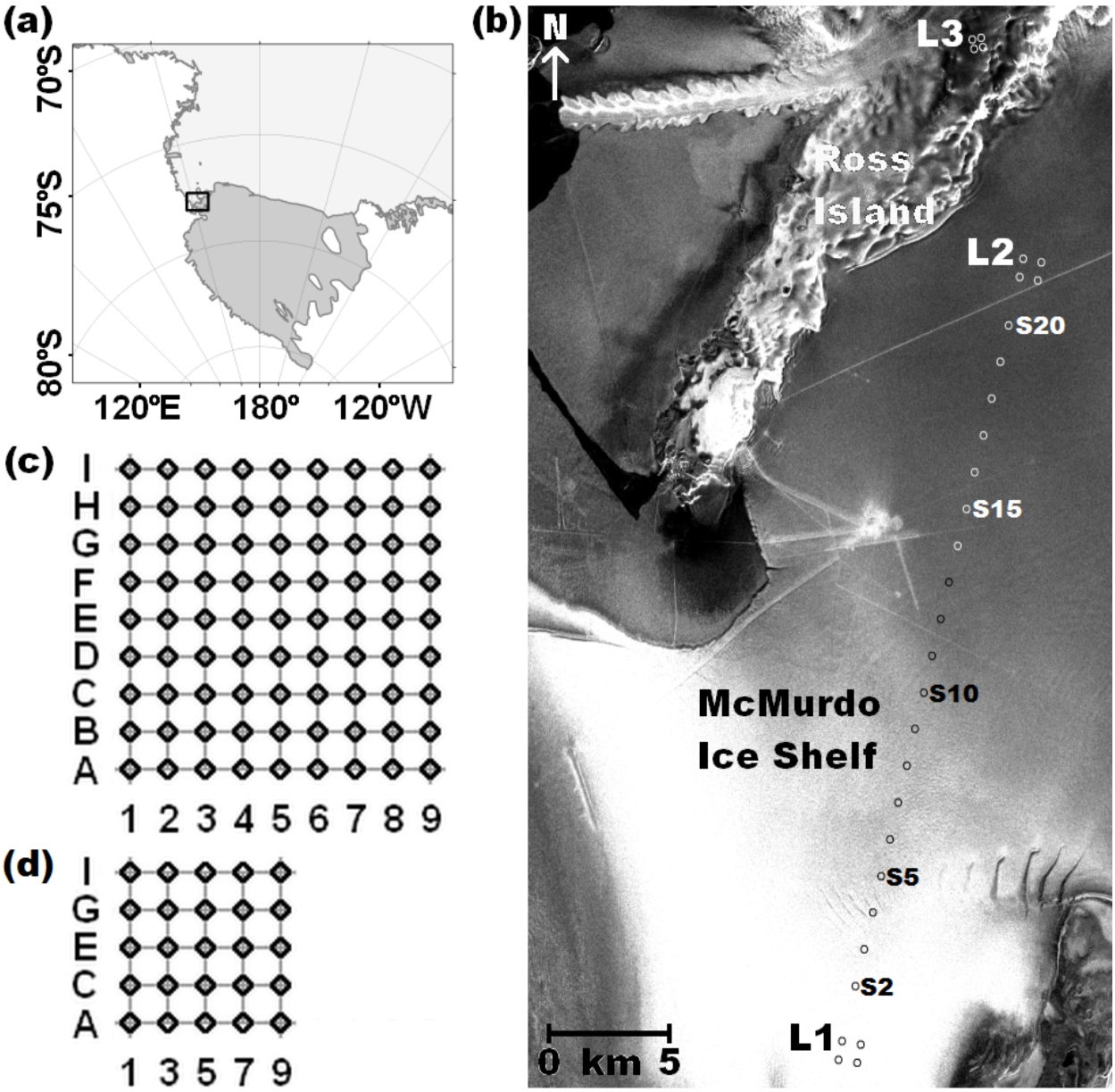

Figure 2.15: (a) The Ross Sea region. (b) Measurement area in the western Ross Sea region and corner points of stake farms on the McMurdo Ice Shelf (L1 and L2) and on Ross Island (L3). The circles between L1 and L2 indicate the locations of additional stakes installed for accumulation and radar measurements, labelled S2 to S20. (c) Outline of the measurement grid and numbering of the stake farms L1 and L2. (d) Outline of the reduced grid at L3. (Envisat ASAR image courtesy ESA)

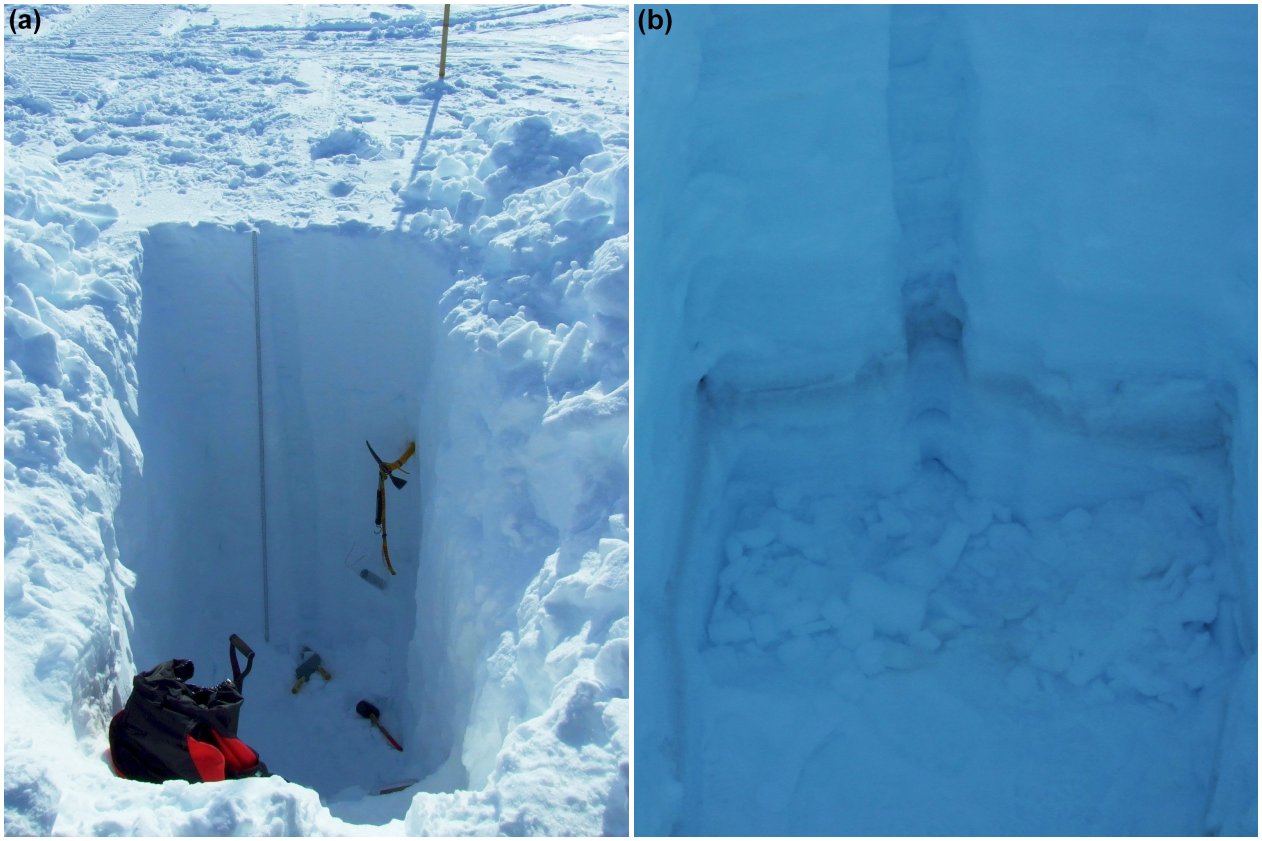

Figure 2.16: (a) 2 *m* snow pit with density profiling equipment and (b) a dust layer found near the bottom of a 3.3 *m* snow pit at L2 in 2008. (Photos: W. Rack)

first stake, "S1´´, closest to the site L1, was not installed), with numbers increasing towards L2 as indicated in Fig. 2.15b.

Previous studies indicate that L1 is located in an area of low accumulation and frequent summer melting (*Heine*, 1967), on an almost stationary part of the ice shelf. L2, situated in Windless Bight, features considerably higher accumulation rates. Based on Scott Base temperature records, occasional summer melting was expected at this site. However, no melt layers were observed in the upper eight metres of snow. GPS measurements corrected with base station data from Scott Base yielded an ice shelf movement of 58 *m* towards the southwest between November 2008 and October 2009. The third test site, L3, is located on the western slopes of Mt. Erebus (Ross Island), at an altitude of approximately 350 *m.a.s.l.*, in the dry snow zone and on undulating terrain. Here, GPS measurements showed that this area had moved 3.4 *m* towards the Erebus Glacier Tongue between the measurement campaigns.

To establish the stratigraphy and depth-density relationship of the top few metres of snow, density profiles were taken in at least one snow pit at each site in both years (Fig. 2.16a). Layers were first identified visually starting from the surface, their depth and thickness was measured and the weight of each layer determined. To this end, a small metal tube (density tube) was pushed vertically into the snow from above until it contained the full layer. The snow column inside the tube was then weighed with a spring balance. By dividing the weight of the snow by the known volume it occupied (cross-section of the density tube

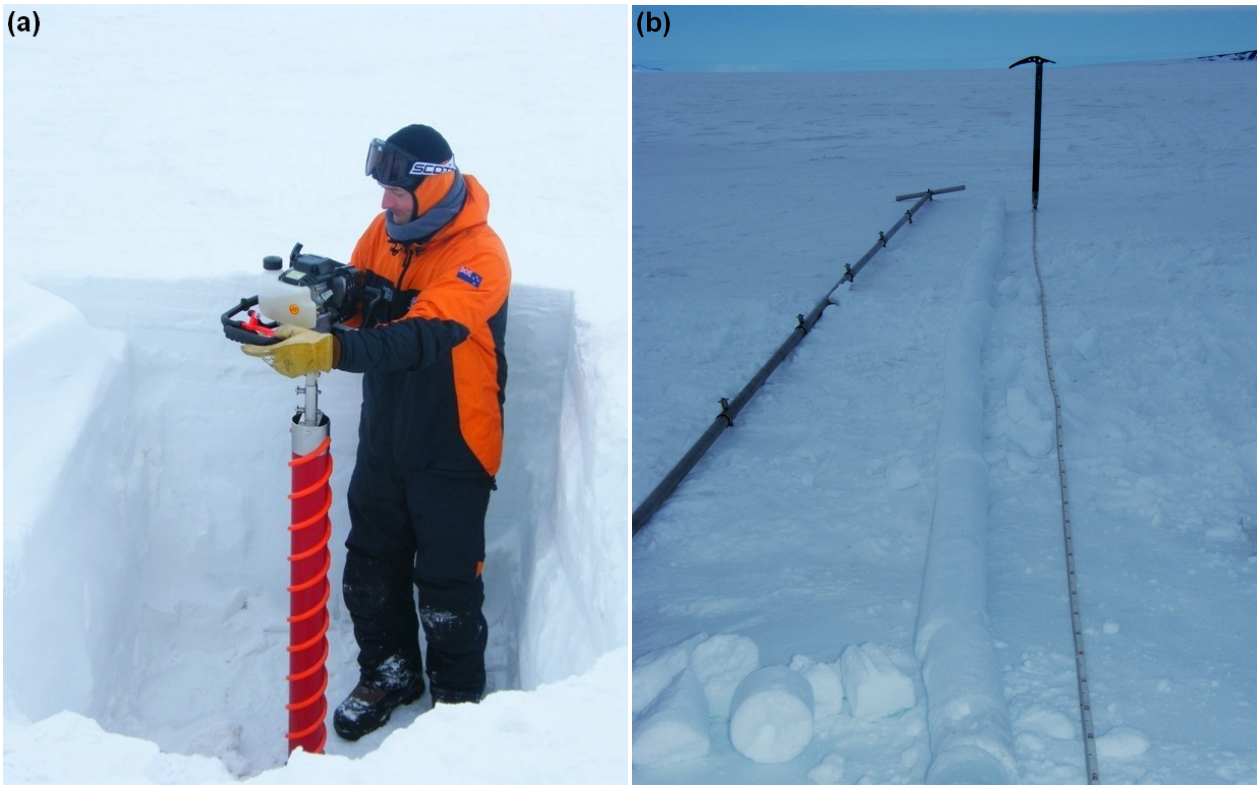

Figure 2.17: (a) Setting up the firn core drill in a shallow snow pit. (b) Firn core extracted during the 2009 field work. A tape measure was laid out next to the core to gauge the depth of individual segments. The notches on the metal rod lying approximately parallel to the core are one metre apart. (Photos: N. Kruetzmann)

× thickness of the layer) the density can be calculated.

Occasionally, darker layers containing considerable amounts of aeolian dust (dust layers) can be found in the snow column caused by, e.g. volcanic eruptions or very strong winds (dust storms). One such dust layer was identified in a 3.3 m snow pit at L2 in 2008 (see Fig. 2.16b). This layer is known to be associated with a severe storm in May 2004 (*Xiao et al.*, 2008). From the depth of the layer combined with the density profile, the accumulation since the storm can be estimated (see Sect. 5.4).

In addition to the snow pits, a firn core was drilled and logged at each site in 2009 to obtain snow density profiles up to eight metres deep. Due to the softness of the surface snow, the drilling was started from the bottom of a shallow snow pit (usually about 1 m deep) to reduce depth errors due to compression of the snow in the core and around the drill hole (see Fig. 2.17a). Density information up to the surface can be drawn from the snow pit profiles nearby. Cores were retrieved in segments of up to 1 m and laid out on the surface for visual inspection and depth calibration (Fig. 2.17b). The density profile was then derived by sawing and weighing the core in 10 cm segments and dividing by the volume of each segment.[24]

To measure the snow accumulation occurring between the two field seasons across the measurement sites, the total length of each bamboo stake and its height above the surface after being installed was recorded in 2008. The measurement of height above the surface was

[24]Occasionally, smaller segments were cut if a particularly distinct layer was visible.

repeated for each stake in 2009. The decrease in stake height is then used to calculate the total accumulation in $\frac{kg}{m^2}$ during the intervening time period. Basic conversion of the difference in stake height to $\frac{kg}{m^2}$ requires information about the average density of the accumulated snow which can be gained from the snow pit density profiles from each site. However, this method tends to underestimate the actual accumulation as it does not take into account that the snow between the bottom of the stake and the original surface is compressed through natural settling and the added overburden pressure of new snow, resulting in an effective lowering of the original surface relative to the stake. *Takahashi and Kameda* (2007) showed that the effect of compaction can be taken into account by using the snow density at the base of the stake when converting the change in stake height to $\frac{kg}{m^2}$. The method is based on the assumption that the density profile remains constant with time (also known as Sorge's law; *Bader*, 1954) and that the base of the stake is 'frozen in place', i.e. does not shift relative to the surrounding snow. Both assumptions are likely to hold as long as there is no excessive summer melting and if the time between measurements is relatively long. Using the recorded total stake lengths and the height above the surface in 2009, the depth of the stake base is calculated. The snow density at this depth is then derived from the snow pit profile measured at the respective site.

2.6.2 GPR of Dry Antarctic Snow

Along the grid lines of the stake farms, a multichannel Sensors & Software pulseEKKO PRO GPR system with two pairs of antennae working at a nominal frequency of 500 MHz and 1 GHz, respectively, was used to acquire reflection profiles of the subsurface. The system setup is illustrated in Fig. 2.18a. The pairs of shielded 500 MHz and 1 GHz antennae (yellow boxes) are mounted on plastic skid plates with an antenna separation of 0.23 m and 0.15 m, respectively. A GPS antenna is installed between the skid plates, and an odometer wheel, which triggers the radar traces at regular intervals, is attached to the rear antennae pair. The pulseEKKO PRO data video logger (DVL) which records and displays the acquired data is installed in a wooden box on a separate plastic sled that is attached in front of the antennae. The box is used to keep the batteries and recording equipment warm and free of snow. It also has a plastic window in its lid to allow viewing the DVL screen without opening the box. However, due to the brightness of the Antarctic environment and the low contrast of the screen, it was nevertheless necessary to open the box to view and operate the DVL. Using a waist harness attached to the plastic sled, the whole system was pulled along the grid lines of the established stake farms at a slow walking pace (Fig. 2.18b).

An analysis of the 1 GHz data is not performed in this thesis because, similar to the results with the 500 MHz data (see Ch. 4), the RE analysis of the 1 GHz recordings was unsatisfactory. Additionally, the 1 GHz system was damaged during the second measurement campaign, before a direct measurement of the emitted wave was performed. Therefore, the deterministic Fourier deconvolution used in Ch. 5 for enhancing the weak reflections from internal snow layers cannot be applied to this data set. Hence, the 1 GHz data is not discussed in the following.

According to the manufacturer's specifications, the 500 MHz system has an effective isotropically radiated power (EIRP) just below 10 mW (Sensors & Software Inc., personal

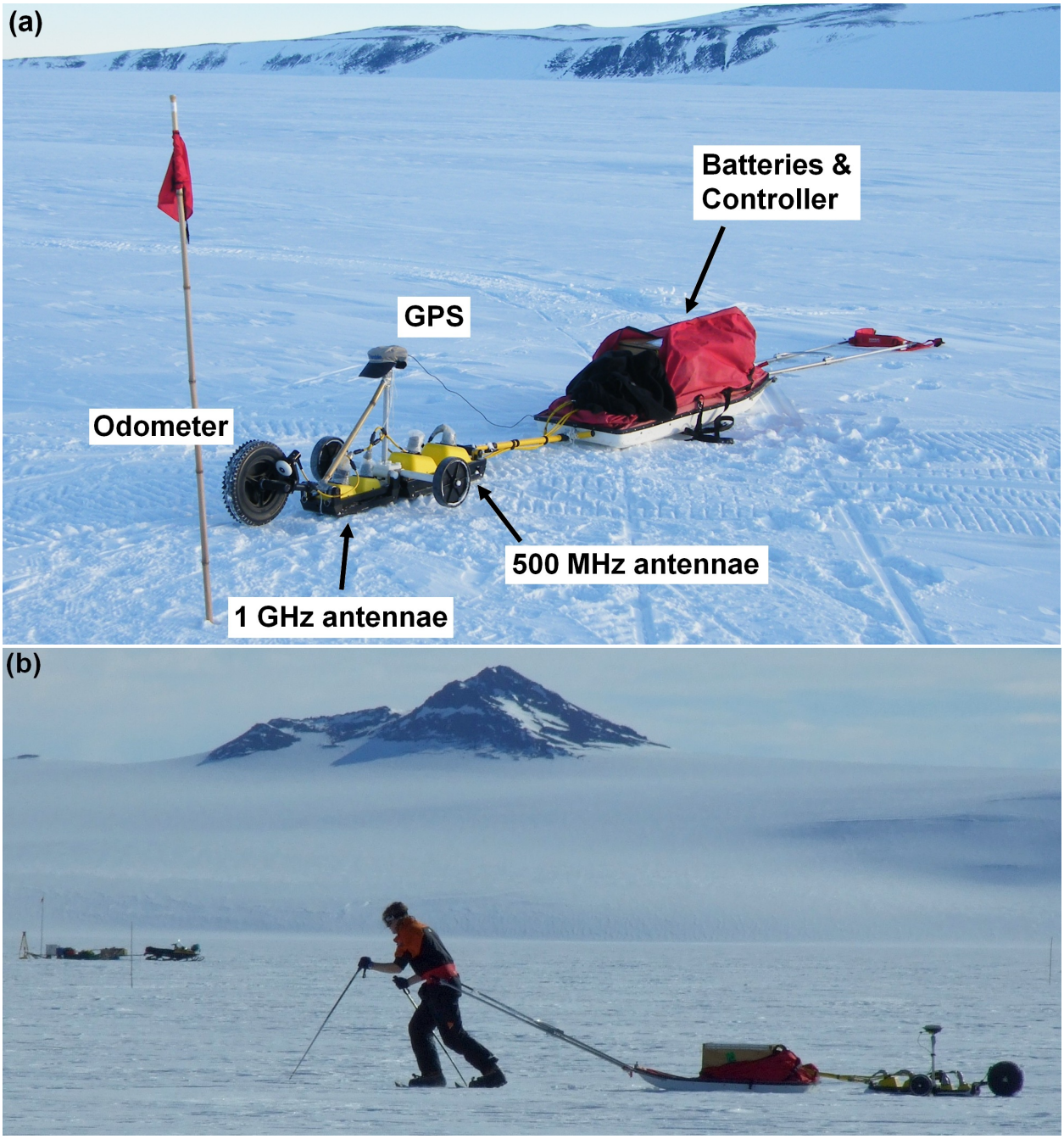

Figure 2.18: (a) High-frequency setup with shielded 500 MHz and 1 GHz antennae pairs (yellow boxes), a GPS antenna, a spiked odometer wheel, and a separate sled with a box keeping the batteries and recording equipment warm. The two 'training wheels' mounted on a rod between the antennae pairs stabilise the system on rough ground. (b) The high-frequency setup as it is being dragged along a grid line at L2. (Photos: (a) N. Kruetzmann, (b) M. Riger-Kusk)

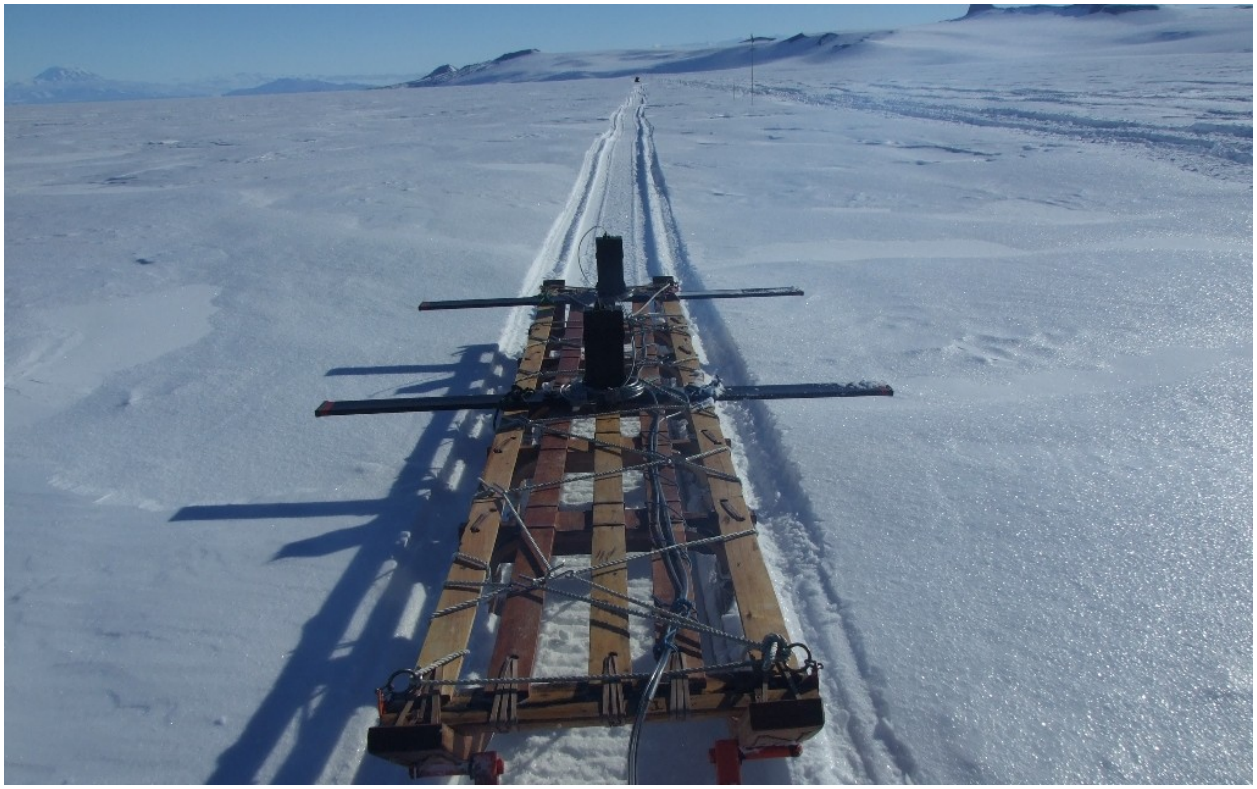

Figure 2.19: The unshielded 50 *MHz* antennae tied to a wooden Nansen sled. The recording equipment was mounted on the back of the skidoo pulling the sled. (Photo: W. Rack)

communication, 2010). With the settings used for this study the pulse repetition frequency (PRF) lies between 50 and 60 *kHz* and the system has a duty cycle of 0.02%. A frequency analysis shows that the system actually operates at an effective centre frequency of about 620 *MHz* (see also Sect. 5.3), which is equivalent to an approximate wavelength of 0.35 m in dry snow (assuming a density of 500 $\frac{kg}{m^3}$). Following *Rial et al.* (2009), the bandwidth of the system is estimated via direct measurement of the emitted wave to be $\Delta f \approx 330\,MHz$ (see also Fig. 5.13b), giving a theoretical vertical resolution of $\Delta_v = c/(2 \cdot \Delta f \cdot \sqrt{\varepsilon_r}) \approx 0.32\,m$, where ε_r is the relative dielectric permittivity of snow calculated via Eq. 2.20 and assuming a snow density of 500 $\frac{kg}{m^3}$. Note that the scale of the internal layers that cause a radar reflection can be considerably smaller than the theoretical resolution determined here, which is rather an estimate of the separation that two discontinuities in the snow need to have to be resolvable as distinct reflections. Moreover, the relative accuracy of (vertical) distance estimates between two reflections was found to be considerably better. This was tested by recording a GPR profile of a snow pit which had metal stakes inserted into one wall at 0.5 m intervals. From the apparent separations of the reflection hyperbolas (not shown) it was found that the average error of relative measurements within the snow is 11%, as long as the thickness of the layer between the reflectors is greater than the theoretical resolution.

Along the grid lines of the stake farms, recordings of radar traces (shots) were triggered at regular intervals with the odometer wheel. Using a temporal sampling interval of 0.1 *ns* and a 135 *ns* time window in 2008 allowed one trace to be recorded every 5 *cm* in the horizontal (along track) direction. In 2009, a time window of 205 *ns* was used in an attempt to image deeper reflections. Due to system limitations, this required an increased horizontal step-size

of 7 *cm*.

L1 did not display coherent layers in radar or density profiles in either year. The irregular and low accumulation, high wind, and frequent summer melting at this site probably prevent the formation of clear stratification in snow pits and GPR images. Consequently, the data from this site are not discussed further in the present work.

An additional 32 *km* long radar profile was recorded on the McMurdo Ice Shelf along a line between L1 and L2. The GPR system was dragged behind a skidoo at about 10 $\frac{km}{h}$, allowing one trace to be recorded every 0.4 *m* with a time window of 180 *ns*. In 2009, this was complemented by a low-frequency GPR recording between the stakes S15 and S12 (moving south, see Fig. 2.15b) in an attempt to estimate the thickness of the ice shelf and identify a known salt water (brine) intrusion extending several kilometres into the ice shelf in this region (*Kovacs et al.*, 1982a). For this purpose, a pair of unshielded 50 *MHz* antennae were fixed on a wooden Nansen sled (Fig. 2.19) attached to a skidoo carrying the remaining recording equipment. The setup had an antenna separation of 1.77 *m* and an antenna height above the ground of 0.33 *m*. Data were acquired using a sampling interval of 1.6 *ns*, a total time window of 2500 *ns*, and four-fold stacking to improve the signal-to-noise ratio. Due to the lack of an odometer wheel for this setup, the system was set to perform measurements at regular time intervals ('free run mode'). Travelling at approximately 10 $\frac{km}{h}$, this resulted in an effective step-size of about 6 *m* between traces.

2.6.3 GPR on an Antarctic Outlet Glacier

While the data described above was acquired for this project by the author, a lower-frequency GPR cross-section of the Touchdown Glacier, Antarctica, is also analysed in Ch. 4, courtesy of Mette Riger-Kusk and the Antarctica New Zealand event K056 in 2008. The 25 *MHz* data was recorded in the Darwin-Hatherton glacial system in the Trans-Antarctic Mountains to measure the depth of the glacier in December 2008. The thick red line in Fig. 2.20 shows the location of the cross-profile at the bottom of the Touchdown Glacier. The data was also acquired with a pulseEKKO PRO system, but using unshielded 25 *MHz* antennae, a time window of 12050 *ns*, a sampling interval of 3.2 *ns*, and four-fold stacking. The whole cross-section is about 4.6 *km* long, and one trace was acquired approximately every 2 *m*. More details on this data set can be found in *Riger-Kusk* (2011).

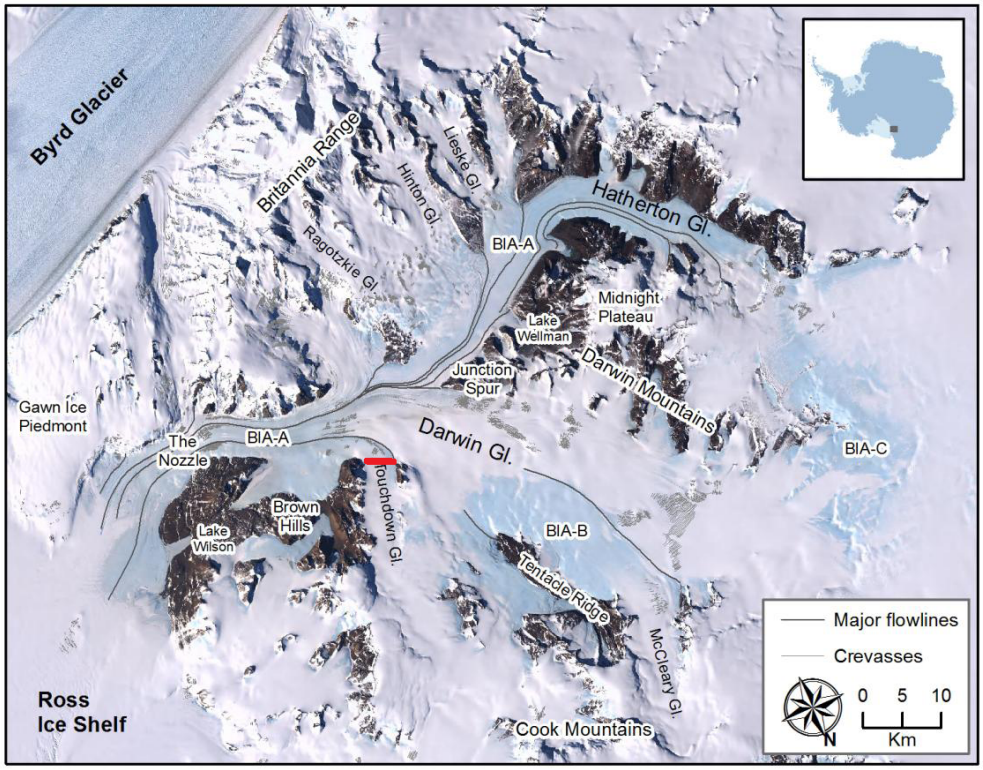

Figure 2.20: The Darwin-Hatherton glacial system. The thick red line marks the location of the 25 *MHz* GPR recording. After *Riger-Kusk* (2011).

Chapter 3

Application of RE to Atmospheric Observations

The present chapter focuses on extending the Rényi entropy (RE) analysis of stratospheric mixing barriers to observational tracer data from the EOS-MLS instrument on board the AURA satellite. Additionally, several events are investigated during which air with increased mixing ratios of nitrous oxide, that are more typical for tropical regions, is found at mid-latitudes in the southern hemisphere during austral winter.

The RE was introduced and applied to atmospheric tracer data from the SOCOL chemistry-climate model in *Krützmann et al.* (2008) and *Krützmann* (2008) for identifying major stratospheric mixing barriers – the southern hemisphere polar vortex edge and the edges of the tropical pipe – in a fast and efficient manner. The RE was able to locate these mixing barriers through their associated concentration gradients in SOCOL methane (CH_4) data, without requiring any dynamical information such as the zonal and meridional wind velocities, and with reduced computational effort compared to more elaborate measures of mixing, such as equivalent length (*Lee et al.*, 2001) or effective diffusivity (*Haynes and Shuckburgh*, 2000). This can be particularly important in the context of observational data, since the availability of observational data of the stratospheric wind fields is limited. Successful application of the RE to satellite observations of chemical trace gases could allow direct comparison of the simulated and observed large-scale dynamical structure of the stratosphere and its evolution. Additionally, as the RE is a purely statistical measure with values between zero and one, independent of the magnitude of the underlying chemical data, it can potentially also facilitate the comparison of observations of different chemical species. Therefore, Section 3.1 focuses on a comparison between the zonal mean distributions and derived RE patterns from three trace species, carbon monoxide (CO), methyl chloride (CH_3Cl), and nitrous oxide (N_2O). This is followed by a more detailed analysis of the location of the mixing barrier at the "tropical pipe edge" (*Neu, 2000* and *Neu et al.*, 2003), identified with the RE, throughout the period from August 2004 to November 2011, with a particular focus on large-scale 'leaks' of tropical air into the southern hemisphere surf-zone observed in several years during austral winter (Sect. 3.2). A potential cause for these leaks is the breaking of planetary waves. This is investigated in more detail by artificially increasing the resolution of the satellite observations with data from several days with the aid of a trajectory model in Sect. 3.3. Animations of the resulting daily high-resolution maps of N_2O at 850 K for 2004

through 2011 are included as an electronic supplement to this thesis, details of which are given in Appendix A. In Sect. 3.4 the utility of the RE results are discussed and a potential link between the increased levels of N_2O observed at southern hemisphere mid-latitudes in some years and the phase of the quasi-biennial oscillation is investigated.

3.1 Application of RE to Several Trace Species

In the initial work on the utility of RE for identifying mixing barriers, the standardised second order RE (see also Eq. 2.18):

$$RE(2, b, N) = -\frac{1}{\ln(b)} \cdot \ln\left(\sum_{i=1}^{b} p_i^2(b, N)\right) \tag{3.1}$$

was shown to give the most useful weighting of the bins of the underlying histogram, $p_i(b, N)$, or rather of the corresponding discrete probability density function (PDF) (*Krützmann et al.*, 2008; *Krützmann*, 2008). An optimal binning algorithm ("optBINS"; *Knuth*, 2006) was applied to define the number of (equally spaced) bins for the histograms, b. This implied that the range spanned by each histogram is determined by the local minimum and maximum tracer concentrations within the data window used for the calculation. Derived in this way, the RE can be considered a local measure of mixing, since the mixing ratios present in a particular histogram are not generally representative of the global distribution of the particular tracer.

3.1.1 Global Binning Approach and RE of Nitrous Oxide Measurements

In the present work a different approach is used for binning the tracer data. Instead of using the optimal binning algorithm, the range of the histograms is based on the global maximum and minimum tracer mixing ratios that occur throughout the analysis period at each vertical level. The width of the histogram bins is roughly based on the precision of the tracer observations. This means that, for each vertical level, the observations of a particular tracer are always binned into the same underlying histogram. The RE value calculated from such a histogram is therefore a global measure of mixing. Additionally, using a fixed number of bins speeds up the calculations considerably and referring to observational precision when determining the bin width can reduce the effects of noise in the observations on the RE. On the other hand, since there are (almost) always empty bins in the histogram the value of the RE tends to be reduced.

Figure 3.1a shows a contour plot of RE_{z10} (using ten days of data at each latitude of the model grid) for the 10 hPa level of SOCOL CH_4 data for the southern hemisphere representative of 1980 conditions, calculated with the optimal binning algorithm. Comparing this to Fig. 3.1b, where the global binning approach is applied to the same data, shows that the latter results in a more coherent pattern throughout the hemisphere and overall lower RE values. The main entropy structures, a band of high RE_{z10} between 60°S and 70°S from day 100 to approximately day 300 and another that shifts latitudinally from 40°S in summer

to approximately 20°S by the end of winter, can be clearly identified in both cases. The former is associated with the barrier to meridional mixing formed by the polar vortex during southern hemisphere winter, while the latter is indicative of the tracer gradient due to the mixing barrier at the edge of the tropical pipe (*Plumb*, 1996; *Neu et al.*, 2003).

Using the global binning approach, the RE_{z10} is calculated for observational tracer data from the EOS-MLS satellite instrument, specifically for version 3.3 of N_2O data (*Waters et al.*, 2006; *Livesey et al.*, 2011) on isentropic levels. Over 3400 observations for each day are sorted into 111 latitude bins from 82°N to 82°S (see Sect. 2.3.3). To determine the range of the histograms used for deriving the RE, the global maximum and minimum observed mixing ratio of N_2O at each potential temperature level are derived from all available data (2004-2011). Using a bin width of 10 *ppbv*, which roughly corresponds to the precision of the N_2O observations (*Livesey et al.*, 2011), should reduce the variability of the RE related to observational noise. With these parameters, the global histogram for, e.g. the 850 K potential temperature level has 34 bins ranging from -40 *ppbv* to 300 *ppbv*. At the other levels, the N_2O histograms have between 20 and 75 bins with a tendency to less bins at higher levels due to the reduction in the N_2O mixing ratios with altitude. Note that the number of bins used for the global binning of SOCOL CH_4 data in Fig. 3.1b was set to 50 to fit into this range.

Figure 3.2 shows the RE_{z10} pattern calculated with the above parameters and using ten days of data as in Fig. 3.1 for the southern hemisphere at the 850 K level in 2008. The 850 K potential temperature level corresponds to a similar altitude as the 10 *hPa* pressure level ($\approx$ 30 *km*). It lies in the middle of the stratosphere and its dynamics should be representative. Therefore, most plots shown in this chapter are for the 850 K level. The general structure in Fig. 3.2 is similar to that of Fig. 3.1b, though the pattern appears noisier. The polar vortex barrier is found further north throughout most of austral winter in Fig. 3.2 and the band of high RE_{z10} values associated with the tropical pipe edge is, on average, closer to the equator than in Fig. 3.1, moving from around 30°S in autumn to near 10°S in winter. Nevertheless, the overall correspondence between the RE_{z10} patterns from model and observational data is good, particularly considering that the two vertical levels are only approximately the same and that data for different chemical tracers is being used. This also illustrates that the RE facilitates the comparison of the distribution of different trace species with similar properties.

3.1.2 RE of Methyl Chloride and the Effect of Noise

To further test the comparability of the RE results from different tracers, it is now applied to EOS-MLS observations of methyl chloride (CH_3Cl). The average lifetime of CH_3Cl is shorter than that of N_2O as CH_3Cl photodissociates more rapidly with altitude, but it has a similar distribution in the lower parts of the stratosphere (see also Sect. 2.1.1 and Sect. 2.3.3.2). Therefore, the RE calculations are performed for the 550 K ($\approx$ 22 *km*) potential temperature level. Figures 3.3a and b show the RE_{z10} calculated for the southern hemisphere in 2008 from N_2O and CH_3Cl volume mixing ratio data, respectively. The two high RE_{z10} bands associated with the tropical pipe and polar vortex can be clearly identified in the N_2O results. Particularly the polar band of high RE_{z10} is more distinct and continuous than in Fig. 3.2 and is centred close to 60°S from June through October, which corresponds well with

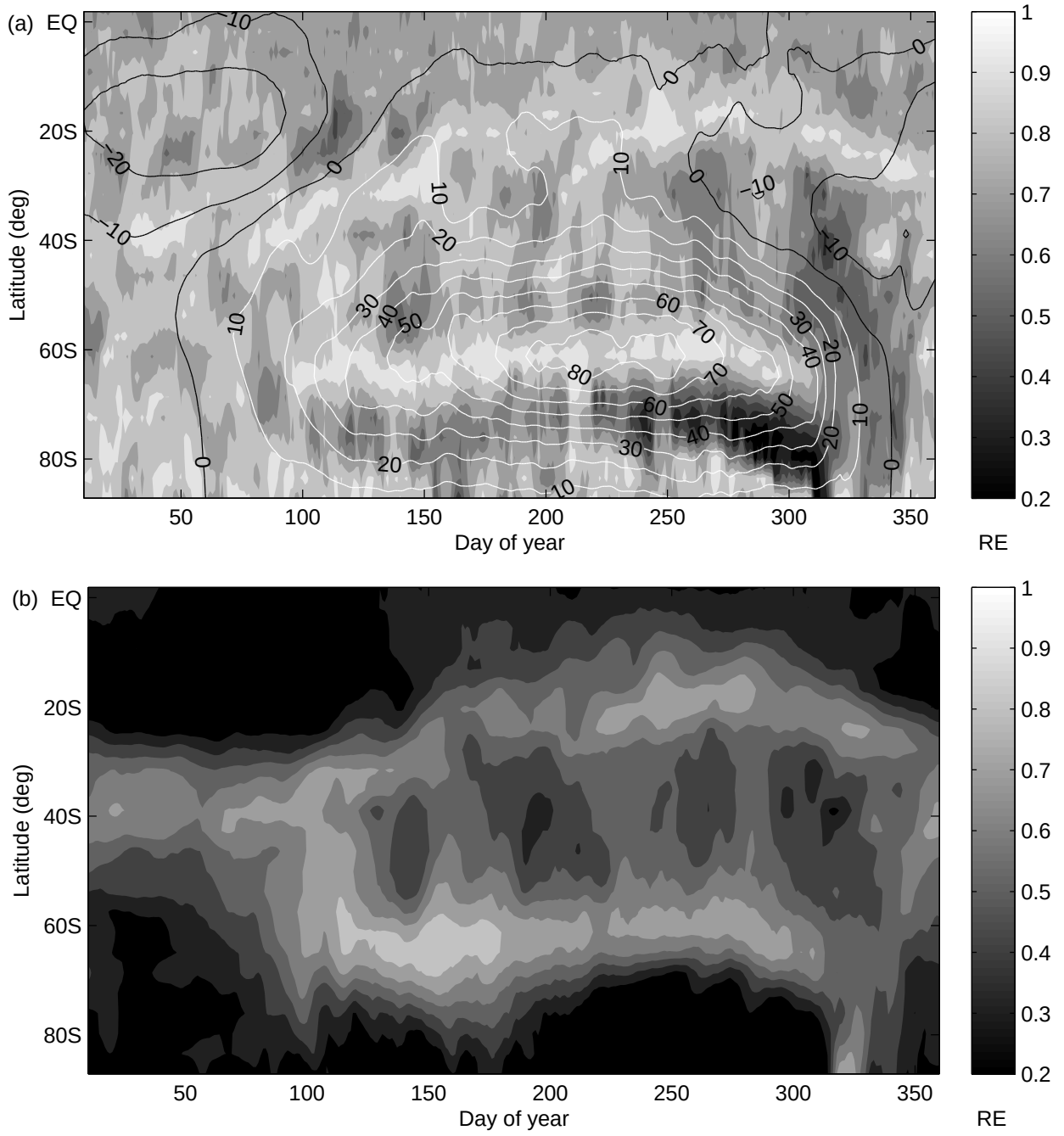

Figure 3.1: Time-latitude filled contour plot of RE_{z10} calculated (a) using the optimal binning algorithm and (b) with global binning, from SOCOL CH_4 data for the 10 hPa level of the southern hemisphere and 1980 conditions. (a) is a reproduction of Figure 1(a) in *Krützmann et al.* (2008) and the superimposed contours represent zonal mean zonal wind velocities in $\frac{m}{s}$ (white = westerly). The RE contour interval in both figures is 0.1.

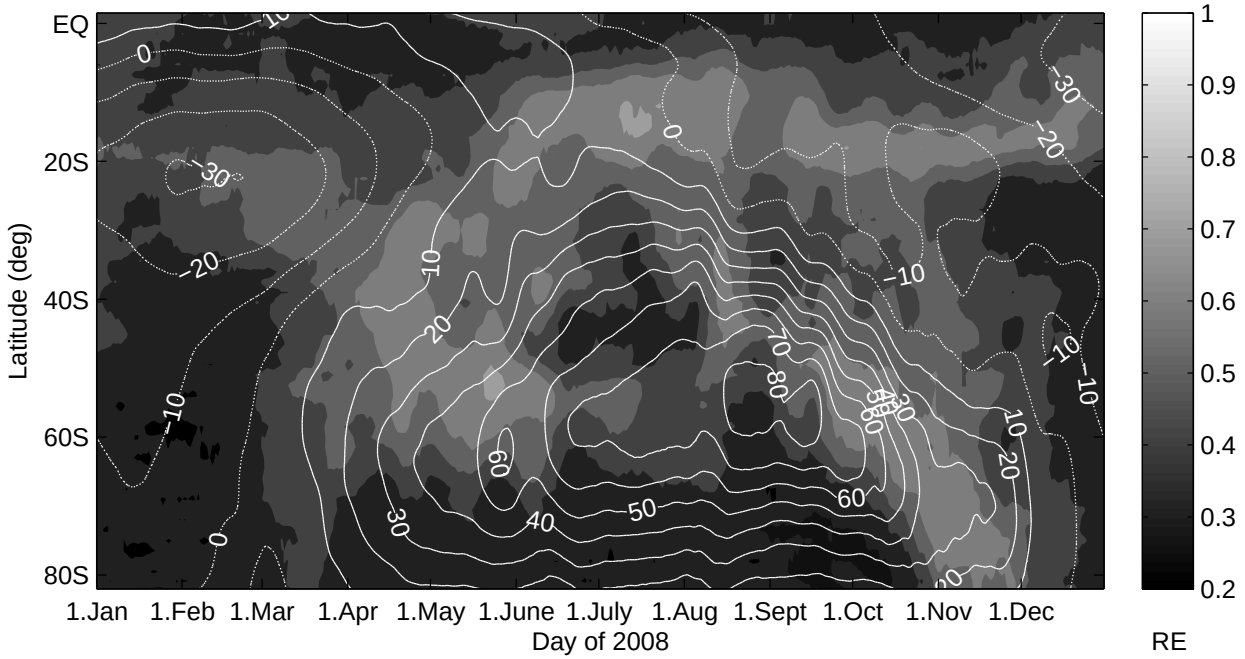

Figure 3.2: RE_{z10} of EOS-MLS N_2O data at 850 K for the southern hemisphere in 2008 using global histogram limits. The contours represent ten-day zonal mean zonal wind velocities in $\frac{m}{s}$ (solid lines are westerly). The RE contour interval is 0.1.

the typical location of the southern hemisphere polar vortex edge in winter and early spring (e.g. *Lee et al.*, 2001). The tropical region of high RE_{z10} shifts from approximately 25°S in May to about 15°S in August. This equatorward shift is also typical for the tropical pipe edge in winter (e.g. *Neu et al.*, 2003). The CH_3Cl results (Fig. 3.3b) on the otherhand show much less detail and have a smaller dynamical range. While there is a region of increased RE_{z10} between 60°S and 70°S during winter and spring, it is very indistinct and the tropical band of increased RE_{z10} is barely visible at all. All in all, the correspondence between the RE_{z10} derived from N_2O and CH_3Cl data for 2008 is surprisingly small.

The overall higher RE_{z10} values in Fig. 3.3b compared to Fig. 3.3a, and the fact that the CH_3Cl data is known to be much more noisy than the N_2O data (*Livesey et al.*, 2011), suggest that the lack of structure in Fig. 3.3b could be related to noise. High RE values are generally associated with relatively broad distributions (for white noise $RE = 1$), while low values of RE correspond to more peaked distributions (see also Sect. 2.2). The higher noise in the CH_3Cl data is likely to increase the value of the RE as it tends to spread out and thereby flatten any peaks in the PDF. This can be tested by adding noise to the N_2O data before calculating the RE. Figure 3.4a is the RE_{z10} derived from the same data as Fig. 3.3a but with Gaussian noise added to each observation. The noise term is based on normally distributed random numbers with zero mean and a standard deviation equal to 10% of the global mean mixing ratio of N_2O at 550 K (≈ 185 $ppbv$). As expected, the added noise reduces the coherence of the high-RE structures and raises the overall values of RE_{z10}, thereby reducing the contrast. High values don't get much higher with added noise but low values are increased more rapidly as the noise distorts the peaks in the PDFs that go along with low RE values.

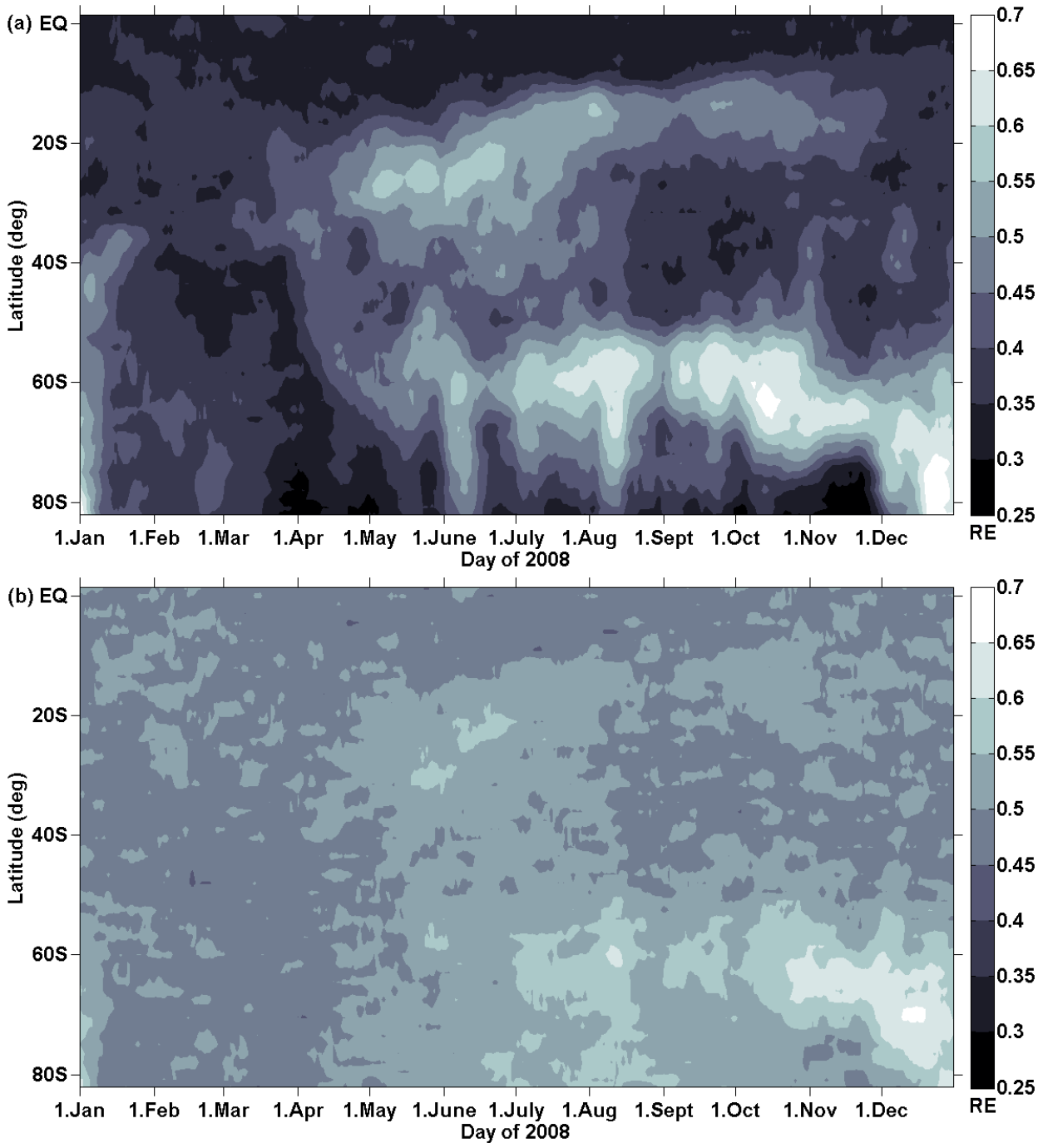

Figure 3.3: RE_{z10} of (a) N_2O and (b) CH_3Cl at 550 K for the southern hemisphere in 2008. Note that the colour scale is limited to values between 0.25 and 0.7 and that the contour interval is reduced to 0.05 compared to Fig. 3.2.

Both the polar and the subtropical bands of high RE can still be made out but are more patchy. Particularly the subtropical RE maximum is much less distinct from the (increased) background values than in Fig. 3.3a. Increasing the standard deviation of the Gaussian noise to 20% of the global mean, results in a complete loss of any structure in the subtropics, and a further increase to 50% ultimately removes any structure from the RE_{z10} diagram (not shown). This illustrates that the noise level has a considerable impact on the clarity of the derived RE patterns, which could be one reason for the limited quality of the RE_{z10} results from CH_3Cl measurements.

One possibility to remediate the noise problem of the CH_3Cl observations is to improve the statistics by using more data points when creating the histograms for the RE, e.g. by expanding the data window in the meridional direction. Figure 3.4b is the result of using a data window that includes ten days of CH_3Cl data from three neighbouring latitude bins, thereby tripling the number of points in each histogram. The resulting structures are somewhat more coherent than in Fig. 3.3b and now resemble the RE_{z10} pattern from the N_2O data with added noise (Fig. 3.4a). As in the noisy N_2O results, a patchy high-RE region near 60°S is observed during winter and spring in Fig. 3.4b, while the tropical barrier is very indistinct throughout the year. The similarity of the RE patterns in Fig. 3.3 suggests that the main reason for the reduced utility of the RE_{z10} from CH_3Cl observations is the higher level of noise in the data. This also demonstrates a limitation of the RE analysis: identifying mixing barriers with RE only works when using tracer data with a high signal-to-noise ratio. Additionally, this shows that the RE methodology for tracer analysis does, to some extent allow a comparison of the distributions of different trace species. However, there are limitations to this comparability, particularly when comparing tracers with different stratospheric distributions. This is investigated in the following section.

3.1.3 RE of Carbon Monoxide and the Comparability of Different Tracers

While N_2O and CH_3Cl have similar sources and sinks in the stratosphere, the distribution of carbon monoxide (CO) has a different morphology, with a polar maximum in winter and very low mixing ratios in the tropics throughout the year (see also Sect. 2.3.3.3). Therefore, the CO gradient between the polar winter vortex and the surf-zone is expected to be stronger than that of N_2O in this region, while the gradient at the tropical pipe edge is expected to be very small or even non-existent. Accordingly, the RE_{z10} pattern derived from CO volume mixing ratios for the southern hemisphere 850 K level only shows a single band of high-RE_{z10} near 65°S during August and September 2008, and low RE_{z10} values in the tropics and the surf-zone throughout the whole year (see Fig. 3.5). Due to the shorter lifetime of CO in the presence of high UV radiation (see Sect. 2.1.1) the levels of CO in the tropics and subtropics are very low (Fig. 2.12) and any effect that the mixing barrier at the tropical pipe edge may have on the CO distribution is likely too small, compared to the EOS-MLS measurement error, to be detectable with the RE_{z10}.

Compared to Fig. 3.2, the polar high-RE_{z10} region is located considerably further south in Fig. 3.5 (note the different colourscale and contour intervals), suggesting that the maximum gradient of CO is closer to the pole than the corresponding gradient maximum of N_2O.

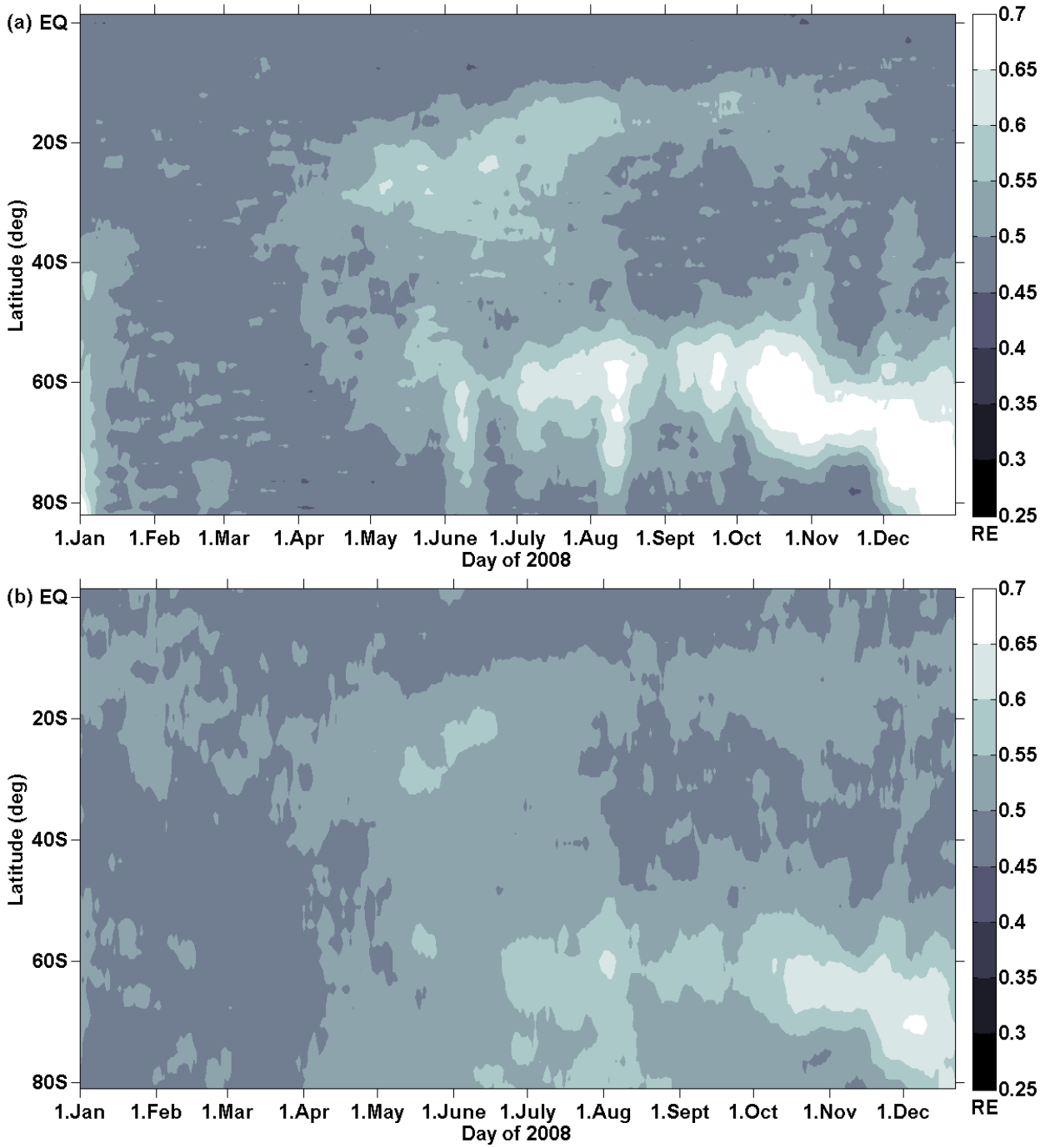

Figure 3.4: (a) RE_{z10} calculated from the same N_2O data as Fig. 3.3a but with Gaussian noise added to each observation. The noise term is based on normally distributed random numbers with zero mean and a standard deviation of 18.5 *ppbv* (10% of the global mean mixing ratio of N_2O at 550 K). (b) RE of CH_3Cl at 550 K for the southern hemisphere in 2008 combining ten days of data from three neighbouring latitude bins for each histogram.

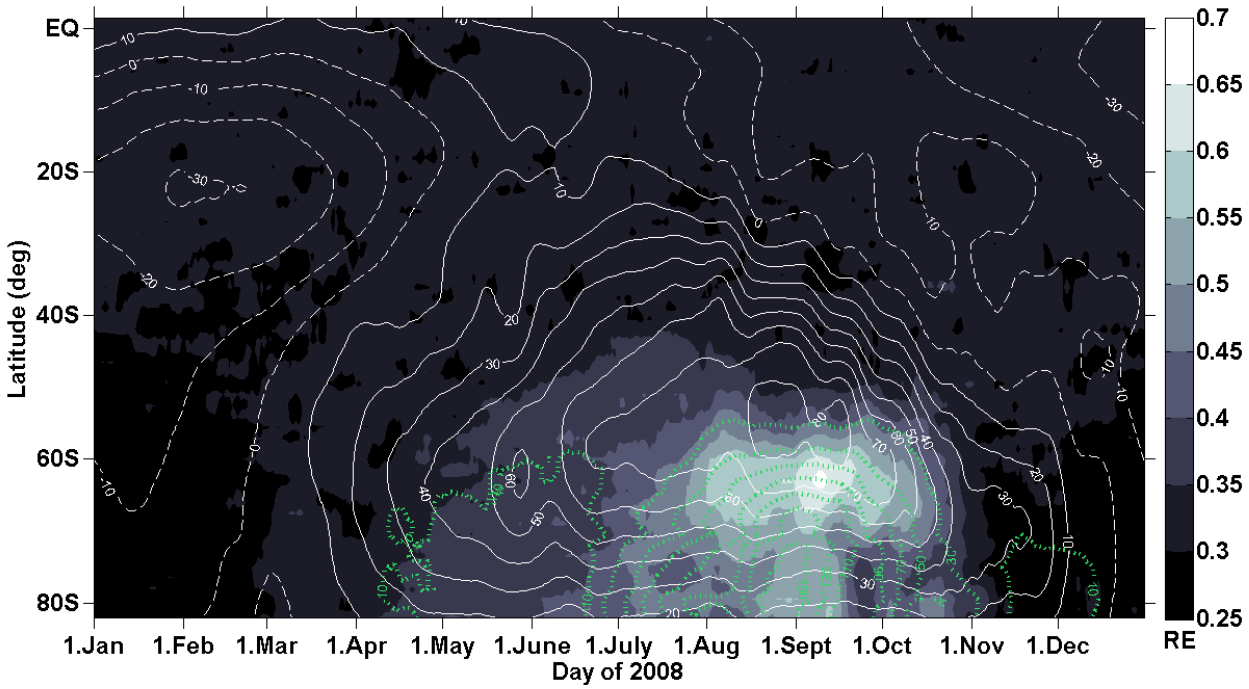

Figure 3.5: Contour plot of RE_{z10} of CO at 850 K for the southern hemisphere in 2008 using ten days of data. Solid and dashed white contours represent ten day zonal mean westerly and easterly winds (in $\frac{m}{s}$), respectively. Green contours are ten day zonal mean CO volume mixing ratios in *ppbv*.

This poses the question which of the high-RE bands better represents the location of the mixing barrier associated with the polar vortex edge. Several criteria have been developed for determining the latter, such as the location of the maximum gradient in PV (e.g. *Nash et al., 1996*), the product of the maximum gradient of PV and the zonal wind velocity (e.g. *Bodeker et al., 2002; Struthers et al., 2009*), or the most likely location of the (locally) least common mixing ratio of a tracer (*Sparling*, 2000; *Neu et al.*, 2003). To a first approximation, the results of applying these criteria coincide with the maximum of the westerly winds at the centre of the polar night jet, particularly for the southern hemisphere polar vortex. The solid white contours in Fig. 3.5 represent the zonal mean westerly wind velocities at 850 K derived from MERRA data. Between August and September 2008, the high-RE_{z10} band at 65°S is approximately 5° further south than the westerly wind maximum, meaning that the maximum gradient of CO is located poleward of the centre of the polar night jet and is therefore probably not coincident with the actual barrier to horizontal mixing.

However, the zonal mean CO volume mixing ratio contours (dotted green lines) in Fig. 3.5 suggest that the RE_{z10} may be identifying another barrier to meridional mixing. Between July and September the amount of CO at 82°S (the maximum latitude of the observations) increases constantly. The CO contours migrate northward over time, where they are eventually stalled and a gradient builds up. It is the location of this gradient that the higher RE_{z10} values near 65°S in Fig. 3.5 represent. This gradient could be associated with the inside of the polar vortex edge region discussed in *Lee et al.* (2001) and *Roscoe et al.* (2012). They describe the polar vortex edge as an extended part of the polar vortex that "is only weakly mixed within itself and with the core of the vortex" (*Roscoe et al.*, 2012). Accor-

dingly, the high-RE_{z10} region near 65°S could correspond to the mixing barrier between the vortex core and the (weakly mixed) vortex edge region. Once the polar night jet begins to weaken in late September the CO gradient diminishes quite rapidly and most of the CO is destroyed by mid-October, when the increased values of RE_{z10} disappear. This fast removal of CO from the vortex core is probably due to increased destruction of CO as the intensity of the UV radiation reaching high latitudes increases, since the final break-up of the polar vortex usually does not occur before the middle of November (*Waugh and Randel*, 1999).

The large differences between the RE_{z10} patterns derived from CO (Fig. 3.5) and N_2O (Fig. 3.2) illustrate that the location of the stratospheric sources and sinks of a particular tracer must always be kept in mind when attempting to gain information about large-scale mixing barriers from tracer distributions. Additionally, applying the RE to various tracer species can give complementary information on the underlying dynamics. Furthermore, the analysis of CH_3Cl showed that the signal-to-noise level must also be taken into account when applying the RE to observational data, as the underlying PDFs can be considerably distorted if the noise is on a similar level as the data values. As the RE derived from CO and CH_3Cl produces rather limited results compared to the RE of N_2O, only N_2O observations are used in the following.

3.1.4 Seven-year Climatology of RE of N_2O

Figures 3.6a and b show the climatological average of RE_{z10} derived from AURA-MLS N_2O observations between August 2004 and November 2011 for the 850 and 550 K potential temperature level, respectively. The dotted green contours represent the corresponding average of ten day zonal mean N_2O volume mixing ratio in *ppbv* and the white contours are the average zonal mean zonal wind velocities from 2004 to 2011 in $\frac{m}{s}$, derived from the MERRA reanalysis. On the whole, the average of RE_{z10} is based on seven years of data, though in some cases the satellite was not operational for a brief period in one or two years. Between August and November the average is calculated from eight years of data. The difference in the number of available data points is the reason for the minor jumps observed in both the RE_{z10} and the mean N_2O contours.

Both levels clearly show the high-RE_{z10} bands associated with the tracer gradients at the edges of the southern hemisphere polar vortex and the tropical pipe. The latter cannot be unambiguously identified from May to July at 850 K, when it is 'lost' in a wide region of high RE_{z10} between about 20°S and 40°S (Fig. 3.6a) and between January and March at 550 K, due to overall very low RE_{z10} values. Otherwise, the centre of the subtropical high-RE band tends to oscillate from approximately 15°S in spring to 35°S in autumn at both levels. This compares well with the location of the southern hemisphere tropical pipe edge found by other studies (e.g. *Neu et al.*, 2003; *Palazzi et al.*, 2011). At higher latitudes, the mixing barrier between the surf-zone and the polar vortex can be identified as a continuous band of high RE_{z10} throughout most of the austral winter and spring time. At 550 K (Fig. 3.6b), it is centred between 55°S and 60°S from June to November and then gradually shifts poleward as the polar vortex breaks up. The high RE_{z10} values associated with the vortex barrier at 850 K (Fig. 3.6a) are generally found at somewhat lower latitudes. The wide region of high RE_{z10} mentioned earlier does not allow definite identification of the polar barrier before

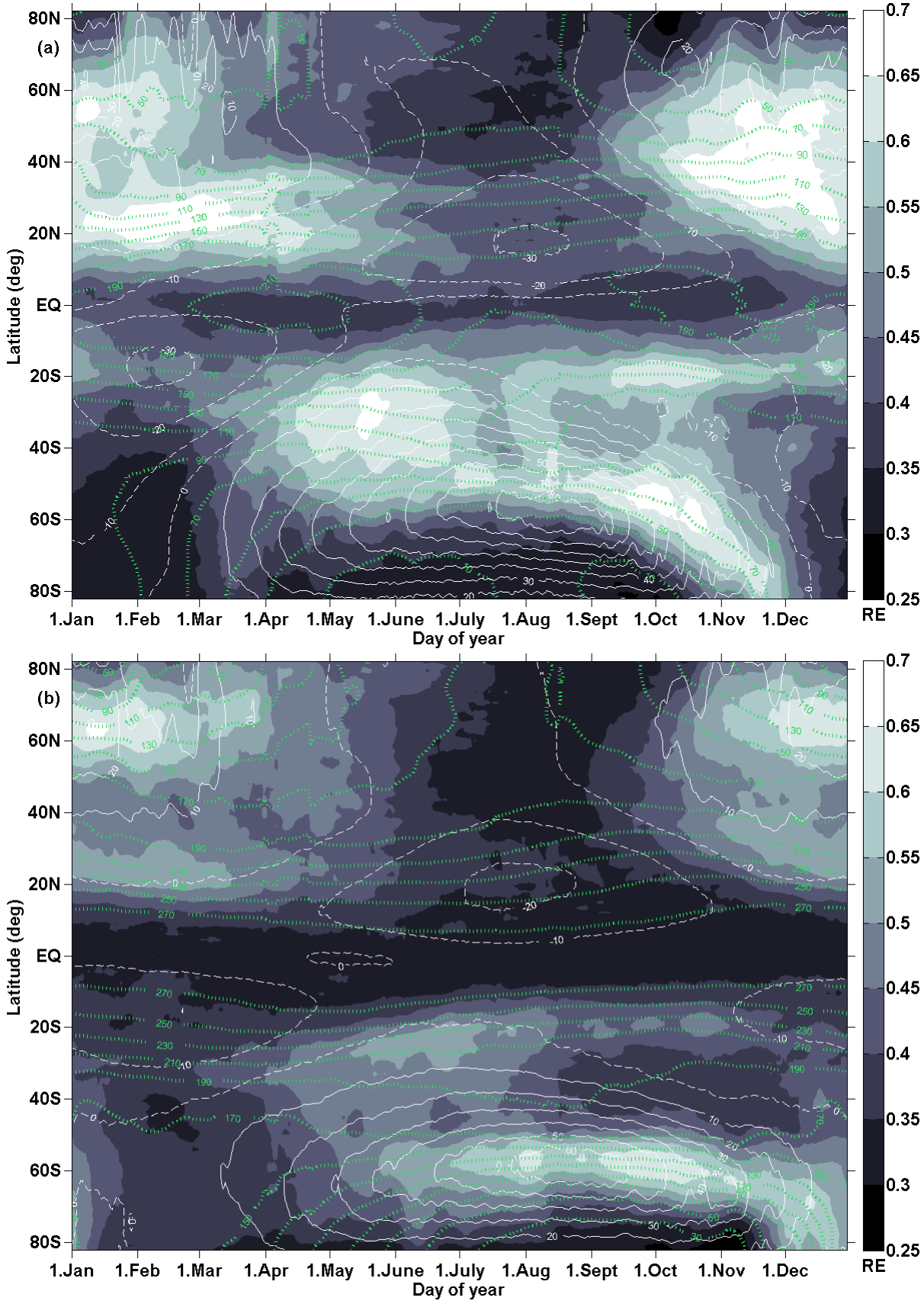

Figure 3.6: Contour plots of the climatology of RE_{z10} at (a) 850 K and (b) 550 K derived from N_2O data from August 2004 through November 2011. Dotted green contours represent the corresponding average of ten day zonal mean N_2O volume mixing ratio in *ppbv*. White contours are the average zonal mean zonal winds of 2004 through 2011 from the MERRA reanalysis in $\frac{m}{s}$. Solid and dashed contours correspond to westerly and easterly winds, respectively.

July, when the polar high values are centred around 50°S. From September to the end of November the polar RE_{z10} maximum gradually moves poleward. In accordance with the known downward propagation of the polar vortex break-up, the band of high RE_{z10} at 550 K reaches the highest displayed latitude (82°S) several weeks later than at 850 K.

In the northern hemisphere, a region of raised RE_{z10} values, the centre of which shifts from 40°N in October to about 20°N in February, can be identified during most of boreal autumn, winter, and spring. This can be associated with the northern hemisphere tropical pipe barrier. Again, the range of latitudes and the equatorward shift from autumn to spring compares well with findings of previous studies (*Neu et al.*, 2003; *Palazzi et al.*, 2011). From December to February, a relatively wide band of high RE_{z10} centred near 65°N can be seen at 550 K (Fig. 3.6b). This probably represents the northern hemisphere polar vortex mixing barrier. This barrier is usually hard to identify at higher levels (e.g. Fig. 3.6a) in a zonal average picture due to the high variability of the location of the polar vortex caused by planetary wave breaking.

All in all, the climatology of RE_{z10} presented here suggests that the RE is a useful tool to identify tracer gradients associated with barriers to horizontal mixing from observational data of N_2O in the middle stratosphere. Comparison with RE_{z10} derived from CH_3Cl in Sect. 3.1.2 demonstrated that similar results are obtained when using a different chemical tracer which has similar source and sink regions as N_2O, but also that the RE only gives reliable results when the signal-to-noise ratio is high. Additionally, tests with CO data in Sect. 3.1.3 showed that the structures identifiable with the RE methodology also depend on the particular chemical tracer used and the location of its sources and sinks relative to the large-scale mixing structures.

On the other hand, the latitudes at which the RE_{z10} climatology identifies the southern hemisphere polar vortex edge are unusually low. Throughout most of winter and spring the zonal mean Antarctic polar vortex edge is expected to be close the maximum of the zonal mean zonal winds (near 60°S) at 550 K (e.g. *Garny et al.*, 2007, *Harvey et al., 2002* and *Waugh and Polvani, 2010*). The centre of the high RE_{z10} band tends to be slightly further north during most of this period (Fig. 3.6b). Similarly, while the Antarctic vortex is known to be wider at higher levels (*Waugh and Randel*, 1999), the latitudes identified by the climatological mean position of the southern hemisphere polar RE_{z10} maximum at 850 K (Fig. 3.6a) are several degrees further north than the zonal mean zonal wind maximum, which is probably too low to be realistic.

This is also in contrast to the results of the original analysis of CH_4 output from the SOCOL climate model (*Krützmann*, 2008), where the identified southern hemisphere polar maximum in RE was found to be very close to the core of the polar night jet (e.g. Fig. 3.1a). There are several potential reasons for this discrepancy. First of all, small differences in the distributions between CH_4 and N_2O can generally be expected, particularly since the analysis of the model data was performed on pressure levels rather than potential temperature. Secondly, climate models are known to have a "cold-pole bias" *Shepherd (2000)* and *(Eyring et al., 2006)* resulting in a stronger polar night jet that is closer to the pole. As the MERRA wind data is largely based on the underlying numerical weather prediction model – the amount of observational data of stratospheric winds is limited – some difference compared

to tracer observations can also be expected. Additionally, a minor offset between the centre of the tracer gradient and the centre of the polar night jet could be realistic, since there is no absolute necessity for these to coincide. Finally, the precision of the N_2O measurements could also play a role as the N_2O volume mixing ratio reduces toward the centre of the polar night jet. The closer the magnitude of the measured mixing ratios is to the precision of the data (about 13 *ppbv* in this case, see Table 2.1), the more noticeable the effect of measurement noise on the histograms for the *RE* will become. This effect is generally likely to be more important at higher levels as the mixing ratios decrease with altitude.

Given the uncertainty about the reliability of the *RE* for identifying the polar vortex edge and the possible link to the low amounts of N_2O in the polar regions, the polar mixing barriers are not discussed any further. Instead, the focus is now turned to an analysis of the mixing barriers associated with the edges of the the tropical reservoir, using the *RE* of N_2O data.

3.2 Analysis of the Tropical Pipe

The relative isolation of the tropical region of mean ascent in the stratosphere from higher latitudes was first observed by *Trepte and Hitchman* (1992) and implies the existence of a permanent barrier to horizontal mixing on either side of the equator. The region within these barriers is referred to as the "tropical pipe" named after a mathematical model developed by *Plumb* (1996). The model was later extended to a "leaky pipe model" (*Neu and Plumb*, 1999) to account for the observational evidence for regular episodic leaks from the tropical pipe region (e.g. *Randel et al.*, 1993; *Waugh*, 1993; *Polvani et al.*, 1995; *Waugh*, 1996, among others). The centre of the tropical region is not always at the equator but tends to shift toward the summer hemisphere throughout the year *(Plumb, 2002)*, as do the boundaries of this region. In the following, the term tropical pipe "edge" is used to designate a single latitude in each hemisphere which is considered to be the centre of the barrier to horizontal mixing between the tropical pipe and the extra tropical stratosphere. The term was originally coined by *Neu (2000)*.

3.2.1 Evolution of the Tropical Pipe Edges

The seasonal shift of the tropical pipe edges was first investigated quantitatively by *Neu et al.* (2003), using a methodology suggested in *Sparling* (2000) based on meridional tracer PDFs of CLAES N_2O and HALOE CH_4. For each hemisphere they define the location of the tropical pipe edge as the 'most likely latitude of the least common tracer mixing ratio' (within a certain range of tracer mixing ratios, see *Sparling* (2000) for details), arguing that the least likely mixing ratio represents the centre of the tracer concentration gradient between the tropics and the subtropics.

In Sect. 3.1 and *Krützmann et al.* (2008) it was shown that the *RE* can be used to identify the location of tracer gradients in observational data of N_2O and that bands of high *RE* between 15° and 40°, presumably coincident with the tracer gradients at the edges of the tropical pipe, are clearly visible in both hemispheres throughout most of the year (Fig.

3.6). Considering that the distribution of a chemical tracer in the atmosphere is generally a smooth function of latitude and longitude (extreme differences in tracer concentrations of neighbouring air parcels are smoothed by chemical diffusion), it is reasonable to assume that a PDF of tracer concentrations created from data near the 'most likely latitude of the least common tracer mixing ratio', contains a relatively wide spread of tracer concentrations. Accordingly, the RE of the tracer distribution at this latitude would probably be a local maximum. Hence, it is reasonable to assume that the subtropical maximum of RE approximately coincides with the location of the maximum gradient and therefore represents the centre of the mixing barrier at the tropical pipe edge.

Figure 3.7a illustrates the detailed evolution of the RE_{z10} at 850 K between 45°N and 45°S from August 2004 through December 2005 and Fig. 3.7b displays the monthly averages. The location of the subtropical maximum of RE_{z10} is shown as a red line for both hemispheres in Fig. 3.7a. Tracking of the tropical pipe edges is performed by identifying the latitude of the maximum RE_{z10} from each day, though limited to the region between 4.5° and 40.5° latitude in the respective hemisphere to avoid confusion with the polar maximum. These latitudinal boundaries are selected because previous studies rarely report the tropical pipe edge at latitudes lower than 10° or higher than 35° (*Neu et al.*, 2003; *Palazzi et al.*, 2011). The subtropical RE_{z10} maximum generally tends to be higher and therefore easier to identify during late autumn, winter, and spring in both hemispheres. During this time, the tracer gradient between the tropics and the mid-latitudes is usually enhanced as large-scale stirring by planetary wave breaking in the surf-zone results in relatively lower tracer mixing ratios on the poleward side of the tropical pipe (*Miyazaki and Iwasaki*, 2008). In summer, the mid-latitudes are dominated by easterly winds (e.g. Fig. 3.6) which do not allow planetary waves to propagate (*Charney and Drazin*, 1961). Therefore, the tracer gradient between the tropics and the mid-latitudes tends to be weaker and the subtropical RE_{z10} values are lower during summer in both hemispheres, making identification of the tropical pipe edge more difficult.

The red lines in Fig. 3.7b represent the respective monthly averages of the latitude of the maximum RE_{z10} and the error bars indicate the standard deviation of the underlying daily latitudes from this average. The standard deviation can be used as an indicator of the uncertainty or (un-)reliability of the identified location of the subtropical maximum. At times when the subtropical mixing barrier is relatively weak, i.e. during summer, the subtropical RE_{z10} maximum is generally lower than during the rest of the year and its location can change considerably on a daily basis (Fig. 3.7a). This explains the high uncertainty in the monthly average latitude of the RE_{z10} maximum in the northern hemisphere during August and September 2005 and during March and April in the southern hemisphere (see Fig. 3.7b). In the former case, the identified peak location oscillates between two regions of similarly high RE_{z10} (at 15°N and 30°N). The resultant monthly average lies between these, at a latitude which has much lower RE_{z10} values, and is probably not a realistic estimate of the location of the subtropical mixing barrier. In the latter case, the rapid changes from one day to the next are related to the lack of a clear peak in RE_{z10} (Fig. 3.7a), since the gradient between the tropics and the subtropics is rather weak in summer. Averaging the identified latitudes could be a reasonable estimate of the location of the tropical pipe edge in southern hemisphere summer months, as the monthly average evolution (Fig. 3.7b)

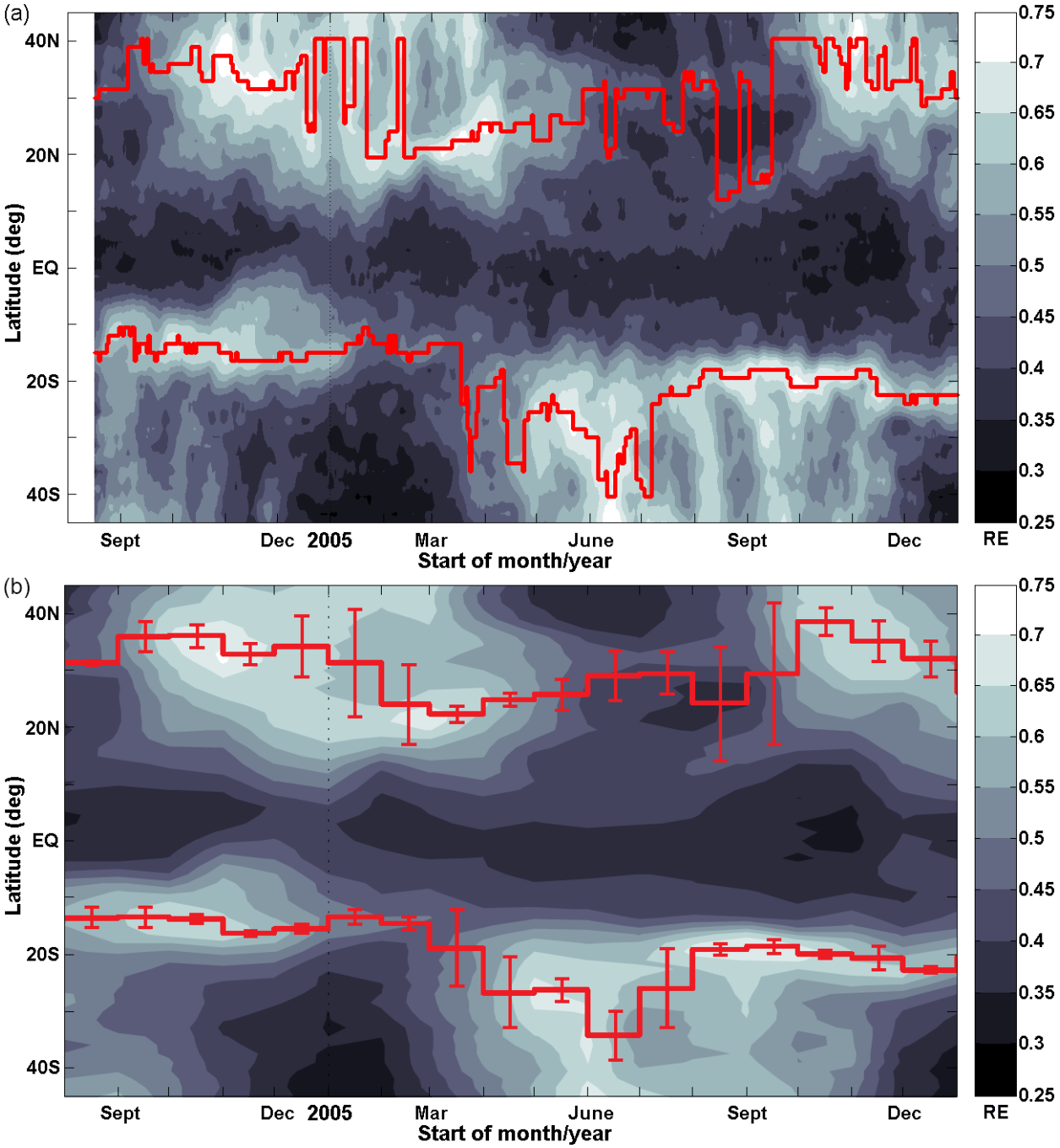

Figure 3.7: (a) Contour plot of RE_{z10} at 850 K from August 2004 to December 2005. The red lines indicate the daily location of the subtropical maximum (between 4.5° and 40.5°) of RE_{z10} in each hemisphere. (b) shows the monthly average of RE_{z10} for the same level. The red lines are the monthly average of the red lines in (a) and the error bars represent the standard deviation of the daily latitude of the RE_{z10} maximum from the respective monthly average.

shows that it results in a gradual transition between the more distinct high RE_{z10} regions in February and May 2005. Generally, the intensity of the meridional tracer gradients in the subtropics is reduced during the summer months (as are the values of RE_{z10}). This is known to cause difficulties in identifying the corresponding edge of the tropical pipe. For example, *Neu et al.* (2003) state that "the summer edge region can occupy as much as 60% of the area of the whole summer hemisphere". Similarly, *Palazzi et al.* (2011) sometimes find it difficult to identify the tropical pipe edge because the tracer PDFs occasionally display more than one local minimum in the summer hemisphere (Fig. 2 of *Palazzi et al., 2011*). Accordingly, the uncertainties in identifying the tropical pipe edge with the RE_{z10} during summer are probably also due to the underlying weakness of the tracer gradient.

On the other hand, high variability in the location of the subtropical RE_{z10} maximum is also observed during winter, when the tracer gradient between the tropics and the surf-zone is expected to be quite strong and the tropical pipe edge should be easy to identify. For example in late December 2004 and January 2005, the location of the northern hemisphere maximum RE_{z10} shows several large jumps between 20°N and 40°N (Fig. 3.7a), resulting in an average latitude of 31.3°N for January (Fig. 3.7b). This monthly average position lies in an area of relatively lower RE_{z10}, between two regions of slightly higher values. While the tropical pipe edge probably lies closer to 20°N at this point (in the high-RE_{z10} region which is closer to the equator), the second patch of high RE_{z10} 'confuses' the tracking and leads to the intermediate monthly average position. In this case, the high RE_{z10} values near 40°N are due to a shift of the Arctic polar vortex away from the pole, resulting in an extended meridional gradient of N_2O in the zonal mean picture which reaches relatively low latitudes within the surf-zone (not shown). This event is likely related to planetary wave breaking activity, but will not be investigated further as a similar situation does not occur in any of the other years considered here. Nevertheless, it shows that such events can have a considerable impact on the reliability of the RE for identifying the subtropical mixing barriers.

Another irregularity in the RE_{z10} pattern is observed in the southern hemisphere during late autumn and early winter in 2005. Instead of gradually moving toward the equator as autumn progresses and the surf-zone becomes increasingly well mixed – thereby steepening the gradient to the tropics and shifting it toward the equator (*Miyazaki and Iwasaki*, 2008) – the RE_{z10} maximum appears to move poleward during May 2005, reaching the highest allowed latitude of 40.5°S in June (see Fig. 3.7a). From there it shifts back toward the equator, interrupted by a short poleward rebound in early July, though this is related to a temporary decrease in the RE_{z10} values between 20°S and 30°S from early to mid-July rather than an actual shift of high RE_{z10} values to higher latitudes. By the end of July, the RE_{z10} maximum is found near 20°S, which is a more expected latitude for this season. The rapid changes in the position of the RE_{z10} maximum lead to the large error bars seen in Fig. 3.7b during these months and explain why the June and July average tropical pipe edge latitudes do not coincide with the monthly mean maximum in RE_{z10}. This effect turns out to be related to large-scale intrusions of tropical air into the southern hemisphere surf-zone. During this time, large amounts of air with high volume mixing ratios of N_2O appear to leak from the tropical pipe into the southern hemisphere surf-zone (Fig. 3.8), resulting in a temporary poleward shift of the subtropical N_2O gradient. Such 'leak events' are observed in several years (black ovals in Fig. 3.8) and are investigated in more detail in Sect. 3.2.2

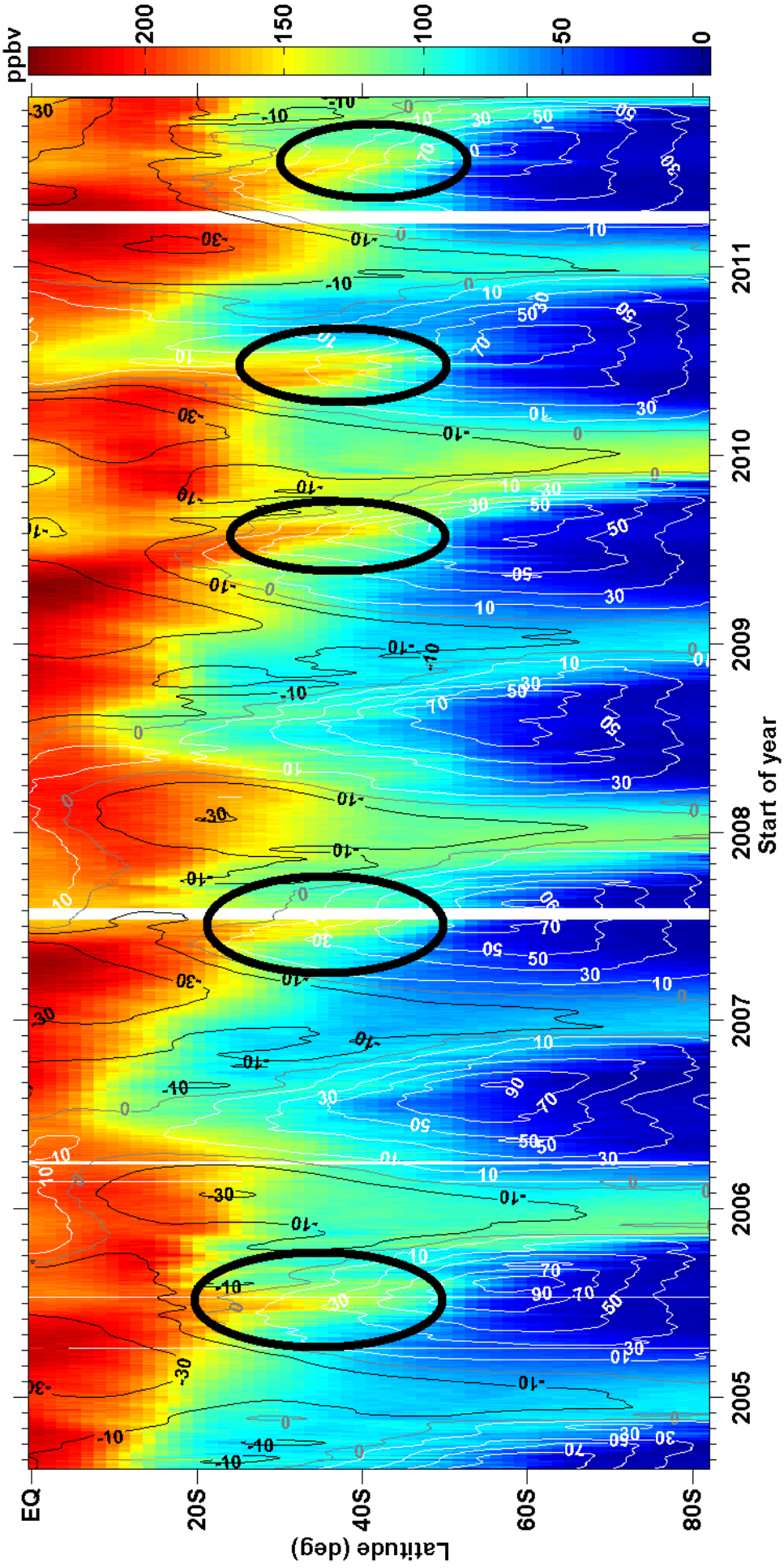

Figure 3.8: Zonal mean N_2O volume mixing ratio in *ppbv* at 850 K in the southern hemisphere from MLS observations between August 2004 and November 2011. Contours are zonal mean zonal wind velocities in $\frac{m}{s}$ from MERRA reanalysis data, smoothed with a nine-day moving average window. Black and white contours represent easterly and westerly winds, respectively. The zero wind line is shown in grey. Thick black ovals indicate 'leak events' when unusually high N_2O mixing ratios are observed at mid-latitudes during austral winter.

and Sect. 3.3.

Despite the high variability during some months, the identified evolution of the edges of the tropical pipe generally compares well with results from other studies. Figure 3.7 represents the time period for which *Palazzi et al.* (2011) calculate the seasonal evolution of the tropical pipe edges from four different sets of satellite data, including EOS-MLS N_2O. To allow a direct comparison, Fig. 3.9 is a reproduction of the bottom left panel of Fig. 4 in *Palazzi et al.* (2011), showing the seasonal average position of the tropical pipe edge as they derive it from different satellite measurements at 830 K. The seasonal average latitude of the subtropical maximum of RE_{z10} (at 850 K) is superimposed as green squares. The error bars represent the standard deviation of the daily values from the respective seasonal average. Aside from the time when two gradients are present in the northern hemisphere (DJF 2004/2005) and the leak period in the southern hemisphere (JJA 2005) the location of the tropical pipe edge identified with the RE_{z10} is in good agreement with the results of *Palazzi et al.* (2011), indicating that the subtropical RE_{z10} maximum is a reasonable estimate for the location of the tropical pipe edge. Note that the values for JJA 2004 in Fig. 3.9 are based on data for August only as no MLS N_2O data is available before 8.8.2004.

A closer look at the RE_{z10} and zonal mean N_2O contours can give some insights into possible reasons for the discrepancies between the barrier locations as detected by the different instruments in *Palazzi et al.* (2011) and the results presented here. For JJA 2005, *Palazzi et al.* (2011) find the northern hemisphere tropical edge on the 830 K level at approximately 18°N in MIPAS observations, but at about 30°N in SMR and MLS data (Fig. 3.9). Comparing just the seasonal averages, the latitude of the RE_{z10} maximum (at 850 K) agrees better with the SMR and MLS result. However, during this time the RE_{z10} values are relatively low throughout the hemisphere (the gradients are weak) and one can see a second 'path' for tracking the RE_{z10} in Fig. 3.7b from June to August 2005 which would be approximately centred around 18°N – the latitude derived from MIPAS data in Fig. 3.9. Figure 3.10 gives a more detailed view of the situation. It shows a meridional cross-section of the monthly average RE_{z10} for August 2005 with zonal mean N_2O contours (dotted green lines) and the monthly average location of the RE_{z10} maximum for each hemisphere superimposed. Above 800 K, the tropical peak in N_2O is found to be centred around 15°N rather than over the equator. This asymmetry is probably caused by the secondary meridional circulation of the QBO (e.g. *Punge et al.*, 2009). It leads to a poleward shift of the subtropical N_2O gradient in the northern hemisphere at higher altitudes. Above 900 K, the strongest gradient between the tropics and the subtropics is clearly centred near 30°N, while it lies between 15°N and 20°N below 700 K. In the transition region between 700 and 900 K, the location of the maximum gradient is not as easily defined and at 850 K there are clearly two separate N_2O gradients present in the northern hemisphere subtropics, one around 15°N and the other centred just over 30°N. This suggests that the MIPAS results in Fig. 3.9 point to the former gradient, while the MLS and SMR analysis identify the latter gradient as the edge of tropical pipe at this level. The monthly average position of the RE_{z10} maximum lies between the two gradients (at 24°N) and the high standard deviation of the monthly average (±10°) reflects this ambiguity (see also Fig. 3.7b and Fig. 3.10).

The apparent shift of the tropical pipe edge from 25°S in mid-May 2005 to 40°S in June coincides with the previously mentioned leakage of air with tropical N_2O mixing ratios into

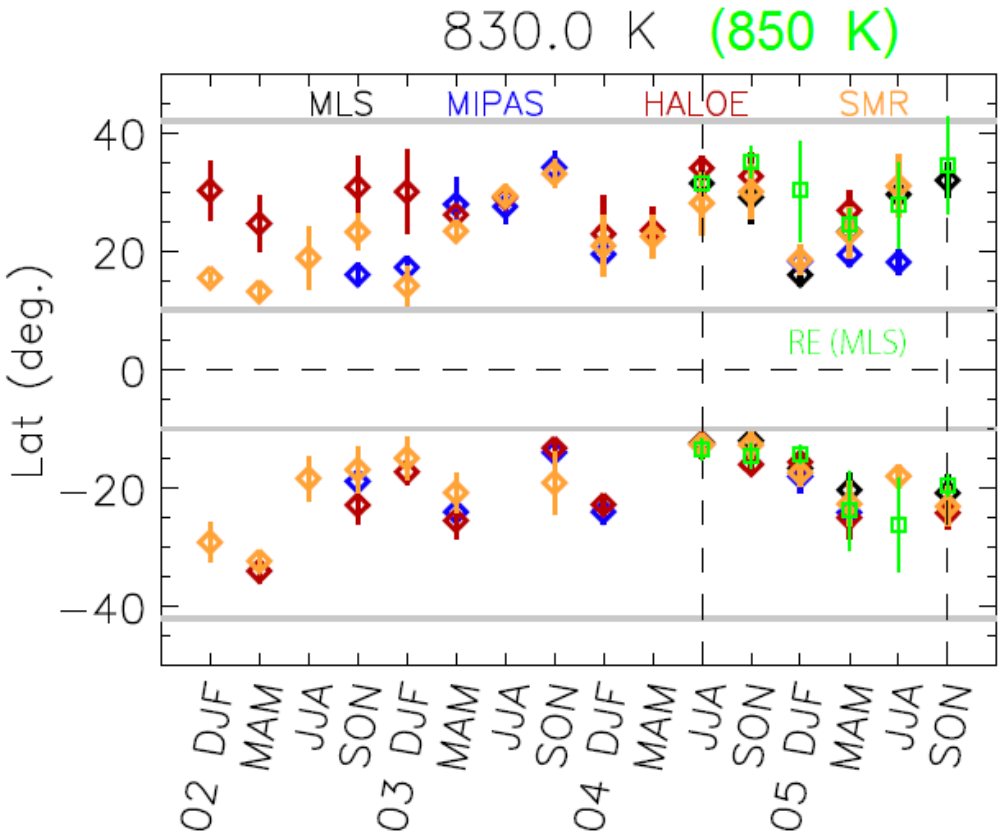

Figure 3.9: Reproduction of the bottom left panel of Fig. 4 in *Palazzi et al.* (2011) showing the seasonal evolution of the tropical pipe derived from four different satellite data sets at 830 *K*. "*Time series (seasonal data) of the subtropical barrier position from DJF 2002 to SON 2005 calculated from MLS (black), MIPAS (blue), HALOE (red), and SMR (yellow) data. Error bars are superimposed to each data point. The horizontal grey lines define the latitude region between 10 and 42 degrees in both hemispheres, while the vertical dashed lines indicate the overlapping time period of all four satellite data.*" (*Palazzi et al.*, 2011) Note that in the case of the HALOE data the tropical pipe edge positions are derived from measurements of CH_4, while N_2O observations are used from the three other instruments. The superimposed green squares represent the seasonal average latitude of the subtropical maximum of RE_{z10} at 850 *K*. The green error bars represent the standard deviation of the daily values from the seasonal average.

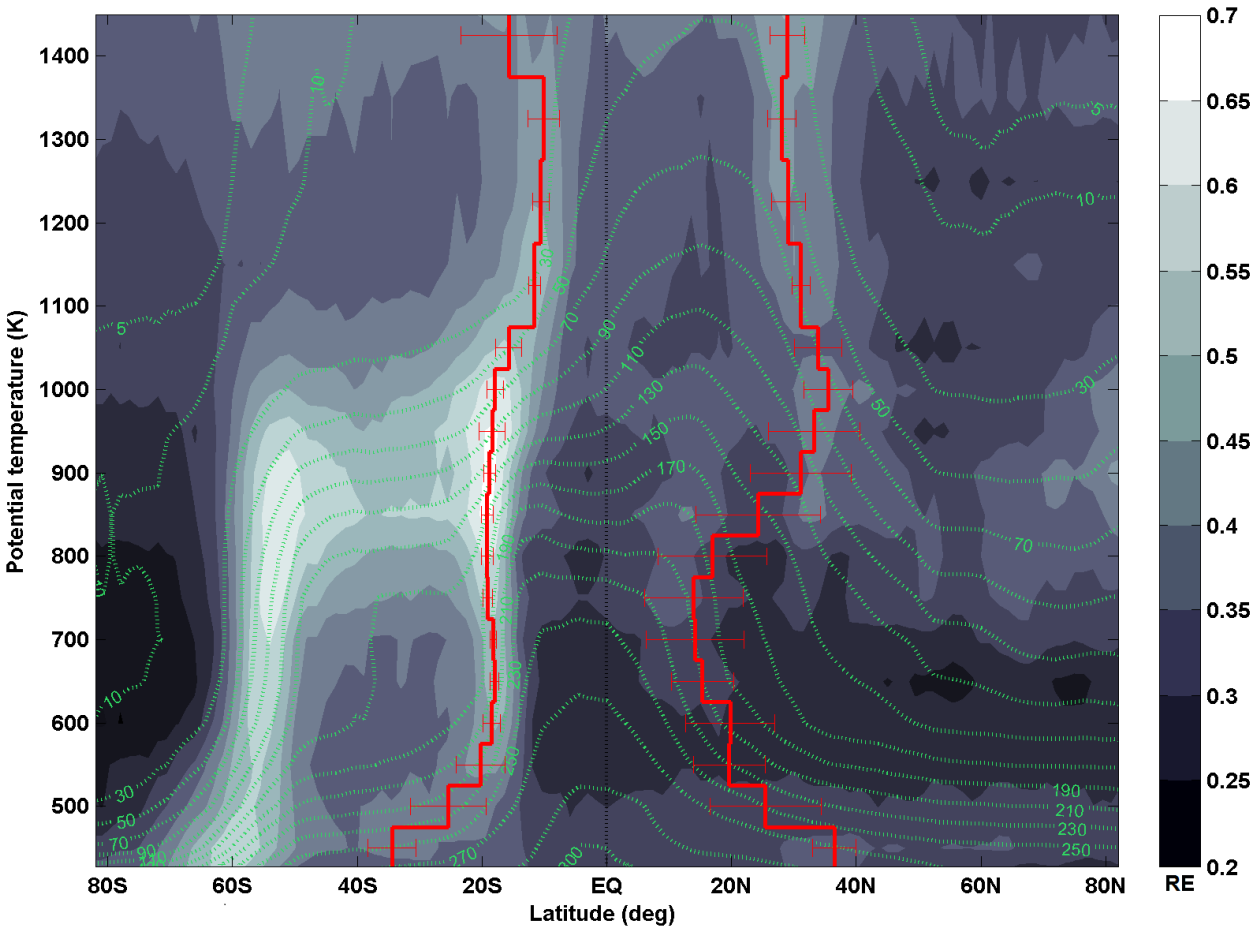

Figure 3.10: Meridional profile of monthly mean RE_{z10} for August 2005. The red lines indicate the tropical pipe edges derived from the average location of the subtropical RE_{z10} maximum in each hemisphere. Horizontal error bars represent the standard deviation of the daily locations from the monthly average. Dotted green contours are monthly zonal mean N_2O contours in *ppbv*.

the surf-zone. Figure 3.11a shows the evolution of the monthly average of RE_{z10} and the location of the subtropical RE_{z10} maximum in each hemisphere at 850 K for the full data period (August 2004 to November 2011). Generally, the RE_{z10} maximum is found at higher latitudes during summer and closer to the equator in winter in both hemispheres, which agrees with the known seasonal cycle of the tropical pipe edges (*Neu*, 2000; *Plumb*, 2002). However, sudden poleward shifts of the southern hemisphere RE_{z10} maximum during austral winter are observed in all those years during which large-scale leaks from the tropical pipe can be seen in Fig. 3.8, confirming that the shift is likely to be linked to the leaks. Interestingly, a corresponding shift is not observed at 550 K (Fig. 3.11b). At this level the position of the subtropical RE_{z10} maximum shows a more regular annual cycle, though some interannual variability is also in evidence. This suggests that the occasional leaks of tropical air into the southern hemisphere surf-zone, which are a very distinct feature at 850 K, are confined to a limited vertical range.

3.2.2 Extent of the Tropical Leak Events

To investigate the vertical scale on which tropical air is mixed into the southern hemisphere mid-latitudes during leak events, Fig. 3.12a shows the temporal evolution of zonal mean N_2O at 36°S between 500 and 1250 K from 1^{st} April to 31^{st} October 2010. Beginning in mid-April, a gradual increase in N_2O mixing ratios is evident above 800 K which continues until mid-May, when a more rapid, step-like increase is observed between approximately 600 and 900 K, while the volume mixing ratios largely stay constant at other levels. After several more such rapid rises, high N_2O mixing ratios (> 180 *ppbv*) that are otherwise only found in the tropics or at lower altitudes, extend all the way from 600 to 800 K by the end of June. Considerably elevated levels of N_2O (increase > 30 *ppbv* compared to April) are also found up to 950 K. From then on, a general tendency towards a lowering of the N_2O mixing ratio sets in, interspersed with occasional temporary increases below 750 K. This trend toward lower mixing ratios continues into September. The suddenness of the change in N_2O in mid-May suggests that it is caused by horizontal mixing, since vertical ascent is unlikely to occur within such a short time at this latitude.

In 2005, considerable increases in N_2O below 750 K appear to start about one month later than in 2010 (Fig. 3.12b). It also appears to be a comparatively weaker leak since N_2O levels at 36°S only reach a maximum of about 150 *ppbv* between 600 and 800 K, though the initial mixing ratios at these levels before the leakage are marginally lower than in 2010. Nevertheless, by early July the N_2O volume mixing ratio at 850 K has been increased by over 60 *ppbv* compared to April. The rapid mixing of tropical air into the mid-latitudes can explain the sudden changes in the location of the southern hemisphere RE maximum observed in Fig. 3.7a. If the N_2O flux into the subtropics is sufficiently large to temporarily raise the local average mixing ratio to near-tropical levels, then the subtropical tracer gradient (and therefore the RE maximum) must shift poleward accordingly.

Figure 3.12b also shows that similar increases in the N_2O mixing ratio at higher levels can precede the events below 900 K by a month or two. Specifically, in late April 2005, there is a sudden spike in N_2O, temporarily increasing the mixing ratios between 900 and 1200 K by 15 to 30 *ppbv*, but not affecting lower levels. While this increase only lasts several days,

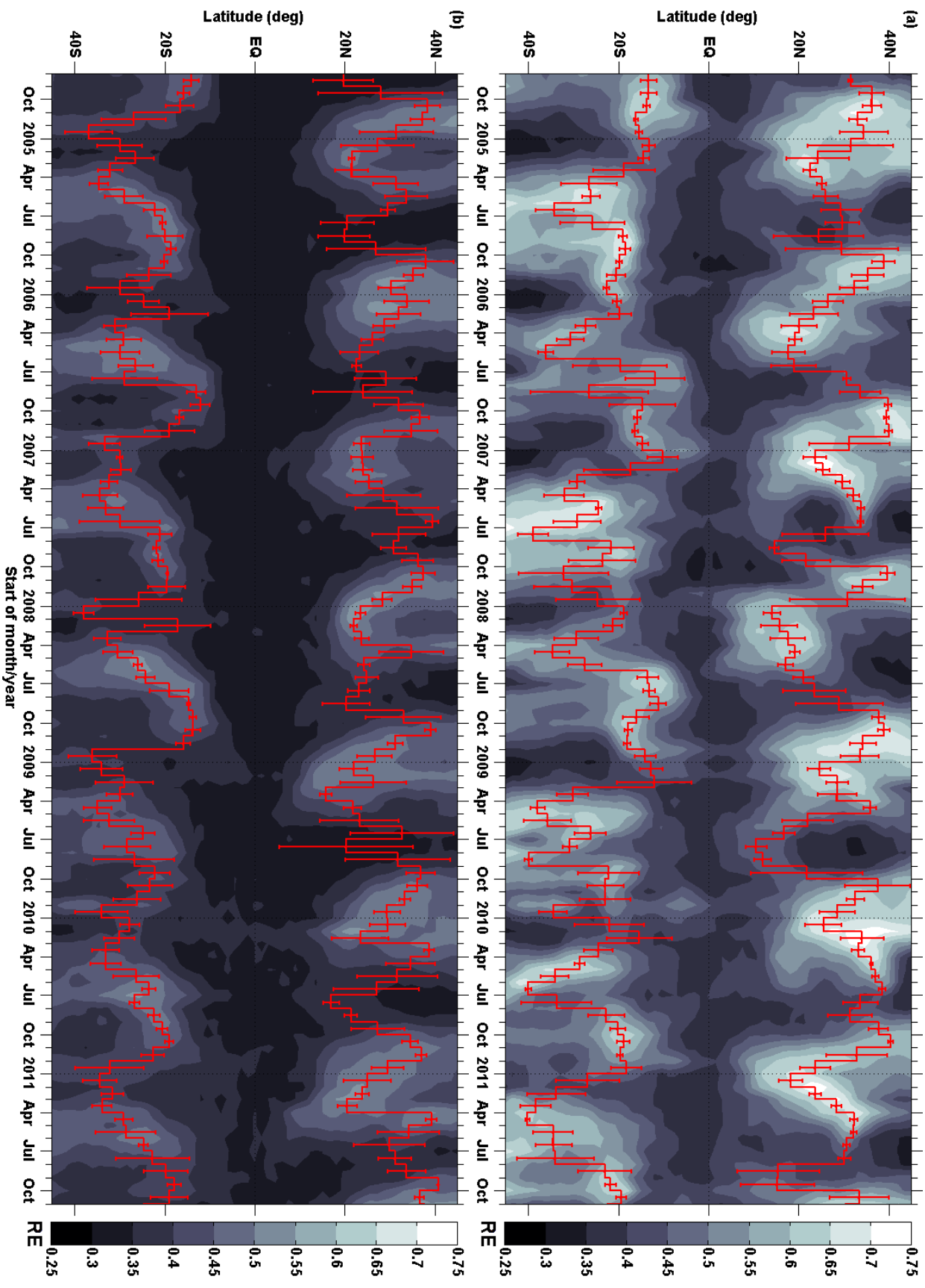

Figure 3.11: Monthly mean RE_{z10} (derived from N_2O observations) and the average location of the subtropical maximum thereof for each hemisphere (red lines) at (a) 850 K and (b) 550 K from August 2004 to November 2011. The error bars represent the standard deviation of the daily latitude of the RE_{z10} maximum from the respective monthly average.

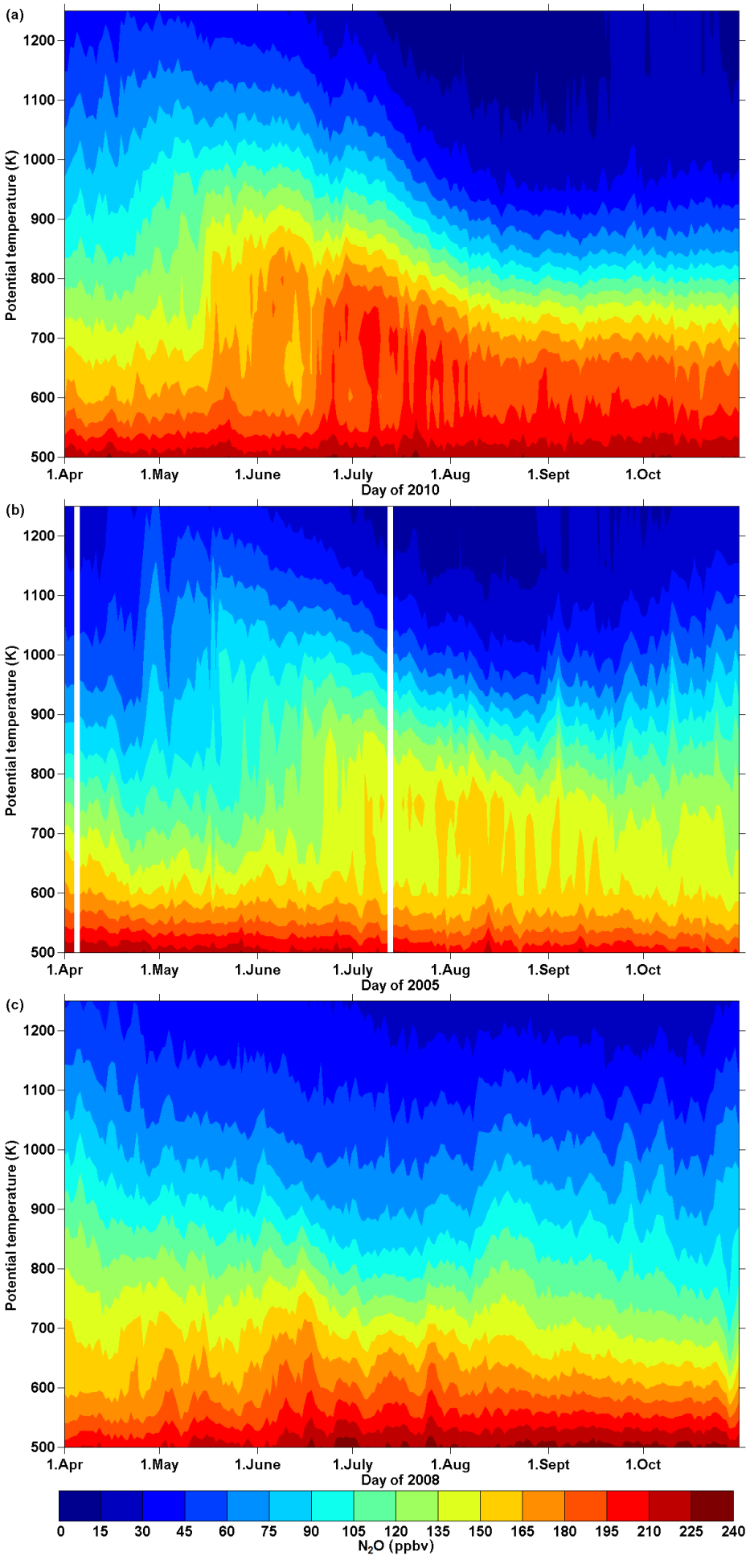

Figure 3.12: Vertical profiles of the zonal mean N_2O volume mixing ratios (in $ppbv$) at 36°S between 1^{st} April and 31^{st} October of (a) 2010, (b) 2005, and (c) 2008.

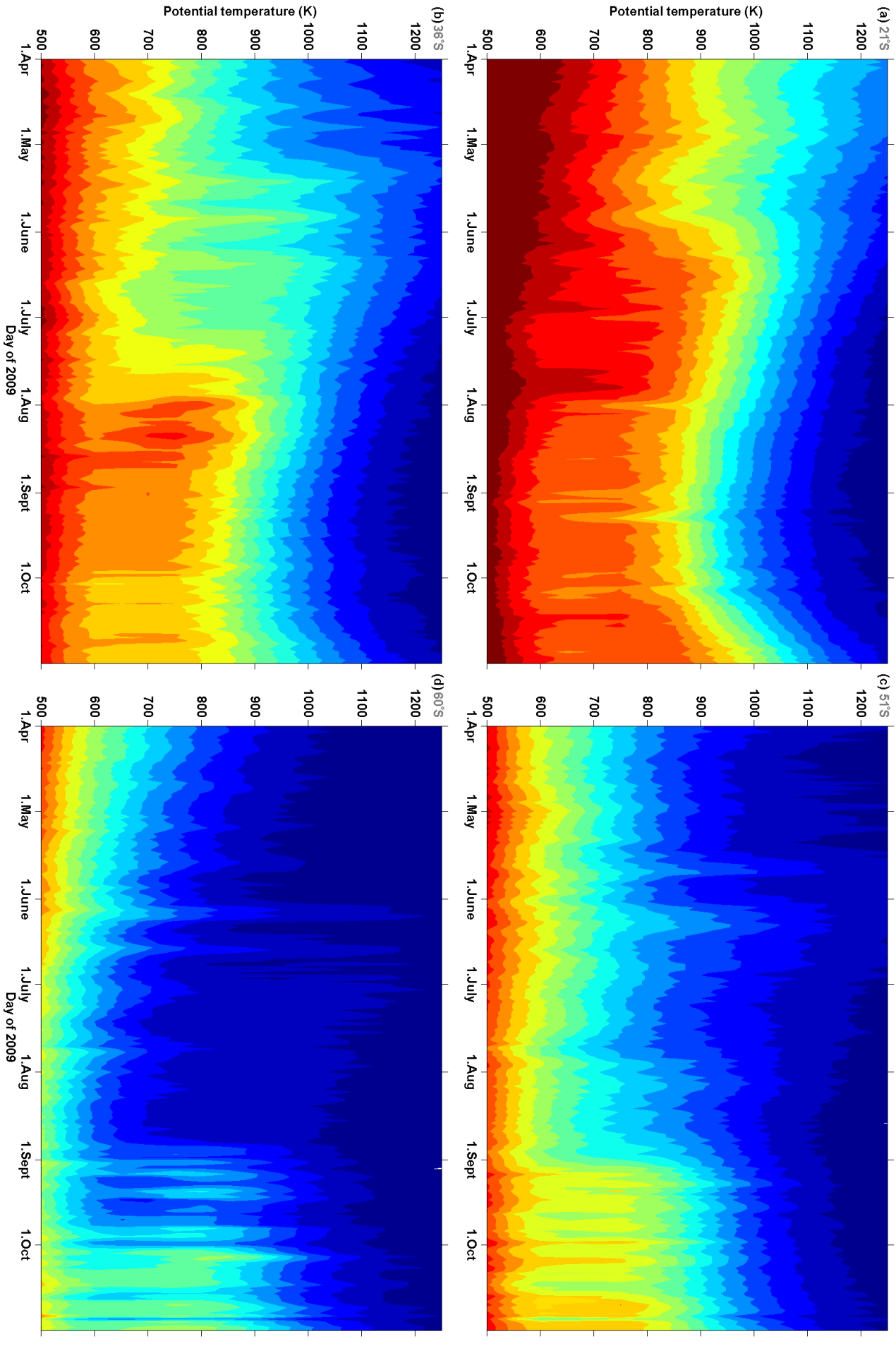

Figure 3.13: Vertical profiles of the zonal mean N_2O volume mixing ratio between 1^{st} April and 31^{st} of 2009 at (a) 21°S, (b) 36°S, (c) 51°S, and (d) 60°S. The colour coding is the same as in Fig. 3.12.

the N_2O mixing ratios then increase rapidly by up to 50 *ppbv* until mid-May. This could mean that the cause for the leakage propagates downward with time. A similar downward progression is observed in 2009 (Fig. 3.13b), but not in 2010.

To further illustrate that these leaks of tropical air into the winter surf-zone do not occur in every year, Fig. 3.12c shows the vertical N_2O profile at 36°S for 2008. Clearly, the large changes in N_2O mixing ratios observed in Figs. 3.12a and b are very different from the behaviour observed in 2008. Throughout the whole period, no sudden major increases in N_2O occur at any of the displayed levels, though some minor temporary increases can be observed. Figures 3.12a to c also show that the tropical leaks only affect a limited vertical range. The variability of the N_2O mixing ratios at and below 550 K in both 2005 and 2010 is small and similar to the variability in 2008. This fits the previous finding that the poleward shifts of the southern hemisphere tropical pipe edge (i.e. the southern hemisphere subtropical maximum of RE_{z10}) at 850 K during leak periods (Fig. 3.11a) are not observed at 550 K (Fig. 3.11b).

The tropical origin of the increased amounts of mid-latitude N_2O is underlined in Figs. 3.13a to d, which are vertical N_2O profiles for 2009 at 21°S, 36°S, 51°S, and 60°S, respectively. Comparing the profile at 21°S (Fig. 3.13a) with the evolution at 36°S (Fig. 3.13b) shows that the increases in N_2O mixing ratios at 36°S are accompanied by decreases in N_2O at 21°S. Particularly the timing of the sudden increase to mixing ratios greater than 165 *ppbv* below 800 K at the beginning of August corresponds well to the simultaneous drop in zonal mean N_2O at 21°S. Additionally, comparison of Figs. 3.13b and c demonstrates that the increase in mid-latitude N_2O only propagates poleward gradually. The maximum value of zonal mean N_2O at, for example, 750 K occurs in early August at 36°S (Fig. 3.13b) but it takes until early September until the N_2O peaks at 51°S (Fig. 3.13c). Around this time, a first brief increase in N_2O is also seen at 60°S (Fig. 3.13d) below 900 K, though really high mixing ratios (> 150 *ppbv*) are not observed this far poleward. While the initial increases in N_2O at 60°S are only temporary with mixing ratios dropping off again after a few days, the changes become more long lasting in early October. By this time, the polar night jet starts to weaken (see also Fig. 3.8) and planetary wave breaking begins to distort the polar vortex or shift it off the pole (e.g. *Waugh and Randel*, 1999). Therefore, most of the variability seen at 60°S later in the season is likely to be related to changes in the polar vortex rather than in the tropics.

The temporal evolution of zonal mean N_2O at 36°S during 2005, 2009, and 2010 suggests that individual events of increased horizontal mixing to higher latitudes 'add up' to an overall increase in mid-latitude N_2O to near-tropical mixing ratios over a period of several weeks. While the strongest increase in N_2O is found between 600 and 900 K, Fig. 3.12b shows that higher levels (> 900 K) can also be affected, and that the region affected by the leakages might be propagating downward with time. Combined with the episodic character of the increases in N_2O, this indicates that the leaks could be related to individual planetary wave breaking events. This suggestion is investigated in further detail in Sect. 3.3. The approximately, but not quite, biennial occurrence of these leaks and the concurrent shifts in the tropical pipe edge also suggest that they may be linked to the quasi-biennial oscillation (QBO). This possibility is discussed in Sect. 3.4.1.

3.2.3 Vertical Structure of the Tropical Pipe in Austral Winter

Having established that the large-scale tropical leak events are observed at a range of levels, the vertical structure of the tropical pipe during austral winter is investigated in the following. Figure 3.14 shows vertical profiles of monthly mean RE_{z10} for July of the years 2006, 2009, 2008, and 2010 (Figs. 3.14a-d, respectively), with monthly zonal mean N_2O volume mixing ratio contours (dotted green lines) and the average location of the subtropical RE_{z10} maximum for each hemisphere (red lines) superimposed.[1] In both 2009 and 2010, the month of July lies in the middle of the leak period, though the leaks start earlier in 2010 (see also Fig. 3.12a). Above 700 *K,* most of the leakage of air from the tropics has already occurred by July in 2010, which explains why no distinct high-RE_{z10} structure is observed between 10°S and 30°S that could represent the southern hemisphere tropical pipe edge (Fig. 3.14d). In July 2009 (Fig. 3.14b), a high-RE_{z10} region is visible between 35°S and 40°S at rather higher latitudes than usual for the tropical pipe edge in winter. This is similar to the situation found in 2005 (Fig. 3.7). The large amount of tropical air that has reached the mid-latitudes by this time has shifted the location of the N_2O gradient poleward (see also Fig. 3.18 and Fig. 3.23b below). The flatness of the N_2O mixing ratio contours in Figs. 3.14b and d between the equator and the subtropical RE_{z10} maximum illustrates how well-mixed the air is between 800 and 1100 *K.* In contrast, the subtropical N_2O gradient of the southern hemisphere tropical pipe edge lies much closer to the equator in July of 2006 and 2008 (between 15°S and 20°S, see Figs. 3.14a and c). At the centre of these gradients a vertically continuous band of high RE_{z10} can be seen between 600 and 900 K in 2006 and up to 1000 K in 2008. This confirms that the high latitudes at which the RE_{z10} identifies the southern hemisphere tropical pipe edge in some years (Fig. 3.11) are not an artefact of the RE_{z10} methodology but are due to the large-scale leaks from the tropical pipe shifting the location of the maximum N_2O gradient poleward.

A high-RE_{z10} structure probably associated with the N_2O gradient at the polar vortex edge is found near 60°S in all four years, but with some distinct differences between the years with and without large-scale tropical leaks. From 400 to 850 *K,* the polar high-RE_{z10} region is centred close to 60°S in 2006 and 2008 (Fig. 3.14a and c). In 2009 and 2010, this is also the case below 550 K and the high-RE_{z10} band is continuous up to at least 1000 K with an equatorward tilt with altitude (Fig. 3.14b and d). Above 750 K in July 2010 the gradient between tropical and mid-latitude N_2O mixing ratios has been shifted so far toward the polar vortex by tropical leakage that it cannot be distinguished from the gradient at the vortex edge anymore. Therefore the red line indicating the southern hemisphere subtropical RE_{z10} maximum in Fig. 3.14d cannot be considered a reliable estimate of the position of the tropical pipe edge during this time. Its location is largely determined by the limitation to the region between 4.5°S and 40.5°S when searching for the RE_{z10} maximum. In July 2009, the southern tropical pipe edge and the polar high-RE_{z10} region are distinct features. The former is centred at 30°S between 650 and 1050 *K,* while the tilt of the latter means that it lies between 55°S and 48°S in this vertical range. These latitudes appear to be too low to be realistic, as was mentioned earlier.

[1] The years 2009 and 2010 were selected as an example for years when leaks are occurring as these were already examined in Sect. 3.2.2 and because 2005 and 2007 both have a data gap in July. 2006 and 2008 are the only available years during which no large-scale leakage is observed.

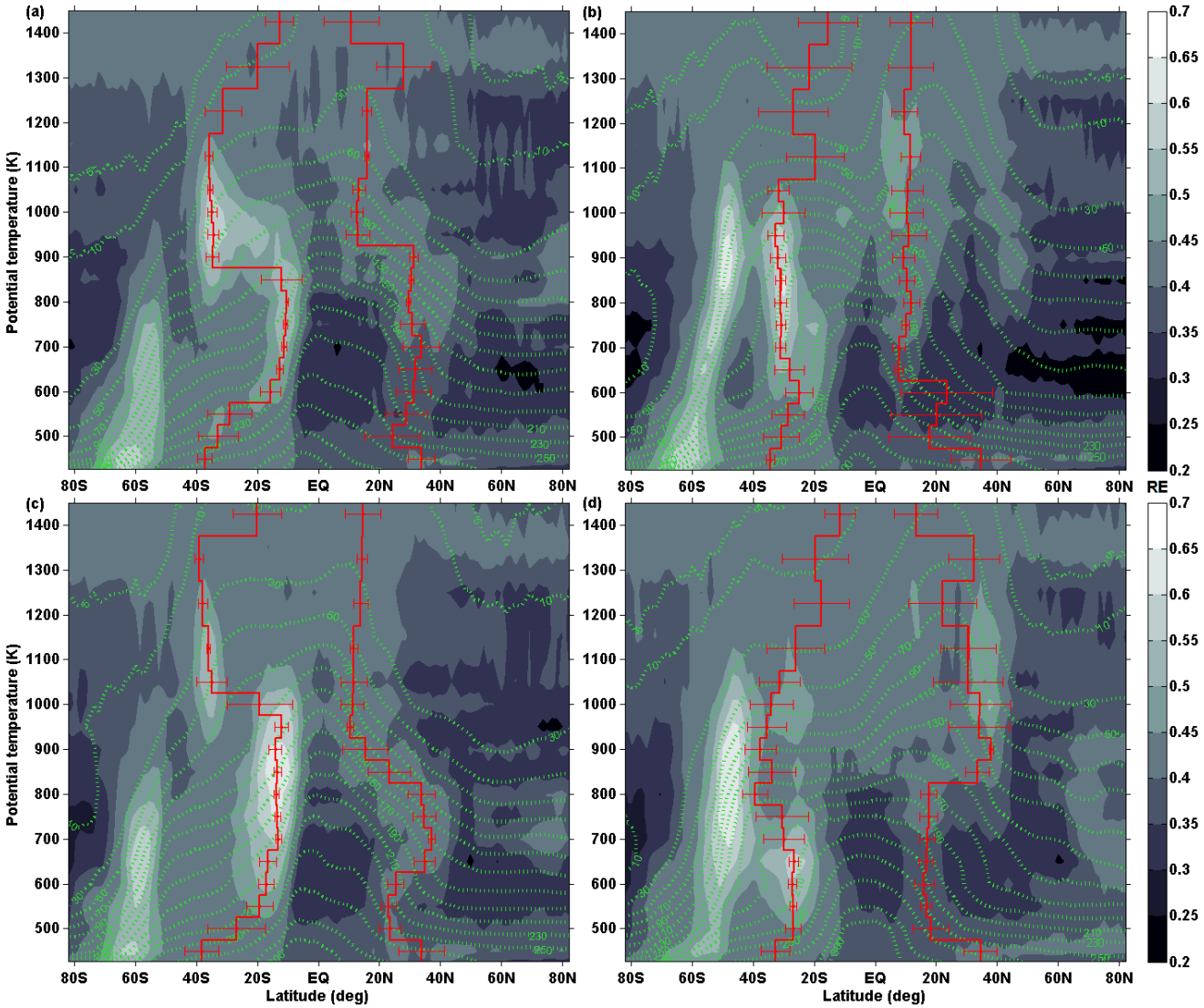

Figure 3.14: Meridional profile of monthly average RE_{z10} for July in (a) 2006 (b) 2009 (c) 2008, and (d) 2010. 2009 and 2010 are years during which large-scale leaks of air from the tropical pipe are observed, while 2006 and 2008 are not. Dotted green contours represent the monthly average N_2O volume mixing ratios in *ppbv*. The red lines correspond to the average location of the subtropical RE_{z10} maximum for each hemisphere and the error bars give the standard deviation of the daily latitude of the RE_{z10} maximum from the respective monthly average.

In 2006 and 2008, a high-RE_{z10} region can be observed around 40°S above 900 K and 1000 K, respectively (Figs. 3.14a and c). At these levels the zonal mean N_2O contours are nearly horizontal from the equator to 30°S, particularly in 2006. This suggests that the high-RE_{z10} region near 40°S does represent the tropical pipe edge at higher altitudes and that there is a sudden jump in the latitude of the tropical pipe edge compared to lower levels. The RE methodology correctly recognises this jump, as can be seen in the red line in the southern hemisphere in Figs. 3.14a and c. On the other hand, the polar high-RE_{z10} region only reaches up to approximately 850 K in these years. This is probably related to a lowering of the signal-to-noise ratio as the volume mixing ratios decrease with altitude. In all four diagrams of Fig. 3.14, the regions of high RE_{z10} values tend to deteriorate above the 30 *ppbv* contour. The single profile precision of the N_2O observations at these altitudes is 13 *ppbv* (*Livesey et al.*, 2011). This implies that the signal-to-noise ratio above the 30 *ppbv* contour is similar to that of the CH_3Cl observations at 550 K (see Sect. 3.1.2). Hence, the uncertainties in the N_2O observations are probably the reason why the RE cannot detect the gradients at higher levels anymore. This also implies that the subtropical maxima of RE_{z10} identified by the red lines in Figs. 3.14a-d have to be considered unreliable estimates of the location of the tropical pipe edges above the 30 *ppbv* contour.

3.3 High-resolution Analysis of Tropical Leaks via Domain Filling

In order to investigate the large-scale leakages of tropical air into the mid-latitudes of the southern hemisphere (identified in Fig. 3.8) in more detail, a technique for artificially enhancing the resolution of the available observations is used in the following. The technique is based on the reverse domain filling methodology introduced by *Sutton et al.* (1994). The number of data points for each day is increased by using a two-dimensional trajectory model (see Sect. 2.3.4) and reanalysis winds (MERRA, see Sect. 2.3.2) to advect tracer observations from previous and subsequent days to the central 'current' day. In particular, five days of observations on either side of the current one are advected to 12:00 (noon) UTC of that day. Observations for the central day that were not acquired at 12:00 UTC ($\pm$ 0 : 30, since the advection model works in hourly time steps) are also advected by the appropriate number of hours, thus creating a synoptic map of the tracer field with approximately eleven times as many data points than in the original observations. No more than five days on either side are used in order to minimise potential errors related to neglecting vertical motion. *Pierce et al.* (1994) showed that the correlation between coincident adiabatically-advected and subsequent measurements of stratospheric tracers remains high for about ten days. The approach differs from the original reverse domain filling methodology (*Sutton et al.*, 1994) in that the resulting synoptic tracer field is not a regularly sampled grid and because it also includes observations acquired after the central day. It will therefore be referred to simply as 'domain filling'. Initially, the focus is on the leak occurring in 2009 as its evolution is representative for most other years and because it is one of the few years during which the EOS-MLS data has no gaps.

3.3.1 High-resolution N_2O Maps at 850 K

Figure 3.15a shows the global synoptic map of N_2O volume mixing ratio at 850 K for 12:00 UTC on 28.6.2009 which includes measurements from 23.6.2009 through 3.7.2009. The tropical pipe region with high N_2O mixing ratios (> 150 $ppbv$), the surf-zone with intermediate values ($\approx 50 - 150$ $ppbv$), the polar vortex with very low N_2O (< 50 $ppbv$), and the summer hemisphere with low and intermediate amounts of N_2O, can all be clearly identified. As can be seen in Fig. 3.15c, the basic structures in the N_2O data very closely match those observed in the potential vorticity (PV) field for the same day. Note that the colour-scale in Fig. 3.15c assigns the same colour to PV values of identical magnitude but opposite sign, facilitating the comparison with Fig. 3.15a. A scatter plot of N_2O volume mixing ratio vs. PV interpolated to the final position of the corresponding trajectory (Fig. 3.15d) confirms that there is a close relationship between the two fields in both hemispheres. In the northern hemisphere (PV > 0), the relationship is particularly compact and follows a close to linear trend of lower mixing ratio with increased PV. In the southern hemisphere, the scatter around the general trend of decreasing N_2O with decreasing (i.e. increasingly negative) PV is slightly higher, reflecting the more active dynamics in the surf-zone. The coherent structure of the result of the domain filling and the strong similarities between the PV and the tracer fields suggests that the technique successfully generates a high resolution image of the tracer distributions on the respective day.

The domain filled maps allow a more detailed analysis of the dynamics leading to the considerable increase in zonal mean N_2O in the southern hemisphere surf-zone in 2005, 2007, 2009, 2010, and 2011 (Fig. 3.8). These will be referred to as 'leak-years' in the following. Animations of the domain filled maps and PV distributions for 2004 to 2011 are supplied as an electronic supplement to this thesis. The animations consist of images like Fig. 3.15 for each day. Details of the available files are given in Appendix A.

A study of the temporal evolution of domain filled maps for the leak-years confirms that the high N_2O mixing ratios in the subtropics during leak-years are the result of several individual events of air being drawn out from the tropics and mixed into the surf-zone (Appendix A). In some cases, filaments of air with low amounts of N_2O (< 50 $ppbv$) are simultaneously extracted from the polar regions and also mixed into the surf-zone (see also Fig. 3.17). The polar filaments tend to be relatively thin and therefore do not have a large effect on the mid-latitude mixing ratio of N_2O, at least not before the beginning of spring. Eventually, most of the southern hemisphere surf-zone is mixed with air from the tropics and contains volume mixing ratios of N_2O that are uncharacteristically high for mid-latitudes (≈ 150 $ppbv$; see Fig. 3.16). These episodic events are likely to be related to planetary wave breaking within the surf-zone (see below) and each event tends to shift the region with high (tropical) amounts of N_2O closer toward the polar vortex edge. This also explains the poleward shift of the tropical pipe edge detected in the RE analysis during these periods (see Sect. 3.2.1). Similar wave breaking events also occur in non-leak-years, but less frequently and without causing large changes in N_2O mixing ratios in the surf-zone.

As has already been mentioned, a number of the observed events causing leakage of N_2O from the tropics are found to be accompanied by deformations of the polar vortex, similar to the planetary wave breaking event detailed in *Randel et al.* (1993) and *Waugh (1993).* The

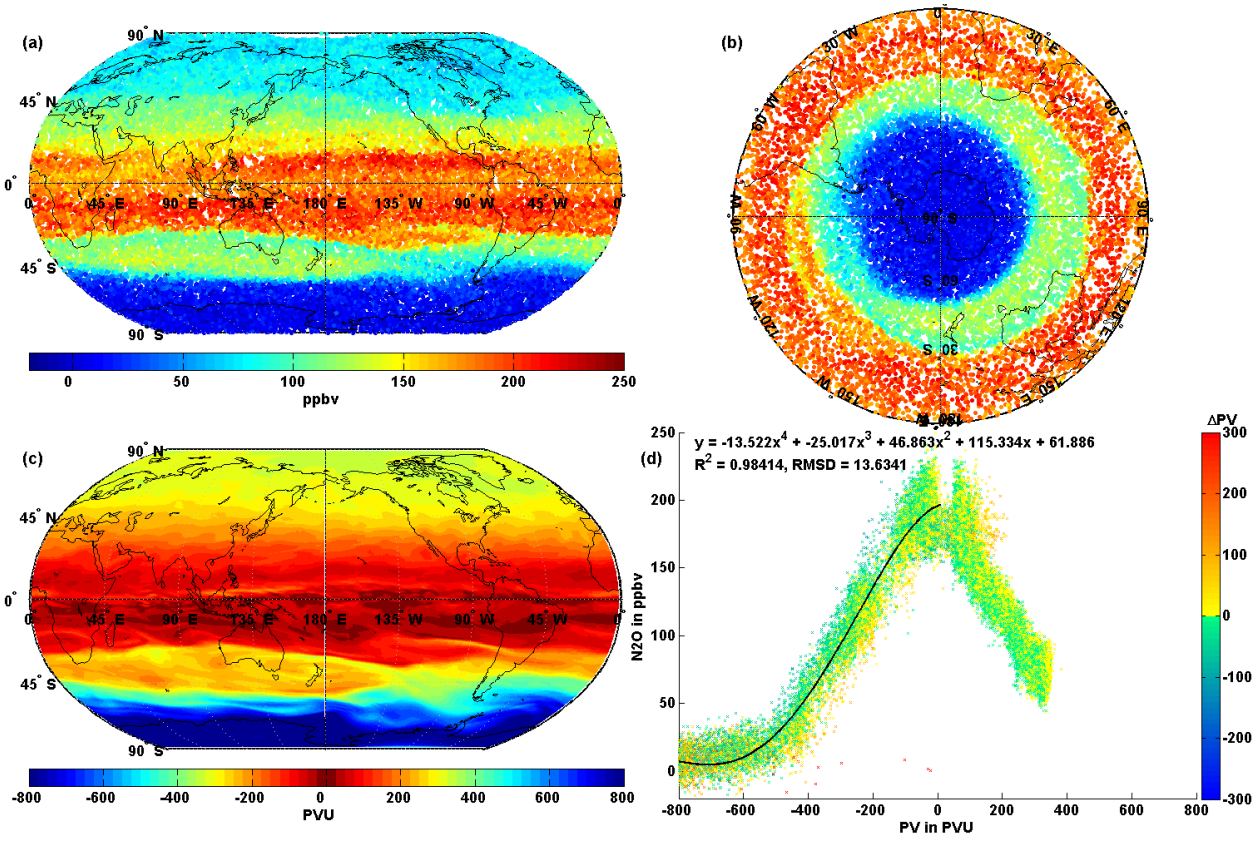

Figure 3.15: (a) Global synoptic map of N_2O volume mixing ratio at 850 K on 28.6.2009 (12:00 UTC) created using domain filling with measurements from 23.6. to 3.7. (b) shows the data just for the southern hemisphere in polar stereographic projection and uses the same colour scale as (a). (c) is the PV field at 850 K on 28.6.2009 derived from MERRA winds and temperature. Note that the colour scale shows positive and negative values of PVU in the same colour. (d) is a scatter plot of N_2O volume mixing ratio vs. PV interpolated to the final position of each air parcel. The colour of each dot in (d) corresponds to the difference in PV between the initial and the final position of the air parcel.

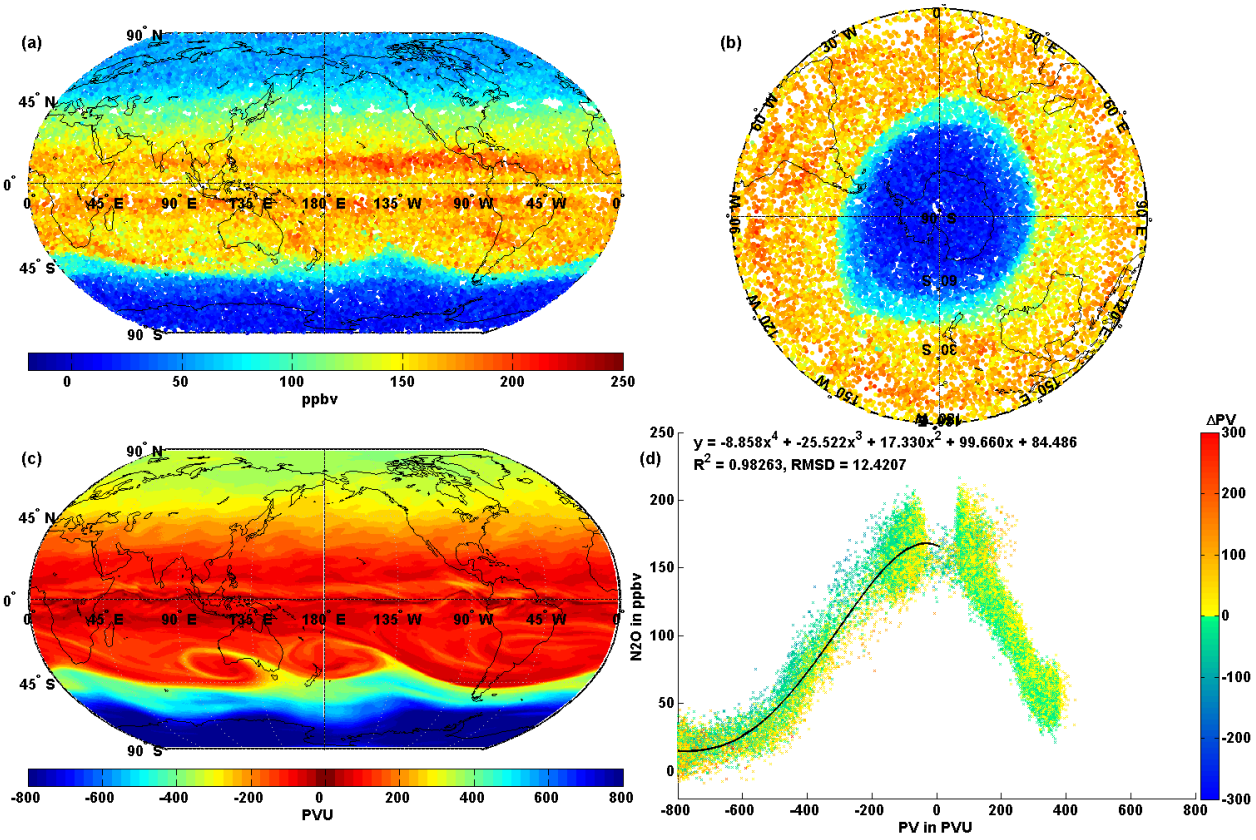

Figure 3.16: Same as Fig. 3.15 for 19.8.2009 (12:00 UTC).

onset of such a wave breaking event is illustrated in Fig. 3.17. The close proximity of the low- and high-N_2O air masses west of South Africa can be clearly observed (black oval in Fig. 3.17b). In subsequent days, the patch of tropical air adjacent to the polar vortex in Fig. 3.17a is drawn further into the surf-zone and eventually disperses there. *Waugh* (1993) argues that planetary wave breaking at the polar vortex edge, which results in strong distortions of the polar vortex, is the actual cause for air being drawn out of the tropics. The polar stereographic projection in Fig. 3.17b illustrates the distortion of the polar vortex occurring in June 2009, suggesting that this could be the kind of event described by *Waugh (1993)*. Additionally, the large anticyclonic structure that can be seen over South America in the PV field (Fig. 3.17c) and the second, smaller one that is forming south-west of Australia, is another indicator that planetary wave breaking is occurring *(Hood et al., 1999; Harvey et al., 2008)*. Anticyclones are particularly efficient at mixing different air masses *(Harvey et al., 2002)* and a connection between poleward movement of tropical (and subtropical) air and the presence of anticyclones has been previously observed in *Trepte et al. (1993)* and *Harvey et al. (1999)*, among others.

However, not all events that contribute to the overall increase in mid-latitude N_2O in 2009 are of this nature. Figure 3.18 shows synoptic maps of N_2O at 850 K for every second day between the 5^{th} and 17^{th} July 2009. During the whole period, the edge of the region containing low (polar) N_2O mixing ratios (< 50 $ppbv$) only undergoes small shifts in latitude. At the same time, an anticyclone containing high-N_2O air starts forming near Australia and moves east toward South America, all the while pulling more air out of the tropics. While some of this air returns to lower latitudes, the average latitudinal location of the region

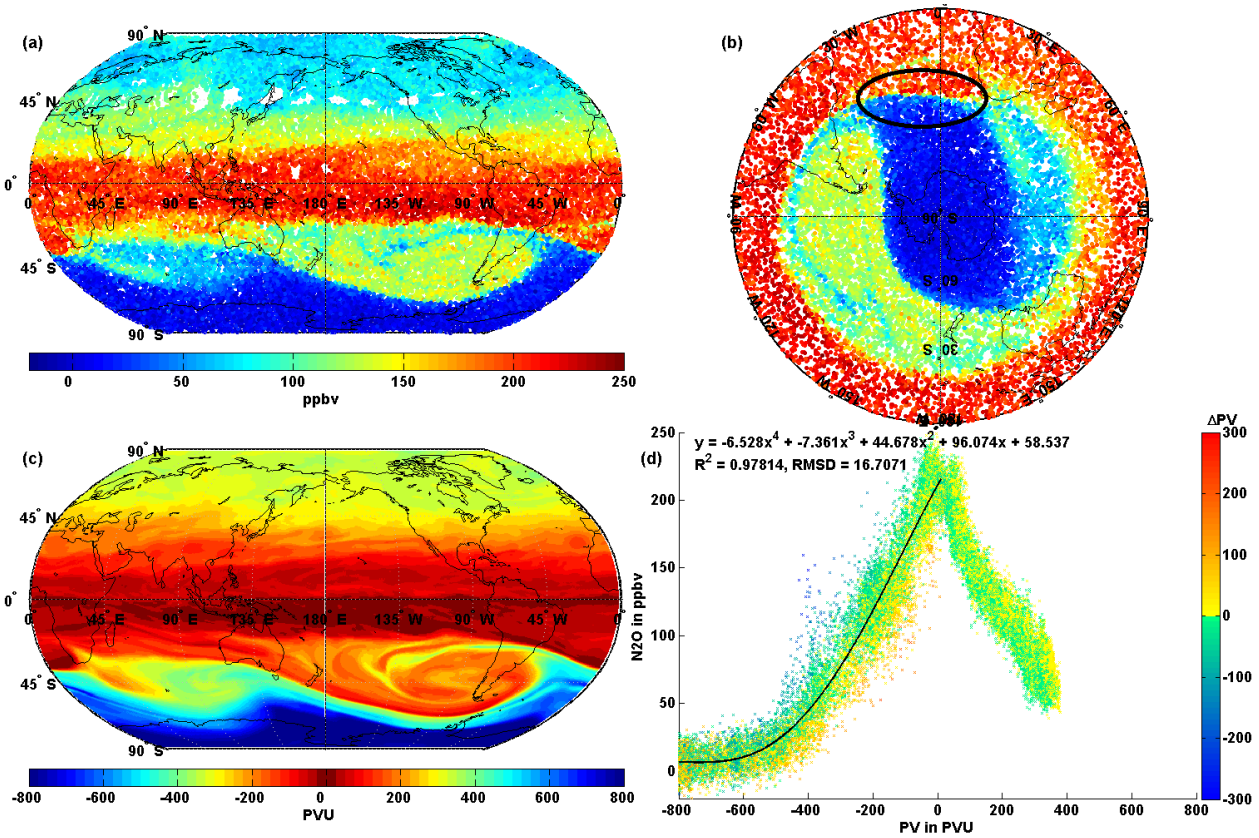

Figure 3.17: Same as Fig. 3.15 for 7.6.2009 (12:00 UTC). The black oval in (b) marks a region where polar and tropical air-masses come very close to each other.

where high N_2O mixing ratios and intermediate subtropical values meet has shifted slightly further poleward by 19^{th} July. This suggests that it is not only planetary wave breaking at the vortex edge that contributes to the large-scale increase in mid-latitude N_2O (as suggested in *Waugh*, 1993), but wave breaking occurring at lower latitudes may also be involved.

For example, the dynamics illustrated in Fig. 3.18 could be similar to the situation described by *Portafaix et al. (2003)* and *Morel et al. (2005)*. They investigate the details of one particular event on 12^{th} July 2000, when a tongue of tropical air (they consider ozone in particular) forms over Madagascar and gets mixed into the mid-latitudes. *Portafaix et al. (2003)* state that the filament "is produced by the erosion of the subtropical barrier caused by a vigorous wave breaking in the surf zone during that time" and *Morel et al. (2005)* go on to show that "the tongue is generated by the combination of several planetary modes", wavenumber 3 being the most important one in that case. The situation appears to be very similar to the dynamics observed during the leak events described here and confirms that leakage of air from the tropical pipe can also be caused by wave breaking events within the surf-zone that do not involve the polar vortex. Such wave breaking events largely occur in late autumn and early winter.

From late August onward, most of the events during which filaments of tropical air are mixed into the surf-zone involve distortion of the polar vortex and in some cases air from both the tropics and the polar vortex is drawn into the surf-zone at the same time (see also Appendix A). Figure 3.19 illustrates such an event. On 5^{th} October 2009, a filament of air is

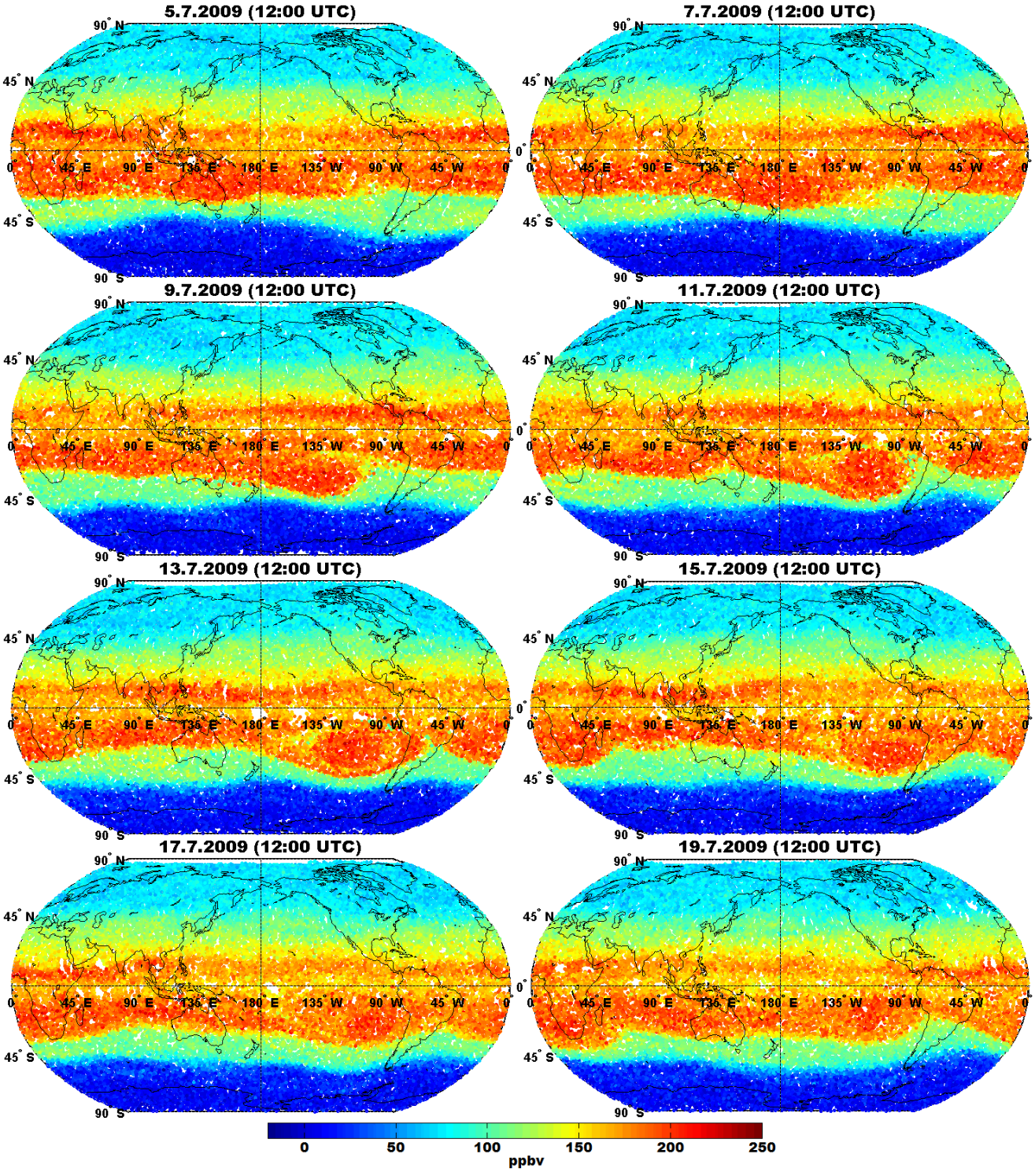

Figure 3.18: Domain filled synoptic maps of N_2O at 850 K for every second day from the 5^{th} to 17^{th} July 2009 (top left to bottom right), illustrating a wave-breaking event within the southern hemisphere surf-zone.

being drawn out from the polar vortex to the east of South America, while an adjacent filament of tropical air is being wrapped around the vortex (see Fig. 3.19b). The corresponding scatter plot of PV vs. N_2O for 5^{th} October 2009 (Fig. 3.19d) shows that the relationship is much less compact than before, with a large, diffuse 'cloud' of points filling most of the area between -600 PVU and -200 PVU. The considerable (temporary) discrepancy between the observed N_2O field and the pseudo-tracer field defined by the PV is probably an indicator of large-scale, irreversible mixing, though it may partially be due to the innaccuracies involved in determining the corresponding PV-values for each air parcel. In the presence of thin streams of high or low PV air, the interpolated PV value from the (MERRA-) grid points closest to the final position of an air parcel (advected over up to five days) might not be a good estimate of the actual PV of that air parcel. Additionally, changes in the volume mixing ratio of N_2O in an air parcel by diffusion have been neglected. Nevertheless, a relationship between the occurrence of large-scale mixing and increased 'cloudiness' in the PV-N_2O-relationship in the southern hemisphere is likely. This is underlined by the large changes of PV (ΔPV) exhibited by most dots that are far away from the fitted PV-N_2O-relationship in Fig. 3.19d, since changes in PV are an indicator for irreversible mixing. For example, consider Figs. 3.15d and 3.16d: in both cases the main PV-N_2O curve is relatively compact and the corresponding N_2O maps (Figs. 3.15a and 3.16a) show little zonal variability. Fig. 3.17d on the other hand, representing the beginning of a leak from the tropics, has noticeably more 'outliers' between 0 and -400 PVU, though the distribution is not as widely spread as in Fig. 3.19d. Particularly in the latter case, multiple patches of low PV (and low N_2O) can be observed that are cut off from the 'tail' of the distorted polar vortex at low latitudes (over Australia and the Pacific between 20°S and 30°S). These are unlikely to return to higher latitudes and must therefore be mixed into the surf-zone eventually. Similarly, the long filament of high PV (and high N_2O) that is being wrapped around the polar vortex over the South Atlantic (Fig. 3.19b), and is thereby pulled to latitudes of 60°S and more, must result in considerable irreversible mixing as this air also does not return to its original latitudes but gets wrapped around the large anticyclone over Australia and New Zealand, where it eventually disperses (see Appendix A). This anticyclone is probably the "Australian High" identified in *Harvey et al.* (2002).

To get a measure of the compactness of the relationship between PV and N_2O a fourth order polynomial is fitted to the PV-N_2O curve for each day. The fit is limited to air parcels between 0°S and 85°S to ensure that only air parcels in the southern hemisphere are included and to avoid very large PV values near the poles distorting the fit. The black lines in Figs. 3.15d, 3.16d, 3.17d, and 3.19d are the fitted polynomials with their equations given in the top left corner of each scatter plot. From the fitted polynomial a 'predicted' N_2O mixing ratio is calculated for each air parcel according to its the associated PV value. The difference between this 'predicted' mixing ratio and the actual, observed amount of N_2O corresponds to the (vertical) distance of each point from the idealised curve. Summing up the square of these offsets from the fitted curve for all air parcels in the southern hemisphere, taking the square root of the result, and dividing by the total number of parcels, results in the root mean square deviation (RMSD) of the observed N_2O mixing ratios from the idealised fit. Accordingly, the RMSD is a measure of the overall mismatch between the N_2O and the PV field in the southern hemisphere.

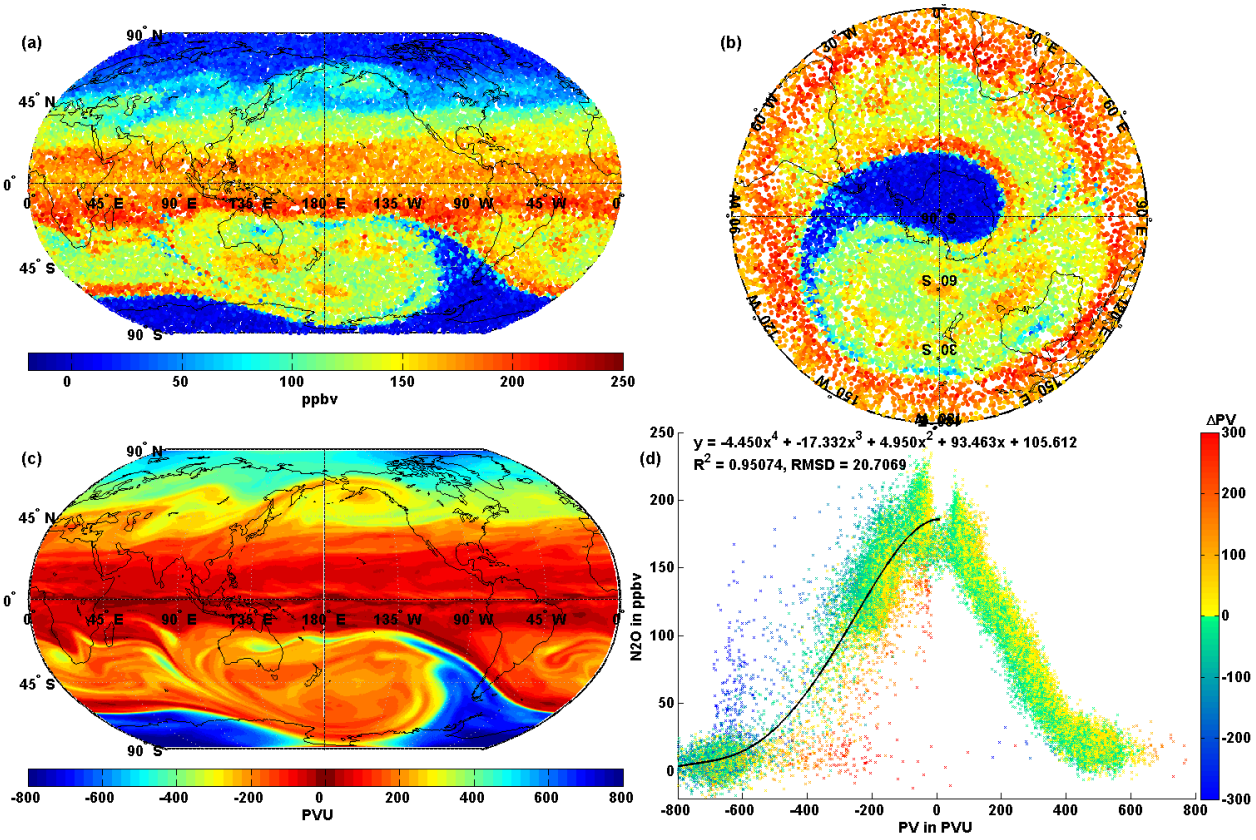

Figure 3.19: Same as Fig. 3.15 for 5.10.2009 (12:00 UTC).

The temporal evolution of the RMSD of N_2O in the southern hemisphere at 850 K from April through October for leak-years and non-leak-years is shown in Figs. 3.20a and b, respectively. The value of the RMSD does not have any inherent meaning but previous considerations showed that a sudden increase in the mismatch between PV and N_2O is probably linked to mixing of distinct airmasses. Before 1^{st} August, the evolution of the RMSD during leak-years and non-leak-years are qualitatively quite different. While the RMSD increases gradually from May to August during the non-leak-years (Fig. 3.20b), multiple local peaks can be seen in the same time-period during leak-years (Fig. 3.20a). For example, in 2009 three major peaks can be seen before the beginning of August. One in mid-May, another in early June and a third in late July. Each of these peaks coincides with large-scale mixing of tropical air into the surf-zone. For example, Fig. 3.17 corresponds to the tip of the peak in early June (magenta line in Fig. 3.20a). At the end of this period the RMSD drops to a local minimum in mid-August 2009. This represents a time during which relatively high N_2O mixing ratios can be found throughout most of the surf-zone. The other leak-years display a similar evolution until early August: a general upward trend with several local peaks along the way. 2005 and 2007 (black and red lines in Fig. 3.20a) are different in that they reach considerably higher RMSD values, but otherwise the evolution is similar.

In late August 2009 the RMSD starts rising again, resulting in a strong peak in early September (Fig. 3.20a). After a brief rebound, the RMSD once more increases rapidly until early October. The same is true for the other leak-years: after August the RMSD tends to increase further until it reaches an overall maximum between mid-September and mid-October. Most of the peaks observed during springtime are probably related to large-scale mixing events

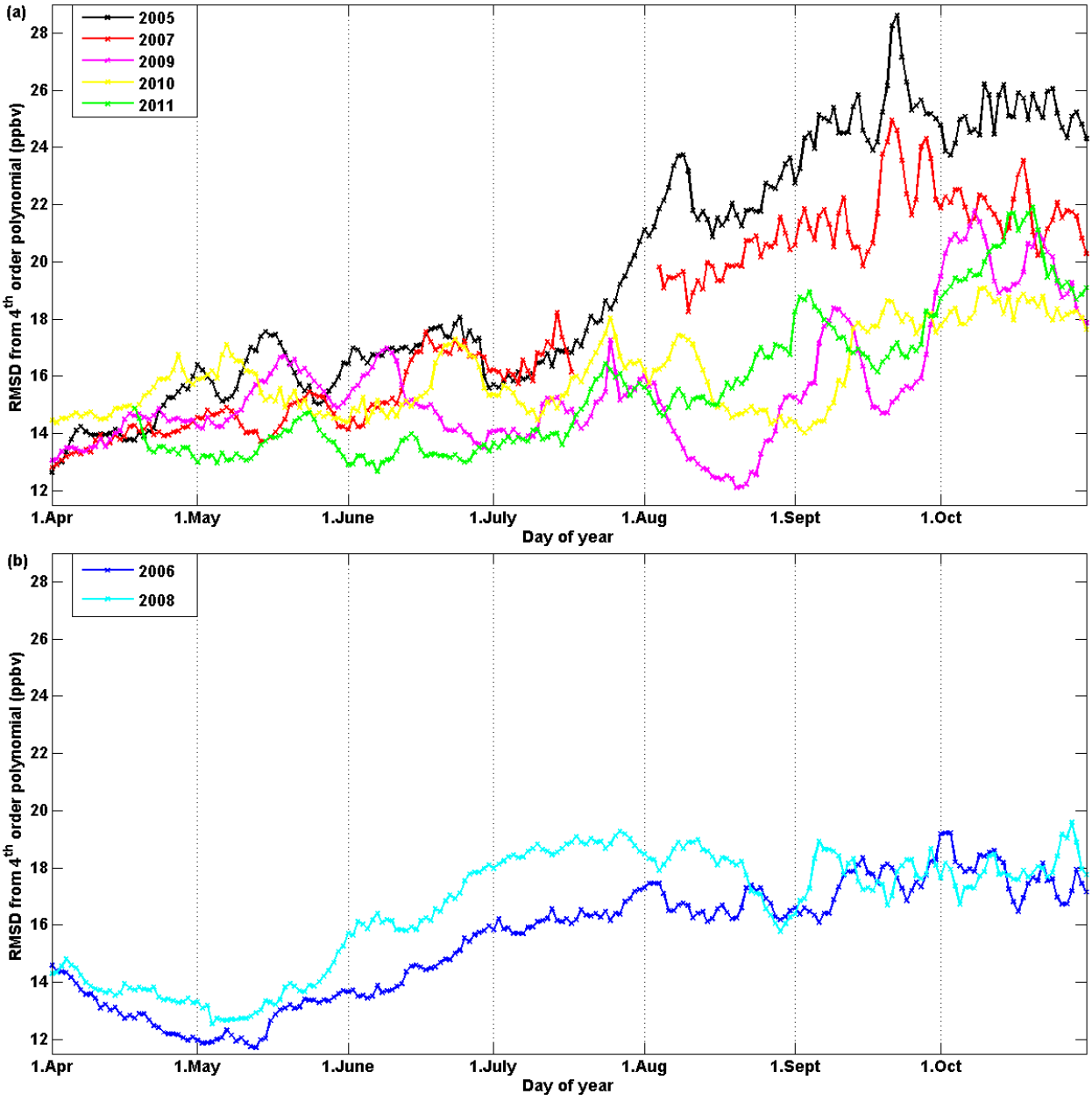

Figure 3.20: Root mean square deviation (RMSD) of the N_2O volume mixing ratio from a fourth order polynomial fitted to the PV-N_2O relationship in the southern hemisphere derived from domain filled N_2O maps at 850 K for April through October during (a) leak-years and (b) non leak-years. The RMSD has units of *ppbv*.

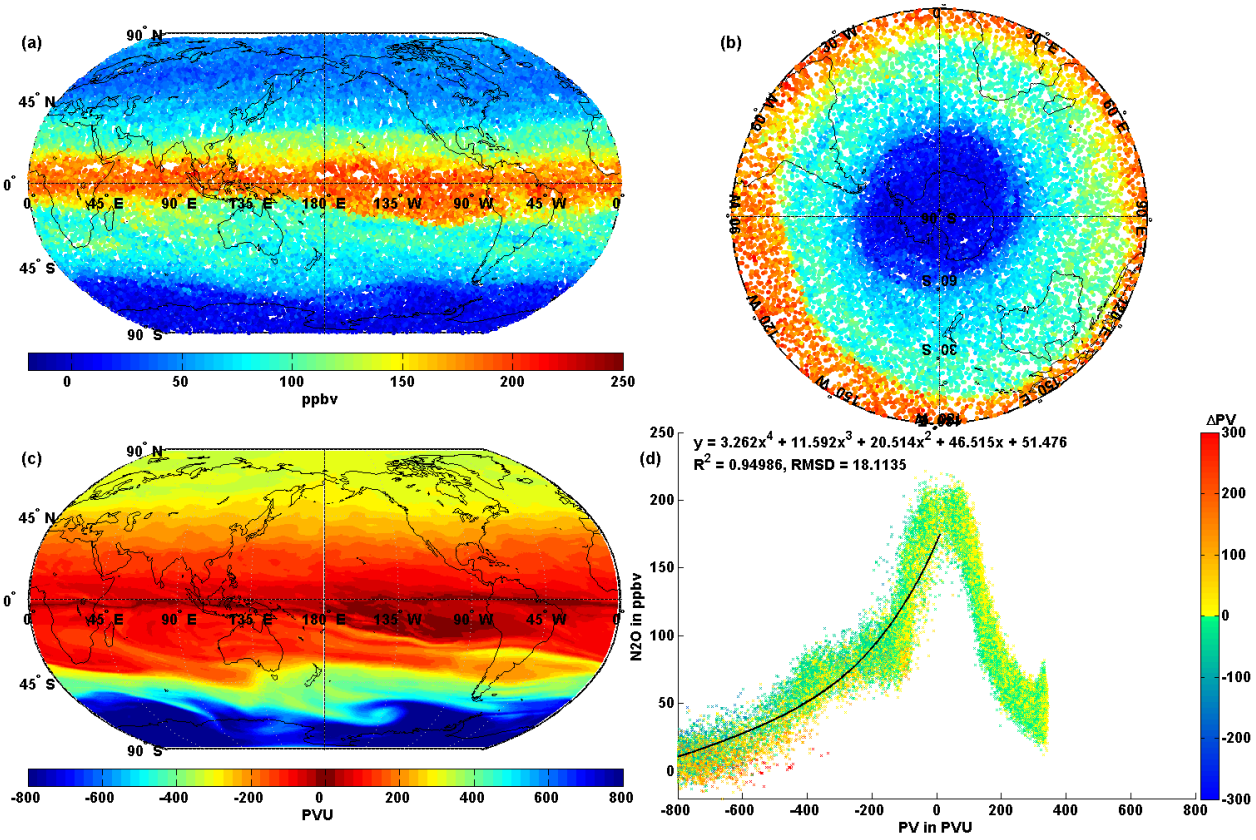

Figure 3.21: Same as Fig. 3.15 for 1.7.2008 (12:00 UTC).

caused by planetary wave breaking at the edge of the polar vortex. For example, Fig. 3.19 corresponds to the first RMSD peak in October. The evolution of RMSD during non-leak-years also becomes more variable in spring, showing several small, local peaks particularly in September and October (Fig. 3.20b). However, the RMSD does not increase much beyond the value reached by August during these years. The reason that the RMSD in 2008 is consistently higher than in 2006 between June and mid-August is that the PV-N_2O relationship has a kink around -100 PVU in mid-2008 (see Fig. 3.21d), resulting in a relatively bad fit between the fourth-order polynomial and the actual PV-N_2O curve, thereby increasing the RMSD. Such a kink does not develop in 2006 and accordingly the RMSD is lower during this time. A similar, more permanent kink between -150 and -200 PVU (not shown) is also the reason for the elevated values of RMSD in 2005 and 2007 (Fig. 3.20a). This also illustrates why the magnitude of the RMSD is not inherently meaningful.

The link between rapid changes in RMSD and the movement of high-N_2O air to higher latitudes is emphasised by Fig. 3.22. It shows the evolution of the zonal mean N_2O volume mixing ratio at 51°S (magenta line) and the RMSD (black line) in 2009 for the 850 K level. The RMSD was multiplied by five compared to Fig. 3.20a to make the values fit into the same range. The particular latitude was selected as it should generally lie outside both the tropical pipe and the polar vortex and because the N_2O values correspond to a crossprofile (at 850 K) of the data previously shown in Fig. 3.13c. The correlation coefficient between the two curves is 0.743, showing that there is a strong relationship between changes in RMSD and changes in N_2O. The first two peaks in RMSD in May and June 2009 coincide with peaks in N_2O (Fig. 3.22). The increase in N_2O only lasts for several days on these occasions, which fits the idea

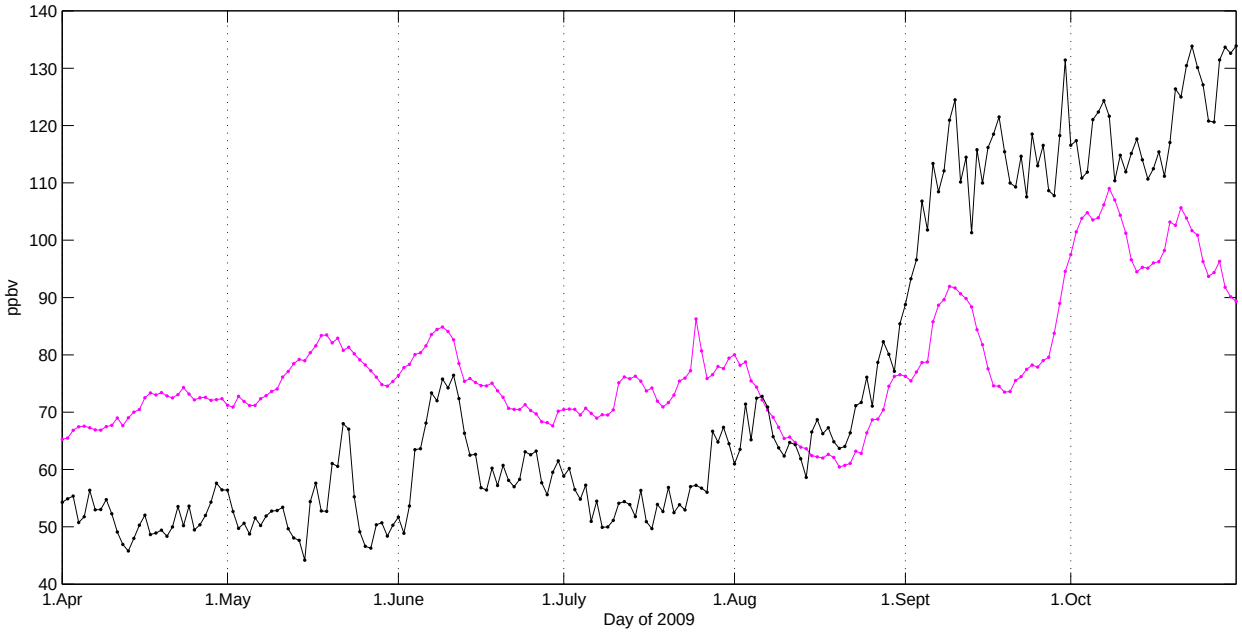

Figure 3.22: Evolution of zonal mean N_2O at 51°S (black) and the RMSD (magenta; multiplied by five to fit into the same vertical range as the N_2O values) at 850 K in 2009 . The correlation coefficient of the two curves is 0.743.

that individual mixing events (associated with the peaks in RMSD) only gradually shift the boundary between tropical and mid-latitude N_2O concentrations poleward. During another peak in RMSD, between the end of July and early August 2009, the N_2O levels rise again (though not as high) and this time the mixing ratio does not return to its previous value but oscillates at a higher level until late August (Fig. 3.16b illustrates the N_2O distribution during this time). The considerable increase in RMSD from the end of August to the peak in early September then coincides with a major and long-lasting increase in N_2O at 51°S. This fits well with the idea that the mixing events before August largely affect lower latitudes, while later peaks in RMSD are related to mixing that also affects higher latitudes and the polar vortex. The double-peak in RMSD in October 2009 is the only one that does not show a simultaneous response in the N_2O mixing ratio in Fig. 3.22. Since these peaks are likely related to planetary wave breaking events that displace or distort the polar vortex (e.g. Fig. 3.19b) the zonal averaging could be disguising some of the effects. This might also explain the delayed increase in N_2O observed just after the second half of the peak.

Rapid variations in the RMSD are useful for identifying large-scale mixing events in the southern hemisphere, with local peaks in the RMSD representing times during which otherwise distinct air masses become mixed. While qualifying what kind of events are occurring, i.e. which air masses are being mixed, requires additional information, the overall evolution of the RMSD shows qualitative differences between leak- and non-leak-years. During southern hemisphere late autumn and early winter (May through July) leak-years tend to display several local peaks in RMSD, while it increases gradually during non-leak-years. Beginning in late winter, the RMSD increases further and shows several local peaks during all years, reaching an overall maximum in mid-Spring. Peaks occurring earlier in the season tend to be associated with air from the tropics being drawn into the surf-zone, while later

peaks are usually coincident with polar vortex air being drawn into the surf-zone, though in some cases both happen at the same time (e.g. Fig. 3.19). The peaks in the RMSD most likely correspond to planetary wave breaking in the surf-zone and at the edge of the polar vortex, but a conclusive analysis of individual events and planetary wave activity is beyond the scope of this study.

3.3.2 *RE* Analysis of Domain Filled Maps

The high resolution maps of N_2O produced by domain filling can also be utilised to calculate the *RE* on a latitude-longitude grid for each day, thereby adding longitudinal resolution to the zonal information previously derived. This involves binning the synoptic data onto a regular grid and using a moving window in which to calculate the *RE*.

The domain filled data for each day is binned to a regular grid with 90 latitude bins (2° each) and 60 longitude bins (6° each). A synoptic map of N_2O for one day at a particular potential temperature level, derived in the manner detailed in Sect. 3.3.1, typically consists of 30,000 to 35,000 data points. Accordingly, the average number of data points at each point of the (2°×6°)-grid is approximately six, though the exact number can vary considerably, depending on latitude and the strength of meridional mixing. Therefore, data from several grid points has to be combined when creating the PDFs from which the *RE* is derived. In the following, the *RE* at each grid point is calculated from PDFs that include the data points from two latitude and four longitude bins on either side of respective grid point.[2] This corresponds to a moving window of 10° latitude and 54° longitude and results in an average of about 300 points per PDF. Such a large data window does of course involve a considerable amount of smoothing but it ensures that sparse PDFs with insufficient data points are avoided. To maintain a consistent latitudinal extent, no *RE* is calculated for the two latitude bins closest to the the poles, i.e. the RE_{la5lo9} is only calculated between 85°S and 85°N.

Figures 3.23a-c are contour plots of the resulting RE_{la5lo9} maps derived from the domain filled N_2O field at 850 K on 1.7.2008, 28.6.2009, and 19.8.2009, respectively. The southern hemisphere winter edge of the tropical pipe shows up as an (almost) continuous band of high-RE_{la5lo9} values in Figs. 3.23a and b. On these days, a part or even the whole of the northern hemisphere (summer) edge also shows up as a band of increased RE_{la5lo9}. Individual leak events that pull air out of the tropics tend to cause large patches of high *RE* that extend meridionally across most of the surf-zone for a few days. The high RE_{la5lo9} values are due to the longitudinal gradients created by the displaced air mass (not shown). During these times the RE_{la5lo9} is unreliable for locating the tropical pipe edge, because high RE_{la5lo9} values associated with the meridional gradient to the tropics cannot be distinguished from high values caused by longitudinal gradients.

The gradual increase in latitude of the gradient between tropical and mid-latitude N_2O values observed during leak-years (e.g. Fig. 3.18), can also be observed in the RE_{la5lo9} patterns. By the 28^{th} June 2009 parts of the southern hemisphere surf-zone already contain

[2]Similar to the previous notation the *RE* calculated in this fashion is referred to as RE_{la5lo9} when distinction is required, indicating that the data from a total of five latitude (*la5*) and nine longitude (*lo9*) bins are being used to calculate each value.

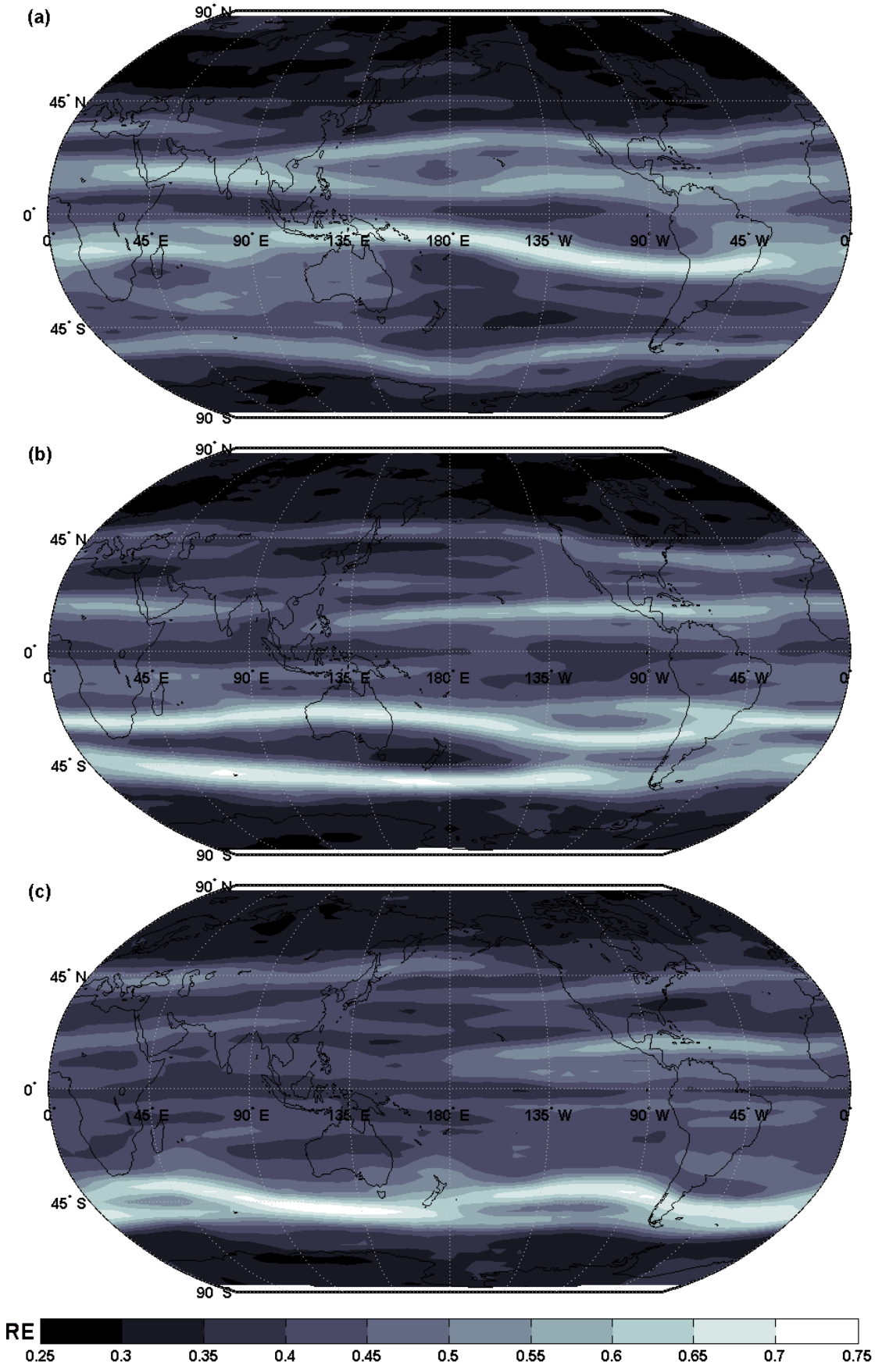

Figure 3.23: RE_{la5lo9} of domain filled N_2O maps at 850 K for (a) 1.7.2008, (b) 28.6.2009, and (c) 19.8.2009. Figures 3.21a, 3.15a, and 3.16a show the corresponding N_2O distributions, respectively.

raised levels of N_2O. Accordingly, the band of high RE_{la5lo9} usually associated with the tropical pipe edge is found at higher than normal latitudes (see Fig. 3.23b), at the current location of the maximum gradient in N_2O (see Fig. 3.15a). After several more leak episodes tropical N_2O mixing ratios are found throughout most of the surf-zone and only a single high-RE_{la5lo9} band remains (Fig. 3.23c). It separates the elevated subtropical values of N_2O from the polar vortex. In such cases, it is uncertain whether it is at all possible to determine a distinct southern hemisphere tropical pipe edge from tracer data in general and from RE patterns in particular (see also Fig. 3.14d).

3.4 Summary and Discussion

In this chapter the RE statistical measure, developed as a tool for identifying tracer gradients associated with stratospheric mixing barriers in SOCOL chemistry-climate model data (*Krützmann et al.*, 2008; *Krützmann*, 2008), was applied to observations of stratospheric N_2O from the EOS-MLS satellite instrument. The analysis was performed on potential temperature levels. The binning approach for creating the histograms from which the RE is calculated was revised compared to the SOCOL analysis. Instead of determining the number of bins for each histogram separately with an optimal binning algorithm (*Knuth*, 2006), the data are binned into a histogram with set minimum and maximum values and a fixed bin width. The bin width (10 *ppbv*) is roughly based on the precision of the N_2O measurements ($\approx$ 13 *ppbv*) and edges of the histogram are determined by identifying the overall minimum and maximum volume mixing ratios occurring at each potential temperature level. These changes considerably decrease the time required to calculate the RE. Additionally, the global binning makes the RE a more global measure of mixing than with the optimal binning algorithm and its values are less affected by data variability related to measurement noise.

The evolution of the RE_{z10} (calculated for PDFs created from ten days of N_2O data around a circle of latitude) shows two distinct regions of high RE_{z10} values in the southern hemisphere throughout most of the year, one at lower latitudes ($< 45°$) and one closer to 60°. These coincide with the meridional tracer gradients associated with the mixing barriers at the edges of the tropical pipe and the polar vortex, respectively. The RE tends to have a local maximum at the centre of the tracer gradients and therefore identifying and tracking the maximum of the RE_{z10} in each latitude region gives a picture of the evolution of the respective mixing barrier. Application of the RE to CH_3Cl observations (a tracer with a similar distribution as N_2O in the lower parts of the stratosphere but smaller volume mixing ratios) confirmed that applying the RE to different tracers with similar distributions results in similar RE patterns. Due to its purely statistical nature, the RE has no units and is largely independent of the magnitude of the underlying data. This is why the RE can be useful for comparing the distributions of different trace gases or of the same trace gas measured by different instruments. In the latter case, instrument biases and systematic errors would likely have only a very limited effect on the derived RE patterns.

However, the CH_3Cl analysis also pointed out that noise can have a considerable impact on the RE values and that a large number of data points and a high signal-to-noise level are important to get reliable results. Additionally, calculating the RE from CO observations

illustrated the limits of comparability between the RE patterns from different trace species. The differences in the sources, sinks, and lifetime of CO compared to N_2O result in very different RE_{z10} patterns in the middle of the stratosphere (850 K). The only high-RE_{z10} region found in the CO results for the southern hemisphere was located near 65°S inside the Antarctic polar vortex, between August and October 2008. This could be related to the mixing barrier between the vortex-edge region and the vortex core as identified in *Lee et al.* (2001) and *Roscoe et al.* (2012), among others, but a more detailed analysis would be necessary to confirm this.

The latitude at which the mixing barrier at the (outer) edge of the Antarctic polar vortex is identified by the RE_{z10} of N_2O observations tends to be about 5° lower than expected and reported in previous studies (e.g. *Waugh and Randel*, 1999; *Harvey et al.*, 2002), particularly in the middle stratosphere. The reason for this apparent bias is uncertain but could be related to the reduction in the signal-to-noise ratio as the N_2O mixing ratios decrease toward the poles. In the northern hemisphere, the RE_{z10} maximum associated with the Arctic polar vortex is not very well defined in most years due to the high zonal variability of the vortex position during winter and spring.

The analysis of the evolution of the mixing barriers at the edges of the tropical pipe in the lower and middle stratosphere was more successful. While the position of the subtropical maximum of RE_{z10} occasionally shows sudden and probably unrealistic jumps of several 10° latitude from one day to the next, the monthly (and seasonal) average locations, calculated from the daily positions of the subtropical RE_{z10} maximum in each hemisphere, represent a more realistic evolution of the tropical pipe edges. Additionally, the standard deviation of the daily locations of the RE_{z10} maximum from the monthly (or seasonal) average can also be used as an indicator of the reliability of the determined average position. Direct comparison of the seasonal averages of the RE_{z10} results for JJA 2004 to SON 2005 (at 850 K) with the seasonal average tropical pipe locations (at 830 K) determined with a different methodology by *Palazzi et al.* (2011) show very good agreement between tropical pipe edge positions in both hemispheres for most seasons, giving confidence in the validity of the RE results.

In the three cases when the RE_{z10} results do not agree with those from *Palazzi et al.* (2011), the discrepancies were found to be related to actual anomalies in the N_2O distributions. In these instances the variability of the location of the RE_{z10} maximum was also found to be very high, which indicates the unreliability of the determined seasonal average. In both DJF and JJA 2005 the presence of two similarly strong gradients in the northern hemisphere subtropics resulted in two separate regions of high RE_{z10}. The tracked daily maximum was found to regularly jump back and forth between the two, resulting in the high standard deviation of the seasonal average. Particularly in JJA 2005 the two gradients evidently also affect the methodology used by *Palazzi et al.* (2011), since they derive considerably different latitudes from MLS and SMR data on the one hand and MIPAS on the other hand. As may be expected, the RE_{z10}-maximum location agrees more closely with the MLS/SMR results in this case but the high variability once again indicates that the result might be unreliable.

The reason for the third discrepancy, in the southern hemisphere during JJA 2005, is somewhat different. During this time the maximum of RE_{z10} is found to temporarily shift to higher latitudes in the middle of the surf-zone and back again. The resulting average

position has a high standard deviation and lies considerably further south than the SMR results – *Palazzi et al.* (2011) do not report any results for the other three data sets which might also be related to the unusual behaviour of the tropical pipe edge during this period. An investigation of the zonal mean distribution of N_2O shows that, during this time, air with volume mixing ratios of N_2O that are more commonly associated with the inside of the tropical pipe, is found in the surf-zone, thereby shifting the position of the gradient between high and intermediate mixing ratios of N_2O toward the pole. Similar tropical 'leak events' are also observed during southern hemisphere winter in 2007, 2009, 2010, and 2011. An investigation of vertical profiles of N_2O at 36°S suggests that these leaks have a limited vertical extent and most strongly affect the region between 600 and 1000 *K*.

In order to identify the mechanism causing the large-scale mixing of air out from the tropics into the surf-zone in mid-winter, the resolution of the EOS-MLS N_2O observations was enhanced by (adiabatically) advecting the measurements from five previous and subsequent days to 12:00 UTC on the central day, using a two-dimensional trajectory model and MERRA reanalysis winds (referred to as 'domain filling'). A study of the resultant high-resolution global maps of N_2O on consecutive days in austral winter showed that the increase in southern hemisphere mid-latitude N_2O during leak years is the cumulative result of several events that draw air from the tropics into the surf-zone, where it undergoes large-scale stirring motions. These individual events are likely equivalent to the "episodic mixing events" caused by planetary wave breaking and reported by *Randel et al.* (1993); *Waugh* (1993); *Polvani et al.* (1995); *Portafaix et al.* (2003), among others, but a conclusive analysis of the link between the tropical leaks and individual planetary wave breaking events is beyond the scope of this thesis.

3.4.1 Tropical Leaks and the QBO

The observed frequency of the tropical leaks suggests a potential connection to the quasi-biennial oscillation (QBO). The QBO is known to have a significant effect on the latitude of the tropical pipe edges (e.g. *Punge et al.*, 2009; *Palazzi et al.*, 2011). The data set used here covers approximately three cycles of the QBO, which is not sufficiently long to ensure proper averaging out of its effects in a climatology. This makes an anomaly-analysis potentially unreliable and a different approach, based on a methodology suggested in *Punge et al.* (2009), is used in Fig. 3.24 to allow a qualitative evaluation of a possible link between the leaks and the phase of the QBO.

Figure 3.24a shows the daily zonal mean N_2O at 36°S plotted against the corresponding phase angle, φ, of the QBO at 850 *K*. Following the methodology of *Punge et al. (2009),* the phase angle is derived from the average zonal mean zonal wind velocity between 0.5°N and 0.5°S and the vertical shear thereof on the given isentropic level. Wind fields are taken from the MERRA reanalysis. The QBO phase advances counterclockwise. The circle can be divided into four equal parts, each of which is assigned to a particular phase of the QBO: phase angles from 45° to 135° correspond to the westerly phase of the QBO, 135° to 225° to easterly-shear, 225° to 315° to easterly phase, and 315° and 45° to westerly-shear. The distance from the centre is proportional to the N_2O volume mixing ratio, with concentric circles indicating 50, 100, 150, and 200 *ppbv*, respectively. The data shown in Fig. 3.24a is

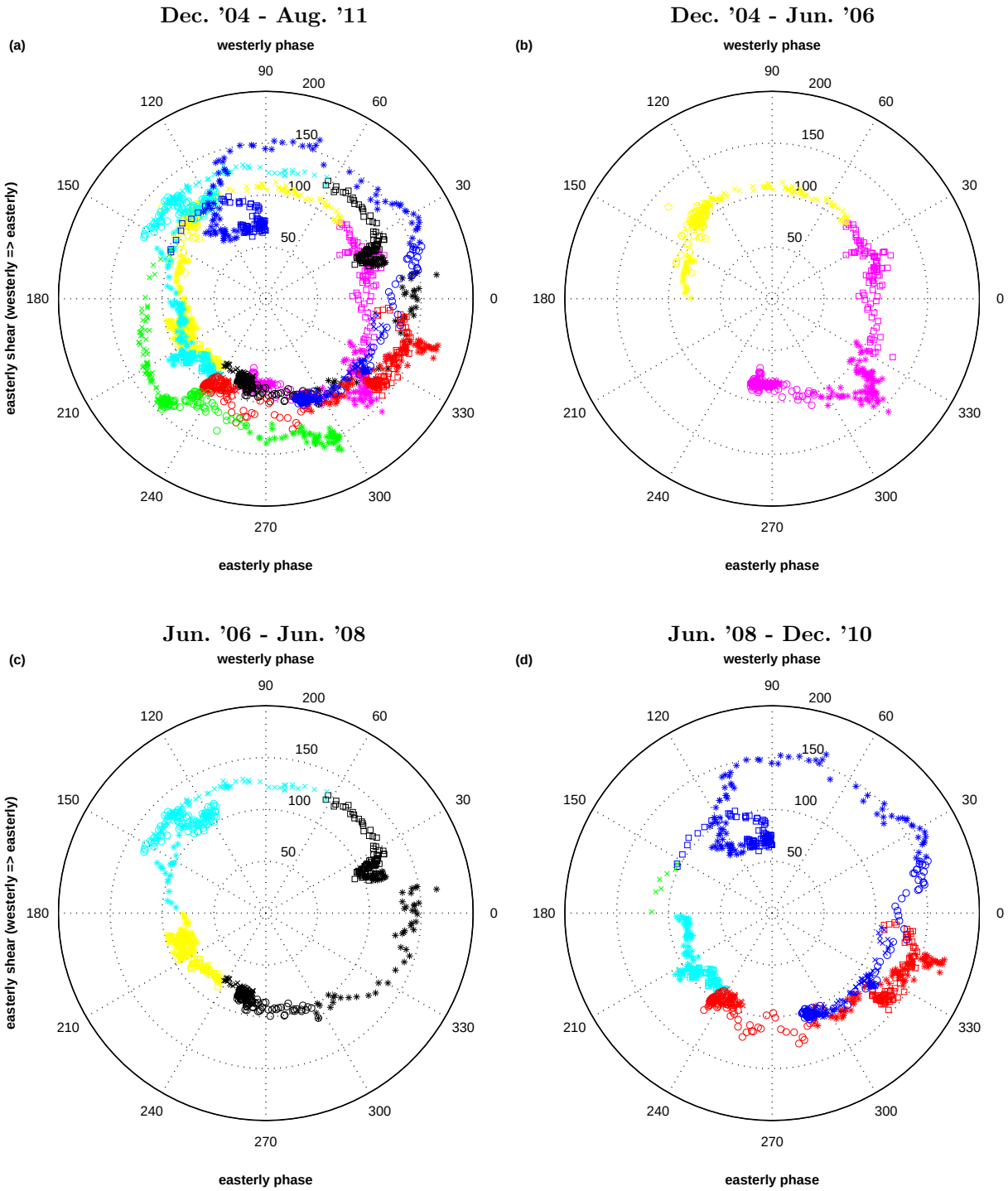

Figure 3.24: Polar plots of the QBO phase angle, φ, vs. N_2O volume mixing ratio on the 850 K potential temperature level at 36°S. The QBO advances counter-clockwise. Different colours and markers correspond to different years (2005 = magenta, 2006 = yellow, 2007 = black, 2008 = cyan, 2009 = red, 2010 = blue, 2011 = green) and seasons (DJF = crosses, MAM = circles, JJA = stars, SON = squares), respectively. DJF for each year includes December from the previous year, i.e. DJF for 2005 is made up of December '04, January '05, and February '05. (a) includes all data from DJF '05 to JJA '11. This is split up into individual cycles of the QBO in (b)-(d), starting at $\varphi = 180°$ (maximum easterly shear). (b) corresponds to the first cycle of the QBO from DJF '05 to JJA '06, (c) is the second cycle from JJA '06 to JJA '08, and (d) the third cycle from JJA '08 to early DJF '11.

for the period from December 2004 to August 2011, covering just over three full periods of the QBO and five large-scale leaks. While there is a minor tendency towards higher mixing ratios in the right half of the diagram, no distinct correlation between QBO phase and N_2O can be made out in Fig. 3.24a, due to the very high inter-annual variability of N_2O at 36°S observed.

Splitting Fig. 3.24a into individual QBO cycles gives a clearer picture of the dependence of mid-latitude N_2O on QBO phase. Figure 3.24b shows the time period from December 2004 (near $\varphi = 250°$) to June 2006 (at $\varphi = 180°$). During most of this period the N_2O mixing ratio stays close to the 100 *ppbv* circle. However, just after the core of the easterly phase ($\varphi = 270°$), when the westerly shear is increasing, there is a distinct peak in N_2O mixing ratio at 36°S with values up to 150 *ppbv* (magenta stars in Fig. 3.24b). This corresponds to the major leak of tropical air into the southern hemisphere surf-zone observed in mid-2005 (see Fig. 3.8). A similar behaviour is found during the second QBO cycle (from June 2006 to June 2008). The increase in mid-latitude N_2O observed after $\varphi = 300°$ in Fig. 3.24c (black stars), corresponds to the leak of tropical air into the surf-zone seen in mid-2007 in Fig. 3.8. In this case the N_2O mixing ratio remains above 100 *ppbv* for most of the westerly-shear and main westerly phase, making the increase in mid-2007 less distinct. Finally, the third cycle of the QBO is nearly six months longer than the previous ones (from June 2008 to December 2010) and shows a more complex behaviour. Particularly, the QBO remains in the "dying off" easterly phase (around $\varphi = 315°$) for a very long time and leaks from the tropical pipe during austral winter are observed in two consecutive years: 2009 and 2010 (red and blue stars in Fig. 3.24d, respectively). In 2010, the high N_2O mixing ratios even persist for a considerable period after the initial leak, lasting well into the main westerly phase.

All in all, this analysis suggests that large-scale leaks of tropical air into the southern hemisphere surf-zone are more likely when the QBO is in a 'dying-off-easterly' or westerly-shear phase. These findings basically agree with the Holton-Tan paradigm (*Holton and Tan*, 1980; see also Fig. 2.8): when the equatorial winds at 850 *K* are westerly, the zero wind line is located in the summer hemisphere and (stationary) planetary waves can propagate across the equator, resulting in reduced planetary wave breaking in the winter hemisphere. This is the case at the onset of winter in 2006 and 2008 when no major tropical leaks occur. On the other hand, when the equatorial winds at 850 *K* are easterly, the zero wind line is in the winter hemisphere and planetary wave breaking in the winter surf-zone is enhanced. This is the case at the onset of winter in 2005, 2007, 2009, and 2011 when large-scale leaks of tropical air are observed. Accordingly, the modulation of the planetary wave activity in the surf-zone by the Holton-Tan effect could be the reason for the timing of the tropical leaks. However, the large-scale leak in 2010 does not quite fit this pattern as the equatorial winds change from easterly to westerly just at the end of autumn and are westerly throughout the winter (Fig. 3.24d) of that year. Furthermore, this does not explain why a similar pattern of tropical leaks is not observed during northern hemisphere winter. Hence, a more detailed study including more QBO cycles would be necessary to conclusively establish a connection between the phase of the QBO and the tropical leak events.

3.4.2 Effect of planetary wave activity on the RE

As the RE detects tracer gradients in a zonal mean sense, planetary wave activity can potentially affect the results. In order to get an idea of the role planetary waves can play in determining the position of mixing barriers, estimates of planetary wave activity are derived in terms of N_2O volume mixing ratios, and wave events of varying intensity are imposed on an idealised tracer gradient in the following.

First, typical amplitudes of planetary wave activity are estimated from the N_2O data at 850 K in 2008. For each of the 111 MLS latitude bins (see Sect. 2.3.3) a function of the form:

$$f(\theta) = A \cdot \sin(\theta + B) + C \cdot \sin(2\theta + D) + E \cdot \sin(3\theta + F) + G \tag{3.2}$$

is fitted to the daily N_2O data. In Eq. 3.2, θ is longitude, A, C, and E are considered estimates of the amplitudes of waves 1, 2, and 3, in units of N_2O mixing ratio, respectively. Similarly, B, D, and F are interpreted as the respective phases. G is the offset from zero and is approximately equal to the zonal mean mixing ratio of N_2O at the respective latitude.

Figure 3.25a shows the evolution of the ten-day running mean amplitudes of waves 1, 2, and 3 at 15°S at 850 K in 2008. At this latitude a particularly high overall wave activity can be seen around day 195 (13.7.2008). Figure 3.25b shows a latitudinal cross-section of the wave activity on that day. The wave activity between 0° and 30°S in Fig. 3.25b is used as a template for 'simulating' a strong wintertime planetary wave event (see Fig. 3.25c) and its potential impact on the RE's ability to locate tracer gradients. A second wave event, consisting of only wave-1 and -2 activity and with a smaller latitudinal extent, is created synthetically (see Fig. 3.25d). This is considered an approximation of a weak spring or summer wave event.

An idealised, zonally symmetric, subtropical tracer gradient is shown in Fig. 3.26a. It is derived from the zonal mean distribution of N_2O in the southern hemisphere tropics and subtropics at 850 K on 18.8.2008[3]. Figure 3.26b displays the RE_{la5} (blue line) derived from this idealised N_2O distribution.[4] The maximum of RE_{la5} at 7.5°S clearly coincides with the strongest gradient of N_2O, which would be considered the centre of the subtropical mixing barrier.

Figure 3.27a shows the idealised tracer field from Fig. 3.26a with a weak wave event superimposed. In this case, the wave-1 activity peak is centred at 7.5°S (as in Fig. 3.25d), i.e. 'on top' of the steepest N_2O gradient. Note that the superimposed disturbance does not change the zonal mean N_2O mixing ratio. Also, in order to simulate the "worst case" effects of a given level of wave activity, no phase-shift is introduced between the wave-1 and wave-2 disturbances, maximising the resulting distortion of the tracer field. The RE_{la5} derived from Fig. 3.27a is shown in Fig. 3.27b. Compared to the RE_{la5} of the plain tracer field, the values in Fig. 3.27b have increased everywhere. This is to be expected as the change of tracer mixing ratios introduced by the planetary wave distortions increases the complexity of the resulting

[3]This date was selected purely because of the smoothness of the subtropical zonal mean distribution of N_2O on that day.

[4]For this test the temporal collation of data points over ten days is replaced by latitudinal collation over five latitude bins in order to ensure a sufficiently large number of data points per histogram. Consistent with previous calculations, a bin width of 10 *ppbv* is used for creating the PDFs.

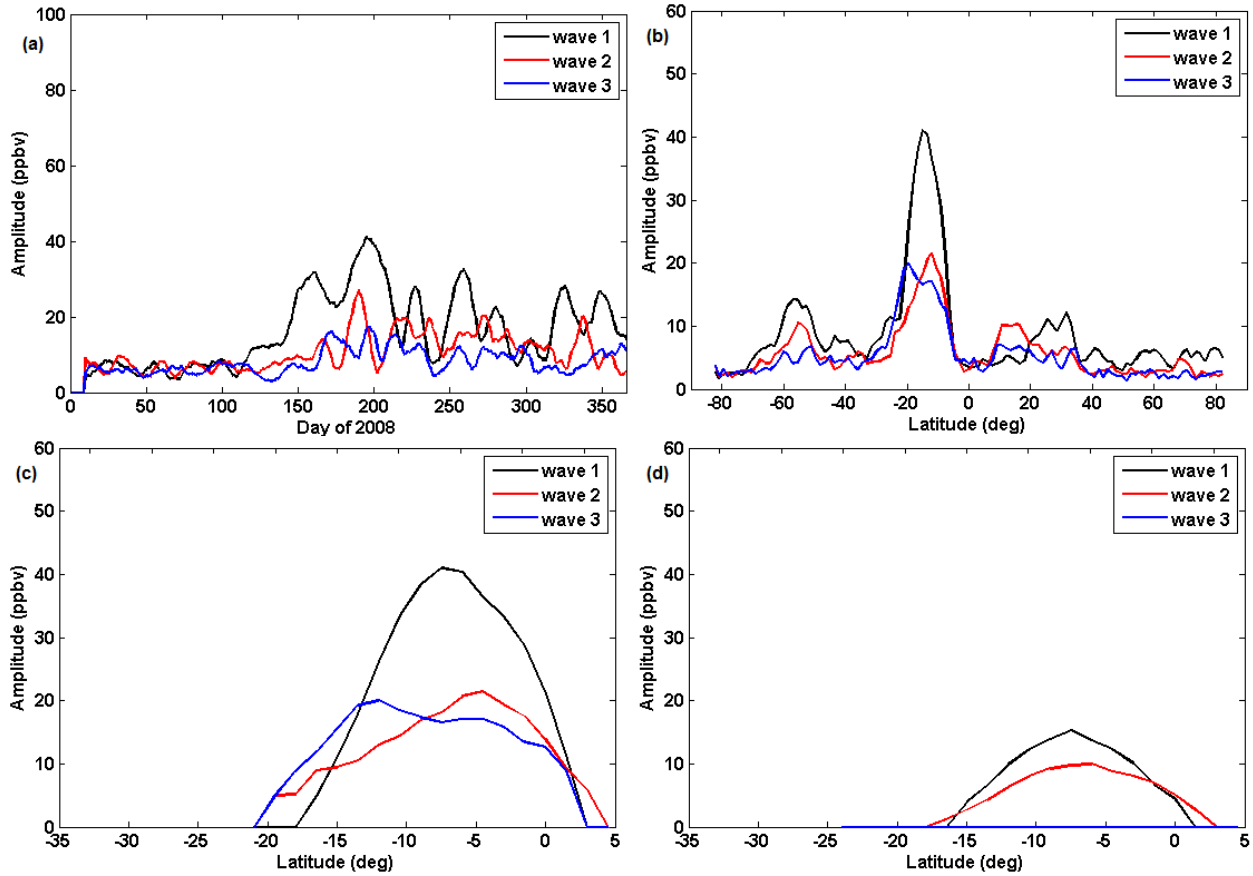

Figure 3.25: (a) Ten-day running mean amplitudes of waves 1, 2, and 3 in terms of N_2O mixing ratio at 15°S for 2008 on the 850 K potential temperature level. (b) Zonal cross-section of wave amplitudes for 13.7.2008 (day 195). (c) Zonal distribution of wave amplitudes for 'simulated' strong wave activity, centred on 7.5°S. (d) Zonal distribution of wave amplitudes for 'simulated' weak wave activity, centred on 7.5°S.

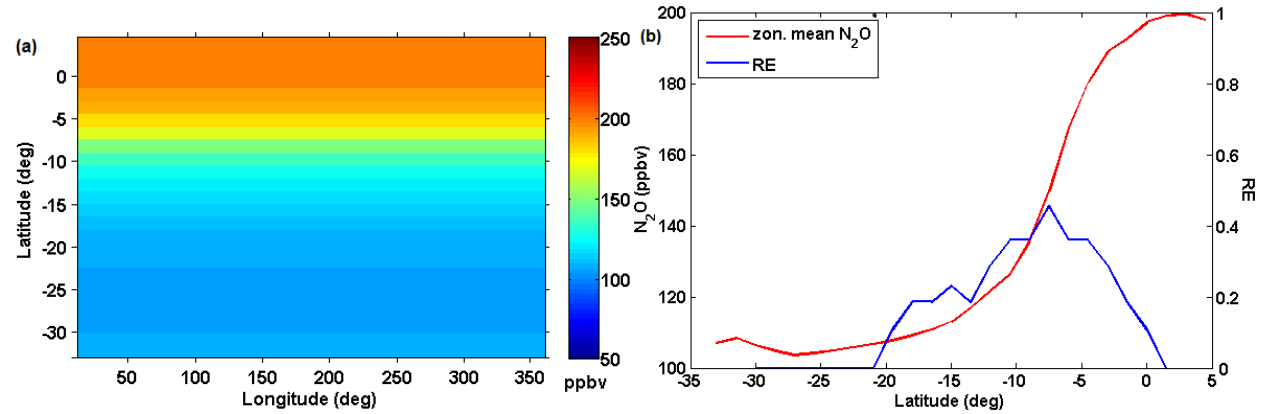

Figure 3.26: (a) A zonally symmetric tracer gradient derived from the zonal mean of N_2O in the southern hemisphere tropics and subtropics at 850 K on 18.8.2008. The longitudinal resolution is 12°, resulting in 30 data points per 1.5° latitude bin, similar to the daily EOS-MLS observation pattern. (b) RE_{la5} (blue line) derived from the tracer field in (a). The zonal mean of N_2O (red line). South of 21°S all tracer concentration values are so similar that they fall within the same bin. In this case the RE defaults to zero.

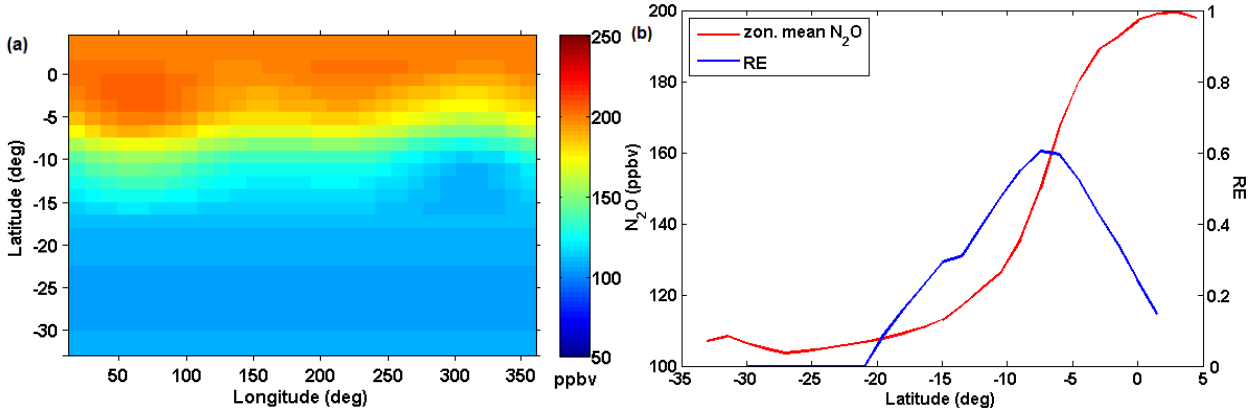

Figure 3.27: (a) The tracer field from Fig. 3.26a with a weak wave event (Fig. 3.25d) centred on 7.5°S superimposed. (b) RE_{la5} (blue line) derived from the tracer field in (a). The zonal mean of N_2O (red line) remains unchanged.

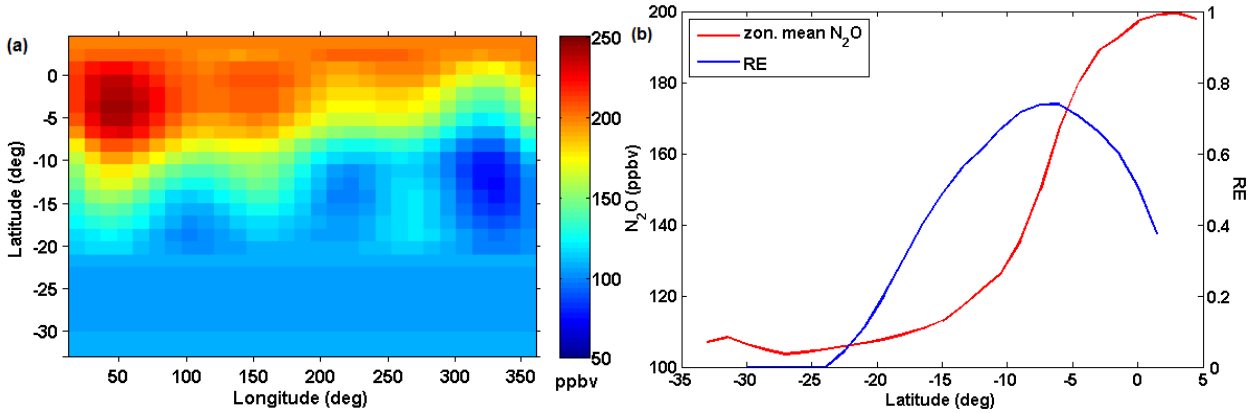

Figure 3.28: (a) The tracer field from Fig. 3.26a with a strong wave event (Fig. 3.25c) centred on 7.5°S superimposed. (b) RE_{la5} (blue line) derived from the tracer field in (a). The zonal mean of N_2O (red line) remains unchanged.

histograms and accordingly raises the RE. The maximum of RE_{la5} is still located at 7.5°S, though the peak is slightly broadened.

Figure 3.28a shows the idealised tracer field from Fig. 3.26a with a strong wave event superimposed. As before, the wave-1 activity peak is centred at 7.5°S (see Fig. 3.25c). The RE_{la5} derived from Fig. 3.28a is shown in Fig. 3.28b. Compared to both Figs. 3.26b and 3.27b the RE_{la5} values are further increased, indicative of the even higher complexity of the tracer distribution. The RE_{la5} maximum is now found at 6°S, though the peak is visibly broadened and therefore the exact location of the maximum is less distinct. This suggests that strong planetary wave activity can affect the RE's ability to locate tracer gradients accurately. While the error in the latitude of the RE_{la5} maximum, introduced by the planetary wave event, is very small in this case, this could be due to the fact that the peak of the planetary wave activity is centred at the same latitude as the tracer gradient maximum.

Figure 3.29a shows the idealised tracer field distorted by a strong wave event which is now centred at 16.5°S. The RE_{la5} derived from Fig. 3.29a is shown in Fig. 3.29b. Clearly, the latitudinal offset between the centre of the tracer gradient and the centre of the wave event causes considerable broadening of the RE_{la5} peak. The RE_{la5} value at 7.5°S even lies outside

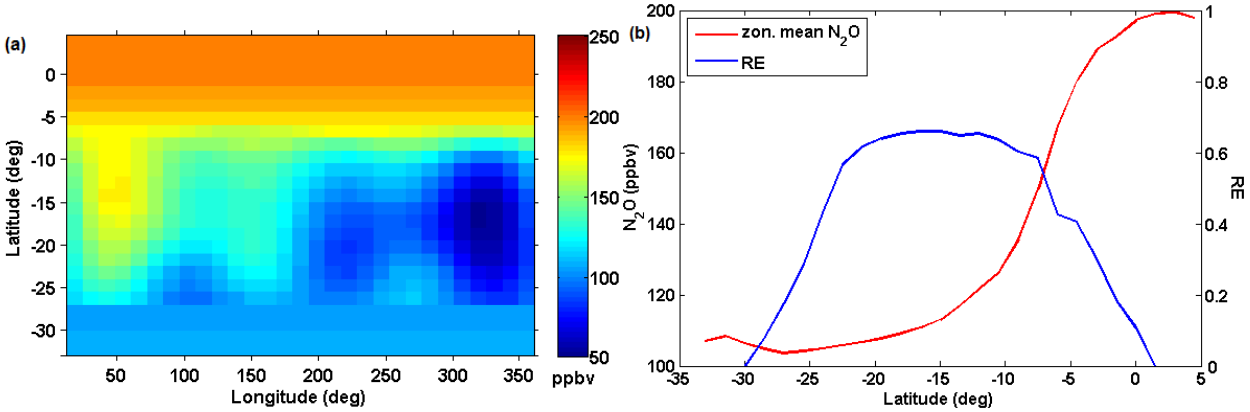

Figure 3.29: (a) The tracer field from Fig. 3.26a with a strong wave event centred on 16.5°S superimposed. (b) RE_{la5} (blue line) derived from the tracer field in (a). The zonal mean of N_2O (red line) remains unchanged.

of the broad plateau of high RE_{la5} values between 10°S and 20°S. This case illustrates that the distortion of the tracer field by strong planetary wave activity can severely compromise the RE's ability to locate tracer gradients, depending on the latitudinal structure of the wave event.

A detailed study of the effects of planetary waves on the RE's ability to identify mixing barriers is beyond the scope of the present work. The above results show that a quantitative estimate of these effects would depend on several factors, such as the strength of the wave activity, its location relative to the tracer gradients of interest, and the latitudinal distribution of wave amplitudes. Qualitatively, strong mid-latitude planetary wave activity, which is regularly observed in winter, could explain the low-latitude bias of the position of the Antarctic polar vortex edge identified with the RE. Similarly, planetary wave activity might explain the high variability in the identified tropical pipe edge positions in some winter months (see for example Fig. 3.11a). It should also be noted that travelling planetary waves are not considered above, since the latitudinal collation of data points when deriving the RE removes any differences that might by related to the zonal movement of waves.

3.4.3 Conclusions

Ultimately, the RE is a useful tool for mixing barrier detection in stratospheric tracer data. Unlike other more complex mixing measures, such as equivalent length (*Lee et al.*, 2001), effective diffusivity (*Haynes and Shuckburgh*, 2000) or Lyapunov diffusivity (*d'Ovidio et al.*, 2009), it cannot be used as a quantitative measure of mixing barrier strength. Instead, the RE can be a simpler, faster, and more efficient way of identifying large-scale dynamical patterns in a zonal mean view, without requiring any dynamical input such as reanalysis winds. This way the RE can be used for quickly analysing and possibly comparing the increasingly large observational data sets from numerous satellite instruments. A detailed comparison between the RE and other mixing metrics can be found in *Grahn* (2012).

By enhancing the number of data points via domain filling, it is also possible to use the RE for a complementary, daily, and more detailed analysis on a global scale. The high

sensitivity of the RE derived from domain filled data to both zonal and meridional gradients makes it potentially useful for investigating the longitudinal variation of the tropical pipe edge or the evolution of the polar vortex over a limited time frame. However, it also means that automated tracking of a particular barrier over a longer time span is bound to fail. Given the large computational requirements of the domain filling process, the RE is probably more effective as a tool for zonal mean analyses of tracer distributions. However, its potential applicability for a global-scale analysis on a regular latitude-longitude grid could become more relevant in the future when chemistry-climate models with increasingly higher resolution will become available. In this regard the RE also has an advantage over measures like the equivalent length or effective diffusivity, which can only be defined in terms of equivalent latitude.

In addition to the RE analysis, the leakage of large amounts of tropical air into the southern hemisphere surf-zone in mid-winter was identified as a regularly occurring phenomenon in the EOS-MLS N_2O observations. Leaks were observed in five of eight years of zonal mean N_2O data (2004-2011). A detailed analysis of the involved dynamics was performed at $850\,K$ with the aid of the domain filling technique. Examination of the leaks suggests they are related to the combined effect of multiple planetary-wave-breaking events redistributing air from the tropical pipe and depositing it in the surf-zone in late autumn and early winter (May through July). While the reason for the irregular occurrence of these leaks could not be identified, a relation to the phase of the QBO seems likely. In particular, all the observed leaks started when the QBO was in a dying-off easterly (or westerly shear) phase at $850\,K$, suggesting that these conditions favour the occurrence of such leaks.

Chapter 4

Application of RE to Cryospheric Observations

The Rényi entropy (RE) is a statistical measure based on probability density functions (PDFs) derived from histograms that can be applied to any kind of numerical data set. In the previous chapter, the RE was shown to be a useful and efficient tool for detecting gradients related to mixing barriers in both climate model data and satellite observations of stratospheric tracer concentrations. Its ability for detecting amplitude gradients related to subsurface reflections in ground penetrating radar (GPR) data is examined in the present chapter.

While the atmospheric gradients that were the focus of Ch. 3 are relatively large-scale features, amplitude gradients in GPR data can be much narrower. Hence, the RE is initially applied to artificial data with gradients of varying extent to determine the limitations of detecting spatially small gradients with the RE (Sect. 4.1). In Sect. 4.2, the RE's utility for detecting radar reflections is tested with a 25 MHz GPR cross-section of an Antarctic glacier and the effects of different parameters such as the window size and the number of histogram bins are investigated. The RE-results are then compared to more standard processing methods in Sect. 4.3 and the potential advantages of using it as a pseudo gain function are discussed. The applicability of the RE to higher frequency data, as well as its limitations, are illustrated in Sect. 4.4, followed by a summary of the results in Sect. 4.5.

4.1 Sensitivity Study with Synthetic Gradient Data

Ground penetrating radar observations are generally considered to be two-dimensional: the along-track direction (horizontal) in which the GPR system is moved and the downward direction (vertical) which relates to depth below the surface. The latter is recorded in terms of two-way travel time (TWT). Successful conversion of TWT to depth requires information on the velocity of the radar wave in the sub-surface medium and therefore its dielectric properties (see also Sect. 2.4.2). While the conversion factor between TWT and depth depends on the average sub-surface wave velocity down to a particular reflection, TWT and vertical depth can, in most cases, be considered approximately equivalent baring a constant factor. When displaying GPR recordings, the vertical axis usually corresponds to time (or depth)

with increasing TWT (depth) from top to bottom, while the horizontal axis represents the distance along the recorded profile. In the following, the 'vertical' (direction) always refers to the time dimension, while 'horizontal' indicates the along-track direction.

When applying the *RE* to two-dimensional data, such as GPR recordings, the effect that a local gradient will have on the value of the *RE* depends on the extent of the gradient relative to the size of the window within which data points are used to create the underlying PDFs. Amplitude gradients corresponding to reflections in the subsurface are usually in the vertical, i.e. the amplitude gradients that are to be identified with the *RE* are oriented along the vertical/time axis. Therefore it is important to establish how the vertical dimension of the data window should be related to the size of the amplitude gradients expected to be found in the data. Synthetic gradients of varying 'vertical' extent are used to test the effects of the gradient width on the *RE* when using a fixed window size. A line of gradients of decreasing width is created by sampling a bell curve of the form:

$$f(x) = \frac{1}{a} \cdot e^{-\frac{(x-b)^2}{2a^2}} \tag{4.1}$$

between $x = \pm 3$ with varying step-sizes. By taking $a = 1$ and $b = 0$, Eq. 4.1 is simplified to a bell curve with a central maximum of value one that dies off to a value of approximately 0.01 at $x = \pm 3$. Starting with 250 equally spaced samples between -3 and 3 (corresponding to a step-size $\Delta x = 0.024$), a decreasing number of values is drawn from the same interval by gradually increasing the step-size, down to a minimum of five points. The thusly created data points between zero and one represent a line of positive and negative gradients with a decreasing number of data points per profile (dotted line in Fig. 4.1). Individual bell curves are separated by a gap of 20 points equal to zero. To simulate 20 neighbouring radar traces, the whole sequence of gradients shown in Fig. 4.1 is replicated 20 times and random noise with a maximum amplitude of 0.01 is added to each profile. This can be thought of as the envelope of a simulated GPR profile of a horizontally homogeneous, stratified medium with a decreasing layer thickness with depth.

The *RE* is then calculated from histogram (or rather the derived piecewise constant PDFs) that include ten data points along the line of gradients (corresponding to the time-dimension of a radar trace) from each of these 20 artificial traces. This data window is then shifted 'downwards' along the gradient profile by one point, where the next value of the *RE* is determined, and so on to the end of the gradient line. For this test the number of bins in the histograms is set to 20 and $\alpha = 2$, as before. The solid black line in Fig. 4.1a shows the resulting *RE* values for the profile. When the gradients are considerably wider than the data window, the *RE* values along the increasing and decreasing slope are consistently high (between 0.8 and 1.0). A slight reduction of the *RE* is observed at the centre of the curve where the gradient reverses, though the *RE* does not necessarily drop below the smallest values found in the gradient region (see for example the centre of second bell curve in Fig. 4.1a). Between the individual bell curves, the *RE* drops to zero since here all data values are zero (no noise was added to the points between the curves).

The very high 'sampling rate' of the first few gradients means that the ten vertical ('temporal') data points inside the window used to calculate the *RE* lie very close together and only span a limited range of values. For example, the difference between the smallest and

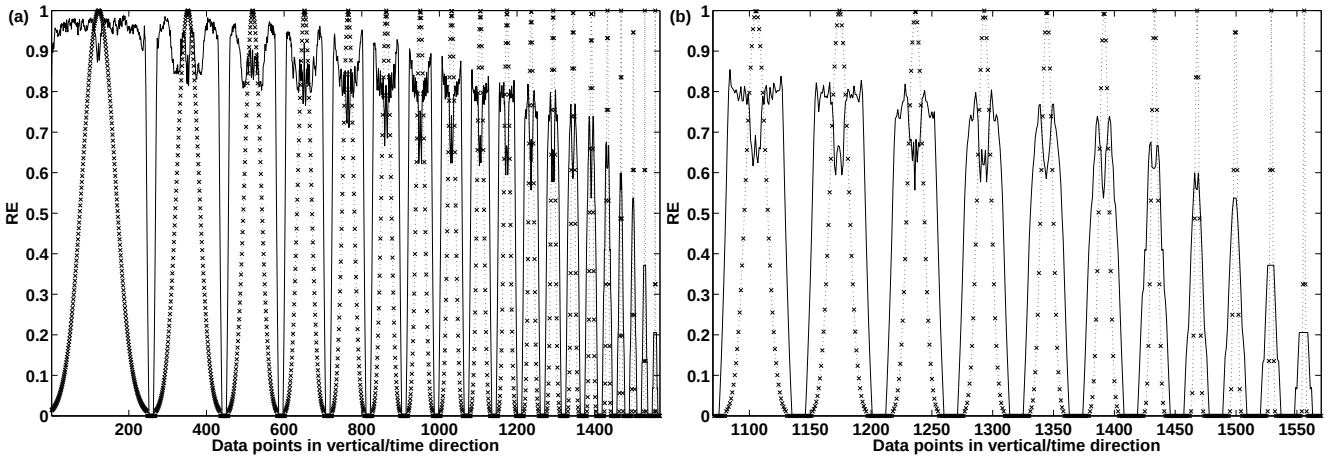

Figure 4.1: (a) The *RE* (solid line) of the synthetic profile of gradients (dotted line with crosses indicating the data points). (b) Close-up of the end of the gradient profile. The gradient profile shown here is shifted to the left by five data points (half the data window width) and does not include the noise term (maximum noise level = 0.01) that was added to the profile before calculating the *RE*.

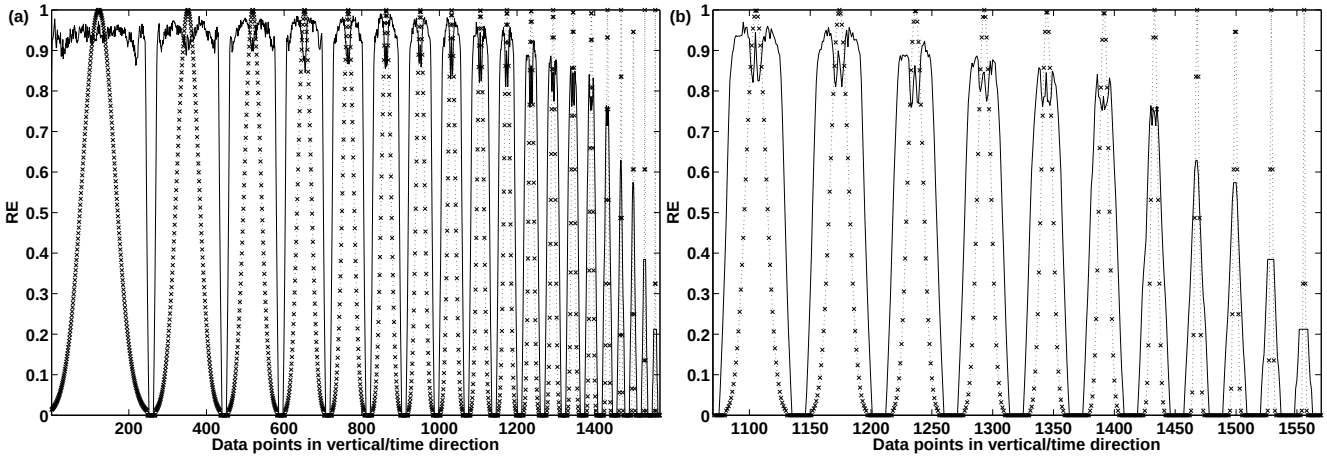

Figure 4.2: Same as Fig. 4.1 but with the an increased maximum noise amplitude of 0.05 added to each gradient profile before calculating the *RE*.

the largest value inside the data window is less than 0.1 at the centre of the first bell curve in Fig. 4.1a. The noise added to the data (being on the order of 0.01) has a considerable effect on the value of the *RE* (the *RE* of white noise is equal to one) and the consistently high values are likely to be related to this noise rather than the gradients. Another test with an increased maximum noise amplitude of 0.05 confirms this interpretation (Fig. 4.2). The higher noise level also increases the overall *RE* values, particularly at the centres of the peaks in Fig. 4.2a and b.

Figure 4.1b is a close-up of the last third of the profile. This is the region where the width of the gradients (in terms of data points) is of a similar size as the vertical dimension of the data window. At this stage the *RE* lies around 0.8 in the gradient regions and drops to values close to 0.6 in between. This contrast between the gradient regions and the peaks is also reduced when the noise level is increased (Fig. 4.2b) since the overall *RE* values are higher. While the two gradient regions (increasing vs. decreasing values) can be clearly seen

as separate peaks in the *RE* for the first six bell curves in Fig.4.1b, this bimodal behaviour becomes hard to identify in the remaining five cases. The transition occurs where the number of data points on each side of the peak drops below the window width used for creating the PDFs. For example, in the sixth bell curve (from the left) in Fig. 4.1b there are still twelve points on each side of the peak and there is a clear reduction in *RE* at the centre. A small reduction in *RE* is also observed at the centre of the seventh curve (with nine points on each side of the peak) but the difference between the maxima in *RE* and the local minimum is considerably reduced. The last four curves consist of a total of eleven, ten, seven, and five data points, respectively. In these cases, the whole bell curve only shows up as a single peak in the *RE*, with a maximum value that drops considerably as the curves become narrower.

Figure 4.1 illustrates that only gradients of sufficiently large extent relative to the width of the data window will be 'detectable' with the *RE*. Therefore, it is important to ensure that the dimension of data window used for calculating the *RE* is approximately of the same order as (or slightly smaller than) the extent of the gradients that are expected to be present along that dimension. A too small window is likely to result in overall very high *RE* values, even when there are no gradients present, as the *RE* will be largely influenced by the background noise in the data. On the other hand, using a window that is much larger than the gradients to be detected will result in very low values of *RE*.

In the following, these findings are used to apply the *RE* to various radar profiles from Antarctica using several GPR setups with different centre frequencies. The first profile used is a 25 *MHz* recording representing a cross-section of the Touchdown Glacier in the Darwin-Hatherton glacial system, Antarctica, featuring a hyperbolic bottom reflection representing the glacier bed (see Sect. 2.6.3). At the centre of the profile, the bed was too deep and the radar reflection too weak to be identified.

4.2 Application of *RE* to a 25 *MHz* Glacier Profile

Being a statistical measure, numerous data points are required to calculate one *RE* value. Individual outliers that might be related to erroneous measurements or data gaps due to disturbances of the measurement system can be omitted without necessarily affecting the results in a negative fashion. Therefore, the *RE* is potentially useful for 'smooth' processing of noisy or discontinuous data. It also has the advantage that it is a relative measure with values always lying between zero and one, making the *RE* easy to use on data sets with a high dynamic range, since it is not affected by continuous changes in the numerical magnitude of the input data. For the application to radar soundings this implies that processing GPR data with the *RE* does not require any gain functions or other amplitude enhancing measures to be applied to the data.

In order to apply the *RE* to radar data, the size of the data window in the horizontal (along-profile) and vertical (time/depth) direction (from which the histograms for calculating the *RE* are derived) needs to be determined. While there is no general criterion for the number of points required to create a representative histogram of a particular data set, it is clear that a very sparse histogram with only a few points is undesirable and that 'more is better' when creating PDFs. For example, the optimal binning algorithm, optBINS (*Knuth*,

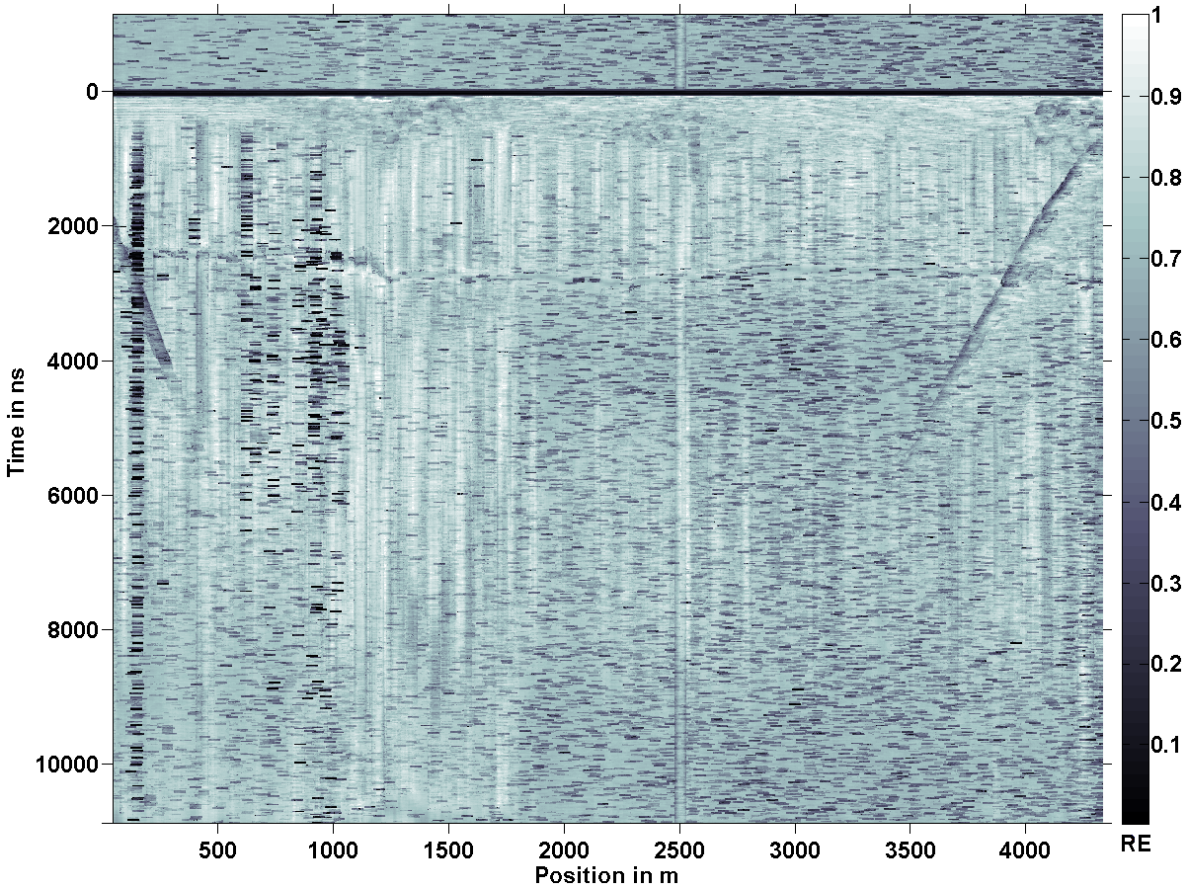

Figure 4.3: RE_{25h8v} of the raw data (no dewow) of a glacier cross-section. The horizontal scale is in metres from the starting point of the recording. The approximate trace-to-trace interval is two metres. The vertical scale is in ns, the sampling interval is 3.2 ns. The bottom of the figure corresponds to about 900 m depth (assuming $v_{ice} = 0.168\ \frac{m}{ns}$), accordingly the vertical exaggeration is approximately 3.75:1.

2006), used previously in the analysis of stratospheric climate model data (see Sect. 3.1.1 and *Krützmann et al.*, 2008), requires a minimum of 150 data points to work reliably (*Krützmann*, 2008). As the global binning approach used in Chapter (Sect. 3.1.1) is not suitable for radar data due to the large range of values contained in GPR recordings (up to four orders of magnitude in this case), the utility of the optBINS algorithm when calculating the RE from radar recordings is tested here. Based on the test results in Sect. 4.1, a vertically narrow data window with 25 horizontal- and 8 vertical points (indicated by the index *25h8v*) is used initially, resulting in a total of 200 data points for each PDF. In the case of 25 MHz profile from the Touchdown Glacier (Sect. 2.6), this window size corresponds to approximately 2 m vertically and 50 m horizontally. Using the 25-by-8 window and taking the absolute value of the data (only amplitude gradients are relevant, not their sign) the RE_{25h8v} is calculated[1], with the optimal binning algorithm testing up to 100 bins. The result when using data without any prior processing is shown in Fig. 4.3.

A continuous, dipping reflection can be identified in both the left and the right part of the profile – the reflection from the glacier bed. It dips down towards the centre of the

[1]With $\alpha = 2$, as usual.

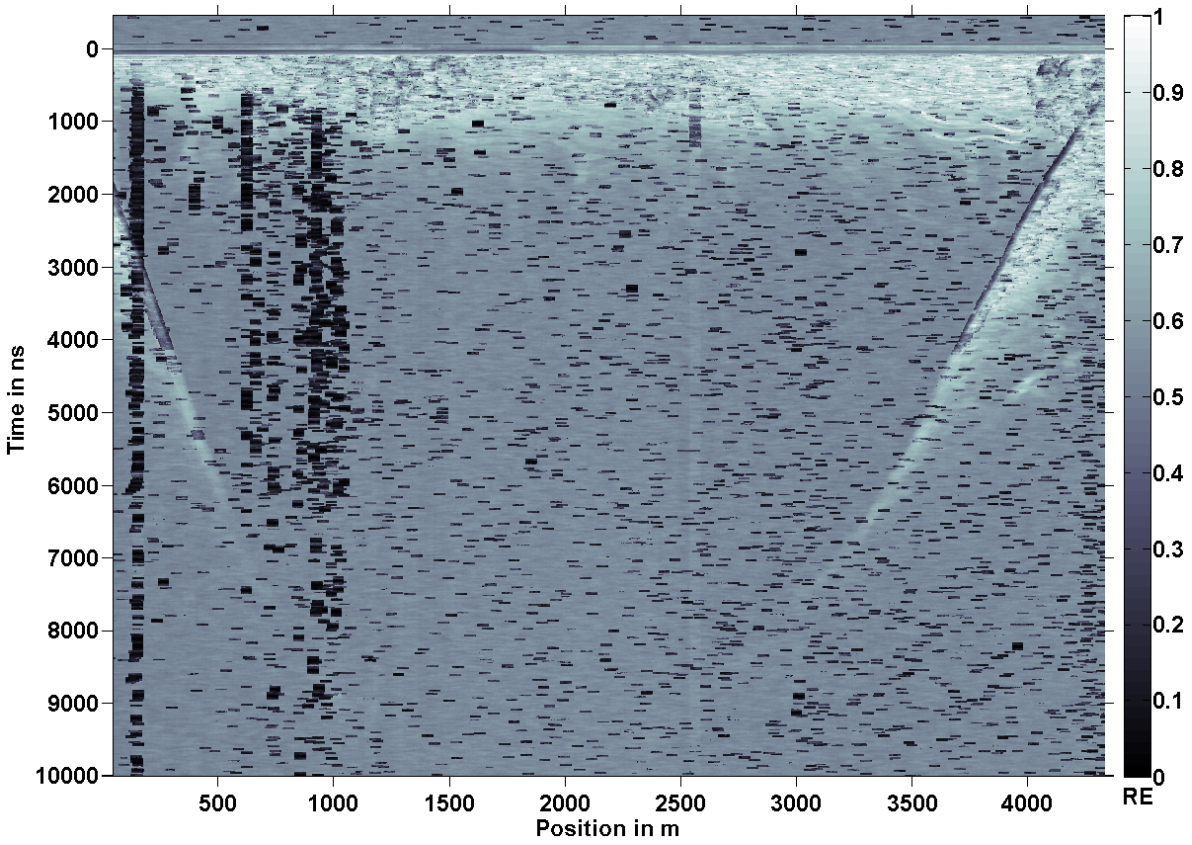

Figure 4.4: Same as in Fig. 4.3 but for dewowed and enveloped data.

profile where the reflection is lost below 9500 *ns*. The overall picture is very noisy, showing numerous 'black boxes' in addition to a rather surprising near-horizontal feature at around 500 *ns*, neither of which correspond to actual subsurface features.

The near-horizontal feature is related to the low-frequency offset or "wow" of the pulseEKKO system. It coincides with the point at which the values in the raw data go from mostly positive to mostly negative. Hence, it is necessary to apply a dewow filter (see Sect. 2.5.1) to the data prior to using the *RE*. Additionally, to get a better picture of the instantaneous amplitude of the signal, the envelope of each trace (determined via the Hilbert transform, see Sect. 2.5.5) is derived before calculating the RE_{25h8v}. Figure 4.4 shows the results derived from the dewowed and enveloped data. The near-horizontal feature has been removed and the overall picture is less 'stripey' and more homogeneous, though the black boxes appear more pronounced.

The black boxes are related to erroneous data. During the data acquisition there was a bad connection between one antenna and a fibre-optic cable, causing numerous data points with random values throughout the data set, particularly in areas of rough surface terrain. As most of these bad data points are outliers, i.e. they have values that are considerably higher or lower than the other values within the data window, they strongly skew the distribution and noticeably change its shape. The resultant histogram is usually heavily one sided, with most data points on one side of the histogram and the outliers on the far other side. Such a distribution tends to have a very low value of *RE*, causing the black boxes of low entropy values in Fig. 4.3 and Fig. 4.4.

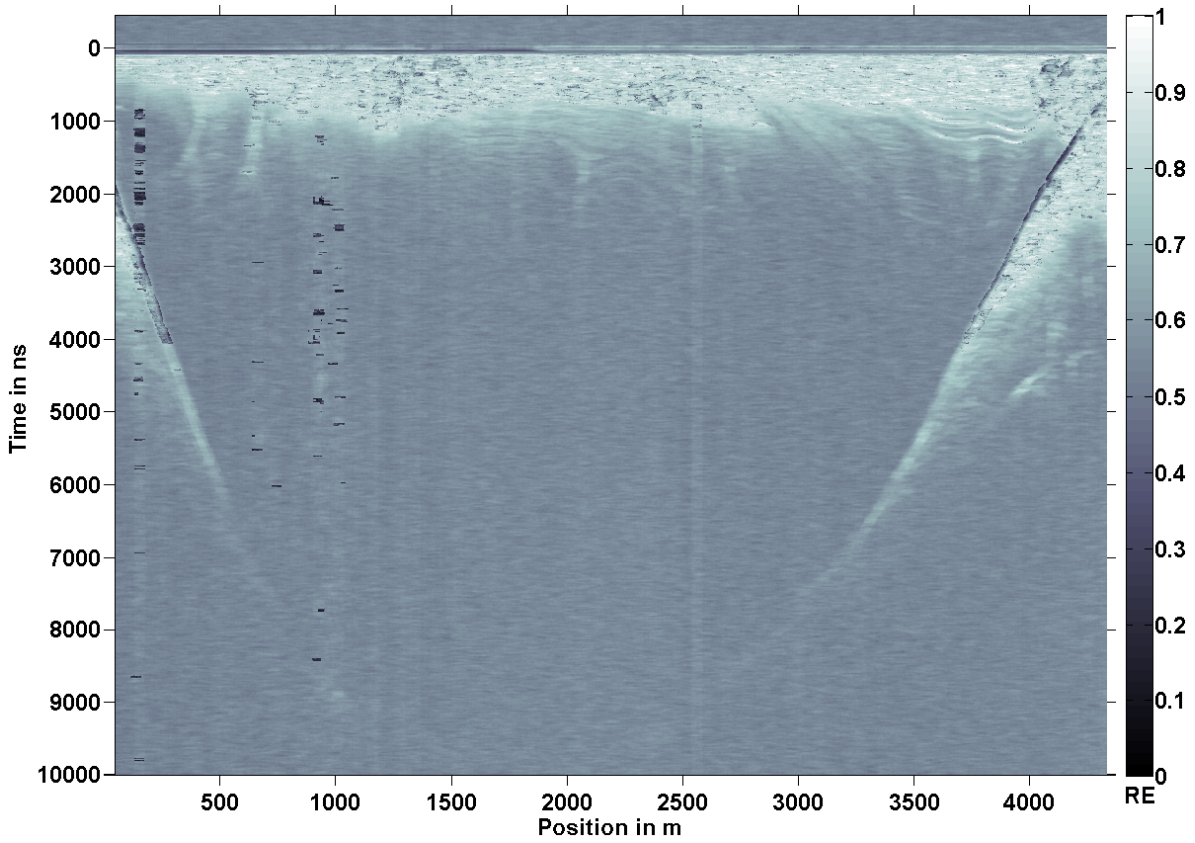

Figure 4.5: RE_{25h8v} of the dewowed and enveloped glacier cross-section with three iterations of the outlier removal procedure applied.

4.2.1 Outlier Removal

In order to avoid this stretching of the histogram range, outliers can be removed with an iterative process. First, the mean and standard deviation of all the values within the data window is determined. Then, all values outside of three standard deviations from the mean are excluded from the histogram. This process can be repeated several times to ensure removal of all outliers. Figure 4.5 shows the results after three iterations of this procedure. While there are still a number of black boxes visible, the subsurface structures in this part of the profile appear more clear now. For example, the bottom reflection is more distinctly delineated in the shallower parts of the profile. The areas in which there are still black boxes are those where the number of outliers is particularly high. To get rid of the remaining outliers in these areas, the removal procedure can be performed several more times. Figure 4.6a and b show the results after a total of five and ten iterations, respectively. The figures are limited to the first 1100 m of the profile since this is where most of the erroneous data points are located.

Clearly, each increase in the number of iterations removes more of the black boxes. After five iterations (Fig. 4.6a) there are only a few black boxes left in those parts of the data with the highest density of outliers. After ten iterations (Fig. 4.6b) it appears that all the ill effects of the bad connection, i.e. the erroneous data points, have been filtered out and more iterations would not make a difference in the results. Generally, the required number of outlier removal iterations depends on the quality of the data. In many cases, five iterations

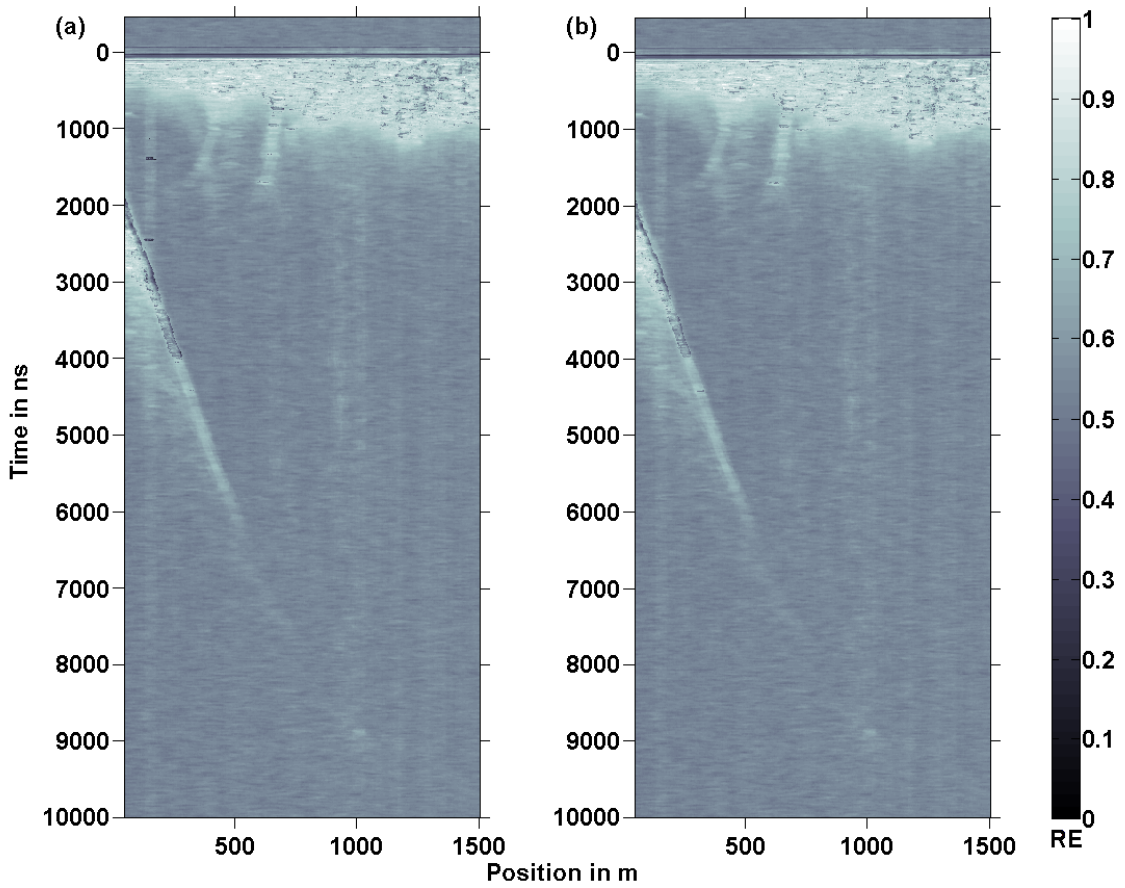

Figure 4.6: RE_{25h8v} of dewowed and enveloped data with (a) five and (b) ten outlier removal iterations. Only the first 1500 m of the glacier profile are displayed.

are probably sufficient.

As the outlier removal procedure is of a merely statistical nature, it does not only remove values that are related to malfunctioning of the equipment, but also some regular and valid data points. Therefore it is important to check how many data points are removed by the outlier filter and whether the remaining number of points is a sufficiently large portion of the data in the selected window. Figures 4.7a to 4.7d show the number of remaining data points after one, three, five, and ten iterations of outlier removal, respectively. As expected, the areas with less remaining data points tend to coincide with the black boxes observed in Fig. 4.4. Obviously, more data points are being removed with each iteration step. The maximum number of omitted points ranges from 14 (after one iteration, Fig. 4.7a) up to 60 points (after ten iterations, Fig. 4.7d). While the latter is equivalent to 30%, which is of course a considerable fraction of the data, this only occurs in very few places. Also, the remaining 140 data points are still sufficient to calculate the *RE*, and throughout large parts of the radargram less than 10% of the data (white and yellow in Fig. 4.7b-d) are removed even after ten iterations.

The fact that the removal of 30% of the data points still allows the calculation of the RE shows that the RE cannot only be used on data sets with erroneous data, such as the present one, but also on data with missing measurements or occasional gaps, as long as these are not too large.

The clear images of Fig. 4.5 and Figs. 4.6a and b allow the identification of the bottom reflection of the glacier bed down to 9000 *ns*, corresponding to approximately 750 *m.* Below this depth, the reflection amplitude from the glacier bed appears to be too small to be detected with the *RE*. Additionally, two relatively shallow (below 1000 *ns)* internal reflections can be seen between 3500 and 4000 *m* of Fig. 4.5. These are probably associated with distinct internal layers within the ice, such as dust layers. To assess the ability of the *RE* to detect the identified structures relative to the dimensions of the selected data window, the usage of other window sizes is tested in the following.

4.2.2 Effect of the Data Window Size

When selecting the data window size there are two competing factors: while a smaller window potentially allows detection of smaller features, i.e. a better resolution, a larger window has the advantage that there are more data points for the statistical calculations which should lead to more robust results. The window size used initially was selected to ensure a sufficiently large number of data points to populate the PDFs for the entropy calculations. The optimal binning algorithm (optBINS) requires a minimum of approximately 150 data points to be used *(Knuth, 2006; Krützmann, 2008)*, though this is not an exact value based on theoretical arguments and the actual useful minimum generally depends on the particular type of data and the underlying distribution. Nevertheless, this sets an approximate lower boundary on the window area that should be used.

The theoretical resolution of the system gives a reasonable estimate for the minimum useful window height. The system resolution is approximately one half of the wavelength at the centre frequency, which is equivalent to seven data points in the vertical direction. In ice

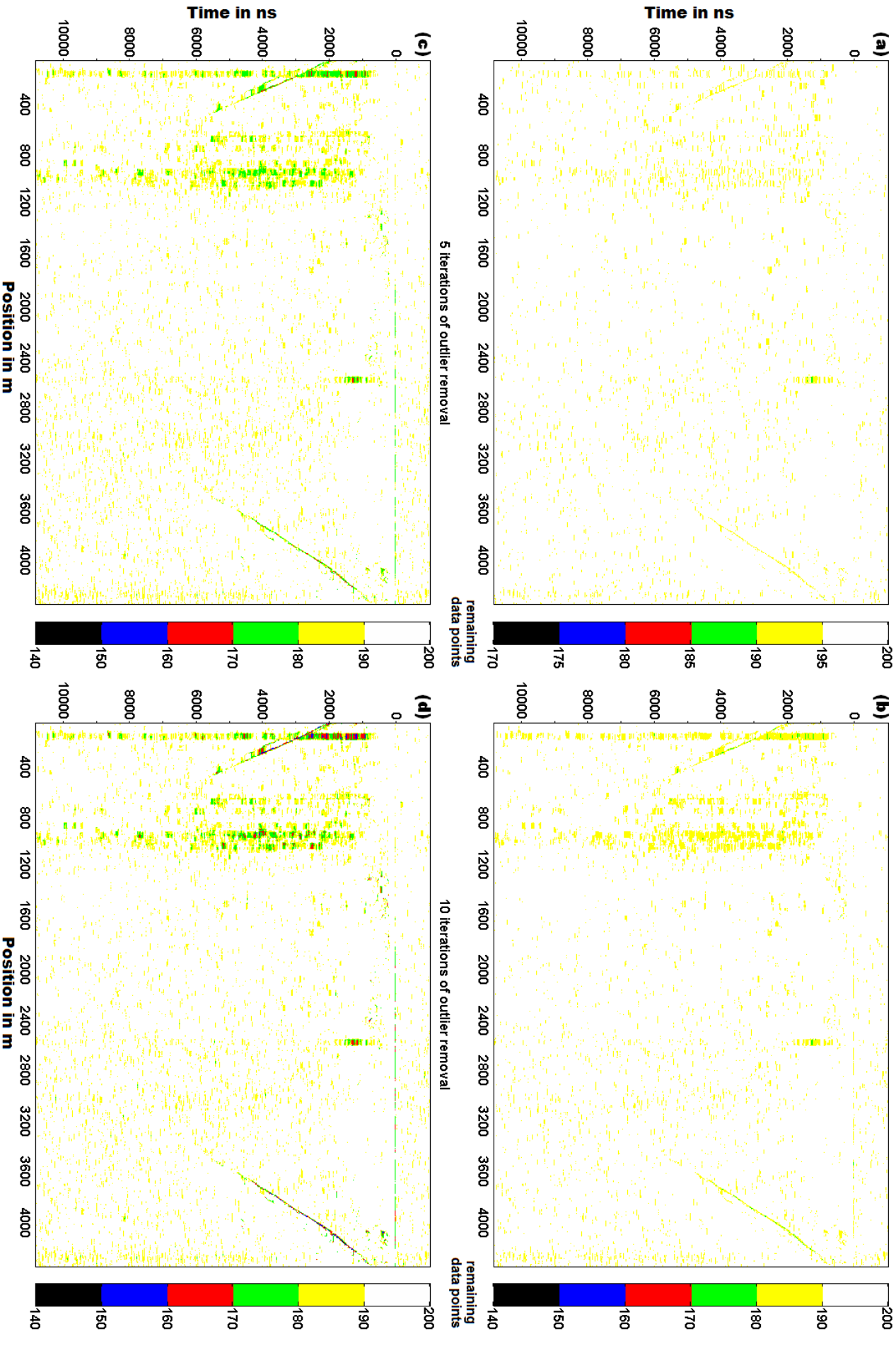

Figure 4.7: Remaining data points in the *25h8v* data window after (a) one, (b) three, (c) five, and (d) ten iterations of outlier removal. Note the reduced colour scale range in (a).

($\rho_i = 917\ \frac{kg}{m^3}$) this corresponds to 1.9 *m*. The horizontal window width on the other hand, is not limited by any theoretical considerations. A narrower window simply provides a higher horizontal resolution. In the present case, one trace (and therefore one horizontal data point) corresponds to 2 *m* along the recorded track. Accordingly, the smallest window should have a height of seven and a width of 22 data points, resulting in a total number of 154 points and corresponding to an approximate physical window size of 2 *m* by 44 *m*. However, due to the relatively large number of (erroneous) data points being filtered out in some parts of the profile (up to 30%), the window size used above (25 horizontal by 8 vertical points, i.e. 50 *m* by 2.2 *m*) is more practical, as it ensures a sufficient number of data points in all PDFs even after the outlier removal procedure.

On the other hand, it might seem prudent to use a somewhat larger window size than those tested so far, in order to improve the statistics of the underlying histograms and obtain more robust results. Larger windows, e.g. *35h25v* or *50h25v* (Fig. 4.8a and 4.8b, respectively), imply a reduced resolution of the *RE* images, since the effective resolution is essentially equivalent to the window size. While larger windows have the theoretical advantage of improved statistics, there do not appear to be any major benefits of a larger data window. In both cases shown in Fig. 4.8a and 4.8b, the increased window size results in a more smoothed picture compared to Fig. 4.5, thereby obscuring some of the weaker reflections.

Considering that most of the relevant amplitude gradients in GPR data are vertical gradients, the vertical window size should be on the order of the expected vertical width of the gradients to be detected (increase in signal amplitude over up to one pulse-width). Therefore, the initial choice of using a vertical window size of eight data points can be considered a good value for detecting subsurface reflections. The horizontal window size could be increased some more to improve the underlying statistics at the expense of increased horizontal blurring of the results. It should be noted that the *RE* results have a relatively strong contrast, even at large depths, without using a gain function but simply due to the 'mechanics' of the *RE*, i.e. because it can only take on values between zero and one.

4.2.3 Number of Bins

Another factor that can affect the quality of the *RE*-results is the number of bins used for creating the underlying histograms. Figure 4.9 illustrates how many bins were found to be optimal by the optBINS algorithm when calculating the RE_{25h8v} after five iterations of outlier removal. Clearly the number of bins used to create the histograms is higher in those areas that are dominated by weak volume scattering, while much fewer bins are needed in areas with stronger signals (close to the surface and near the reflections from the glacier bed). Accordingly, the maximum number of bins tested (half the number of data points) is used throughout most of the radargram.

According to *Knuth et al. (2005)*, consistent selection of the maximum number of bins can be an indicator of a problem related to rounding errors in the underlying data. Since the usage of very high numbers of bins largely coincides with the areas where the numerical values of the signal amplitude are small, there could be a connection. The pulseEKKO PRO system records the data as 16-bit signed integers, i.e. the received signal is converted to integer values between -32767 and 32767. The data is stored in the same format when it

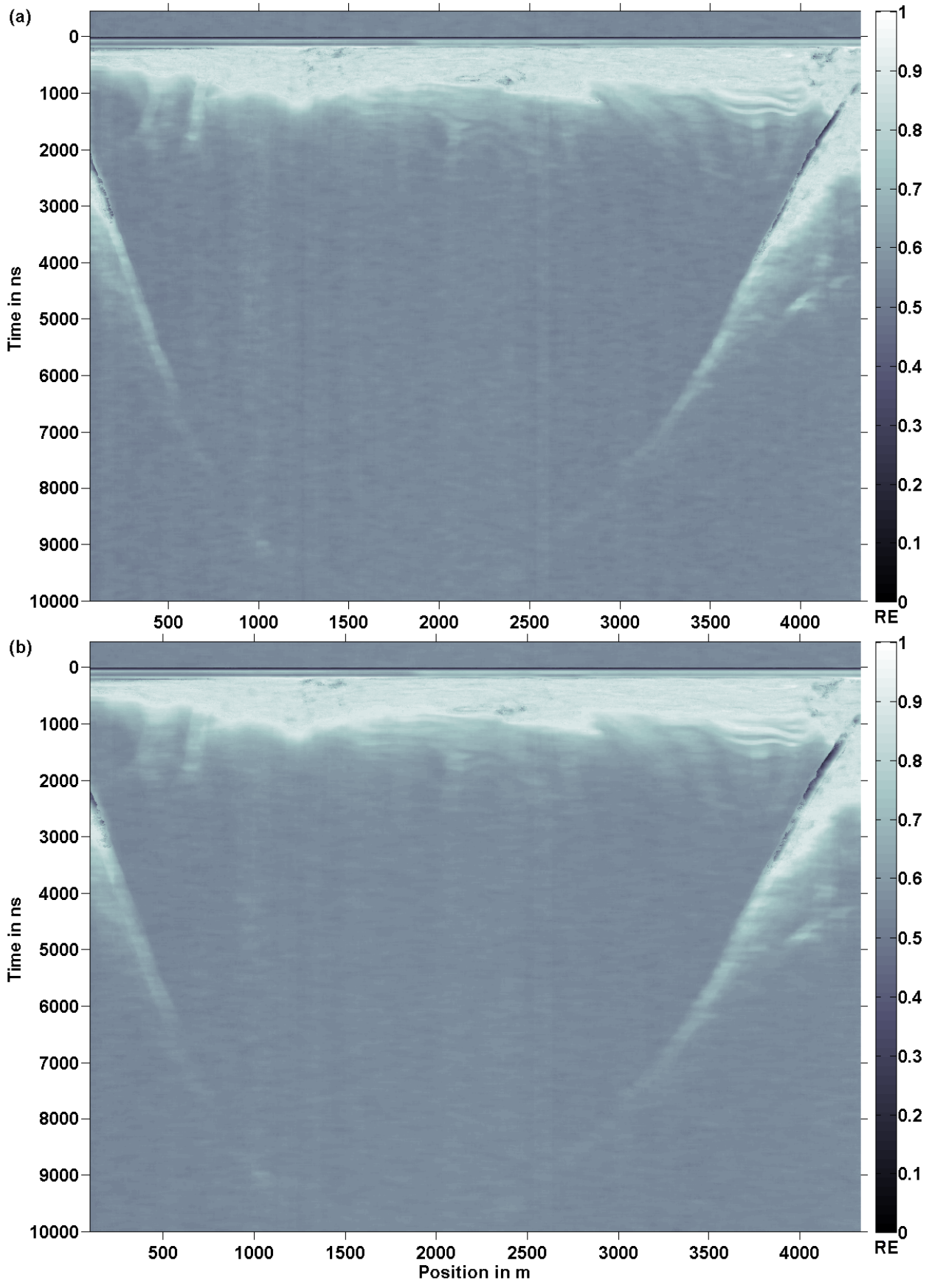

Figure 4.8: *RE* calculated from histograms using 25 vertical and (a) 35 and (b) 50 horizontal data points. In both cases, five outlier removal iterations were performed.

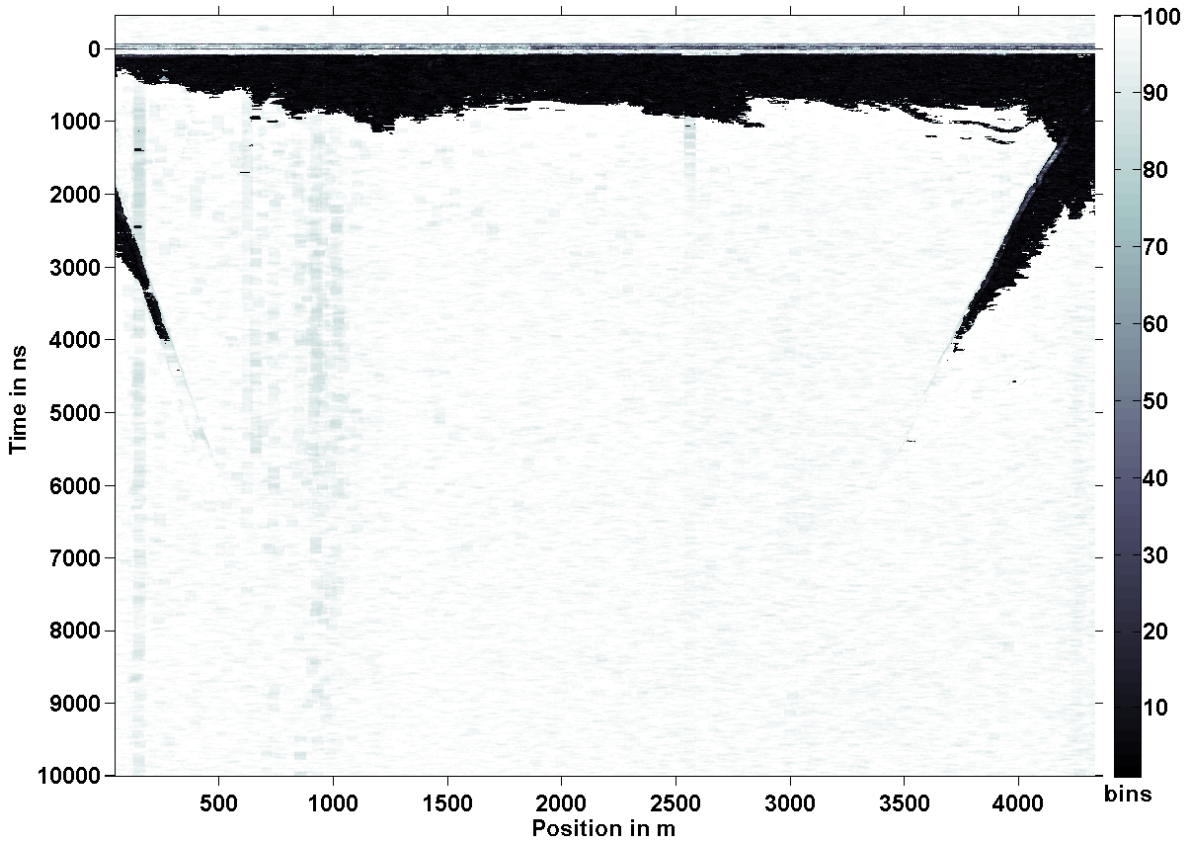

Figure 4.9: Number of bins selected by the optBINS algorithm using the *25h8v* data window and five iterations of outlier removal.

is processed with the EKKO_View Deluxe software. Therefore, after applying the dewow filter and calculating the envelope with EKKO_View Deluxe, the possible range of amplitude values is between 0 and 32767. At a depth of 435 *ns* the average amplitude along the whole profile already drops to 100, that is, below this level the data points will largely have integer values less than 100. This is probably the cause of the "problem" indicated by the high output of the optBINS algorithm. For the given data window (*25h8v*) the maximum number of bins tested usually lies between 80 and 100, depending on the number of points removed by the outlier removal process. When all data values lie between 0 and 100, testing up to 100 bins will of course lead to the result that the data was drawn from an integer distribution. This is the apparent rounding-error problem detected by optBINS and could indicate that a reduced maximum number of bins tested might be sufficient.

The *RE* can also be calculated by using a fixed number of bins for all histograms. Figures 4.10a and 4.10b show the RE_{25h8v} calculated with a fixed number of 10 and 30 bins, respectively. Clearly the main features found in Fig. 4.6a can also be observed in both cases. Generally, the plots have less contrast (are overall brighter) and are more blurred than with the optimal binning algorithm. Comparison of Fig. 4.10a and 4.10b also illustrates that a larger number of bins tends to give slightly lower entropy values, which explains the overall brightness of both images compared to Figs. 4.6a and b. While using a fixed number of bins does allow the identification of the same reflectors as with the optimal binning algorithm, and is also less computationally demanding, including the optBINS algorithm results in a more detailed picture of the individual reflections and a better contrast. Accordingly, for

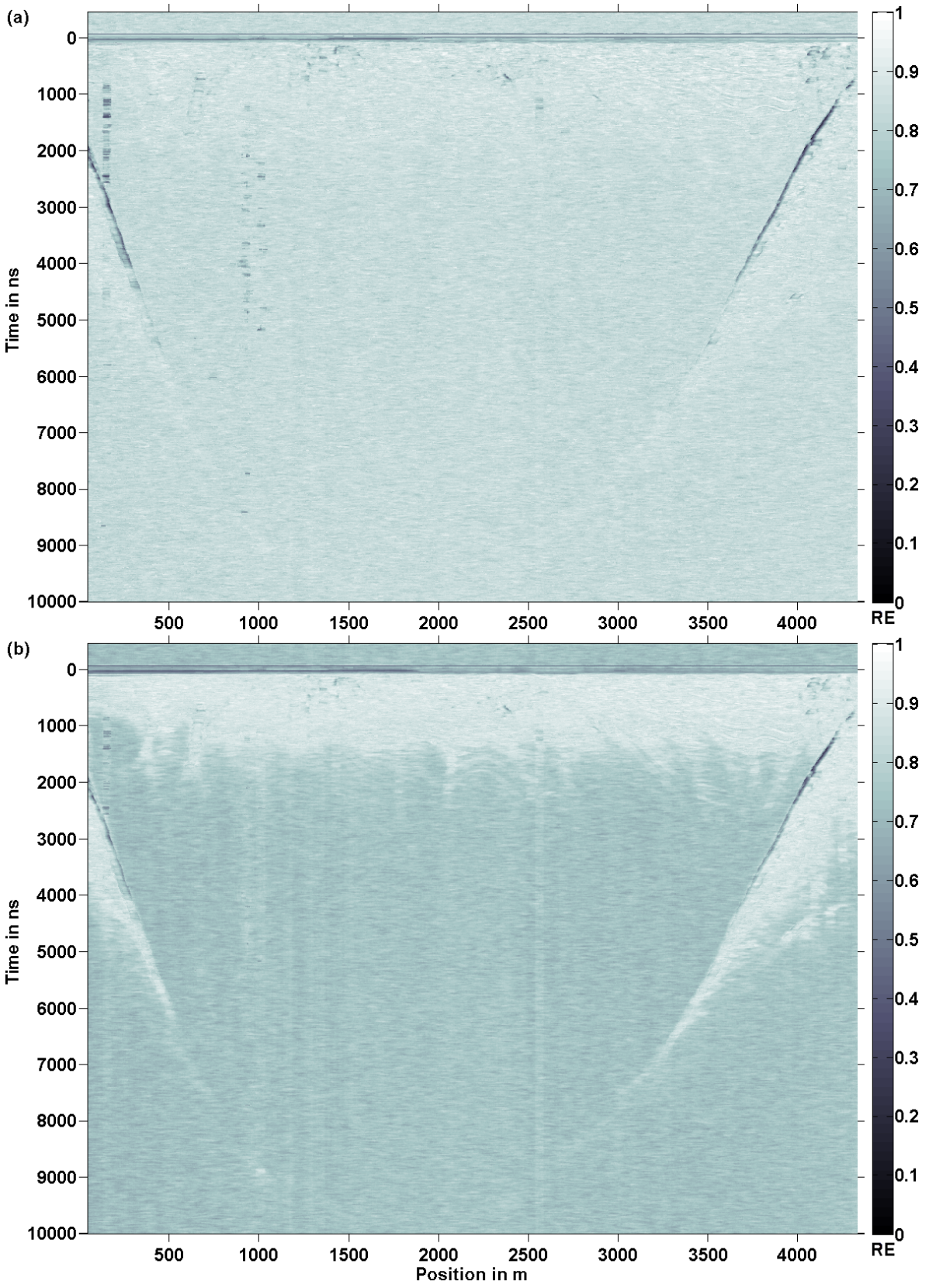

Figure 4.10: RE_{25h8v} calculated using a fixed number of (a) ten and (b) thirty bins when creating the histograms. In both cases, five outlier removal iterations were performed.

a more thorough post-acquisition analysis of GPR data it is beneficial to use the optBINS algorithm. On the other hand, when wanting to process GPR data in the field it can pay to sacrifice some of the detail in exchange for a reduced demand for computational power by merely using a fixed number of bins, though this number should be higher than in Fig. 4.10a and 4.10b to increase the dynamic range.

It is also interesting to note that, when only considering the part of the radargram which does not use the maximum number of bins, i.e. the part that is close to the surface and wherever the signal from the bottom reflection is strong (Fig. 4.9), the algorithm selects a relatively small number of bins for creating the histograms, less than 30 in most cases. This is similar to the original results with stratospheric tracer data from SOCOL where the optimal number of bins selected also lay between 1 and 30 in the vast majority of cases (*Krützmann*, 2008).

4.2.4 Other Orders of Rényi Entropy

Thus far the *RE* was calculated with an exponent of $\alpha = 2$. Generally, any value greater than one can be selected for α. The resulting *RE* values are a monotonically decreasing function of α *(Beck and Schlögl, 1993)*. When setting the exponent $\alpha = 1$, the general definition of *RE*, given in Eq. 2.17, is equivalent to the more well known Shannon entropy:

$$RE(1, b, N) = -\sum_{i=1}^{b} p_i \cdot \ln p_i \tag{4.2}$$

Therefore, using the Shannon entropy (Eq. 4.2), multiplied by the standardisation factor $\frac{1}{\ln(b)}$, will result in overall higher entropy values while higher orders of α tend to emphasise more peaked distributions.

Calculating the Shannon entropy ($RE_{25h8v}(\alpha = 1)$) of the glacier profile after five iterations of outlier removal results in Fig. 4.11a. As expected the overall entropy values are higher, making the image appear brighter than for example in Fig. 4.5. Similarly, using $\alpha = 5$ leads to the expected overall decrease in *RE* (Fig. 4.11b). Interestingly, the bottom reflection now has lower values than the surroundings in the upper part of the profile, down to about 4000 *ns*. The reason for these low *RE* values is related to the drop-off in *RE* seen at the centre of the first few peaks of Fig. 4.1b. Close to the surface the reflection is quite strong. At the centre of this strong reflection most of the points within the data window have similar, high values. This results in a PDF with a relatively strong peak and therefore gives low *RE* values. Increasing the exponent α enhances this effect, resulting in the particularly low *RE* values of the bottom reflection observed in Fig. 4.11b.

Using different values of α shows that the exponent can affect the contrast in the resulting image. However, there is no clear advantage to using a higher or lower value and hence the default value of $\alpha = 2$ is retained.

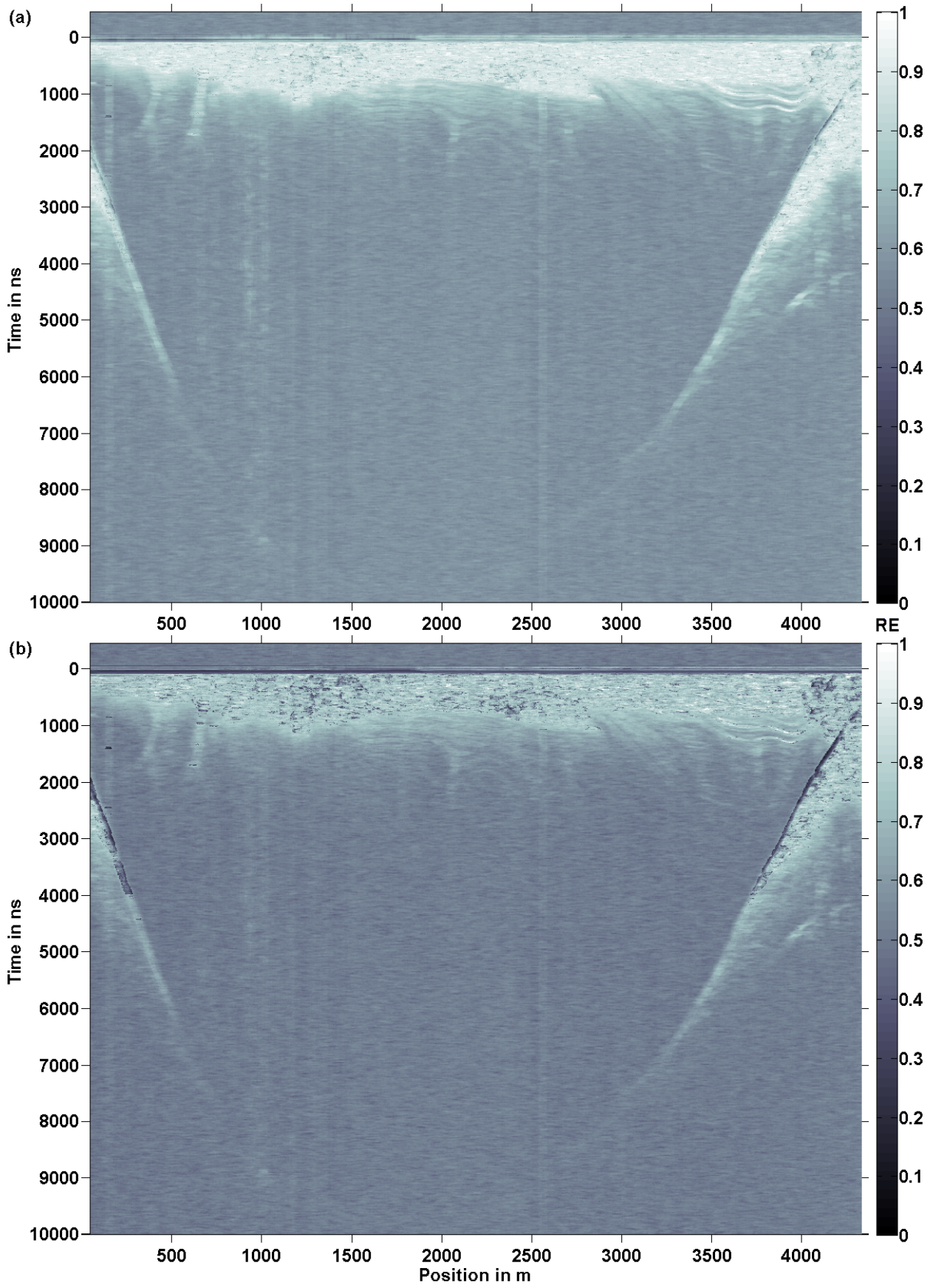

Figure 4.11: RE_{25h8v} calculated using five iterations of outlier removal and (a) $\alpha = 1$ (Shannon entropy) or (b) $\alpha = 5$.

4.3 Discussion and Comparison to Regular GPR Processing

In order to judge the utility of the *RE* results, Fig. 4.12 shows the radar data processed with more standard GPR processing techniques for comparison. More specifically, the processing used for Fig. 4.12 involves three steps: dewow, bandpass filtering (0/5 - 40/60 *MHz*), and AGC (maximum gain = 2000) *(Riger-Kusk, 2011)*. This kind of processing resolves more small-scale features (e.g. internal layers) than the results with *RE* (compare with Fig. 4.5), but it also requires more effort, particularly in terms of a priori information, such as the actual bandwidth of the emitted pulse to select appropriate filter parameters, which is not necessarily available until after the data has been acquired. However, Initial analysis with the aim of merely checking whether anything at all or one reflection in particular can be seen in the data (e.g. the reflection from the glacier bed at a certain depth), usually only includes a few basic steps. For the pulse EKKO system these tend to be the dewow correction and a gain function. Typical types of gain functions are the AGC (automatic gain control), which attempts to achieve a constant mean signal level within a fixed time window throughout the data, and the SEC (spreading & exponential compensation), which uses an exponential function to account for geometrical spreading losses and signal attenuation (see also Sect. 2.5.2). Both of these gain functions commonly require the user to identify a maximum gain value and one additional parameter. For the AGC this parameter is the time window width which is typically chosen to equal the pulse width of the system, while the SEC requires the input of an attenuation coefficient for the exponential function *(Sensors and Software Inc., 2006)*.

Selecting appropriate gain function parameters is a crucial point when performing initial analysis of acquired data in the field. As the received signal decays rapidly with time, the (absolute) amplitude values measured tend to span several orders of magnitude, four in the present case. Accordingly, the most useful gain function and gain function parameters (such as maximum gain, decay coefficient, etc.) depend on the details of the system setup such as transmitter power, transmitter-receiver geometry, receiver gain, and the dielectric properties of surface and subsurface materials. The latter are not generally well known prior to a survey and can have a significant impact on the decay of the signal with time/depth, and thereby on the appropriate gain-function parameters. Since the clarity of a reflection depends on its contrast relative to the no-reflection background (volume scattering), i.e. the relative magnitudes of the amplitude gradients after applying a gain, it is not always trivial to identify appropriate gain-function parameters in the field on the spot. Too much gain can over-amplify both the reflection amplitude and the background noise, making an actual reflection hard to discern, while too little gain may lead to the same problem in reverse. The *RE* inherently remediates this issue as it is applied before using any kind of gain function and creates relatively high-contrast images since all resulting values lie between zero and one rather than covering several orders of magnitude. The latter is usually the case in raw data, and deep reflections that might be relatively strong (compared to the background of volume scattering) can nevertheless be hard to recognise even after applying a gain. The small range of *RE* values can make such amplitude gradients easier to identify straight away, since the value of the *RE* is independent of the absolute magnitude of the gradient in the data. For

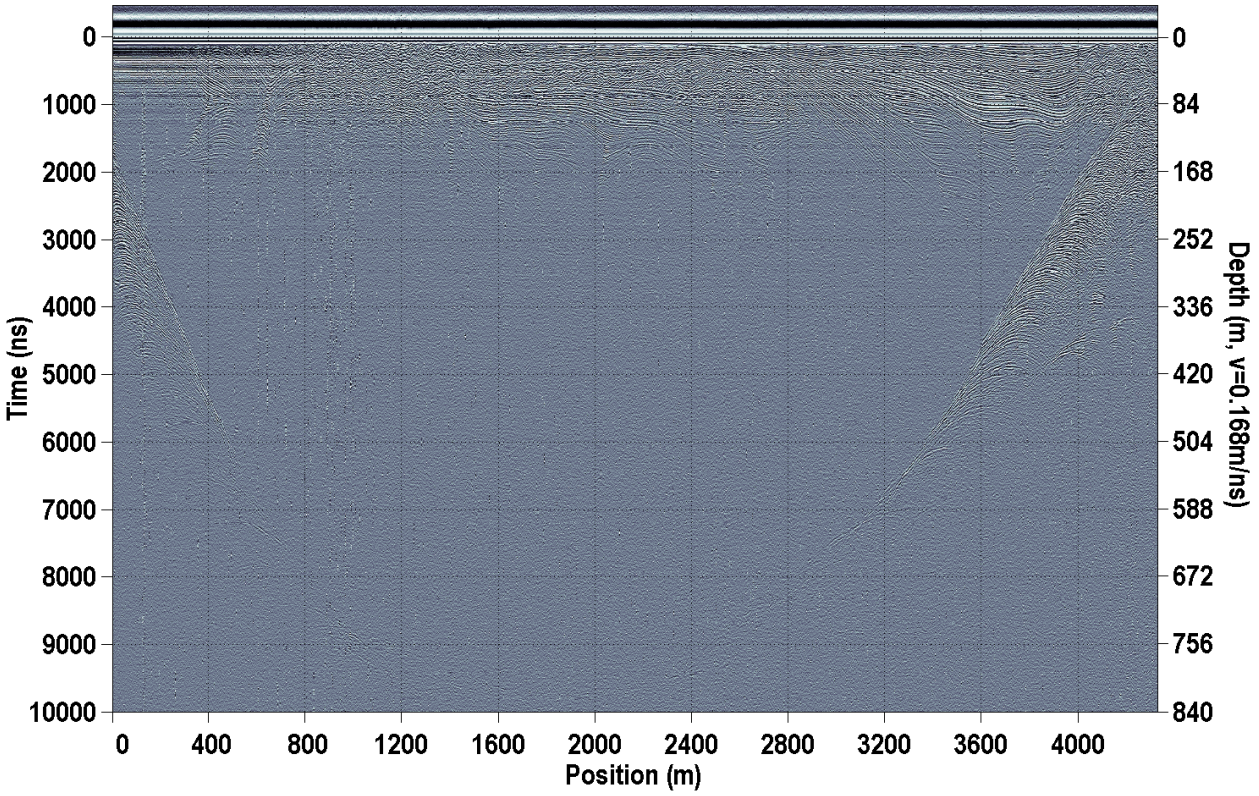

Figure 4.12: Radargram processed in a more standard GPR fashion. The processing steps applied are: dewow, bandpass filtering (0/5 - 40/60 *MHz*), and AGC (maximum gain = 2000). After *Riger-Kusk* (2011).

example, an increase in the signal amplitude by one order of magnitude – be this from 1000 to 10000 or from 10 to 100 – will result in a similar value of *RE* (assuming that a variable bin width is used). So all that is required to get a noticeable change in *RE* is a sufficiently wide (see also Section 4.1) amplitude gradient, independent of the absolute values in that part of the profile. For this reason the *RE* has the potential to be a useful tool for initial analysis of GPR data.

To make the *RE* methodology more easily and widely applicable for fast initial analysis of GPR data, it is important to develop guidelines for its usage that depend on the details of the GPR system used for data acquisition, i.e. guidelines for determining the window size parameters. Similar to the parameters of gain functions like the AGC or the SEC, these generally depend on the details of the system setup such as centre frequency, bandwidth, sampling interval, trace interval, transmitter-receiver separation, and the dielectric characteristics of the ground. However, while the latter are one of the most important factors when determining the parameters of standard gain functions, the window size for the *RE* can be determined purely from a priori knowledge of the system setup and can even be generalised to most GPR systems.

Most (commercial) pulsed GPR systems have a pulse width of 2-3 wavelengths at centre frequency and a resolution on the order of one such wavelength *(Rial et al., 2009)*. The sampling frequency is usually chosen to ensure an adequate sampling of the centre frequency, i.e. between eight and twelve samples per cycle. Combined with the minimum number of data

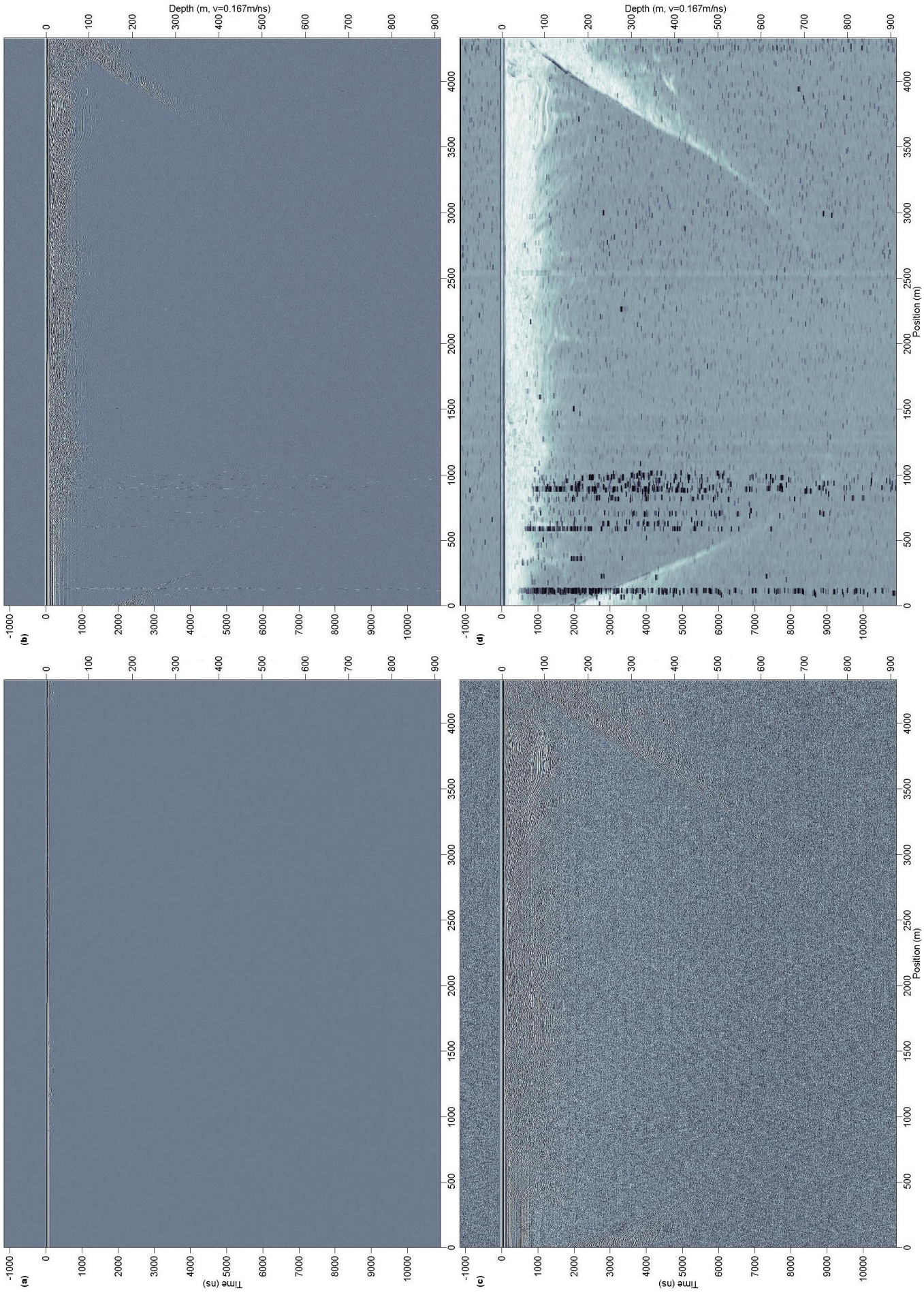

Figure 4.13: Comparison of (a) dewowed 25 MHz data with basic processing in the form of automatic gain control with a maximum gain of (b) 300 and (c) 3000 and (d) the results with the RE_{20h10v} using 100 bins and no outlier removal.

points required for adequate statistics (≈ 150) this knowledge can be used to determine a widely applicable window size for RE calculations: 10 vertical (time dimension) and 20 horizontal (along-track dimension) data points and a fixed number of 100 bins. This should give serviceable RE-results for most pulsed GPR systems, independent of their centre frequency. The total of 200 data points per histogram ensures robust statistics of the calculations. Setting a fixed and relatively high number of bins ensures good contrast between gradient regions and the background of volume scattering and improved performance compared to the optimal binning approach. Applied in this manner, the RE can serve as an alternative (almost) parameter-free pseudo gain function for quick analysis of GPR data in the field.

The effect and possible advantage of using the RE_{20h10v} as a gain function is illustrated by direct comparison with the automatic gain control (AGC). Figure 4.13a shows the 25 *MHz* profile with only the dewow filter applied. Due to the large amplitude of the initial signal no other features can be made out. For the pulseEKKO PRO system used to acquire this data the default gain for displaying data while it is being recorded is an AGC with a maximum gain of 300 (*Sensors and Software Inc.*, 2006). This results in the glacier bed reflection becoming visible down to about 4800 *ns* or about 400 *m* (Fig. 4.13b). Other features, such as two distinct internal layers between 3300 and 4000 *m* at a depth of approximately 100 *m*, can now also be seen. In order to view deeper sections of the glacier bed, the maximum gain of the AGC has to be increased. However, this can lead to 'over-gaining'. For example, if the maximum gain is set to 3000 (Fig. 4.13c), the bottom reflection can be identified down to about 600 *m* but the gained noise in the data disguises some of the weaker features such as the two internal layers mentioned before. This is where the gain-like effect of the RE is particularly useful. As long as the signal level is not too low, the RE assigns all gradients a relatively similar value, independent of the absolute changes in amplitude involved. In Fig. 4.13d, the bottom reflection is clearly visible down to approximately 600 *m* (and more faintly for another 100 *m*) and the two internal reflections in the upper right section of the profile can also be identified. Figure 4.13d is calculated directly from the data shown in Fig. 4.13a, using the 'standard window size' (*20h10v*) and a fixed number of 100 bins. The envelope calculation is simplified to taking the absolute value of each data point which further increases the performance of the RE processing. Clearly the RE_{20h10v}-results improve the visibility of the major features in the data, though some of the weaker internal reflections seen in the top 100 *m* of Fig. 4.13b, cannot be identified in Fig. 4.13d, due to the overall high RE values near the surface. This shows that, for initial analysis of data during or just after acquisition in the field, the RE_{20h10v} approach can have an advantage over standard gain functions, as it results in a considerable contrast enhancement without requiring any tuning of parameters.

To illustrate the wider applicability of the 'standard window size', the RE_{20h10v} is applied to 50 and 500 *MHz* data acquired on the McMurdo Ice Shelf in the next section.

4.4 Application of RE to Higher Frequency Data

Figure 4.14 shows the RE_{20h10v} of data recorded with a 50 *MHz* setup of the pulseEKKO PRO system on a part of the McMurdo Ice Shelf that is known to have a large-scale brine

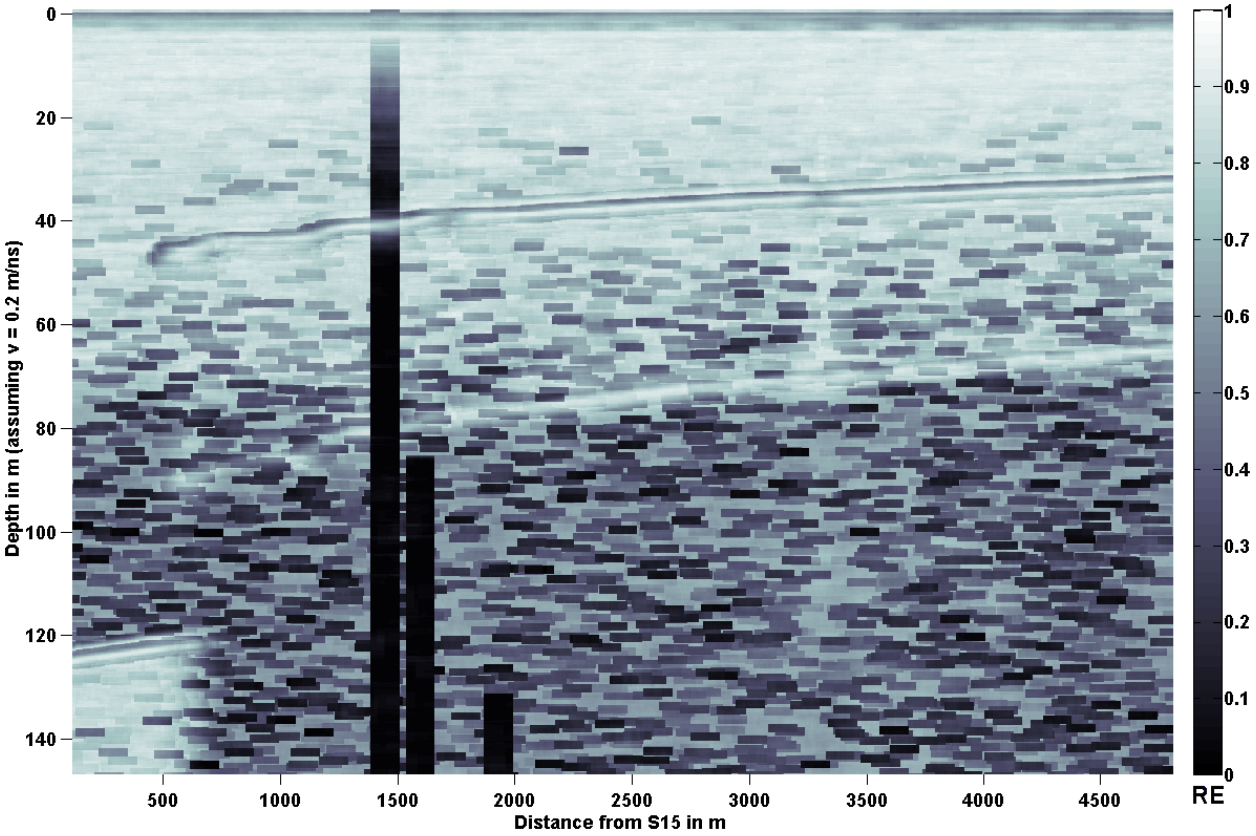

Figure 4.14: RE_{20h10v} of a 50 *MHz* profile between S15 and S12 (calculated using a fixed number of 100 bins). The brine layer reflections starts about 600 *m* along the profile at an approximate depth of 45 *m*. The deeper reflection visible earlier on probably represents the bottom of the ice shelf. The vertical exaggeration is roughly 23:1.

intrusion extending several kilometres into the ice shelf (*Kovacs et al.*, 1982b). This layer contains salt water which reflects and absorbs most of the radar energy and therefore prevents any deeper reflectors to be detected. The data shown in Fig. 4.14 corresponds to a 4.8 *km* long part of the transect across the ice shelf between the stakes S15 and S12, moving south (see Fig. 2.15). Only the dewow and the absolute value calculations were performed prior to calculating the RE_{20h10v}, since these two steps are easy to apply even in the field while outlier removal is not. Accordingly, the numerous black boxes are related to outliers caused by the same fibre-optic cable problems as in the 25 *MHz* glacier profile (e.g. Fig. 4.4). The three dark vertical lines are caused by more erroneous data through interference from radio transmissions (the 50 *MHz* antennae were unshielded).

The reflection at approximately 120 *m* and slowly decreasing in depth along the first 700 *m* in Fig. 4.14 is probably the bottom reflection from the ice shelf / sea water interface. This reflection is suddenly cut off and a different one appears at about 40 *m* depth, which is most likely associated with the brine layer. It also slowly decreases in depth along the profile as the ice shelf becomes thinner in this direction (*Kovacs et al.*, 1982b). The vertical scale in Fig. 4.14 assumes an average wave velocity of 0.2 $\frac{m}{ns}$ (corresponding to an average snow density of 591 $\frac{kg}{m^3}$). This is a reasonable estimate down to the brine layer, but too large when deeper reflections are concerned, i.e. the actual thickness of the ice shelf is probably overestimated in Fig. 4.14.

Due to the strong reflection and some absorption of the radar wave by the brine layer, the bottom of the ice shelf is not visible in those parts of the profile where the brine layer is present, except between 600 and 700 m where both reflections can be observed. This region marks the maximum extent of the brine intrusion into the ice shelf and therefore the layer is probably very thin at this point, reducing the amount of reflection and absorption, and allowing some of the radar energy to penetrate through to the bottom of the ice shelf (*Kovacs et al.*, 1982a). The apparent horizon at around 80 m depth that runs parallel to the brine layer is not an actual reflection, but a secondary image (sometimes referred to as a 'ghost' or 'multiple') of the brine layer reflection. This is a common artefact when strong reflectors are present and is caused by a part of the returned radar signal being reflected back down by the snow-air interface and therefore travelling between the surface and the brine layer twice.

Figure 4.15a is a close-up of the top 40 m of Fig. 4.14. The brine layer shows up as a continuous band of low RE_{20h10v} between two bands of higher values (and another thinner band of low RE_{20h10v} below these). The brighter bands correspond to the increasing and decreasing amplitude gradients of the reflection, while the lower values in between relate to the centre of the amplitude peak. This is similar to the pattern of the RE for the 5^{th} and 6^{th} peak in Fig. 4.1b. While the horizontal continuity of the pattern clearly delineates this reflection from its surroundings, the distinction between high RE_{20h10v} values related to this particular reflection and similarly high RE_{20h10v} values above, is difficult. Comparison with the RE_{20h10v} calculated in the same manner for a 500 MHz recording along the same line (Fig. 4.15b) illustrates the coarseness of the resolution of the 50 MHz system. Clearly, the 500 MHz system has a considerably better resolution than the 50 MHz setup, resulting in a much narrower band of high RE_{20h10v} corresponding to the brine layer reflection with a higher contrast relative to the RE_{20h10v} of the surroundings. Furthermore, several internal layers between the surface and the brine infiltration can be identified in Fig. 4.15b, e.g. at about 11 m depth and at 18 m depth, none of which are visible in Fig. 4.15a.

All internal layers move closer to the surface from left to right. While this trend is similar to the one seen in the brine layer, it is not as steep. A closer look at Fig. 4.15b shows that the brine layer 'cuts through' some of the internal layers, which underlines the fact that the brine infiltration happened after the formation of the rest of the internal structure (see also Fig. 4.16a and b). However, most of the other internal layers are relatively blurred and the contrast to the background is low. Similar to Fig. 4.14, the high signal variability close to the surface (top quarter of the profile) causes relatively high RE_{20h10v} values everywhere, disguising any distinct individual reflectors.

The overall raised RE_{20h10v} in Fig. 4.15a is probably due to high variability in the GPR signal caused by numerous internal layers in the upper part of the snow pack, all of which partially reflect the radar wave. These reflections are weaker than the one from the brine layer, as is illustrated in Fig. 4.16a which shows the underlying radargram for Fig. 4.15a. Several continuous reflections from internal layers can be made out between the surface and the brine layer but the reflection amplitudes are smaller. The ubiquity of internal layers is further illustrated by the 500 MHz GPR radargram of the same profile in Fig. 4.16b. The higher resolution of the 500 MHz system allows the identification of an even larger number of layers, some of which are also highlighted by the RE_{20h10v} in Fig. 4.15b. The resolution of the 50 MHz data is too coarse to resolve the weak reflections individually, but they

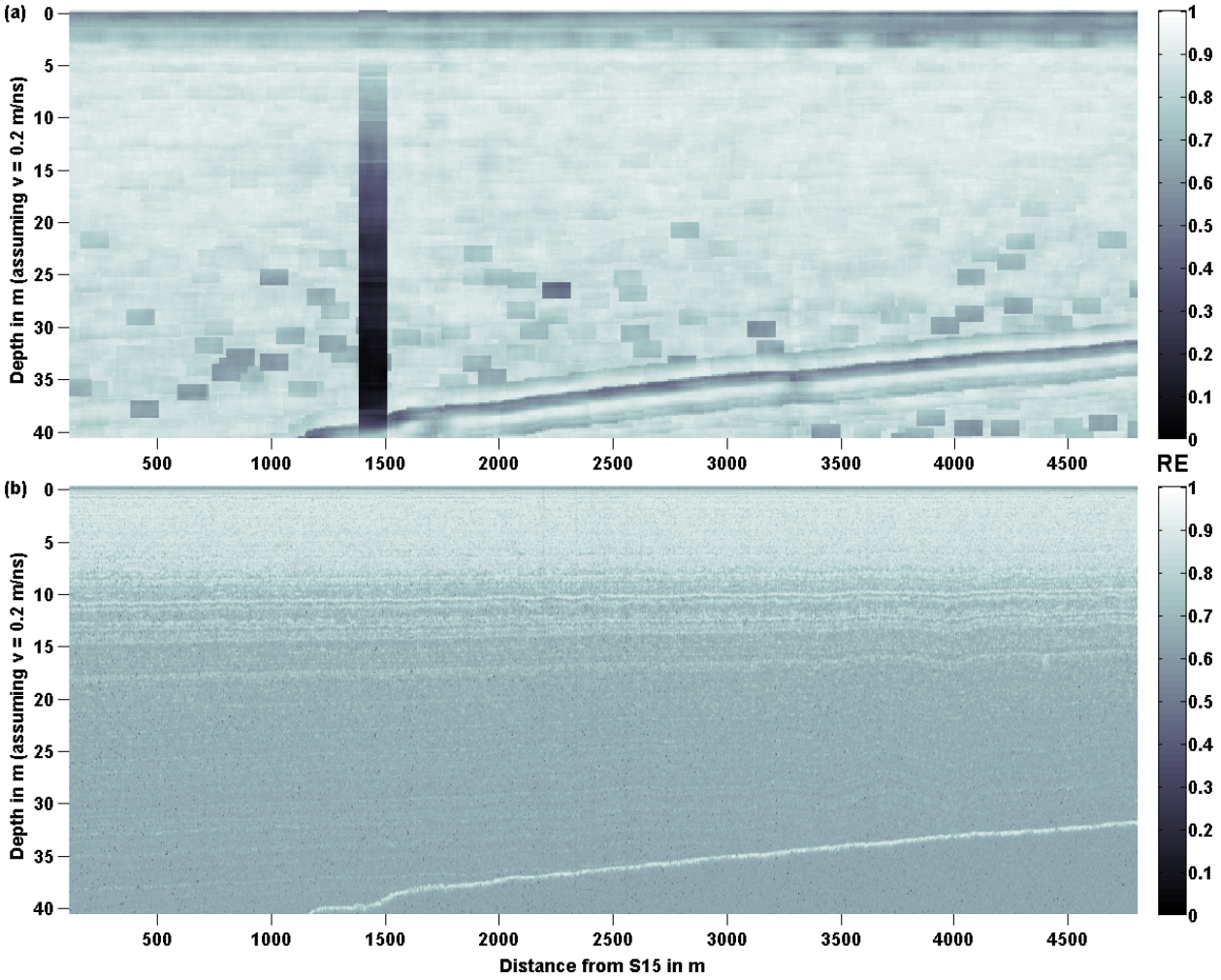

Figure 4.15: RE_{20h10v} of (a) 50 MHz and (b) 500 MHz GPR data collected along the same line between the stakes S15 and S12 on the McMurdo Ice Shelf (see Fig. 2.15b) in 2009. In both cases only the dewow filter is applied before calculating the RE_{20h10v} from the absolute values of the data using a fixed number of 100 bins. The vertical exaggeration is roughly 47:1.

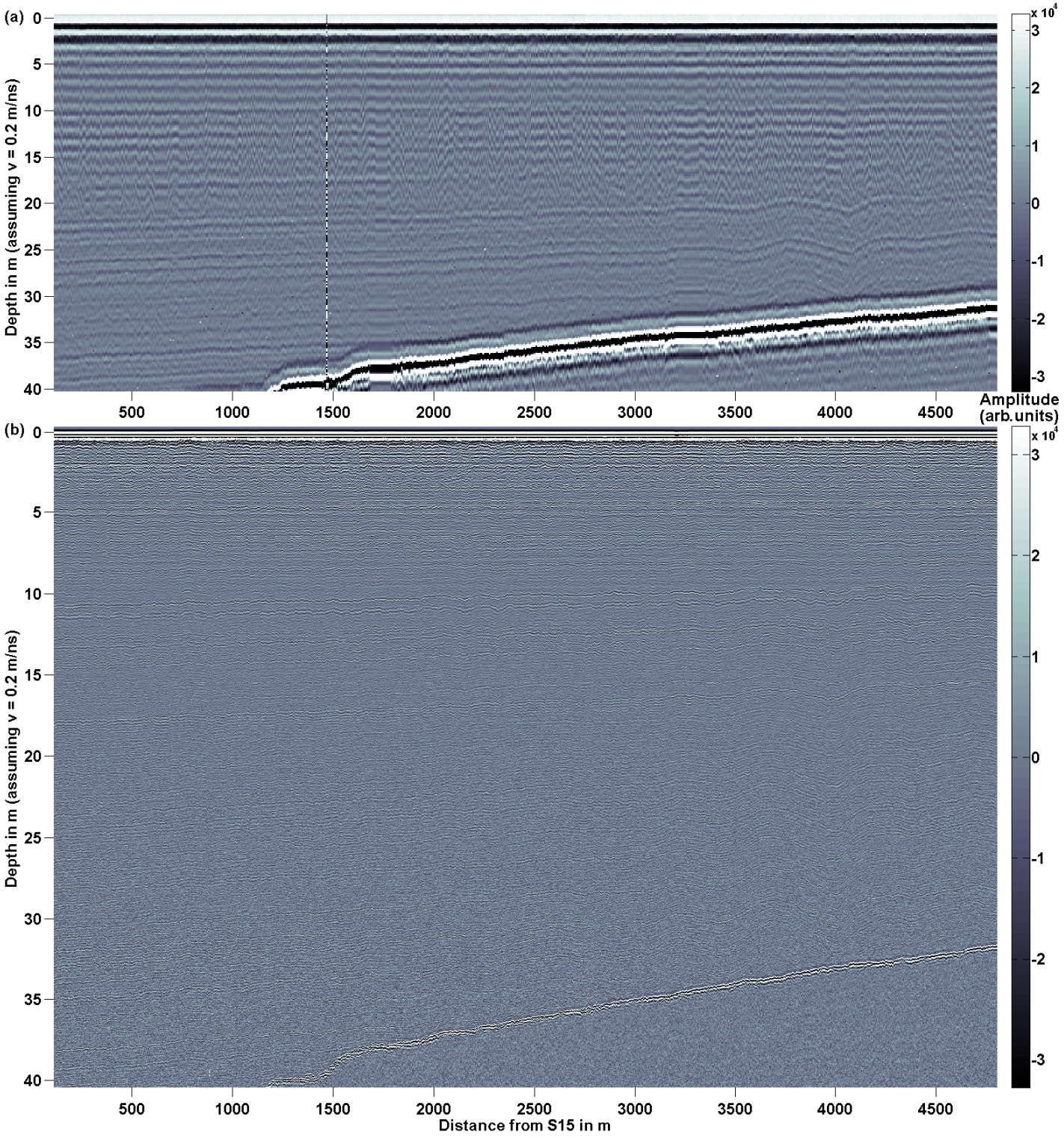

Figure 4.16: Radargrams underlying the RE_{20h10v} profiles in Fig. 4.15. In addition to the dewow filter a linear gain was applied to both (a) the 50 *MHz* and (b) the 500 *MHz* data. Furthermore, ten-fold stacking was performed on the 500 *MHz* data. The vertical scale is expanded in (b) to improve the visibility of weak internal reflections. The resulting vertical exaggeration in (b) is approximately 82:1.

still cause a large variability in the returned signal amplitudes. The resulting overall high values of RE_{20h10v} above the brine layer reflection in Fig. 4.15a disguise the few individual reflections that can be made out in the plain radargram (Fig. 4.16a). At greater depths, the signal variability – and therefore the RE_{20h10v} values – are found to be much lower, and the contrast to the higher RE_{20h10v} values of the amplitude gradients from what is probably the bottom reflection of the ice shelf in the first 700 m of Fig. 4.14 is considerably improved. A similar effect is probably the reason for the lack of clear structure in the top ten metres of the RE_{20h10v} profile derived from the 500 MHz data (Fig. 4.16b). This shows that the RE_{20h10v} is more useful for identifying individual deeper reflectors in that part of the profile where the signal amplitudes are relatively small, rather than for detecting closely spaced, weaker horizons near the surface.

All in all, Figs. 4.15 and 4.16 illustrate both the utility of the RE as a kind of gain function, the wider applicability of the standard window dimensions determined above (20h10v), as well as the limitations when it comes to identifying more closely spaced and weaker reflections.

4.5 Summary and Conclusion

The aim of this chapter was to test the applicability of the RE statistical measure for the detection of amplitude gradients (corresponding to reflections from subsurface boundaries) in cryospheric GPR recordings. Initially, synthetic gradient data was used to establish how the size of the data window, used for creating the histograms from which the RE is calculated, should be proportioned relative to the expected extent of the amplitude gradients to be detected. The test showed that only gradients with an extent similar to or larger than the window width in the corresponding direction lead to a considerable increase in RE. Accordingly, a relatively small vertical window size of eight data points was used when applying the RE to the raw data from a 25 MHz recording of a glacier profile. To ensure a sufficiently large number of data points in each histogram for the optimal binning algorithm optBINS (*Knuth et al.*, 2005), a horizontal window width of 25 data points was selected.

The results showed that the RE_{25h8v} is able to detect the amplitude gradients caused by the reflection from the bedrock, at least in the upper part of the profile where the signal level is relatively high. Additionally, the RE_{25h8v} produced a horizontal artefact and a large number of 'black boxes' which are small regions of very low RE, usually the size of the data window. Further testing showed that it is necessary to dewow the GPR data before applying the RE to avoid the horizontal artefact, while the black boxes are due to individual erroneous data points caused by a bad fibre-optic connection. These points tend to have a much larger (or smaller) value than any of the surrounding points, which results in highly skewed histograms and therefore low RE values. Calculating the envelope of each trace and applying an iterative outlier removal step produced a much clearer RE diagram that allowed the identification of the bottom reflection of the glacier down to about 7000 ns ($\approx 600\,m$), as well as some internal reflections in the shallower region of the profile. Improving the statistics by using larger window sizes did not show any advantage in terms of maximum detection depth of the bedrock reflection and only led to the expected blurring of the visible structures

since the effective resolution of the *RE* results is determined by the window size. Similarly, different orders of the *RE*'s exponent α also did not to lead to any consistent improvements of the image quality, though in some cases a different exponent may improve the contrast with higher exponents leading to overall smaller values of *RE*.

Generally, the RE_{25h8v} is able to identify the bedrock reflection in the 25 *MHz* profile quite well, particularly when calculating the envelope and including an outlier removal step before deriving *RE* values. However, when compared to a more elaborate standard processing approach the RE_{25h8v} does not show any significant improvement. Several internal reflections visible in the processed data are disguised by the overall high RE_{25h8v} values in the shallower parts of the profile. Moreover, the bottom reflection can be identified to somewhat greater depths when using more standard GPR processing methods. Hence, the *RE* can only be considered an improved processing methodology for glacial GPR soundings in relation to simplicity and, in some cases, in terms of processing speed.

With the optimal binning algorithm the *RE* processing is relatively time consuming since optBINS involves a large number of calculations. Using a fixed number of bins on the other hand, potentially allows for near real-time processing of data during collection in the field, particularly when further simplifying the calculations by omitting the outlier removal process and taking the absolute value of each point instead of the envelope of the trace. *RE* diagrams calculated from histograms with 100 fixed bins in this manner still show almost the same detail as before but with considerably reduced computational effort. The advantage in this case is that the *RE* acts as a pseudo gain function that does not require any prior knowledge about the subsurface properties or expected maximum depth of detectable reflectors. While normal gain functions often have to be tuned to give a good contrast between reflections and background noise over the whole range of the profile, the *RE* tends to assign all detectable amplitude gradients a similar value and therefore automatically results in a clear contrast between reflections and background scattering in many cases. This can be useful for initial data analysis in the field, particularly when working in places like Antarctica where the cold conditions and bright sunlight can make it very difficult to discern low-contrast images on the digital displays of the recording equipment.[2] Additionally, it is possible to define a data window size that is likely to work for various pulsed GPR systems and frequencies, since the temporal sampling is often similar. Usually between eight and twelve samples per cycle of the nominal centre frequency are recorded and therefore a window size of 10 vertical (in the time direction) and 20 horizontal (in the along-track direction) points can be useful in a large number of cases.

This was tested by calculating the RE_{20h10v} for a 50 *MHz* and a 500 *MHz* GPR profile which were recorded along the same track on the McMurdo Ice Shelf. In both profiles, the RE_{20h10v} clearly identifies the reflection from a brine-layer that is known to be present in the region at around 40 *m* depth, illustrating the wide applicability of the '*20h10v*' data window as well as the utility of the RE_{20h10v} as a pseudo gain function. However, the result from the 500 *MHz* data also underlined that the *RE* is not ideal for identifying multiple weak reflections that are close to each other, such as might be caused by internal layers of varying

[2]Digital displays tend to loose contrast in very cold conditions. This effect is particularly strong for the pulseEKKO PRO DVL (Data Video Logger), as experienced by the author during the data acquisition for the present work.

density in dry snow. Additionally the RE tends to have relatively high values close to the surface which also makes weak reflections hard to discern. All in all, the RE_{20h10v} can be considered a useful tool for fast initial analysis of GPR data that is expected to contain only a few strong reflectors, but it is less serviceable when weak and closely spaced reflectors are to be examined in detail.

Chapter 5

Deterministic Fourier Deconvolution of GPR Profiles of Dry Snow

Large parts of this chapter are from the article "Snow accumulation and compaction derived from GPR data near Ross Island, Antarctica" published in the online journal The Cryosphere (Kruetzmann et al., 2011).

In the previous chapter it was demonstrated that the Rényi entropy (RE) can be used to identify amplitude gradients associated with strong reflections in ground penetrating radar (GPR) recordings of snow and ice. However, it was also established that weak, closely spaced reflections from the boundaries between internal layers in snow can not be reliably identified with the RE methodology. As the tracking of internal layers in snow was one the main objectives of the Antarctic measurement campaign, a different approach is required to analyse the acquired high-frequency GPR recordings. Therefore a more conducive processing methodology for GPR data of dry snow – in which most reflections are caused by small differences in snow density – was developed: the deterministic Fourier deconvolution.

Using an estimate of the emitted waveform from direct measurements, deterministic deconvolution via the Fourier domain is applied to GPR recordings with a nominal frequency of 500 *MHz*. This reveals unambiguous reflection horizons which can also be observed in repeat measurements made one year apart. The processing methodology based on deconvolution is detailed in Sect. 5.1 and tested on simulated GPR data in Sect. 5.2. It is then applied to field measurements in Sect. 5.3 to improve the reliability of the detected horizons and allow point measurements of snow density and accumulation from snow pits and firn cores to be extrapolated to larger areas in Sect. 5.4. Additionally, it is illustrated that estimates of the compaction rates of dry snow can be obtained by tracking internal horizons in GPR data and comparing layer separations in different years. This is particularly interesting since the GPR based methodology can give complementary information to point measurements, such as those made by *Arthern et al.* (2010), in that it can measure compaction over larger regions with a high vertical resolution, albeit on a longer timescale. The results are discussed in Sect. 5.5 and summarised in Sect. 5.6.

5.1 Deterministic Fourier Deconvolution

Several common processing steps for GPR traces were introduced in Sect. 2.5. While calculating the instantaneous amplitude (envelope) of the received signal (Sect. 2.5.5) does remove some of the oscillating characteristics from GPR traces, the resulting images are usually still strongly influenced by the shape of the source pulse. Deconvolution, the common remedy to this problem in seismics, has been shown to be more difficult for GPR data (e.g. *Turner*, 1994; *Irving and Knight*, 2003). Two key reasons for this difficulty are dispersion of the emitted waveform and its non-minimum-phase character (*Belina et al.*, 2009). The former causes changes in the shape of the radar wave as it travels through the medium, making the task of removing one specific waveform inaccurate. The latter relates to the energy distribution of the waveform emitted by most commercial GPR systems, which has its maximum close to the centre of the time domain pulse rather than being front-loaded like a seismic (shock-)wave. This can lead to non-convergent deconvolution operators. Recently, *Xia et al.* (2004) and *Belina et al.* (2009) successfully tested deconvolution techniques for GPR recordings on low-dispersion soils. Additionally, *Spikes et al.* (2004) used a "spiking deconvolution in RADAN" (S. Arcone, personal communication, 2011) for simplifying firn radar profiles. For the present study a similar method, the deterministic Fourier deconvolution, is developed for analysing internal radar reflections of dry Antarctic snow, which is also a low-dispersion material.

The high-frequency GPR data recorded for this project (see Sect. 2.6) can be assumed to measure a medium which consists of well-defined layers with variable dielectric properties. The succession of snow layers of different density (ρ), and therefore different ε_r' (see Eq. 2.20), can be thought of as a line of spikes similar to delta functions but with a finite and variable amplitude. Each spike represents an interface between two layers and its amplitude is proportional to the magnitude of the dielectric contrast. This is referred to as a reflectivity profile because the GPR signal is partially reflected at each interface as it travels through the medium. The intensity of the reflection depends on the magnitude of the dielectric gradient at the internal layer boundary: stronger gradients cause stronger reflections. Therefore, assuming that changes in density are the only cause of reflections in the considered volume of snow, the reflectivity profile, $r(t)$, is directly related to snow density variations (*Eisen et al.*, 2008) and, ideally, should be recovered from the recorded radargram.

The received radar signal, $s(t)$, can be described as the convolution of an emitted waveform, $e(t)$, with $r(t)$ and a noise term, $n(t)$:

$$s(t) = e(t) \star r(t) \star n(t) \tag{5.1}$$

Taking the Fourier transform (FT) of both sides and using the convolution theorem (Eq. 2.27), Eq. 5.1 can be transformed to:

$$FT(s) = FT(e \star r \star n) = FT(e) \cdot FT(r) \cdot FT(n) \tag{5.2}$$

Thus, if the emitted waveform, $e(t)$, is known, and the noise term, $n(t)$, can be considered negligible, calculating the Fourier transform of the signal, $s(t)$, and dividing[1] it by the Fourier

[1]Note that this division is, in general, a division of complex numbers.

transform of $e(t)$, should result in the Fourier transform of the reflectivity profile:

$$FT(r) = \frac{FT(s)}{FT(e)} \tag{5.3}$$

An inverse Fourier transform can then be used to retrieve $r(t)$:

$$r(t) = IFT\left(\frac{FT(s)}{FT(e)}\right) \tag{5.4}$$

If the source waveform is known and does not change with time (i.e. depth in the medium), this is referred to as deterministic deconvolution (*Yilmaz*, 1987), since it is a well defined mathematical problem that has a single solution. This 'deterministic Fourier deconvolution', detailed in Eq. 5.4, theoretically provides a method for recovering the reflectivity series of the subsurface from a radargram.

An important assumption underlying the idea of deconvolution of GPR data is that the distribution of dielectric contrasts in the ground is random. This assumption is also known as the whiteness hypothesis (*Ulrych*, 1999), because a (successfully) recovered reflectivity profile is expected to have a spectrum that is similar to that of white noise. While the whiteness hypothesis is widely accepted in a geological context, though sometimes modified to a 'blueness hypothesis' (*Walden and Hosken*, 1985; *Ulrych*, 1999), it is not immediately evident that it should also apply to the reflectivity structure of stratified snow. Snow deposited in different weather conditions will have variable permittivity based on the thermodynamic properties of the environment at the time and thus successive layers may be correlated. Nevertheless, the small-scale details of the contrast between these layers are still likely to be random in nature, even if there is some correlation. Hence, the assumption that the spectrum of the output of the deconvolution should be at least whit*er* than the recorded radargram is likely to be true. This can also be used to test whether the deconvolution was successful.

The reason for attempting to use (Fourier) deconvolution for the GPR data is as a mechanism for distinguishing strong reflections from weaker ones that may appear to be continuous initially, but cannot be tracked reliably over longer distances. Due to the resolution limit, only layer-interfaces that have a relatively strong dielectric contrast and reflect the incoming wave in such a way that the signal is significantly stronger than that of any weaker interfaces close by, will be turned into good approximations of a spike or delta function by the deconvolution algorithm. Weaker, mixed signals from several close minor reflectors will probably not be well deconvolved in this process, thereby reducing the number of apparent reflections/layers in the radargram. In order to test whether the deterministic Fourier deconvolution produces valid results, it is applied to simulated GPR data in the next section.

5.2 Fourier Deconvolution of Simulated Data

A finite-difference time-domain (FDTD) model for GPR simulation is used to create artificial radargrams for testing the Fourier deconvolution algorithm. The model is written in

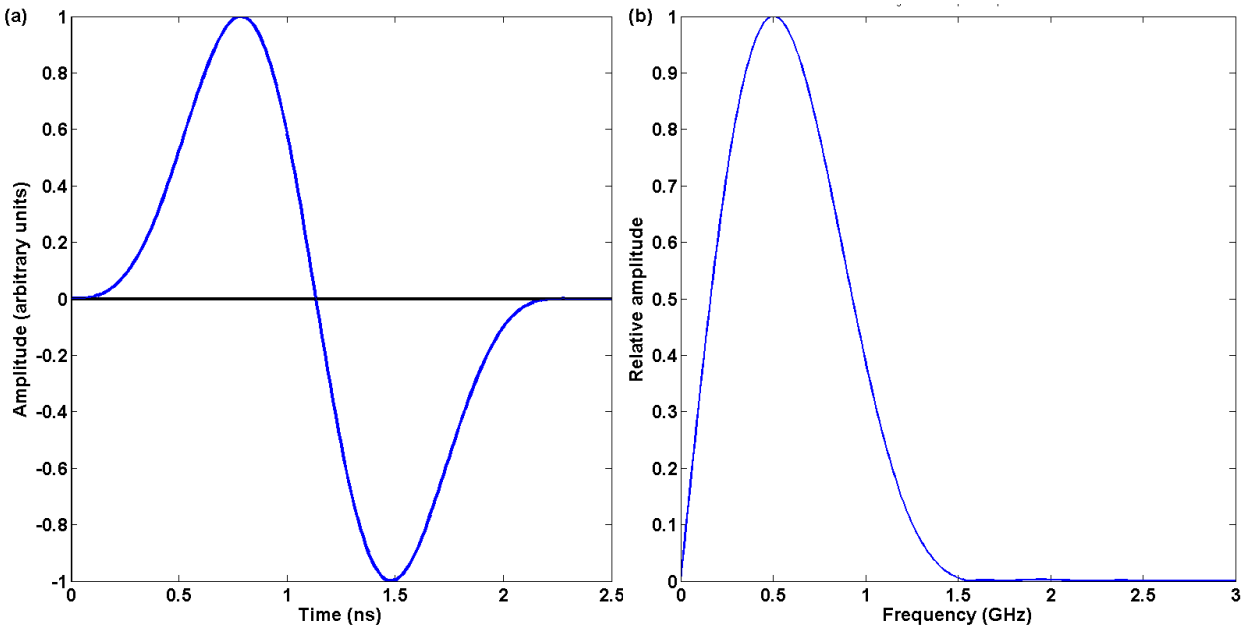

Figure 5.1: (a) The Blackman-Harris pulse used to initialise the E_y-field at the location of the emitter in the radar simulation and (b) the magnitude of its frequency spectrum, centred at 500 *MHz*.

MATLAB™ and is documented in *Irving and Knight* (2006).[2] It has two separate parts, one for simulation of common offset and common midpoint (reflection-)surveys and one for borehole cross-profiles. Only the former is used here. This part of the model uses a transverse magnetic (TM-)mode formulation to simulate a two-dimensional system (along-profile vs. depth)[3], assuming infinite symmetry in the third dimension. It does not include any dispersive terms, so attenuation is frequency-independent and mainly due to spherical spreading of the source pulse. The only exceptions are the grid boundaries. Here, a so-called perfectly matched layer (PML) is used to absorb any incoming waves without causing reflections. For more details see *Irving and Knight* (2006) and references therein.

The input to the model consists of three two-dimensional matrices of dielectric properties. These describe the relative dielectric permittivity, ε_r, the relative magnetic permeability, μ_r, and the conductivity, σ, of the transect to be simulated. Additionally, two vectors, x and z, describe the physical extent of the simulated fields in metres. If the dielectric matrices have a size of 50 by 200 data points, then the x-vector has to be 50 data points long and the value of each point is the horizontal coordinate (along the profile) of the corresponding grid-row in metres. Accordingly, the z-vector has to be 200 points long and describes the depth of each grid-column in metres. Normally, the increments between points are kept constant for both dimensions, but they do not have to be – the grid is recalculated at a higher resolution for the actual simulation. As the air above the ground (which usually contains the emitting antenna) is also part of the grid, the z-vector can have negative values, representing height above the ground.

Finally, a source pulse is required. This is calculated by taking the first derivative of

[2]The code can be downloaded from http://wwwpeople.unil.ch/james.irving/JI_GPR_modeling_codes.zip (last accessed on 24.08.2013).

[3]The three relevant field components are E_y, H_x, and H_z (x = along-profile, z = depth).

a Blackman-Harris window. The resultant Blackman-Harris pulse is used to initialise the E_y-field at the chosen location of the emitter. Figure 5.1a shows the pulse for a centre frequency of 500 *MHz* and Fig. 5.1b its frequency spectrum. While this initial pulse has only one maximum and one minimum, "the resulting pulse that travels through the grid and is recorded at the receiver location(s) roughly resembles a Ricker wavelet" (*Irving and Knight*, 2006) in the sense that it has three extrema, a common shape for a GPR-pulse (see *Irving and Knight* (2006) for more details).

The main cause of reflections in radargrams of dry snow are changes in density (*Eisen et al.*, 2003). In terms of dielectric properties, this means that the main component of interest is the real part of the relative dielectric permittivity, ε_r', and very simple assumptions can be made for the other two parameters. For the whole grid, the relative magnetic permeability is taken to be equal to one ($\mu_r = 1$) and the conductivity only takes on two different values: $\sigma = 0\ \frac{S}{m}$ above the ground and $\sigma = 0.001\ \frac{S}{m}$ below.[4] The values of the dielectric permittivity used are illustrated in Fig. 5.2. These were chosen to resemble real values for dry snow in the top four metres below the surface. A homogeneous volume of snow with $\varepsilon_r \approx \varepsilon_r' = 1.8$ – corresponding to snow with a density of 404 $\frac{kg}{m^3}$ (Eq. 2.20), similar to the average from measurements in a snow pit at L2 – is interrupted by a layer of higher permittivity with $\varepsilon_r = 2.2$ (corresponding to a density of 572 $\frac{kg}{m^3}$) at a depth of 1.74 *m*. This layer is 1.8 *m* thick to ensure that there is no interference between the reflection from the top and the bottom boundary. The bottom of the profile is made up of another layer with an increased permittivity of $\varepsilon_r = 2.0$, corresponding to a density of 490 $\frac{kg}{m^3}$.

In the field, a common offset radargram is created by dragging the radar receiver and transmitter antennae along the surface, keeping their separation constant and taking measurements at regular intervals. Accordingly, the model repeatedly simulates the propagation of the wave – emitted at a certain location – for a given time span, 80 *ns* in this case, each time shifting the position of the transmitter and receiver by 5 *cm*. For this test, an antenna separation of 1 *m* is assumed and the antennae are set to a height of 1.8 *m* above the surface (z = -1.8 *m*).[5] This rather large separation and vertical offset is chosen to avoid interference in the 'direct wave'[6]. The model does not actually simulate any physical antennae. Instead, it uses the source function shown in Fig. 5.1a to drive the E_y-component at the position of the transmitter and simply records the resultant wave-field at the position of the receiver. Effectively, this means that the simulated 'emitter' emits its energy isotropcially and that the 'receiver' can potentially record incoming waves from any direction, similar to unshielded antennae. As the direct wave is generally a complicated mixture of the wave that travels straight from the transmitter to the receiver (which is referred to as the 'air-wave' in the following and which theoretically should be zero for pairs of shielded antennae) and the reflection off the surface of the ground (which is referred to as 'ground-reflection'), it is not

[4]The latter value was used as it is the one assumed in the example-simulation from *Irving and Knight* (2006). For snow a value of $\sigma = 3 \cdot 10^{-5}\ \frac{S}{m}$ might be more appropriate. However this only affects the decay in amplitude with depth and does not make a significant difference in the following.

[5]Note that this is different from the actual setup of the equipment during the field campaign. There, the antenna separation was 0.23 *m* and the transducer-sleds were sitting directly on the ground. While the plastic sleds are about 5 *cm* thick, the distance between the antennae and the ground is somewhat uncertain, since it is not exactly known where inside the transducer boxes the antennae are located. The actual vertical displacement of the antennae probably lies between 10 and 20 *cm*.

[6]This term can be confusing. Here it is used to indicate the first recorded signal in a GPR trace.

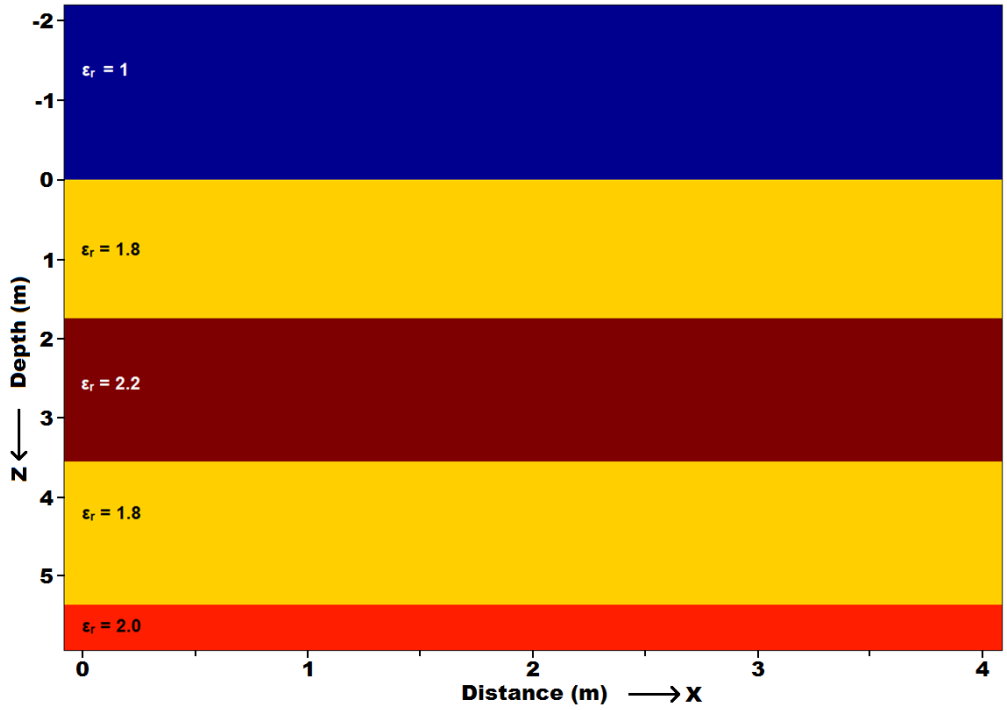

Figure 5.2: Dielectric model used for the simulation. The layer of higher 'snow density' ($\varepsilon_r = 2.2$) starts at a depth of 1.74 m and is 1.8 m thick. The deepest layer ($\varepsilon_r = 2.0$) starts at a depth of 5.35 m.

unusual for the direct wave in real GPR data to look rather different from the subsurface reflections, e.g. it may have a different shape, a different frequency spectrum, and may not be a useful representation of what was actually emitted (*Belina et al.*, 2009). The chosen setup for the simulation ensures that the air-wave and the ground-reflection can be clearly distinguished. The wavelength in air of a 500 MHz wave is 0.6 m, which is less than the antenna separation of 1 m. The 1.8 m distance from the ground ensures that ground-reflection has to travel significantly further than the air-wave (3.74 m for the ground-reflection vs. 1.0 m for the air-wave), and therefore shows up as a distinctly separate reflection in the radargram. The arrival time of the ground-reflection can be used as the zero-point (or timezero) when calculating the depth of internal reflections.

Figure 5.3a shows a simulated trace from the centre of the model grid. Due to the simplicity of the underlying dielectric structure (Fig. 5.2), the radargram merely consists of five horizontal lines and all 60 traces are very similar. Note that the air-wave and the ground-reflection have opposite polarity, due to the 180° phase shift caused by the reflection off the ground. The third and fourth reflection, from the top and the bottom of the internal layer, have opposite polarities. While the simulation time step is 0.0125 ns, only every fourth value is recorded, resulting in a sampling interval of 0.05 ns for the radargram. Figure 5.3b shows the complete radargram of the simulated grid. It is composed of 60 traces with 1600 points per trace. The horizontal position of a trace is usually determined as the half-way point between the antennae. Accordingly, the first trace, with the transmitter at 0 m and the receiver at 1 m, is assigned an x-coordinate of 0.5 m.

From the generated radargram the depth of the higher density layer can be calculated by determining the difference in two-way travel time (TWT) between the ground-reflection

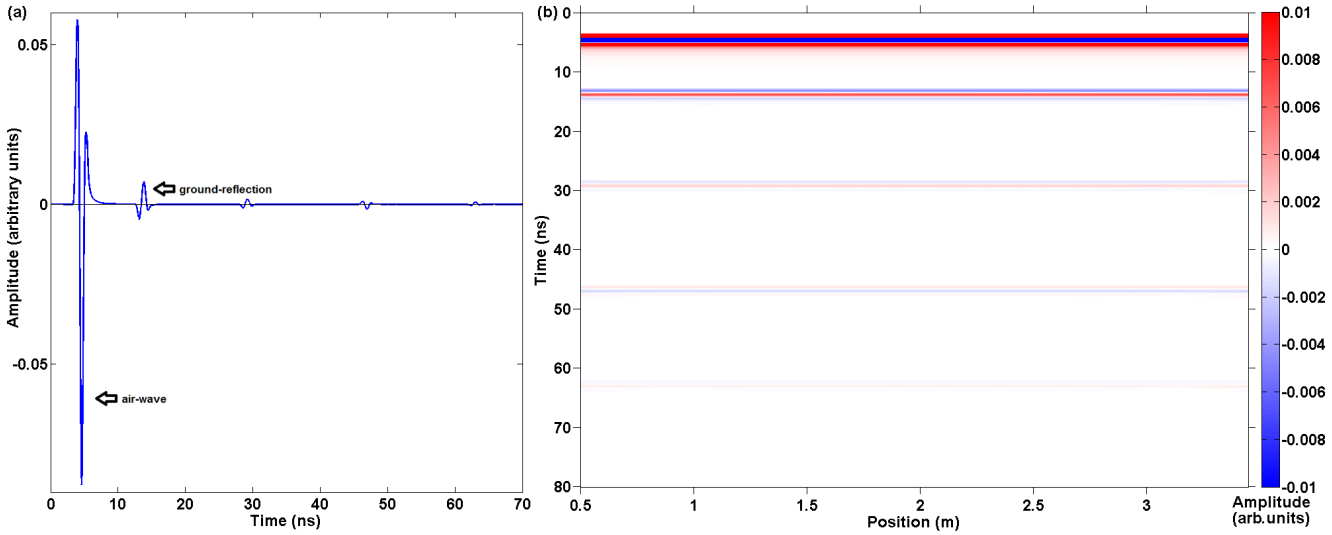

Figure 5.3: (a) A simulated trace from the centre of the simulated grid. The air-wave is the signal that goes straight from the transmitter to the receiver, while the ground-reflection indicates the first indirect signal that is reflected off the air-ground interface (hence the polarity is reversed). (b) Simulated radargram of the model in Fig. 5.2. It consists of 60 equally spaced traces (one trace every 5 *cm*) with 1600 points per trace. The colour scale is truncated to allow the deepest reflection to be (just) visible.

and the first internal reflection and multiplying it by half the speed of light in the medium (the factor $\frac{1}{2}$ is due to the fact that the measured time corresponds to *two-way* travel time, but only '*one-way* distance' is calculated). Similarly, the thickness of the internal layer can be derived from the difference in TWT between the first two internal reflections. Since these differences in TWT can be determined for every single trace, doing so for all traces of the radargram allows some statistics for the depth and thickness estimated of the internal layer to be calculated. In order to avoid ambiguities due to the changes in polarity of different reflections, the location of the peak of the trace envelope is used to determine the TWT between individual reflections. The peak-to-peak difference in TWT is a measure of the distance between the reflection events.

A simple tracking algorithm is used for automating the process of finding the peak of the envelope. The algorithm looks for the overall maximum within a window of a given number of data points. Since the focus of this study is to identify (relatively) horizontal reflection horizons, a limit is set on the number of data points that the location of the maximum can change by from one trace to another. The maximum difference in peak-location is set to 40 data points, which is equivalent to approximately one wavelength of the centre frequency. Thereby, sudden large jumps of the tracking algorithm are avoided. Additionally, the first and last two traces are excluded in the following to avoid potential edge effects when the transmitter or receiver antenna is located at or very close to the edge of the simulated grid.

Figure 5.4 shows the envelope of the radargram in Fig. 5.3b and the tracked maxima of the ground-reflection and the first internal reflection (dashed black lines). In this noise-free, simulated data all the peaks match up perfectly from one trace to the next and the locations of the tracked extrema are perfectly horizontal lines. Subtracting the TWT of the ground-reflection peak from the TWT of the first internal reflection peak results in a TWT difference

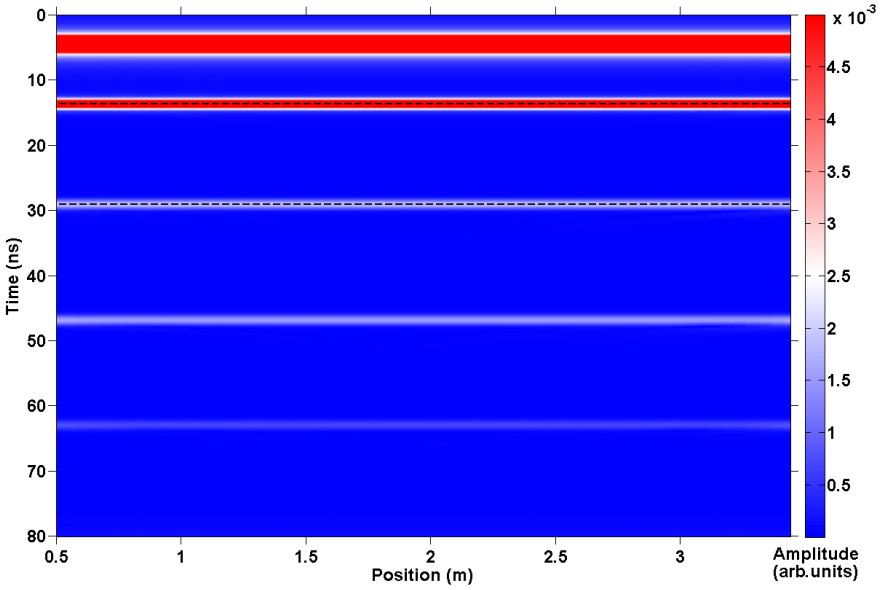

Figure 5.4: Envelope of the radargram in Fig. 5.3b. The two dashed black lines mark the peak locations tracked for layer depth calculation.

of $\Delta TWT = 15.4\,ns$ which is the same everywhere. Given the known value of the dielectric permittivity in the top layer ($\varepsilon_r = 1.8$), the velocity of the radar wave between the two reflections is $v = \frac{c}{\sqrt{\varepsilon_r}} \approx 2.236 \cdot 10^8\,\frac{m}{s}$ (according to Eq. 2.21). Therefore, the depth of the first internal reflection calculated from the radargram is $d = \frac{(v \cdot \Delta TWT)}{2} \approx 1.722\,m$. While this is slightly less than the actual layer depth in the model (1.74 m), the discrepancy (about 2 cm) is small and would clearly be within experimental uncertainties of any realistic measurement. For example, the pulseEKKO PRO system has a theoretical resolution of about 32 cm (see Sect. 5.3), more than one order of magnitude greater than the error from the model data. Nevertheless, the error could potentially be systematic and may be related to inaccuracies when calculating the envelope of the traces. A small phase error in this conversion could shift the maximum of the envelope of a particular reflection by several data points.

Tracing the first two internal reflections in the same manner gives an average TWT of 17.753 ns between the top and the bottom of the 'high-density' layer. Due to the weaker signal the peaks of the reflection envelopes at the bottom of the internal layer do not line up perfectly, but are shifted by one data point in a few cases (see Fig. 5.5a). Using $\varepsilon_r = 2.2$ the TWT is converted to an average layer thickness estimate of 1.795 m with a standard deviation of $0.0011\,m$ (Fig. 5.5b). Like the depth of the internal layer, this estimate is slightly smaller than the real value (1.8 m) but also clearly within any measurement uncertainties.

To test the validity of the Fourier deconvolution approach, the same calculations are performed with data processed accordingly. Before the Fourier deconvolution can be applied, an estimate of the radar wave that travels through the grid is required. It is obtained by averaging over all ground-reflections from the radargram since this waveform should resemble the deeper reflections. Figure 5.6a shows the averaged ground-reflection, illustrating that the actual waveform propagated during simulation really does have a different (three-peaked) shape than the source pulse (Fig. 5.1a). Interestingly, the frequency spectrum of the waveform (Fig. 5.6b) also shows that the peak frequency is relatively high at 606 MHz.

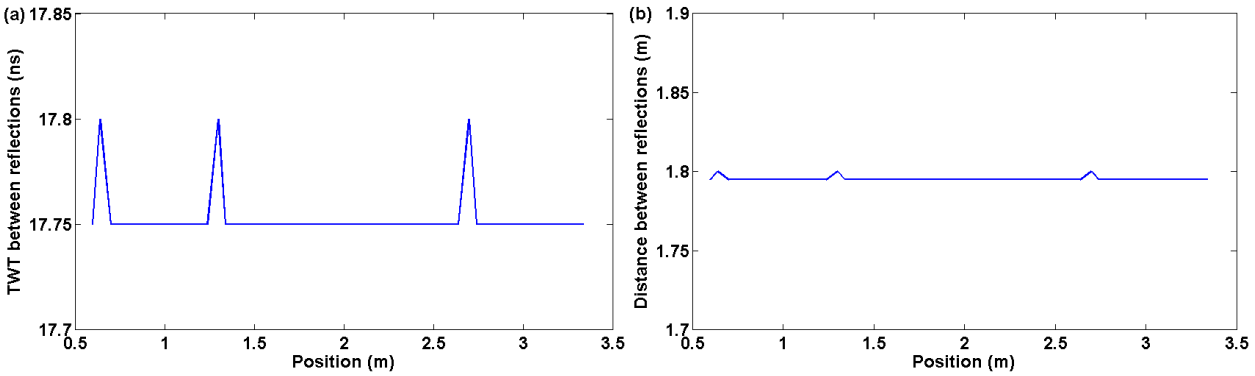

Figure 5.5: (a) The TWT between the top and bottom of the internal layer determined from the envelope of the simulated traces can be converted to (b) an estimate of the layer's thickness by using the known value of $\varepsilon_r = 2.2$.

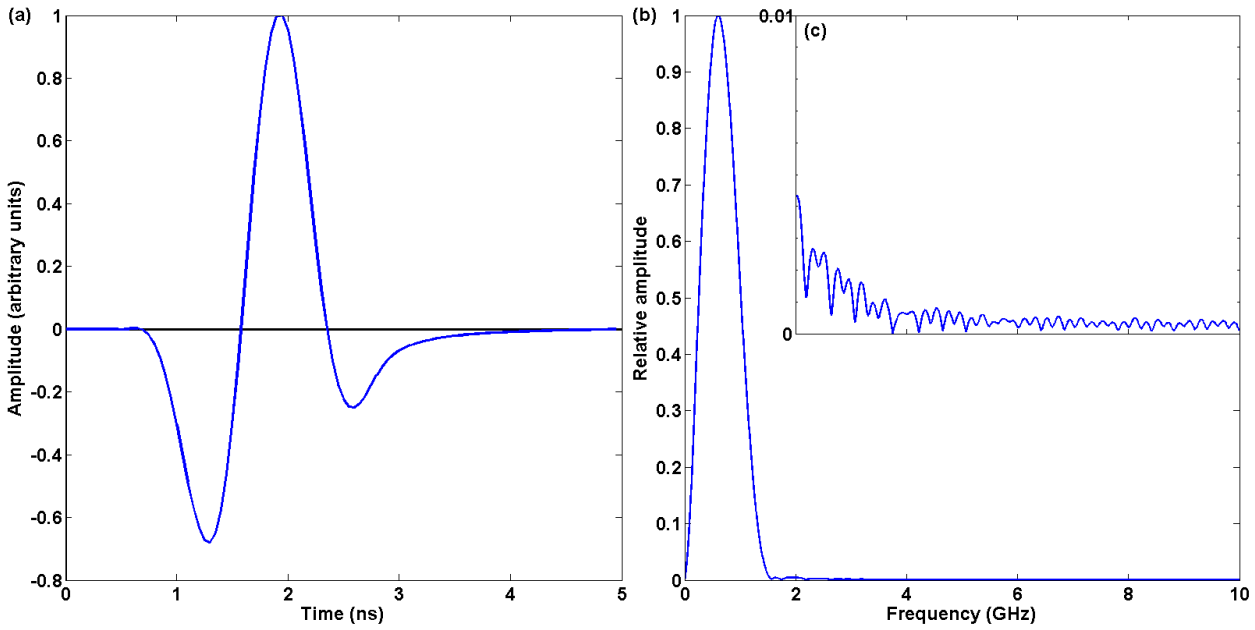

Figure 5.6: (a) The average ground-reflection and (b) its frequency spectrum. The frequency peak is at 606 *MHz*. This waveform is used for the deterministic Fourier deconvolution. (c) is an enlargement of the spectrum in (b) between 2 and 10 *GHz*. The maximum of the vertical scale in (c) corresponds to one hundredth of the peak amplitude in (b).

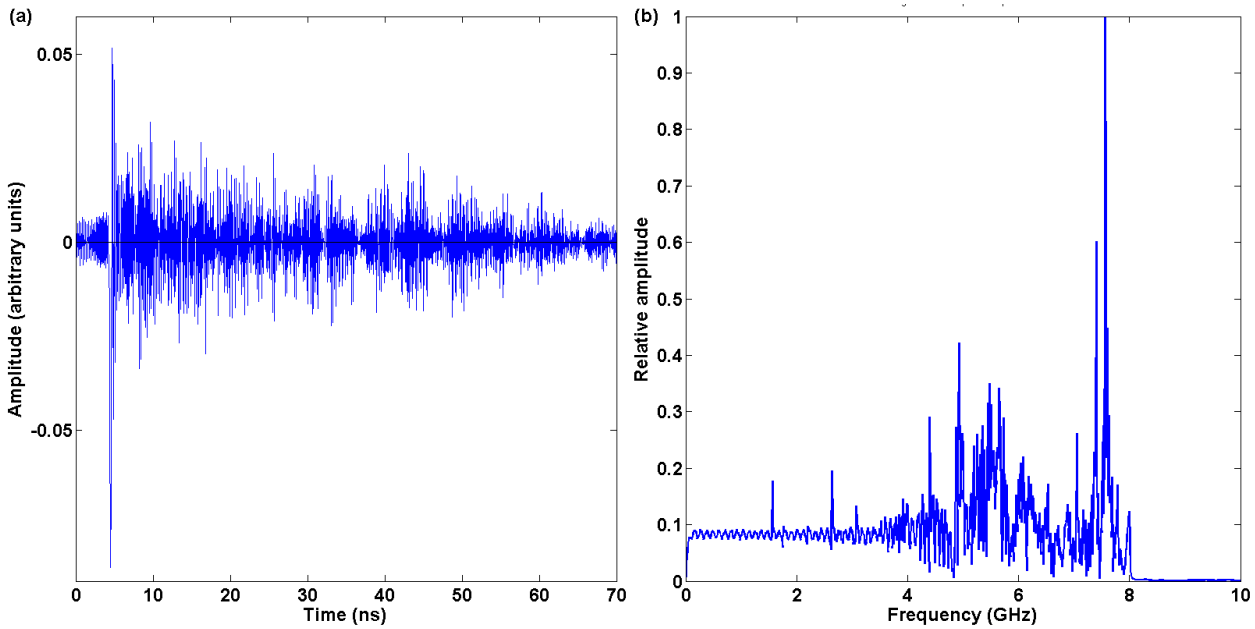

Figure 5.7: (a) The trace from Fig. 5.3a after Fourier deconvolution without low-pass filtering and (b) its frequency spectrum.

Now the deterministic Fourier deconvolution is applied. The spectrum of each trace is divided by the spectrum of the averaged ground-reflection (Fig. 5.6b). Figure 5.7a shows the result of deconvolving the trace in Fig. 5.3a, and its frequency spectrum (Fig. 5.7b). Clearly, the deconvolved trace is dominated by high-frequency noise. The large peaks between 4 and 8 *GHz* (Fig. 5.7b), some of which might be caused by local minima in the spectrum of the averaged ground-reflection (Fig. 5.6c), disguise the actual signal.[7] The amplitudes of these high frequencies should generally be small, particularly in the spectrum of the averaged ground reflection. Dividing this part of the spectrum of each individual trace by the even smaller values in the averaged ground-reflection spectrum (Fig. 5.6c) can lead to relatively large values in the result. Such enhancement of high frequencies is a common problem when attempting to deconvolve GPR data and a low-pass filter can be used to remove these frequencies (e.g. *Xia et al.*, 2004). Another possibility is the so-called pre-whitening: a fixed value – usually several percent of the spectral maximum – is added to all frequencies in the spectrum of the waveform estimate before dividing by it. This process will be used in Sect. 5.3 and combined with low-pass filtering in the frequency domain, but only a simple time-domain filter is used here.

Applying a 127 point windowed-sinc filter with a cut-off frequency[8] of 1100 *MHz*, gives a less noisy picture and five peaks can be identified similar to the original trace (see Fig. 5.8a). The spectrum of the trace has also been whitened (Fig. 5.8b), meaning that the spectrum is no longer dominated by a particular peak frequency, but that most frequencies, which have

[7]The reason for the sudden drop-off at frequencies above 8 *GHz* is uncertain. It is probably related to the internal workings of the simulation model, since the simulation time-step used ($0.00125\,ns$) theoretically allows much higher frequencies to be resolved and setting an even smaller time-step gives the same result (not shown). However, these frequencies are not very important here and can be ignored.

[8]In this case the cut-off frequency refers to the frequency at which the spectral amplitude is damped to half of its original value. The damping increases toward higher frequencies until 1500 *MHz*, above which all frequencies are fully suppressed.

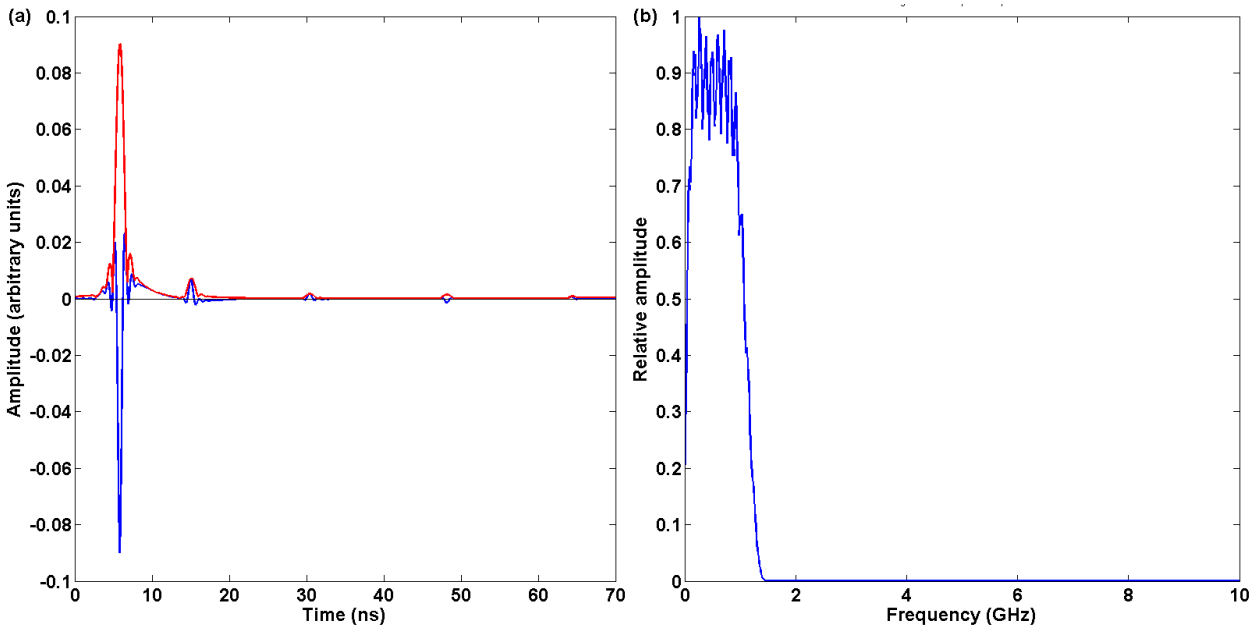

Figure 5.8: (a) The trace from Fig. 5.3a after Fourier deconvolution and 1100 *MHz* low-pass filtering (blue), and its envelope (red). The deconvolution and time-domain filtering has shifted the trace 1.4 *ns* toward higher TWT. (b) The whitened spectrum of the deconvolved trace.

not been filtered out by the low-pass, have a similar relative amplitude. This is the effect of deconvolution: as both the recorded trace and the source-pulse tend to have a spectral peak near the centre frequency of the system, dividing the former by the latter tends to remove the dominating spectral peak. Accordingly, the spectrum becomes 'flatter', i.e. whiter (white noise has a perfectly flat spectrum). Compared to Fig. 5.3a the location of the peaks has shifted by 1.4 *ns* toward higher TWT in Fig. 5.8a. This is the combined effect of the deconvolution shifting the trace by -1.75 *ns* (to lower TWT)[9] and the convolution with the time-domain frequency filter causing a +3.15 *ns* shift (to higher TWT). The former corresponds to the time between the start and the peak of the waveform used for deconvolution (Fig. 5.6a), while the latter is equal to half of the length of the time-domain filter. Since only differences in TWT are required for estimating the depth and thickness of the internal layer, this shift is not corrected for in the present example. As before, the envelope of the deconvolved trace is used (red line in Fig. 5.8a) for reflection tracking.

The full deconvolved profile with a 1100 *MHz* low-pass applied is shown in Fig. 5.9, together with the tracked peaks of the first and second internal reflection (dashed black lines), corresponding to the top and bottom boundary of the internal layer. The layer depth calculated from the deconvolved traces is 1.716 *m* (Fig. 5.10a), in close agreement with the result from the raw data (1.722 *m*) and the actual value (1.74 *m*). The average layer thickness estimate from the deconvolved shots is 1.795 *m* with a standard deviation of 0.0011 *m* (Fig. 5.11b), which is identical to the value previously determined from the envelope of the raw

[9]The negative sign of this shift is as expected: the aim of the deconvolution is to undo the effects of the convolution of the emitted waveform with the reflectivity profile of the subsurface. If the convolution were performed in the time-domain, the locations of the peaks in the reflectivity profile would shift 'to higher TWT' by half of the width of the emitted waveform (assuming it is symmetric). The deconvolution undoes this process, resulting in a shift to lower TWT.

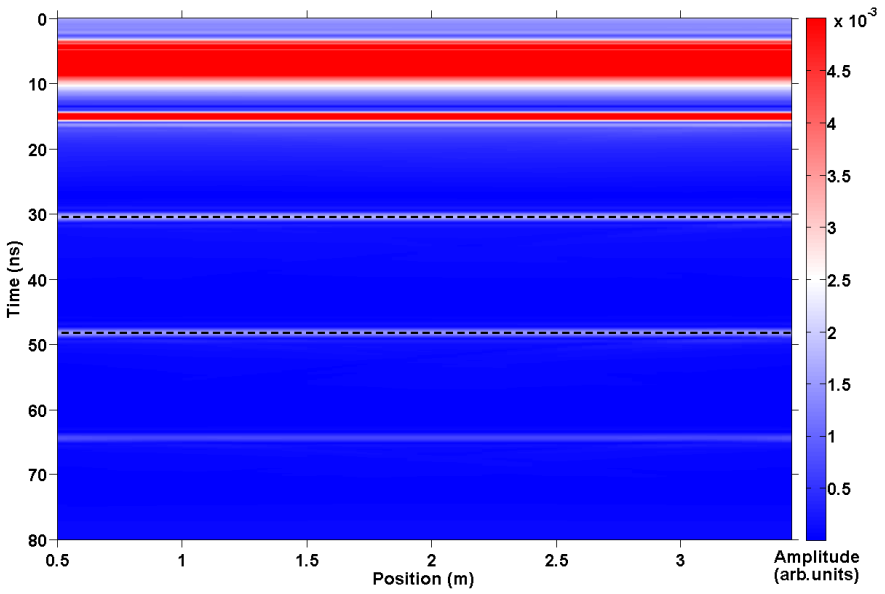

Figure 5.9: The envelope of the deconvolved radargram from Fig. 5.3b. The dashed black lines are the tracked first (top) and second (bottom) internal reflection peaks, corresponding to the top and bottom boundary of the internal layer.

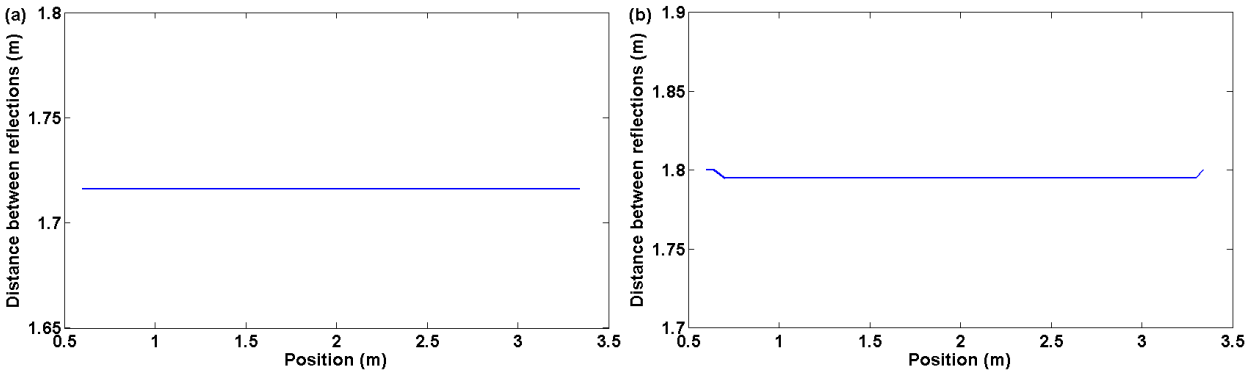

Figure 5.10: (a) The layer depth derived from the Fourier deconvolved traces. The value of 1.716 m is close to the value from the raw data. (b) Layer thickness determined from the deconvolved traces. The average is 1.795 m.

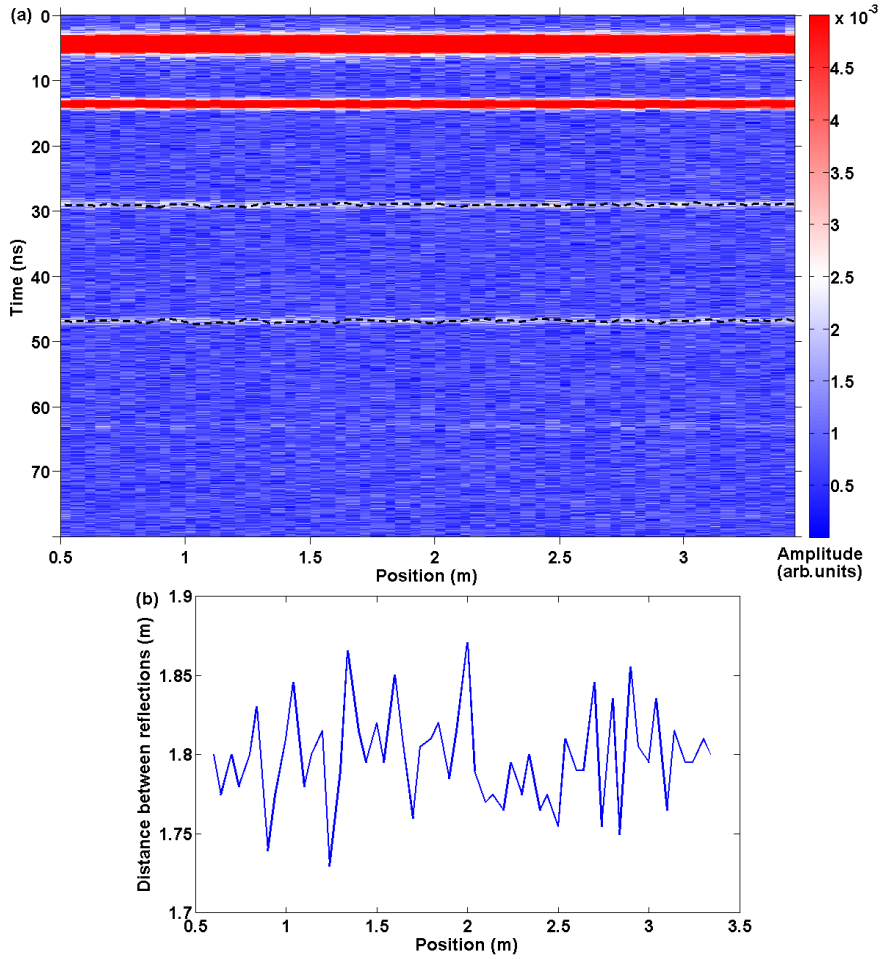

Figure 5.11: (a) Envelope of the simulated radargram with noise of a maximum amplitude of 14% of the ground-reflection amplitude added. The dashed black lines indicate the top and bottom reflection from the internal layer. (b) Thickness estimate of the internal layer tracked in the noisy radargram. The average is 1.798 m, with a standard deviation of 0.305 m.

data (actual layer thickness: 1.8 m).

Clearly, the results in Fig. 5.9 are highly idealised. To test the reliability of the Fourier deconvolution results in the presence of noise, random noise is added to the raw data and the calculations of layer depth and thickness are repeated, both for the noisy raw data and the deconvolved traces. The standard deviation of these values is considered a measure of the reliability of reconstructed distances. The added noise consists of random numbers between $\pm 14\%$ of the amplitude of the positive peak in the ground reflection.[10] Figure 5.11a shows the envelope of the radargram with added noise and the tracked reflections for the thickness calculations. The depth of the internal layer is estimated as 1.719 m from the noisy raw data, with a standard deviation of 0.0224 m (not shown). The average thickness of the layer is determined as 1.798 m, with a standard deviation of 0.305 m (Fig. 5.11b). From the deconvolved radargram (Fig. 5.12a) the estimated depth is 1.716 m, with a standard deviation of 0.0222 m (not shown), and the average layer thickness is determined as 1.795

[10]The amplitude of the added noise was selected in such a way to ensure considerable distortion of the simulated traces without making the subsurface reflections indistinguishable from the noise.

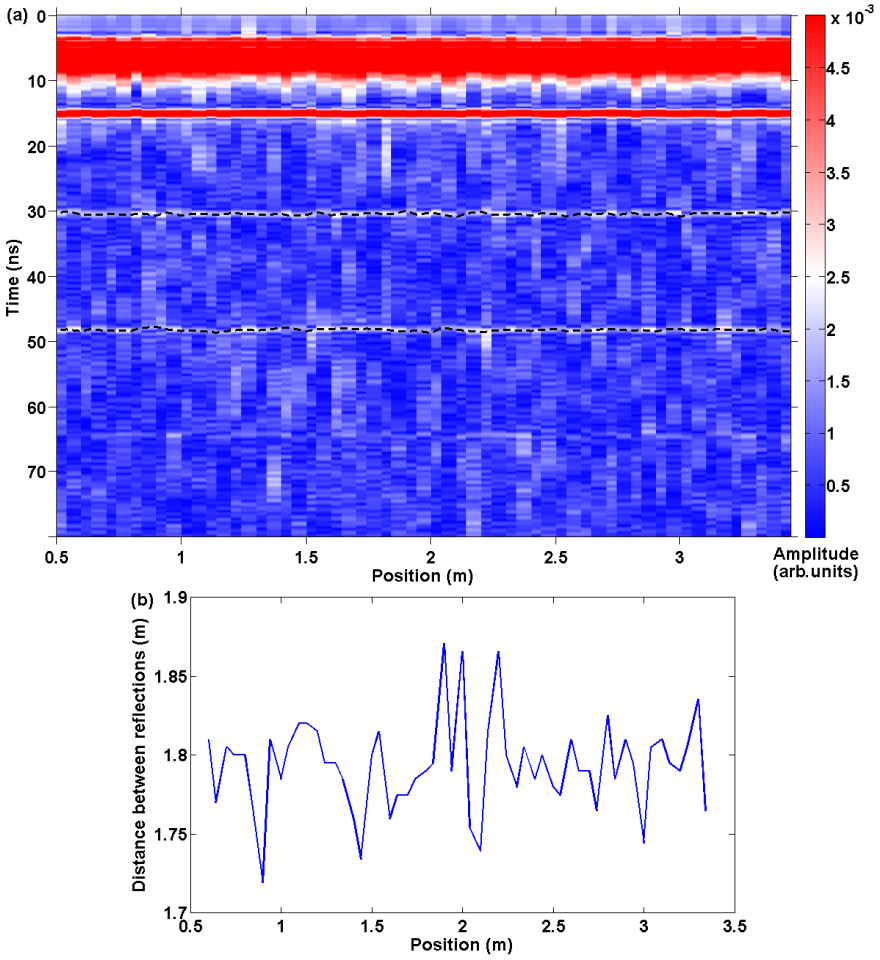

Figure 5.12: (a) Same as Fig. 5.11a but for the Fourier deconvolved traces. (b) Thickness estimates from the tracked peaks in the deconvolved radargram. The average is 1.795 m, with a standard deviation of 0.293 m.

m, with a standard deviation of 0.293 m (Fig. 5.12b). Even after adding noise to the simulated data, all these distance estimates are very close to each other and are good approximations of the actual values. Additionally, the variability of the thickness estimates is on the order of the wavelength of the simulated signal and even decreases slightly after deconvolution, though this reduction is rather small and could be coincidental.

All in all, the results above demonstrate that the deterministic Fourier deconvolution algorithm does not alter the data in any unwanted fashion and can be considered a valid processing approach. Therefore it is applied to actual GPR soundings from Antarctica in the next section.

5.3 Fourier Deconvolution of Antarctic GPR Data

Before the deterministic Fourier deconvolution can be applied to the Antarctic GPR recordings, the data has to be dewowed with the EKKO_View Deluxe software to correct for system-specific artefacts (see Sect. 2.5.1). Additionally, a linear gain is applied in order to compensate for the power loss due to the spherical spreading of the radar wave. The gained amplitude, A_g, is calculated according to:

$$A_g(Z) = \begin{cases} A_i & for\ 1 \leq Z \leq 120 \\ A_i \cdot (0.02 \cdot Z - 1.4) & for\ Z > 120 \end{cases} \tag{5.5}$$

where A_i is the recorded (initial) amplitude and Z is the data point number along the trace. The gain does not come into effect until the 120^{th} data point. This is to avoid gaining the very first reflection and air-wave, since these are already strong signals compared to the internal reflections and there is no need to increase their amplitudes any further. The additional gain per data point is related to an approximate velocity of the radar wave in snow of $0.2\,\frac{m}{ns}$. With a sampling interval of $0.1\,ns$, the wave travels approximately $0.2\,\frac{m}{ns} \cdot 0.1\,ns = 0.02\,m$ between each data point. The spherical spreading loss is proportional to this travelled distance and therefore increasing the gain by 0.02 for each point compensates for this loss. Figure 5.14a shows a 200 m long GPR profile after applying these corrections. The 500 MHz profile was recorded in 2008 between the stakes C2 and C4 at site L2 in Windless Bight (see Fig. 2.15), using a sampling interval of 0.1 ns, a 135 ns time window, and an inter-trace-interval of 5 cm.

In order to successfully use Eq. 5.4 for recovering the reflectivity profile, $r(t)$, a good estimate of the emitted waveform, $e(t)$, is required. This step can be difficult when using commercial GPR systems, since most manufacturers do not provide a detailed description of either the emitted waveform itself, or the antenna characteristics required to calculate a reasonable approximation thereof. Hence, the emitted waveform was measured by holding the transmitting and receiving antennae above the ground, directly facing each other. To avoid interference between the air-wave and the ground-reflection, the transmitter and receiver were placed 2.3 metres above the surface and 3 metres apart. Note that this geometry is somewhat similar to the setup in the simulation model (Sect. 5.2).

Figure 5.13a shows the returned signal as a function of time for 100 superimposed shots. Two distinct returns are observed, the air-wave that travels directly from the transmitter

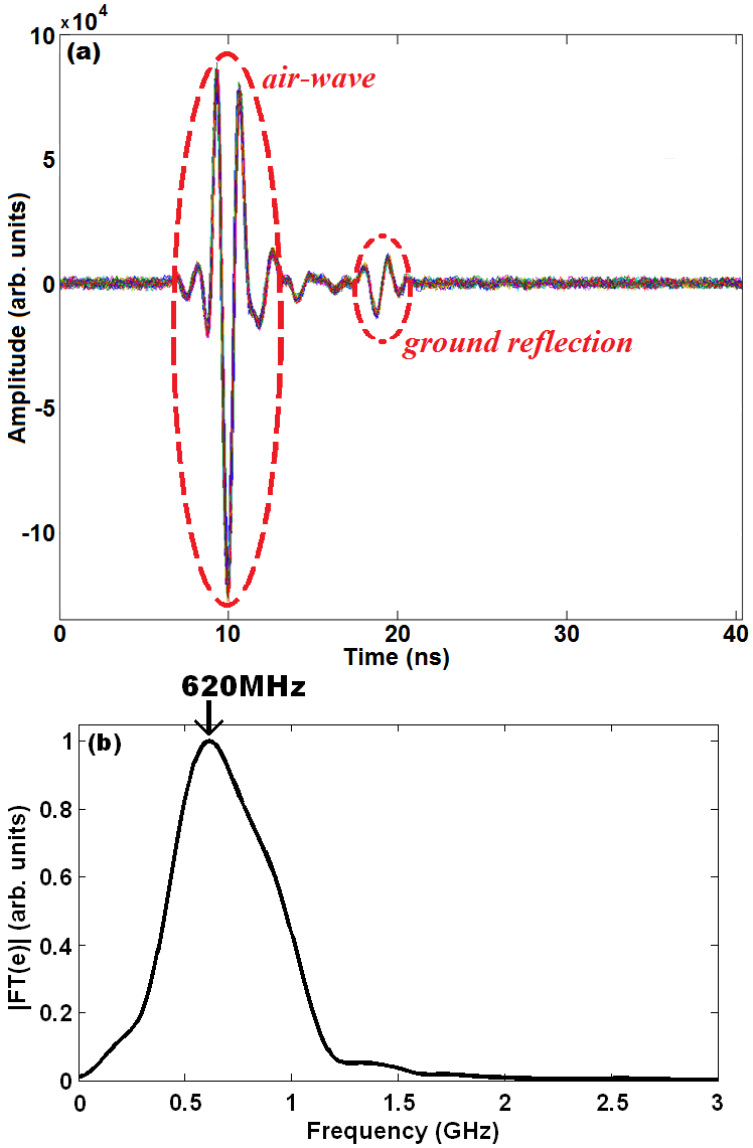

Figure 5.13: (a) One hundred superimposed shots recorded with facing antennae. The air-wave and the ground reflection can be clearly distinguished. (b) The amplitude spectrum of the averaged air-wave shows the centre frequency to be around 620 *MHz*. The bandwidth of the signal, estimated from the width of the peak at 0.707 times the peak amplitude, is $\Delta f \approx 330$ *MHz*.

to the receiver, and the ground-reflection.[11] The small variation between shots displayed in Fig. 5.13a illustrates that the pulse emitted by the system is transmitted at a consistent phase and can be assumed to have the same form from one shot to another. An integrated version of the air-wave is used as an estimate of the emitted waveform for the deconvolution process. The frequency spectrum of the averaged trace, Fig. 5.13b, shows that the centre frequency of the pulse lies close to 620 *MHz*. Before performing the division in Eq. 5.3, the spectrum of the emitted wave is whitened by ten percent of the spectral peak in order to avoid over-amplification of frequencies of small amplitude (*Yilmaz*, 1987).

An overview of the processing steps and the order in which they are applied is given in the following list:

1. Dewow – a DC-correction to remove a localised offset caused by receiver saturation (*Sensors and Software Inc.*, 2006).
2. Linear Gain – compensates for the loss of signal power due to the spherical spreading of the wave as it propagates through the medium (Eq. 5.5).
3. Fourier deconvolution – removes the effects of the carrier wave (Eq. 5.4).
4. Low-pass filter – applied in the frequency domain with a 1550 MHz cut-off based on the spectrum of the emitted wave.
5. Background subtraction – to remove interference due to ringing. This distorts the radargram in the first 6 to 8 *ns* which are therefore not analysed.
6. Envelope calculation using the Hilbert transform.
7. Integration (horizontal stacking) – used to improve the signal-to-noise ratio.

Step (7) also allows a matching-up of the horizontal sampling intervals of the data from the two seasons. After ten-fold stacking of the data from 2008 and seven-fold stacking of the data from 2009, the horizontal sampling of both data sets reduces to approximately $0.5\,m$. Also, as the emitted waveform is not minimum-phase, the deconvolved data is offset by -1.8 *ns* (upwards). This corresponds to the time from the start of the waveform used for deconvolution to its peak amplitude (*Yilmaz*, 1987). Accordingly, the timezero for all data is adjusted by this amount after step (3).

Figure 5.14 illustrates the benefits of the Fourier deconvolution scheme for a representative 200 *m* long radar profile from the L2 site. The simple application of dewow and gain in Fig. 5.14a shows that the carrier wave is still present in the data. After applying all processing steps except deconvolution, a reduced number of distinct reflections can be clearly identified in Fig. 5.14b. Including the deconvolution step (Fig. 5.14c) significantly sharpens these horizons. Comparison of the different panels in Fig. 5.14 shows that the deterministic Fourier deconvolution results in a more focused radargram.

A more stringent test of the quality of the deconvolution processing methodology is to analyse both the autocorrelation and the frequency spectrum of traces before and after

[11] With the given the geometry the ground-reflection has to travel approximately 2.5 metres further than the air-wave, which allows for a clear separation of the two in Fig. 5.13a.

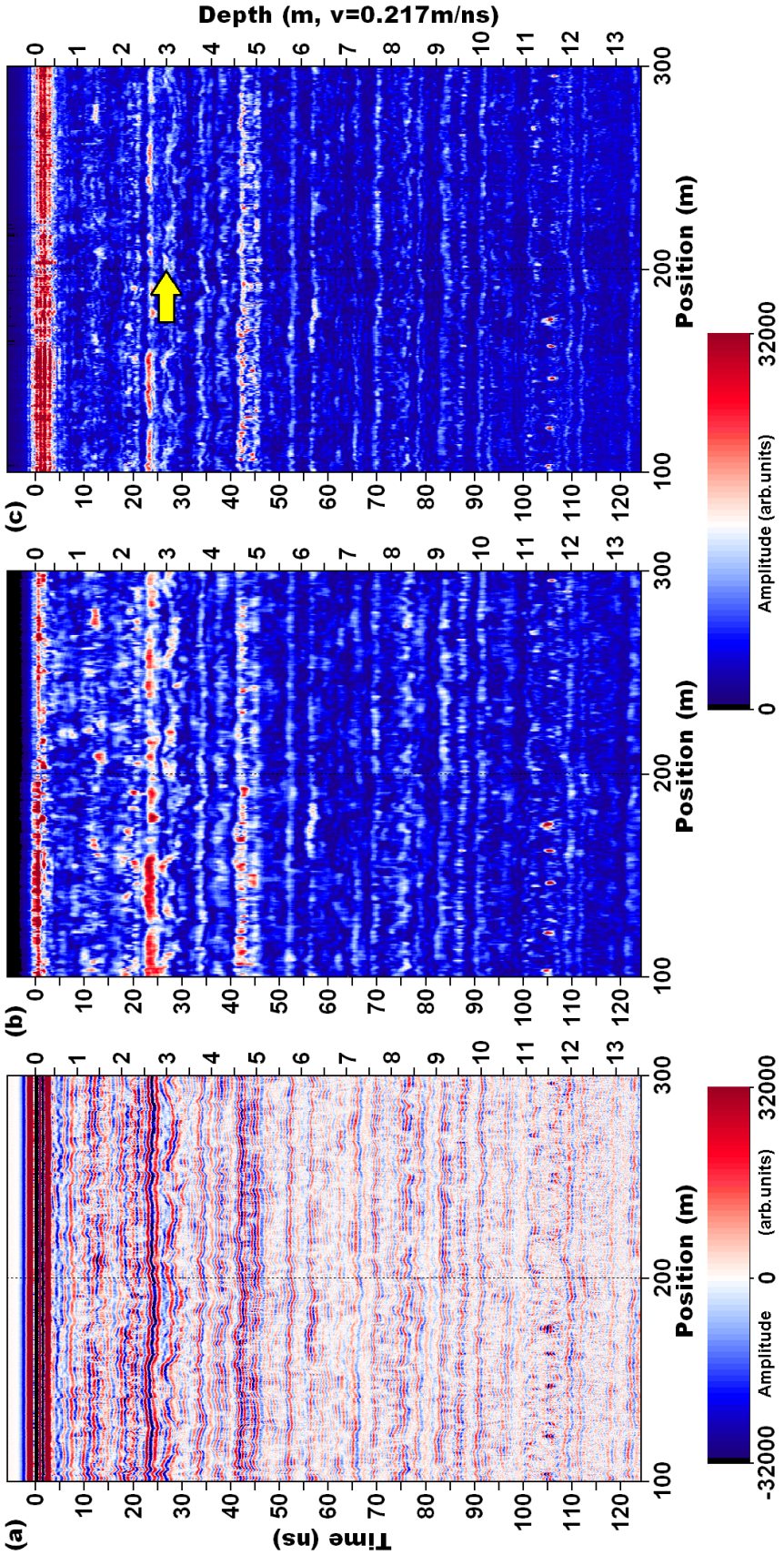

Figure 5.14: Radar profile at L2 between the stakes C2 and C4 (2008) after applying (a) dewow and gain filters, (b) the full processing excluding- and (c) including deconvolution. The yellow arrow in (c) indicates the depth and location of the dust layer identified in the snow pit. Representing 200 m in the horizontal direction and about 13 m vertically, the vertical exaggeration is approximately 22:1.

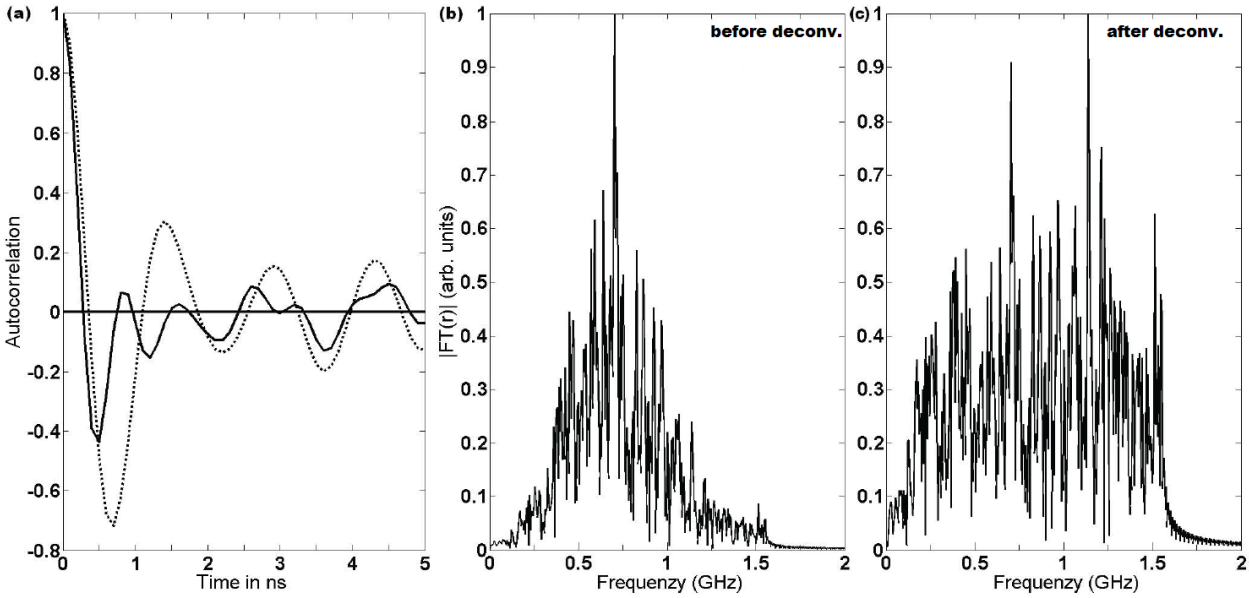

Figure 5.15: (a) ACF of a radar trace at L2 before (dotted line) and after deconvolution (solid line). (b) Amplitude spectrum of the same trace before deconvolution and (c) afterwards. The spectra are normalised to a maximum value of one.

processing. Effective deconvolution should whiten the spectrum, reduce the characteristic correlation duration and flatten the tail of the autocorrelation function (ACF) of a radar trace (*Ulrych*, 1999). Figure 5.15a shows the ACF of a trace before (dotted line) and after (solid line) deconvolution – there is a decrease in autocorrelation time after deconvolution (first minimum is shifted from 0.7 *ns* to 0.5 *ns)* and a flattened tail. As expected, the spectrum of the same trace (Fig. 5.15b) is also clearly whitened after deconvolution (Fig. 5.15c). Note that the ACFs and the spectra in Fig. 5.15 were computed from a truncated version of the trace that does not include the first 8 *ns* for reasons mentioned above.

While the main aim of using Fourier deconvolution is to remove the effect of the carrier signal from the GPR data, it is more commonly used for achieving an improvement in the resolution of the radargram by narrowing the individual reflection peaks (e.g. *Yilmaz*, 2001; *Xia et al.*, 2004; *Belina et al.*, 2009). An example of a reflection and its envelope before (blue) and after (red) deconvolution is given in Fig. 5.16. The narrowing of the peak is clearly visible in the envelope. However, the examination of an individual reflection is quite selective and the direct comparison of the processed data in Fig. 5.14 illustrates the achievements of the Fourier deconvolution more conclusively. The improved clarity of layers in Fig. 5.14c compared to Fig. 5.14a is not merely due to the standard processing steps (low-pass filtering, background subtraction, stacking, and envelope calculation) since these have also been applied in Fig. 5.14b. Distinct layers that are visible in both Fig. 5.14b and c are narrower after deconvolution and the whole image in Fig. 5.14c appears more in focus than Fig. 5.14b. For example, at the lower end of the profile, between about 12 and 12.5 *m* depth, two layers can be clearly distinguished in Fig. 5.14c, while they are difficult to distinguish or even identify at all in Fig. 5.14b.

A particularly important assumption of the Fourier deconvolution is that the emitted waveform is well known and does not change significantly with depth and from one trace to

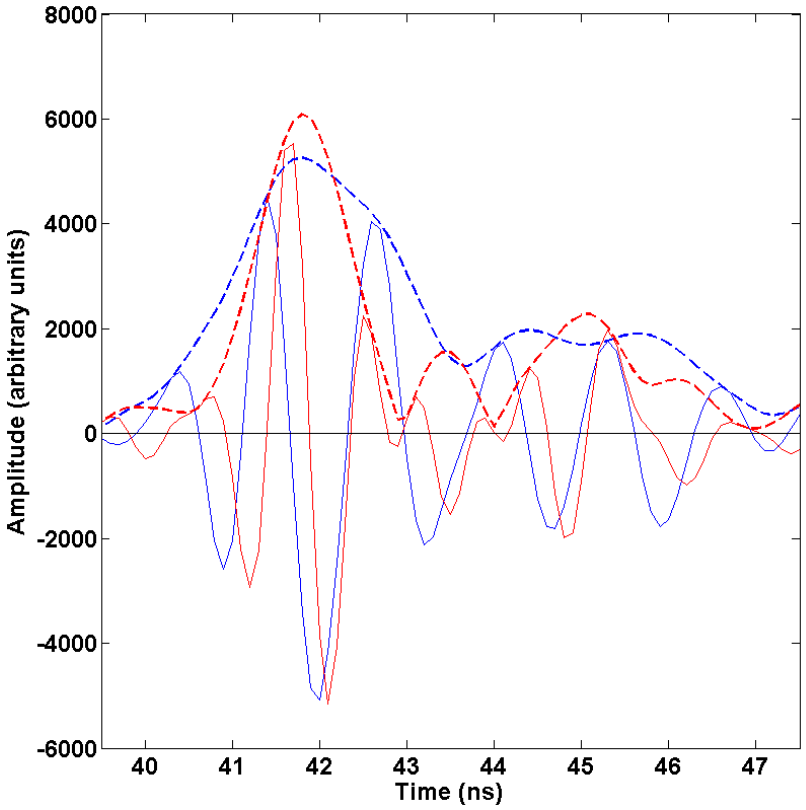

Figure 5.16: Example of an internal reflection and its envelope before (blue) and after (red) deconvolution from a trace at L2 in 2008.

the next. Common causes for changes in the waveform are frequency-dependent attenuation and ground loading. The former tends to reduce the effective centre frequency of the radar pulse as it travels through the medium because higher frequencies are attenuated faster than lower frequencies, while ground loading reduces the effective centre frequency of the emitted waveform when the antennae are placed close to or on the ground. Both effects are very small in dry snow due to its low conductivity, but can become more important in the percolation zone. Figure 5.17a shows a distinct reflection found at around 13 m depth at L2. The apparent centre frequency of this deep reflection is 642 MHz (Fig. 5.17b), which is even slightly higher than the centre frequency measured in air (620 MHz), though this increase is of course relatively small ($\approx 3.5\%$) and within measurement uncertainties (the noise level at this depth is relatively high). As with Fig. 5.16, this represents a rather selective consideration. However, since there is no mechanism that can increase the centre frequency of a radar pulse relative to its free-space value, the presence of even just one deep reflection with such a high apparent centre frequency illustrates that there is at least no measurable systematic reduction of the centre frequency due to ground loading or attenuation. Accordingly, the assumption that the emitted waveform does not change considerably as it travels through the medium is likely to be valid.

The processing detailed above can be used to identify and track internal reflections in GPR profiles of snow. The tracking was performed using the KINGDOM Suite 8.2 software. From a starting point somewhere within the radargram (determined by the user), the program follows the reflection peak from trace to trace. The vertical guide window within which

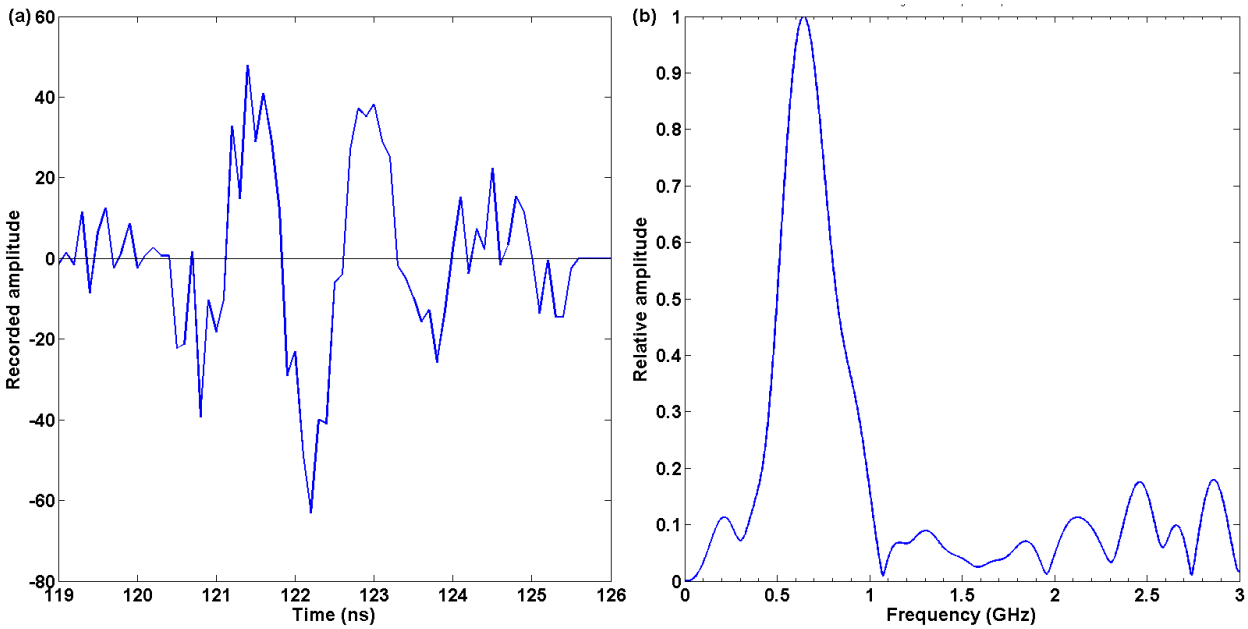

Figure 5.17: (a) A distinct reflection found at around 13 m depth near stake C1 of L2 in 2008. Its frequency spectrum (b) has a peak at 642 MHz.

the algorithm searches for the amplitude maximum was set to 2 ns. This corresponds to approximately 0.2 m, which is close to the estimated resolution limit. If a reflection is weak or distorted in some part of the profile the selection is corrected manually.

The tracked internal reflection horizons are used for extrapolating accumulation measurements from snow pits and firn cores to larger areas and for deriving compaction rates as a function of depth, d, at the sites L2 and L3. In order to analyse the GPR profiles it is necessary to establish a time-depth relationship. With the density information from snow pits and firn cores, ε_r' is estimated via Eq. 2.20 and the velocity of the radar signal in snow is calculated with Eq. 2.21. Using this analysis, the TWT from a radargram can be converted to depth and vice versa, allowing accumulation estimates to be derived from the GPR data if individual horizons can be dated.

5.4 Accumulation and Compaction

5.4.1 Accumulation Estimates from Stake Farms, Snow Pits, and Firn Cores

Stake farm and firn core measurements provide independent sources of accumulation data which are summarised in Table 5.1. The stake farms at L2 and L3 were installed in November 2008 and revisited in November 2009. Recordings of the stake heights above the snow in both years allow the measurement of one year of accumulation in these areas using the conversion detailed in *Takahashi and Kameda* (2007) (see also Sect. 2.6.1). Taking the mean and standard deviation of the snow depths at the 81 stakes from L2 gives an average reduction in stake height of $60.2 \pm 8.1 cm$ or, using the snow densities recorded in a snow pit, $224 \pm 21 \frac{kg}{m^2 a}$. At L3, only 25 stakes were installed. The measurement from one stake was omitted because

of an error in the height recording. The average decrease in stake height measured at the remaining 24 stakes was $70.1 \pm 11.1\,cm$, equivalent to $304 \pm 83\,\frac{kg}{m^2a}$ of accumulation.

A previously identified dust layer (*Dunbar et al.*, 2009) originating from a severe storm (with maximum southerly wind speeds exceeding 55 $\frac{m}{s}$) that occurred on 16^{th} May 2004 (*Xiao et al.*, 2008) served as a reference point for dating. In 2008, the dust layer was found at a depth of $2.93\,m$ in a snow pit near stake C3 at L2 (Fig. 2.16b). Using the dust layer for dating, an average annual accumulation of 251 $\frac{kg}{m^2a}$ can be derived. In 2009, it was not possible to clearly identify the dust layer in a snow pit. However, a firn core was drilled one metre east (grid-east that is – in the following, all directions are relative to grid-north/east, unless stated otherwise) of the stake G7, to a depth of $8.46\,m$. Figure 5.18a shows the density profile of the firn core and some of the snow pit data from 2009. Approximately at the depth at which the dust layer was expected, the core contained an unusually coarse grained low-density layer (starting at $3.42\,m$). A similar low-density layer was found just below the dust layer in the previous year, which could be a depth hoar layer that formed either as surface hoar prior to the storm or underneath the wind crust afterwards. Considering this as a marker for the storm in May 2004 gives an accumulation rate of 245 $\frac{kg}{m^2a}$.

At L3, no particularly distinct features could be found in a two metre snow pit in either year. Slight changes in snow grain size and hardness at about one metre depth are indicative of the previous year's summer layer, but it was not possible to determine this with any certainty. Generally, the snow at L3 was found to be very homogeneous, with a slightly higher average density than at L2. In 2009, a firn core was drilled down to about $7.5\,m$ near stake C3 at L3. The resulting density profile is shown in Fig. 5.18b. At $5.3\,m$ depth a dust layer was identified similar to the one found at L2 in the previous year. Assuming that this is also associated with the May 2004 storm yields an average accumulation of 437 $\frac{kg}{m^2a}$. This value is considerably higher than the one measured by the stake farm and could either indicate an error in the dating of the dust layer, or a high inter-annual variability in snow accumulation in this area.

The firn core data can also be used to determine a depth-density relationship for the two sites as a reference for converting the vertical scale of the radargrams to depth. Following *Alley et al.* (1982), an empirical depth(d)-density(ρ) relationship is determined for each site by fitting an exponential model of the form:

$$\rho(d) = \rho_i - a \cdot e^{-c \cdot d} \tag{5.6}$$

to the firn core data, where $\rho_i = 917\,\frac{kg}{m^3}$ is the density of ice, and a and c are the constants to be fitted. For the upper $0.6\,m$ at L2, where the snow was loose and density difficult to measure by coring, snow pit data were used for obtaining the fitted depth-density curve (Fig. 5.18a). The core at L3 was drilled two weeks after the snow pit had been recorded as weather conditions prevented earlier attempts to return to the site. The core was started at the previous surface level by removing the fresh snow. However, the additional overburden will have caused some densification below. Therefore, the top $1.9\,m$ of the firn core were replaced by snow pit data when determining the depth-density relationship (Fig. 5.18b). The resulting equations for L2 and L3 are shown in Figs. 5.18a and b, respectively. As the radar profiles extend below the maximum depth of the firn cores, the same equations are

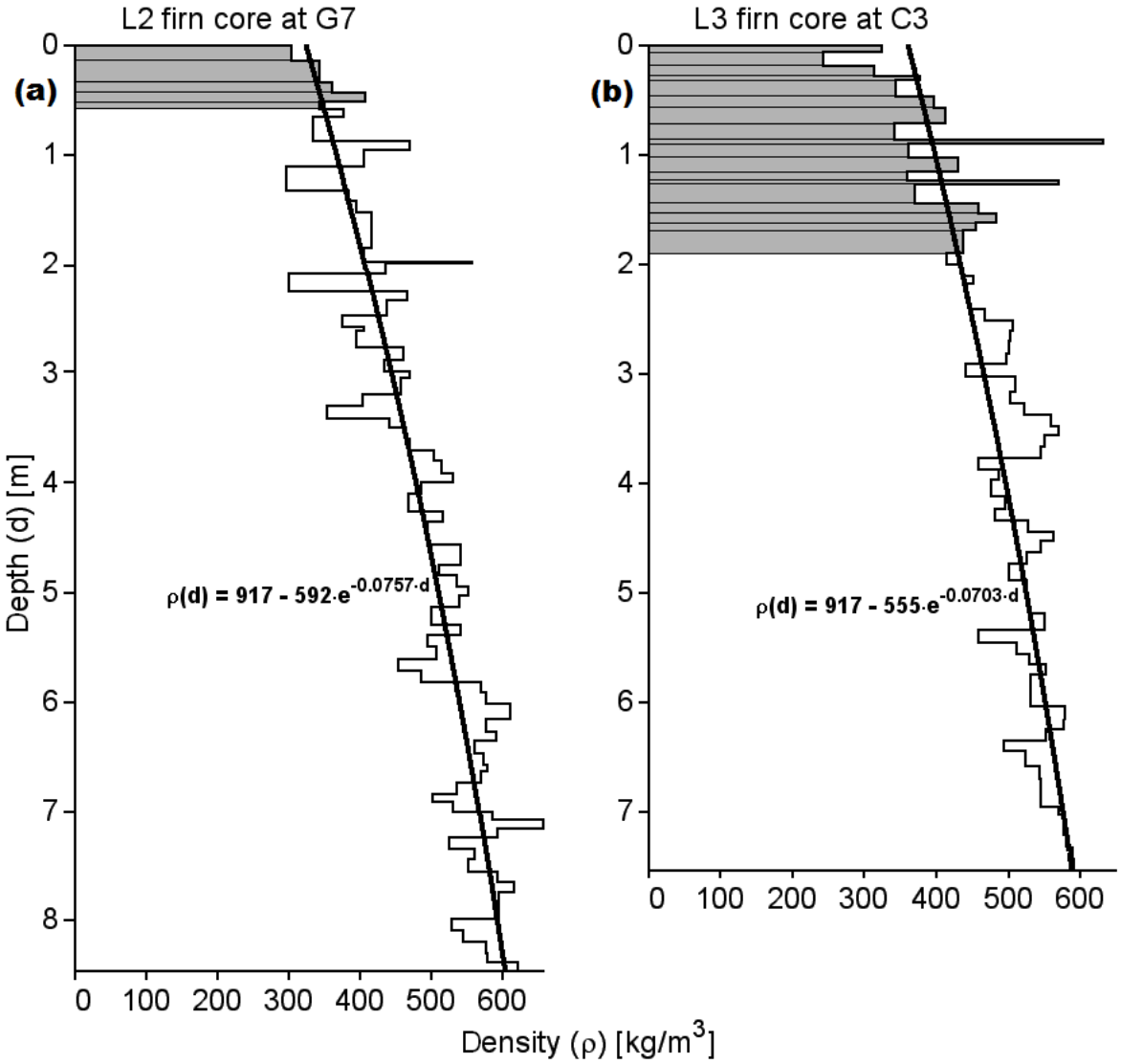

Figure 5.18: Snow density profiles in 2009 from snow pits (grey shaded area) and firn cores at sites (a) L2 and (b) L3. In both cases, the snow pit was logged according to visually identified stratigraphy, while the core was largely logged in 10 *cm* intervals.

Table 5.1: Summary of accumulation measurements at L2 (77°45'S, 167°17'E) and L3 (77°40'S, 167°11'E). Error terms represent geophysical variability rather than measurement error.

Site	observation period	years	accumulation kg m^{-2} a^{-1}	measurement technique
L2 – 81 stakes	13.11.08 – 12.11.09	1	224 ± 21	stake reading
L2 – at stake C3	May 2004 – November 2008	4.5	251	snow pit/dust layer
L2 – at stake G7	May 2004 – November 2009	5.5	245	firn core/dust layer
L2	May 2004 – November 2008	4.5	269 ± 9	GPR/dust layer
L3 – 24 stakes	18.11.08 – 9.11.09	0.97	304 ± 83	stake reading
L3 – at stake C3	May 2004 – November 2009	5.5	437	firn core/dust layer
L3	May 2004 – November 2009	5.5	404 ± 22	GPR/dust layer
14 km transect	May 2004 – November 2008	4.5	270 to 165	GPR/dust layer

used to extrapolate the density to greater depths in the following analysis. Integrating these empirical relationships allows the estimation of the total snow mass to a certain depth, which can then be used to determine the mean column density, and therefore the TWT, to this depth.

5.4.2 Accumulation Estimates from GPR Measurements

The snow pit logged at L2 in 2008 is approximately located at the centre of the radar profile in Fig. 5.14c. The yellow arrow corresponds to the dust layer depth and coincides with a horizon which is more undulating than other horizons in its vicinity. The particularly strong roughness might be related to buried sastrugis caused by the storm event in May 2004 (*Steinhoff et al.*, 2008; *Dunbar et al.*, 2009). Figures 5.19a and b show processed radargrams from line E4 to E6 at L2, recorded in 2008 and 2009, respectively. The more undulating horizon, as well as several other reflections, are observed throughout the entire survey grid in both years (not shown). The results of tracking the dust layer horizon and eight other distinct reflections in the radar lines in Figs. 5.19a and b, are shown in Figs. 5.19c and d, respectively. The tracked reflection horizons are numbered with roman numerals from top to bottom for easier referencing. The vertical scale in Fig. 5.19d is shifted by $4.7\,ns$ to align the first horizon (I) in both years to facilitate comparison. The yellow line (II) in Fig. 5.19c is the reflection previously associated with the dust horizon. Comparing its path with the neighbouring horizons further illustrates that it is unusually variable; its standard deviation from the linear trend is $0.65\,ns$, as opposed to $0.30\,ns$, $0.44\,ns$, and $0.34\,ns$ for the red (I), purple (III), and black (IV) horizons, respectively.

Assuming that the undulating horizon is related to the storm event allows an estimation of the accumulation over the whole grid since May 2004. Tracking this reflection along all 18 grid lines gives an average TWT of $27.5 \pm 0.8\,ns$, which is equivalent to an average accumulation of approximately $269 \pm 9\ \frac{kg}{m^2 a}$. The error term is the standard error of the measured depths, reflecting the geophysical variability of the accumulation over the whole site rather than measurement error. The latter is estimated by assuming that the actual depth of the tracked layer is $16\,cm$ (half of the theoretical resolution) above or below the

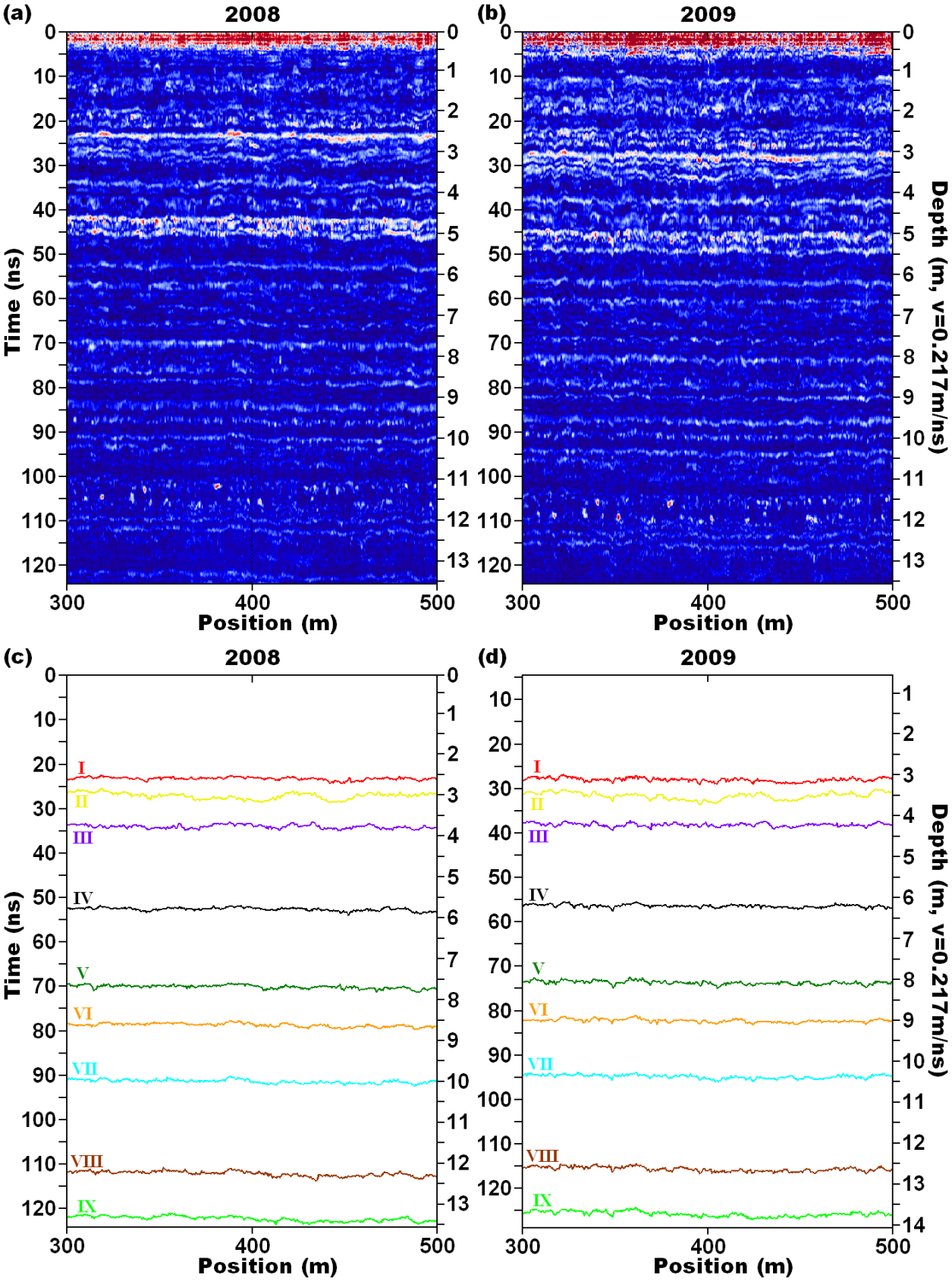

Figure 5.19: Processed radargrams from stake E4 to E6 at site L2, recorded in (a) 2008 and (b) 2009. Nine tracked reflection horizons (I-IX) are shown for (c) 2008 and (d) 2009. The vertical scale in (d) is shifted up by 4.7 *ns*, aligning horizon I. The vertical exaggeration is approximately 22:1.

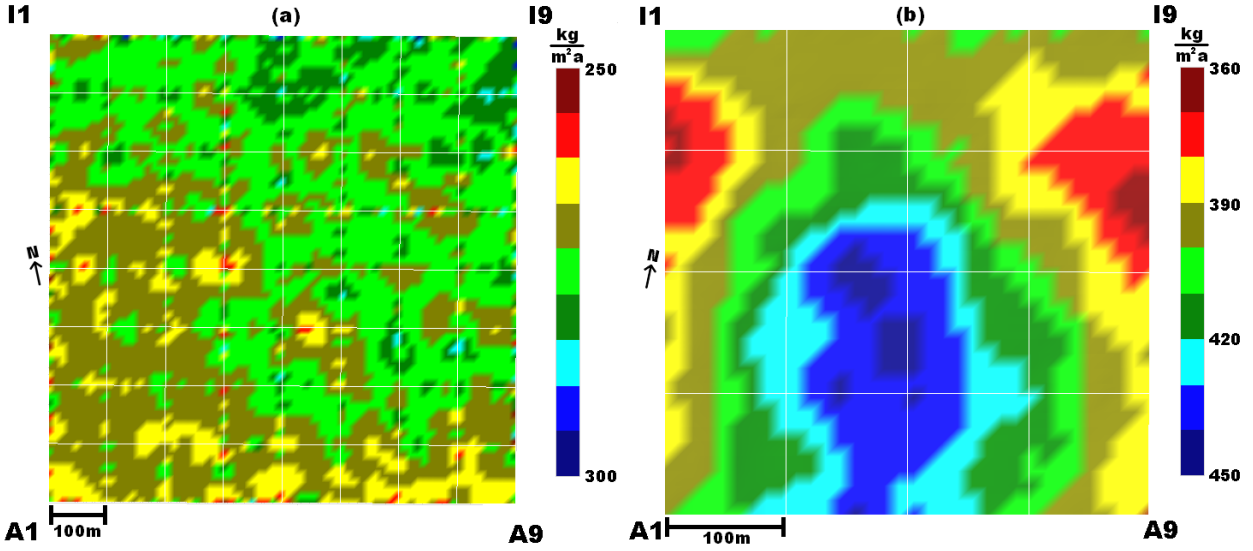

Figure 5.20: Accumulation maps for (a) L2 and (b) L3, based on the reflection horizon associated with the dust layer tracked along each line. A four metre interpolation grid resolution was used in both cases.

measured value, giving an error of $\pm 14\ \frac{kg}{m^2 a}$. Figure 5.20a illustrates the variability of this reflection's depth over the L2 area. While there is no particularly distinct pattern, it appears that accumulation is slightly higher in the north-east part of the grid.

Figure 5.21 displays a radargram of the C-line at L3 from 2009. The location of the firn core is indicated by the red box. Using the dust layer depth ($5.3\,m$) and the densities from the firn core at stake C3, the expected TWT to the dust layer is calculated to be $49\,ns$ (yellow arrow in Fig. 5.21). Comparing this with the radargram shows that there is a clear reflection horizon at approximately this TWT (tracked in yellow in Fig. 5.21). Analogous to the approach at L2, this is considered as a marker for the May 2004 dust storm. Accordingly, the average accumulation over this site is calculated to be $404 \pm 22\ \frac{kg}{m^2 a}$. In this case the measurement error due to the resolution of the system is approximately $\pm 13\ \frac{kg}{m^2 a}$.

The internal horizons in Fig. 5.21 are noticeably deeper in the middle of the profile, indicating more accumulation at the centre of the grid than at the edges. This inhomogeneity is probably related to local topography since L3 is situated on sloping terrain. The elevation difference between the lowest (I1) and the highest point (A9) is almost $20\,m$, with A9 located on a local crest and the terrain sloping down towards the north-west. The dip in the observed reflection horizons is on the leeward side of this crest where more drift snow accumulates. Hence, the accumulation rate calculated above needs to be considered as a large scale average for the whole area, rather than an accurate estimate at any particular location. The interpolated accumulation grid for L3 (Fig. 5.20b), calculated from the tracked dust layer reflection, illustrates the overall pattern. The central dip in the terrain clearly captures more snow than the surrounding areas.

The decreasing trend in the depth of the dust horizon from north to south observed at L2 (Fig. 5.20a) can be followed south along a GPR transect (Fig. 5.22) that was recorded as an extension of the line going from I1 to A1. Along this profile, the internal horizons gradually migrate upwards (not shown). After about $14\,km$, the horizon associated with the dust layer

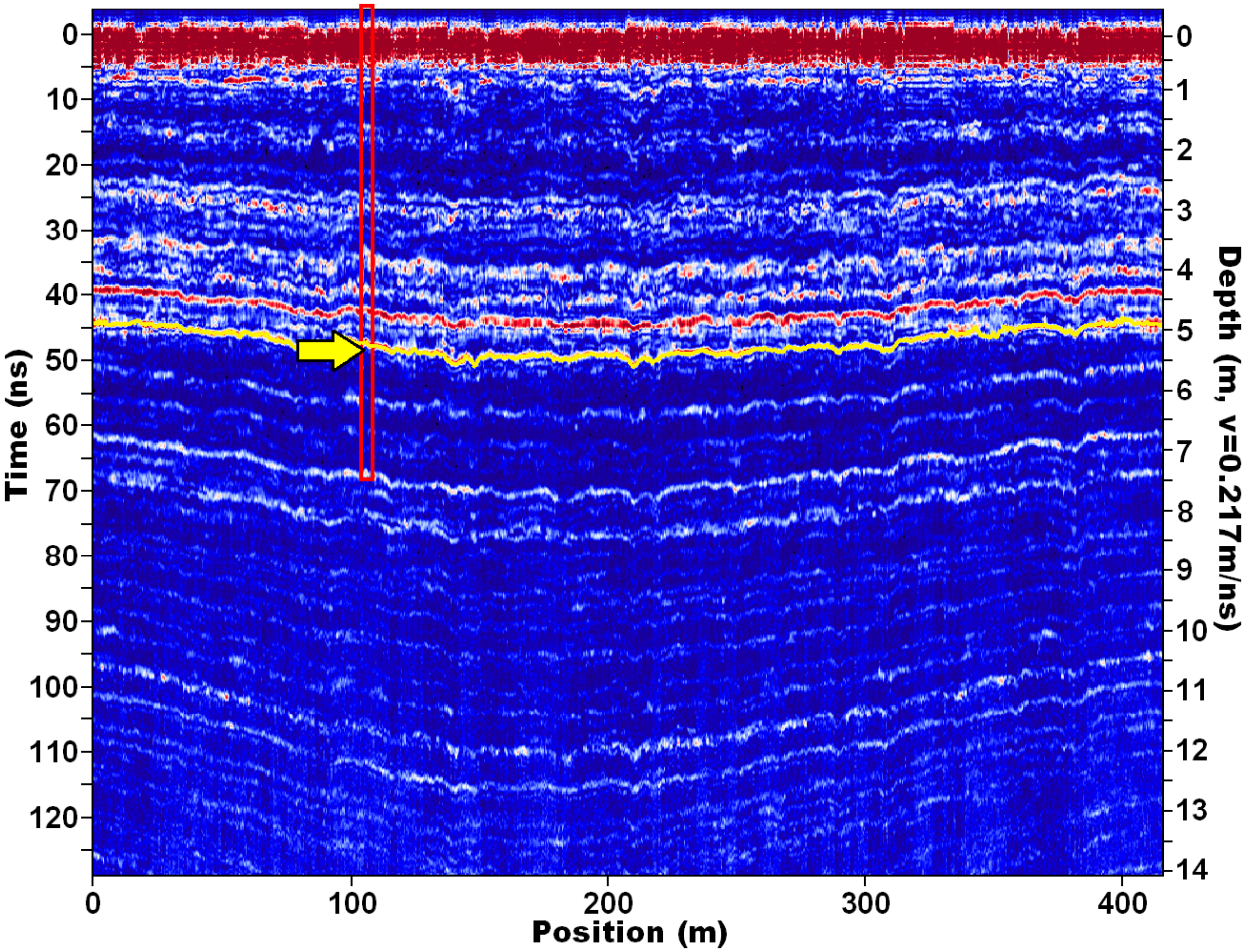

Figure 5.21: Processed radargram from line C1 to C9 at site L3 (2009). The red box marks the approximate location of the firn core; the yellow arrow indicates the expected TWT to the dust layer and the yellow line follows the closest reflection. The vertical exaggeration is roughly 23:1.

becomes too indistinct to be reliably identified. At this point, the dust layer reflection is found at a depth of about 1.9 m, which is equivalent to a reduced average accumulation of approximately 165 $\frac{kg}{m^2 a}$ (see Fig. 5.22). This has to be considered a crude estimate, since it assumes the same average snow density between the surface and the dust layer as at L2. A qualitatively similar trend was previously reported by both *Heine* (1967) and the McMurdo Ice Shelf Project (*McCrae*, 1984).

Unfortunately, it was not possible to reliably date other layers within the snow pit or firn core profiles and associate them with discrete reflections in the radargram. However, due to the high precision of the system, the vertical separation of other apparent horizons can be used to estimate compaction, which is the focus of the next section.

5.4.3 Snow Compaction

Most of the apparent internal horizons found in the 2008 GPR data can also be identified in the following year's record. Figure 5.19c shows nine reflections tracked between stakes E4 and E6 at L2 in 2008, and Fig. 5.19d shows the same horizons tracked in the 2009 data. One might expect that compaction, caused by temperature metamorphosis and the additional overburden on the surface, will reduce the separation between horizon pairs. This is confirmed by the poor alignment of the bottom horizon (IX) in Fig. 5.19d compared to Fig. 5.19c. Clearly, the total separation between the top (I) and the bottom (IX) reflection has been reduced. Assuming that the same horizons have been identified, calculating the average separation between two successive horizons in 2008 and comparing it with that of the same horizon pair in the 2009 data allows an estimation of the compaction of the snow in the intervening time period.

Not all horizons in Fig. 5.19c and d are suitable for compaction calculations because the high variability of, for example, the undulating horizon does not allow it to be tracked reliably enough to be confident that the same horizon was selected in both years. Similarly, the relatively strong double-horizon visible between 41 ns and 46 ns in 2008 (Fig. 5.19a) and between 45 ns and 49 ns in 2009 (Fig. 5.19b) may be easy to recognise visually, but the noise between both horizons makes them unreliable for automated tracking. In order to establish which of the reflections are likely to be reliably tracked in both years, the TWT profile of each horizon in 2008 is correlated with its counterpart in 2009. Additionally, the distance between pairs of horizons in terms of TWT for each year and the correlation of these relative TWT profiles is calculated. Only those horizons that show a correlation greater than 0.5 in both cases are used for compaction calculations. To ensure accuracy, a minimum average TWT difference between horizons of 10 ns, corresponding to approximately 1 m vertical separation is required.

For example, the average separation of horizon III and horizon IV in 2008 is 18.7 ns (Fig. 5.19c), but only 18.4 ns in 2009 (Fig. 5.19d). This means that the snow between these two horizons was compressed by about 1.6% during the intervening time period, assuming a constant wave speed. Using the density information from the firn core, this translates into a compaction of about 1.6 $\frac{cm}{m}$. The same calculations for five other horizon pairs result in the compaction diagram shown in Fig. 5.23. Clearly, the compaction decreases with depth. The horizontal error bars are the standard errors of the respective horizons' depths along

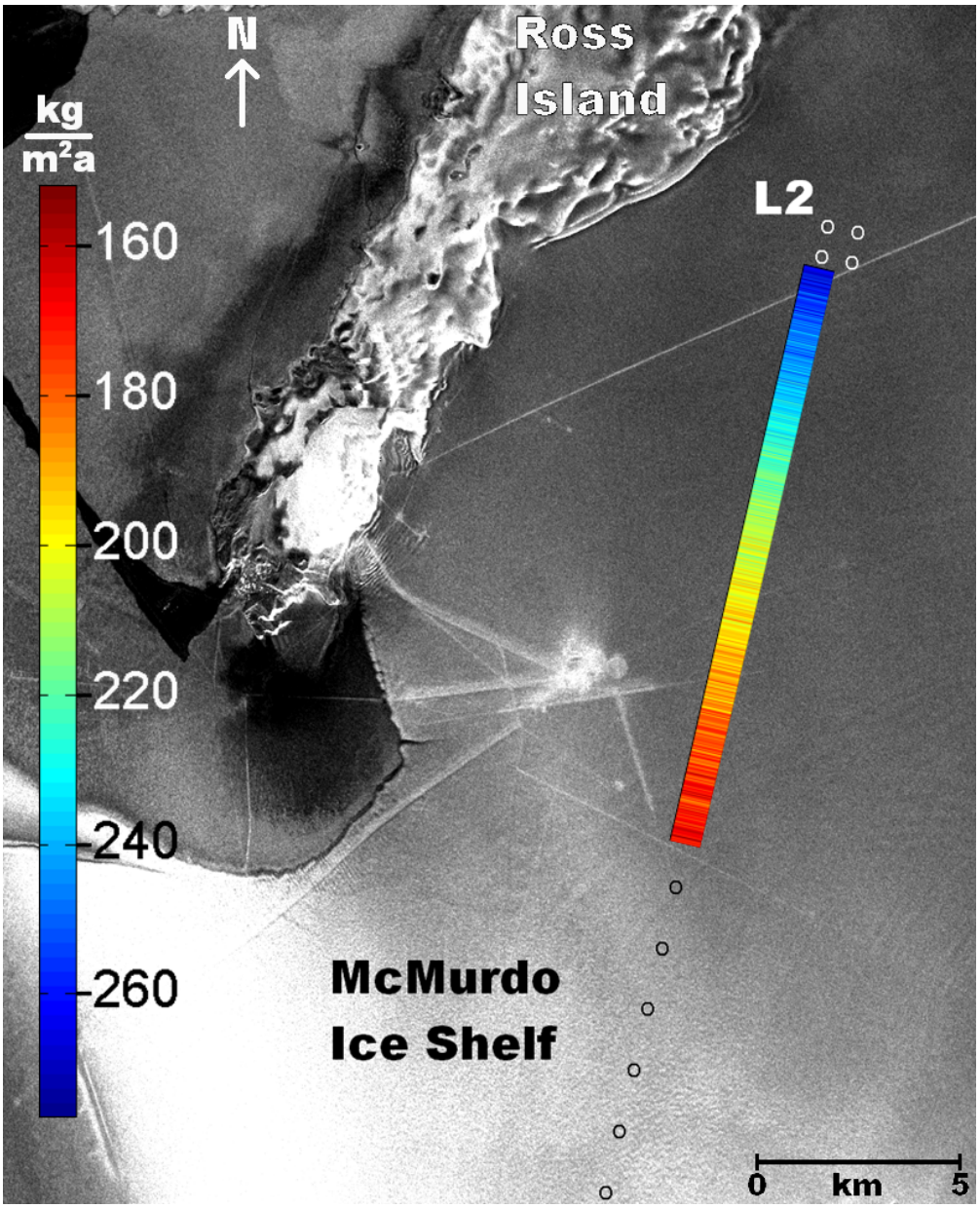

Figure 5.22: Accumulation along a transect from L2 to L1, estimated by tracking the dust layer reflection for 14 *km*.

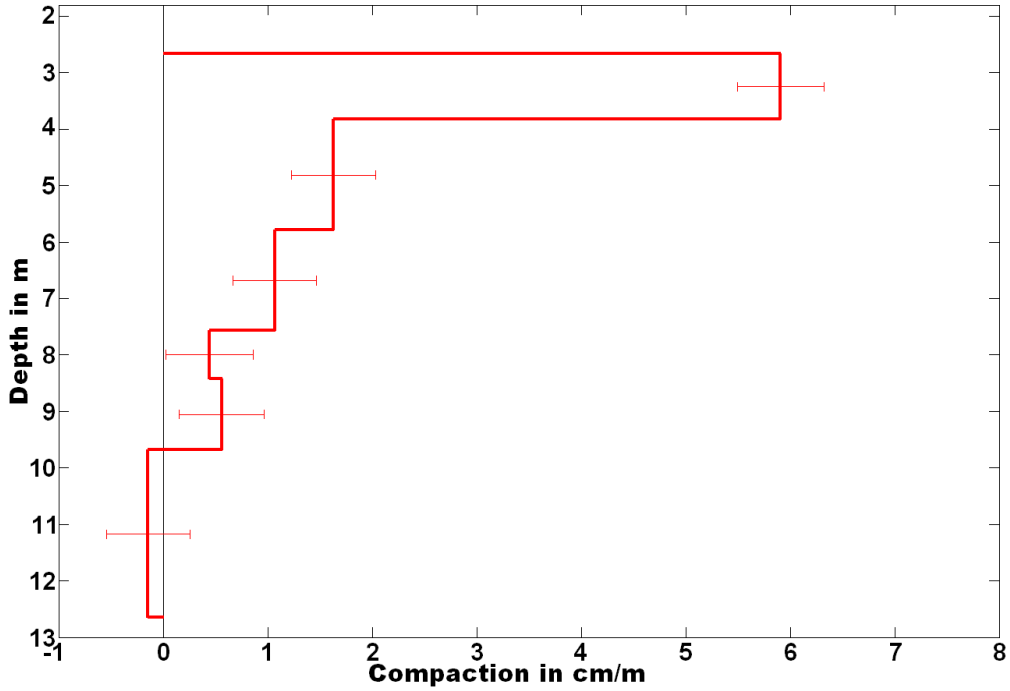

Figure 5.23: Snow compaction along the line from stake E1 to E9 at L2, calculated from the changes in the average separations between some of the horizons shown in Fig. 5.19c and d. Horizontal error bars are a combination of the relative accuracy of the radar system and spatial variability of the horizons along the line.

the whole line added in quadrature. The vertical scale in Fig. 5.23 relates to the depth of the horizons in 2008, i.e. before the compaction has occurred. Since the time between the acquisition of the GPR data sets was nearly one year (355 days), the values in Fig. 5.23 can be considered estimates of annual compaction rates.

The TWT difference between two horizons is converted to a physical separation by calculating the mean depth between the two horizons for the whole profile in 2009, determining the density at this depth with the formula shown in Fig. 5.18a, and then using this density to estimate the radar velocity between the two horizons via Eqs. 2.20 and 2.21. The density of the snow between two horizons is determined from the TWT in 2009 (post-compaction) and assumed to be the same in 2008 (pre-compaction), as the empirical depth-density relationship is purely based on data from 2009. Therefore, the radar velocity and hence the distance between the horizons in 2008, are probably underestimated, making the determined compaction rates conservative estimates. For example, assuming a constant density profile with time (Sorge's law; *Bader*, 1954), the average snow density in the layer initially between 5 to 10 m depth at L2 would increase by 2.5% between 2008 and 2009. This translates to an underestimation of the wave velocity in 2008 by approximately 1% and an increase in the compaction rates of about 0.5 $\frac{cm}{m}$.

The apparent expansion observed below 10 m in Fig. 5.23 is probably an indicator of the error in the measurements, and the actual amount of compaction over a one year time period at this depth is too small to be measured with the system used for this study. Furthermore, below 8.4 m the conversion from TWT to depth is based solely on an extrapolation of the exponential fit to the density data from the firn core, causing additional uncertainties in the

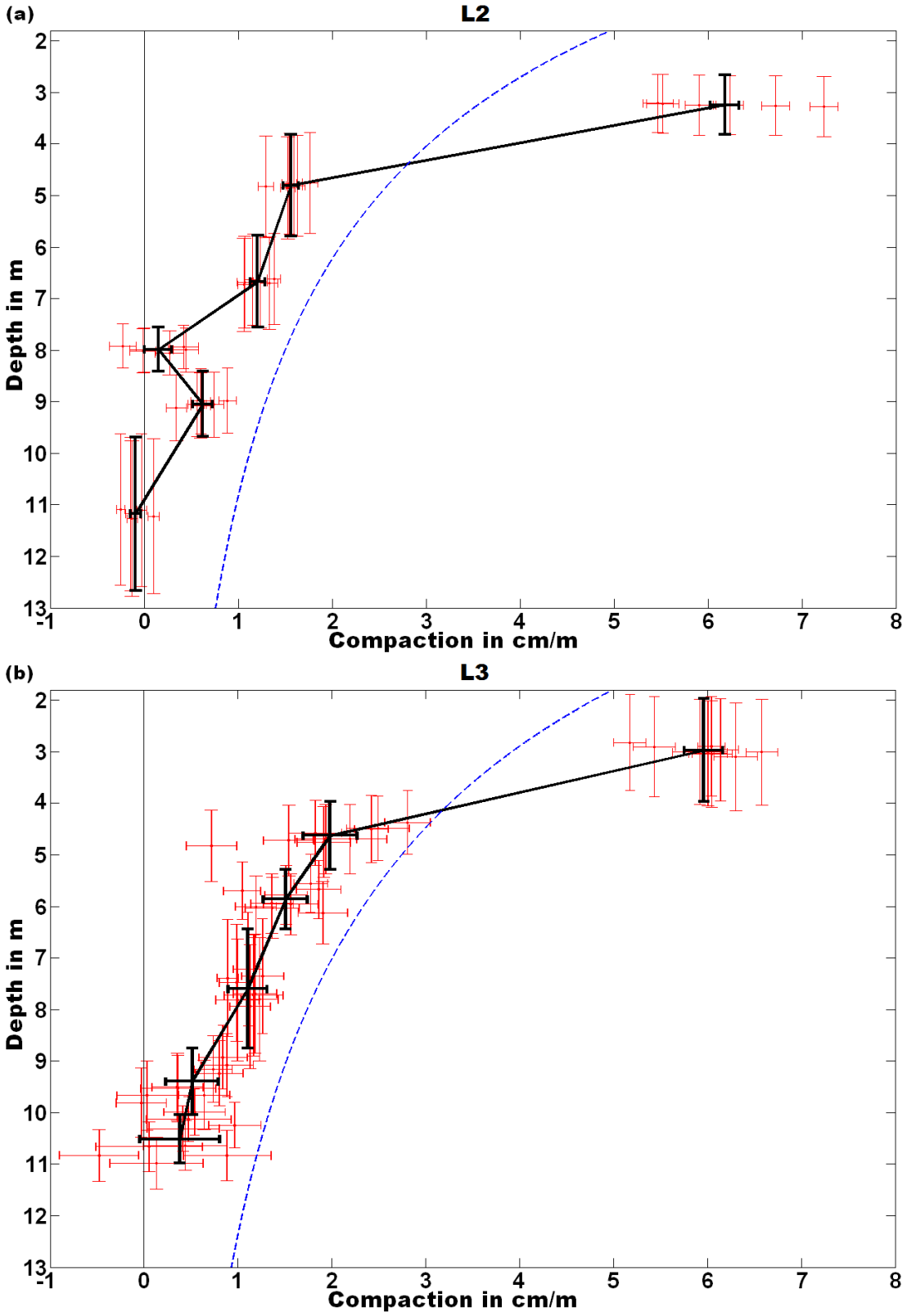

Figure 5.24: Snow compaction vs. depth for (a) L2 and (b) L3. (a) shows the compaction calculated from six lines at L2, while (b) includes all lines from L3 except one. The vertical axis represents depth before compaction has occurred. The horizontal error bars illustrate only the spatial variability along each of the lines, not measurement error. The vertical error bars show the thickness of the layers before compaction. The thick black line represents the average compaction for each horizon pair and the dashed blue line represents the expected compaction when assuming a constant density profile with time (Sorge's law).

calculations.

The same calculations were performed for five more lines at L2 (A2-I2, A5-I5, A7-I7, B1-B9, and H1-H9) and are summarised in Fig. 5.24a. The vertical error bars indicate the average separation of the two horizons in 2008. Figure 5.24a shows that the variability in layer depths and compaction between these six lines are small and thus tracking was not repeated for the remaining lines. The thicker, black data points present the average compaction between each of the horizon pairs and the connecting line illustrates the decreasing trend.

Figure 5.24b was calculated using the same methodology on seven internal horizons at L3. At this site, the variability of the compaction rates and the average depths is significantly higher. Therefore, the calculations were performed for all grid lines, except for A9-I9 due to corrupt data. The larger spread is in accordance with the observed spatial variability in the accumulation pattern and the resulting dipping of the internal horizons (see Fig. 5.20b and Fig. 5.21). Nevertheless, the mean compaction rate (black line in Fig. 5.24b) shows a clear trend of reduced compaction with depth, similar to that observed at L2.

Assuming constant density profiles with time (Sorge's law) and using the measured average accumulation from the stake farms to determine the initial offsets, theoretical compaction curves can be calculated. The results are the dashed blue lines in Figs. 5.24a and b. In both cases the general trend matches that of the compaction measurements, but above about $4\,m$ measured compaction rates are higher than those predicted by the model, and lower at greater depths.

5.5 Discussion

Table 5.1 summarises the results relating to accumulation. At both L2 and L3, the measurements derived from the stake farms showed significantly less accumulation than the combined firn core and GPR measurements. This discrepancy is probably largely due to temporal variability. If the readout of the stake depths had occurred one week later, the measurements at both sites would have been noticeably higher due to the occurrence of a high precipitation event from 13^{th} to 15^{th} November 2009. The accumulation rates derived from the snow pit and firn core observations should therefore be considered more reliable, since they consider a longer time period.

The average accumulation at L2 was found to be $269 \pm 9\,\frac{kg}{m^2 a}$, which is much lower than the value reported by *Heine* (1967) at the closest station ($510\,\frac{kg}{m^2 a}$ at station 200, about $6\,km$ north east of L2). There is a strong accumulation gradient in this area and L2 is close to the $320\,\frac{kg}{m^2 a}$ contour suggested by *McCrae* (1984), a value that still lies above the estimate presented here.

Generally, a reasonably accurate conversion of TWT to depth based on measured densities is critical and a potential source of error. A bias in the density data would lead to over- or under-estimation of the wave velocity in the snow and therefore the accumulation estimates, but good agreement between core- and snow pit densities from the two different seasons at both sites (not shown) suggests that the density measurements can be used with confidence. As the dust layer is a reliable reference point for dating, the difference between the present results and previous studies could indicate an overall reduction in annual accu-

mulation or a high natural variability in this area. Historic accumulation rates derived from stake measurements are even likely to be underestimates since the consideration of snow compaction – as suggested by *Takahashi and Kameda* (2007) – is not reported. Additionally, the gradient in the accumulation map for L2 (Fig. 5.20a) is found to continue along the transect toward L1 (Fig. 5.22). The southernmost point up to which it was possible to track the dust horizon lies relatively close to the location of a 20 m firn core analysed in *Dunbar et al.* (2009). They estimate an accumulation rate of 53 ± 20 cm of snow per year. If an average density of 600 $\frac{kg}{m^3}$ is assumed for the whole length of their core, this corresponds to 318 ± 120 $\frac{kg}{m^2 a}$. Again, the estimate from the tracked reflection lies significantly lower at 165 $\frac{kg}{m^2 a}$. However, the two points are approximately 3 km apart and the conversion from TWT to depth uses the average column density down to the dust layer determined at L2, which is likely an underestimate for this location.

Unfortunately, only one reflection horizon could be associated with a layer in the snow stratigraphy acquired via simple glaciological tools and visual observation. Such difficulties in linking snow pit and radar observations are quite common (*Harper and Bradford*, 2003) and are due to the limited resolution of the density profiles acquired for this study (*Eisen et al.*, 2003). Furthermore, the study sites investigated here were located in areas of low dielectric variability. The snow was dry and homogeneous and therefore contained few major dielectric contrasts, such as might be caused by occasional melt layers (e.g. *Dunse et al.*, 2008). *Alley* (1988) and *Arcone et al.* (2005) suggest that a combination of thin layers and depth hoar are the most likely sources for GPR reflections in dry snow. While not many distinct hoar layers were observed in the snow pit and core data, some may have been overlooked due to the coarseness of the recorded density profile. Accurate identification of the origin of the radar reflections would require high-resolution data from dielectric profiling as suggested by *Eisen et al.* (2004) and *Hawley et al.* (2008).

The locations of the various horizons at the crossover points of the measurement grid are consistent between perpendicular profiles. In most cases, the same reflection tracked along different profiles can be found within two time samples (2×0.1 ns which corresponds to 4 cm) at the point of intersection. The concurrence of the horizon depths is equally high for all reflections at both L2 and L3, showing that the precision of the processed radar data is higher than the theoretical resolution might suggest. This high precision allows snow compaction with depth to be estimated from changes in the separations of internal horizons from one year to the next.

At both L2 and L3, the average compaction measured between 2 and 13 m depth over a one year time period ranges from 0 to 7 $\frac{cm}{m}$. The sudden drop in compaction observed below about 4 m at both sites (see Fig. 5.24) could be related to a change in the compaction mechanism. For example, fresh snow largely compacts via settling, but above a density of 550 $\frac{kg}{m^3}$ sintering is usually considered to become dominant (*Maeno*, 1982; *van den Broeke*, 2008). According to the density profiles in Fig. 5.18, the 550 $\frac{kg}{m^3}$ level lies around 6 m depth at both sites, which compares well with the model estimate by *van den Broeke* (2008), who gives a range of 5 to 8 m depth for the 550 $\frac{kg}{m^3}$ level in this area. However, the depth at which a change in compaction rate is observed (4 m) is more shallow than this theoretical threshold density. A recent study by *Hoerhold et al.* (2011) suggests that the 'classic' picture of snow compaction is too simple, but better resolved density measurements would be required to

explain the origin of the observed step in compaction rate. Similarly, the origin of the dip in compaction rate between 7.5 and 8.5 m at L2 (Fig. 5.24a) could be a result of above average snow density at this depth, possibly related to one or two particularly warm summers, but there is insufficient data to test whether this is a measurement error or a subsurface feature.

High-resolution measurements of densification rates to directly compare with the present results are sparse. As the 2008 surface cannot be identified in the radargrams from 2009, it is not possible to calculate the total compaction of the whole snow column. However, total compaction between 5 m and 10 m depth can be estimated from Fig. 5.24 and compared to the measurements from *Arthern et al.* (2010). Summing up the average compaction (black lines in Fig. 5.24a and b) between 5 m and 10 m, gives a total compaction of approximately 4.3 cm at L2 (assuming zero compaction for the deepest 30 cm, where the results are negative) and 5.5 cm at L3, over a time period of 355 days. Using the daily rates given in Table 3 of *Arthern et al.* (2010) to calculate the total compaction over the same time span and depth range gives 5.7 cm for their "Berkner Island" site, the only site at which their strainmeters worked throughout the whole trial time. While the present results qualitatively agree with the "Berkner Island" data, the other sites detailed in *Arthern et al.* (2010) show considerably higher compaction rates. As mentioned above, one reason for this could be that the change in snow density due to compaction, and its effect on the velocity of the radar signal, is not taken into account, since this would require additional density data for 2008. Ultimately, the discrepancies could also be due to a difference in climatic conditions, since most of their sites are located in regions with lower mean annual temperature, lower latitude, higher elevation and higher annual accumulation. Therefore, considerable differences in the compaction behaviour of the snow could be expected.

5.6 Summary and Conclusion

The deterministic Fourier deconvolution scheme suggested in Sect. 5.1 can be used to remove some of the effects of the carrier signal from any pulsed GPR data of dry firn, provided that it was recorded with a system that has a very stable output. The result is a more focused radargram with improved contrast. This type of processing improves the identification and precise tracking of weak internal reflection horizons associated with density variations. The processing also facilitates recognition of the same horizons in follow-up surveys. The deconvolution methodology has the potential to work successfully for recordings in areas that are subject to sporadic melt events, although one should keep in mind that an essential assumption of the deconvolution is that there is no – or only very little – frequency dependent absorption and dispersion in the medium.

Using the thusly processed radargrams, point measurements of average accumulation from a snow pit at site L2 ($251\ \frac{kg}{m^2 a}$) and a firn core at site L3 ($437\ \frac{kg}{m^2 a}$), were extrapolated to a larger area by identifying a dateable dust layer horizon in the radargram. From the GPR data the extrapolated average accumulation over the 800 m × 800 m site on the ice shelf in Windless Bight (L2) was found to be $269 \pm 9\ \frac{kg}{m^2 a}$. The 400 m × 400 m grid on Ross Island showed higher variability in the internal horizons with an overall average accumulation of $404 \pm 22\ \frac{kg}{m^2 a}$. Stake farm readings at both sites, maintained over approximately a one year

time period, resulted in accumulation estimates of $224 \pm 21 \frac{kg}{m^2 a}$ at L2 and $304 \pm 83 \frac{kg}{m^2 a}$ at L3. The discrepancy between these values and the combined firn core and GPR measurements was probably caused by the short time period spanned by the stake observations and the high temporal variability of precipitation events. Additionally, a decreasing accumulation trend was measured along a 14 km long GPR transect heading south from L2. At the southernmost point, the accumulation was approximately 165 $\frac{kg}{m^2 a}$.

By comparing vertical separations of internal reflection horizons from one year to the next, it was possible to estimate compaction rates from GPR measurements down to 13 m depth. This technique might have implications for the validation of the CryoSat-2 satellite altimeter which measures the surface height of ice sheets and -shelves in order to monitor the polar mass balance.

The results in Sect. 5.4.3 show that internal reflectors found in GPR data, combined with density information, can be used for estimating compaction rates of dry snow. However, estimating densification in percolation areas is probably much more difficult due to the more complex snow morphology (*Parry et al.*, 2007). Frequent repetition of GPR measurements over a longer time period, combined with high resolution dielectric profiling of firn cores, could be used to establish a more detailed representation of time-dependent firn densification for the validation of current firn densification models. The suggested method is applicable over large areas in an efficient and non-invasive manner and is complementary to point measurements of snow compaction at a higher temporal resolution, such as those performed by *Arthern et al.* (2010) and *Heilig et al.* (2010). Using a higher frequency system, it might also be possible to improve the vertical resolution of snow compaction data from GPR measurements.

The measurements were conducted within the ESA CryoSat-2 calibration and validation activities for project AOCRY2CAL-4512.

Chapter 6

Conclusions and Future Work

6.1 Final Summary and Conclusions

This study was originally motivated by the success of the Rényi entropy (RE) statistical measure in previous analyses of stratospheric mixing barriers from chemistry-climate model data (*Krützmann et al.*, 2008). The aim of this thesis was to build on this success by analysing mixing barriers using observational data of stratospheric tracers and to determine whether this measure of complexity can be used to identify internal boundaries in other geophysical systems, particularly the cryosphere. The RE was to be tested as a tool for identifying amplitude gradients in ground penetrating radar (GPR) observations of snow and ice with the aim of facilitating the identification and tracking of internal reflections. As part of the project, high-resolution GPR soundings of Antarctic snow were acquired near Scott Base, Antarctica, with the intention of using the RE for tracking subsurface reflections in this data to allow extrapolation of accumulation measurements from snow pits and firn cores to larger areas.

In its atmospheric application (Ch. 3), the RE was used to identify the mixing barriers at the edges of the tropical pipe region using nitrous oxide (N_2O) observations from the EOS-MLS satellite instrument for August 2004 to November 2011. During most of this period, one local maximum of RE exists between 5° and 40° in each hemisphere in the lower and middle stratosphere (500 to 1250 K). This coincides with the tracer gradient between the tropics and mid-latitudes (Fig. 3.10), corresponding to the edge of the tropical pipe (*Sparling*, 2000). Monthly averages of the latitude of the RE maxima showed an equatorward shift in autumn and a return to higher latitudes in spring of the respective hemisphere (Figs. 3.11a and b), which agrees well with the expected behaviour of the tropical pipe edges (*Neu et al.*, 2003). Additionally, comparison with the seasonal average latitudes of the tropical pipe edges at 830 K from *Palazzi et al.* (2011) showed good agreement with the 850 K RE-results (Fig. 3.9).

Further analysis of the latitudinal evolution of the tropical pipe edges at 850 K revealed several occasions during which the southern hemisphere edge shifts poleward relatively suddenly during austral winter. These events are accompanied by increased mid-latitude N_2O levels (e.g. Fig. 3.8 and Figs. 3.12a-c). With the aid of the domain filling technique (Sect. 3.3) it was illustrated that this increase is the result of the cumulative effect of large-scale,

episodic leaks of N_2O-rich air from the tropical pipe (see also Appendix A). The detailed picture of the on-going dynamics during the leak events given by the domain filling technique, combined with a comparison between the global distributions of N_2O and the potential vorticity field (Fig. 3.19), strongly suggests that irreversible mixing related to planetary wave breaking is the most likely cause of the leak events. The observed dynamics were found to be similar to those reported by other studies of wave breaking (e.g. *Randel et al.*, 1993; *Waugh*, 1993; *Morel et al.*, 2005; *Portafaix et al.*, 2003), some of which involve distortions of the polar vortex. These leaks were observed every second year between 2005 and 2008, followed by three consecutive leak-years: 2009, 2010, and 2011 (Fig. 3.8), suggesting a link to the phase of the quasi-biennial oscillation (QBO). A brief comparison between the zonal mean volume mixing ratio of N_2O at mid-latitudes and the phase of the QBO at 850 K supports this idea. The leaks were found to preferentially occur when the QBO is in a dying-off easterly or westerly shear phase (Fig. 3.24). However, the N_2O data set analysed here is too short to establish this connection conclusively.

Application of the RE to observations of carbon monoxide (CO) and methyl chloride (CH_3Cl) showed that the RE can be used to compare the distributions of different tracers. Due to the very different source region of CO compared to N_2O, the RE of CO at 850 K could not identify the edge of the tropical pipe (Fig. 3.5). Instead it displayed high values near 65°S in austral mid-winter which might be associated with the inner boundary of the polar vortex edge region (*Roscoe et al.*, 2012). Methyl chloride on the other hand has a similar distribution to N_2O in the lower parts of the stratosphere and the RE of CH_3Cl at 550 K displayed similar features to that of N_2O (Fig. 3.4b), though less coherently because of the lower signal-to-noise ratio of the CH_3Cl observations. The deterioration of the high-RE bands with increasing noise level was confirmed by adding noise to the N_2O observations which led to similar RE structures to those derived from CH_3Cl (Fig. 3.4a). Overall, the comparison of RE patterns derived from different tracers showed that a relatively high signal-to-noise ratio is required for reliable identification of mixing barriers with the RE and that tracers with different source and sink regions can give complementary information about stratospheric mixing barriers.

The application of the RE methodology for detecting amplitude gradients (corresponding to subsurface reflections) in cryospheric GPR soundings (Ch. 4), which was the second main objective of this thesis, was only partially successful. After a variety of tests with a 25 MHz glacier sounding (Sect. 4.2), the RE was found to be effective as a pseudo gain function for initial analysis of GPR data in the field, when relatively strong and distinct reflections, such as the bedrock reflection in a glacier profile, need to be identified. In such cases, the RE tends to assign all detectable amplitude gradients a similar value, automatically resulting in a clear contrast between individual reflections and background scattering, while other gain functions often require parameter tuning or prior knowledge of subsurface properties and expected reflector depth to give a good contrast over the whole vertical range of a profile (Fig. 4.13). Only a non-stationarity correction (dewow) needs to be applied to the GPR data before calculating the RE. Using a fixed number of bins potentially allows near real-time processing of data during collection in the field.

As the recommended temporal sampling relative to the centre frequency is similar for most commercial pulsed GPR systems, it was also possible to define a 'standard' data window

size for creating the histograms from which the *RE* is calculated: 20 horizontal (in the along-track direction) and 10 vertical (in the time direction) data points (Sect. 4.3). Using these window dimensions the RE_{20h10v} is applicable to pulsed GPR data with various centre frequencies. To illustrate the utility and wider applicability of the RE_{20h10v} as a parameter-free pseudo gain function, it was applied to a 50 *MHz* and a 500 *MHz* sounding of a transect on the McMurdo Ice Shelf (Sect. 4.4). In both cases the reflection from a brine intrusion that was known to be present in this region could be easily identified. On the other hand, the results with the 500 *MHz* data showed that the *RE* is not as useful for identifying more closely spaced signal gradients caused, for example, by the (weaker) reflections from internal layers of varying density in dry snow. These tend to result in overall high *RE* values that make it difficult to distinguish individual reflections, particularly close to the surface (e.g. Fig. 4.15b). Accordingly, the *RE* can only be considered an improved processing methodology for GPR surveys that focus on individual, strong reflections. In this context, the *RE*'s simplicity and low computational demand can be advantageous for initial data processing in the field.

All in all, the *RE* is a versatile tool for gradient detection in a variety of circumstances. Due to its purely statistical nature, it has no units and only depends on the relative distribution of the underlying data, rather than their absolute values. This can be particularly useful when analysing data sets with values spanning several orders of magnitude such as unprocessed GPR recordings (e.g. Fig. 4.13). On the other hand, the general applicability of the *RE* also means that some of the details of the way the *RE* is applied to different data sets (number of data points required and associated data window size, the bin width used for creating the histograms, etc.; see Sect. 4.2) have to be separately tested and tuned to suit the required purpose, which can lead to a considerable amount of trial and error. In the applications tested here, the *RE* was used as an alternative for data processing to other analysis methods. While the *RE* did not lead to significantly better results than those achieved with other methods in any of the tested cases, it nevertheless has its potential uses as a one-off initial analysis tool for low-frequency GPR data that can be calculated very easily in the field as it does not have a high computational requirement. In its application to stratospheric trace gas observations, the *RE* was found to be a viable method for identifying the edges of the tropical pipe, thereby confirming some of the results of previous studies (Fig. 3.9). Compared to other stratospheric mixing metrics, such as equivalent length (*Nakamura*, 1996; *Lee et al.*, 2001) and effective diffusivity (*Haynes and Shuckburgh*, 2000), the *RE* has the advantage that it does not require conversion to equivalent latitude. While the *RE* can of course also be calculated in the equivalent latitude frame, this introduces an unnecessary reliance on dynamical information such as wind fields, measurements of which are not always readily available. Accordingly, the *RE* requires less computational effort than these other mixing metrics.

The third objective of the present work was to use high-resolution GPR soundings of dry snow, acquired during field work in Antarctica in November 2008 and 2009, to estimate accumulation over extended areas. The idea was to use the *RE* for identifying and tracking internal reflections in the snow that can be associated with particular layers of known origin from a snow pit or firn core. However, due to the limited ability of the *RE* to distinguish weak, closely spaced reflections (Sect. 4.4), a different processing approach was required. Consequently, the deterministic Fourier deconvolution scheme was developed (Ch. 5). By

removing some of the effects of the carrier waveform, it results in a more focused radargram with improved contrast that facilitates the identification and precise tracking of weak internal reflection horizons (e.g. Fig. 5.14).

This processing methodology was applied to the acquired 500 *MHz* GPR soundings of dry Antarctic snow from two measurement sites near Scott Base, Antarctica. With a dust layer from May 2004 as a reference, point measurements of average accumulation were acquired from a snow pit at site L2, in Windless Bight on the McMurdo Ice Shelf and a firn core at site L3, on Ross Island (Fig. 2.15). Using GPR profiles acquired along the measurement grid established at each of these sites and the Fourier deconvolution scheme, it was possible to identify and track a radar reflection associated with the dust layer (Sect. 5.4). Thereby the average accumulation across the whole measurement sites could be estimated (see Table 5.1 for detailed results). Stake farm measurements over a one year time period, gave between 15% and 25% lower accumulation estimates at both sites. This discrepancy is most likely related to the different time periods on which the estimates are based and the annual variability of precipitation events. Despite the smaller grid size, the local variability of accumulation at L3, determined from both stake farm and GPR measurements, was found to be much higher than at L2 (Fig. 5.20). This is in accordance with topographic differences, since L2 is located on the (flat) McMurdo Ice Shelf while L3 is on the undulating slopes of Mount Erebus. In addition, the dust layer reflection could be tracked along a GPR transect heading south from L2, illustrating the gradually decreasing accumulation trend in this direction and allowing rough estimates of accumulation rates for 14 *km* (Fig. 5.22).

The deterministic Fourier deconvolution was also shown to facilitate recognition of the same horizons in follow-up surveys (Fig. 5.19). All GPR measurements from 2008 were repeated in 2009. By comparing vertical separations of internal reflection horizons from one year to the next and assuming a constant density profile (Sorge's Law), it was possible to estimate snow compaction rates down to 13 *m* depth with a vertical resolution between one and two metres. The results agree well with theoretical estimates (Fig. 5.24). This GPR-based methodology is complementary to point measurements of snow compaction at a higher temporal resolution, such as those performed by *Arthern et al.* (2010) and *Heilig et al.* (2010), since it can be applied to larger areas in an efficient and non-invasive manner.

6.2 Future Work

Having established the *RE* as a tool for identifying mixing barriers in stratospheric tracer data from both observations and model simulations, future work should focus on a comparison of results from these two sources. A comparison of the *RE*-results from observations and simulations of the same long-lived tracer (e.g. N_2O or CH_4) can highlight differences in the basic dynamics, independent of potential biases in the absolute values of the tracer concentrations. Such a comparison would also allow a better understanding of the effects of the precision of observational data on the *RE* values, which in turn could shed some light on the cause for the equatorward bias of the *RE* of N_2O with respect to the location of the mixing barrier at the edge of the polar vortex throughout the middle stratosphere (e.g. Fig. 3.14).

Applying the RE to tracer observations from other satellites (e.g. MIPAS on Envisat) would enable a more long-term analysis of the seasonal evolution of the edges of the tropical pipe. A longer data set would also allow a more complete analysis of the tropical leak events and could establish if the apparent link to the phase of the QBO, found between 2004 and 2011, is a real connection or mere coincidence. For this purpose an even longer data set, such as HALOE CH_4 observations, would be preferable, though in that case the irregular geographical coverage has to be taken into account. Additionally, a comparison of the timing of the poleward shift of high-N_2O mixing ratios with detailed information on planetary wave activity could lead to further insights about the physical mechanisms that result in high amounts of N_2O inside the southern hemisphere surf-zone during leak-years.

The domain filling technique can also be used to investigate the zonal structure of the edges of the tropical pipe (Fig. 3.23). While domain filling is computationally very demanding, global RE maps derived from the high-resolution N_2O data can give a very detailed picture of the tropical pipe on a day-by-day basis which is not possible with other mixing measures such as the equivalent length or effective diffusivity, since these are defined on equivalent latitude. One exception is the Lyapunov diffusivity used in *d'Ovidio et al.* (2009). More recently *Pukite et al. (2012)* suggested a method for using the PDF-based technique from *Sparling* (2000) and *Neu et al.* (2003) for identifying the seasonal average position of the tropical barriers in latitude and longitude. Accordingly, additional testing of the reliability of the global RE maps and a comparison with other non-zonal-mean measures is another potential area for future work which can improve the understanding of the dynamics in the middle stratosphere in general and the tropical pipe in particular.

With regards to the detection of signal gradients in pulsed GPR recordings, the RE_{20h10v}'s contrast enhancing properties can be utilised in future measurement campaigns of glacier profiles, particularly in Antarctica. The code for the RE calculations is currently written in MATLAB as well as MATLAB-executable C (MEX-file format) for enhanced performance and can therefore be easily adapted to most other platforms. Unfortunately, the pulseEKKO PRO system used in the present work currently does not allow the data collection to be performed with standard PC hardware, but many other commercial GPR systems do. Hence, testing the RE_{20h10v} as a pseudo gain function for GPR data acquired with a variety of other systems is a potentially useful area for future investigations.

Similarly, the deterministic Fourier deconvolution can be used to enhance the quality of other GPR soundings of dry snow, provided they are recorded with a system that has a very stable output and that the emitted signal can be measured directly. Additionally, the deconvolution methodology has the potential to work for recordings in areas that are subject to sporadic melt events, although it should be kept in mind that an essential assumption of the deconvolution is that there is no – or only very little – frequency dependent absorption and dispersion in the medium. Therefore, further testing with GPR recordings of various snow conditions would be useful to determine the limits of the applicability of the Fourier deconvolution approach. This could be particularly useful in regions with relatively high accumulation and regular summer melting, since the summer ice layers are likely to give distinct reflections that can be tracked over relatively large distances, allowing accumulation estimates from one snow pit or firn core to be extrapolated to even wider areas. However, estimating densification in regions with regular melting will always be difficult due to the

more complex snow morphology (*Parry et al.*, 2007).

In dry snow, applying the deconvolution methodology to higher frequency GPR measurements, such as the 1 *GHz* data that was also collected during the field work for the present study, could allow a further improvement of the vertical resolution of the GPR-derived compaction information. Unfortunately, this could not be tested as the 1 *GHz* system was damaged during the second measurement campaign. Accordingly, acquisition of further high-frequency snow profiles is desirable. Additionally, more frequent repetition of GPR measurements in the same area and over a longer time period, combined with high resolution dielectric profiling of firn cores, could be used to establish a more detailed representation of time-dependent firn densification for the validation of current firn densification models.

Bibliography

Alley, R., J. Bolzan, and I. Whillans (1982), Polar firn densification and grain growth, *Annals of Glaciology*, *3*, 7–11.

Alley, R. B. (1988), Concerning the deposition and diagenesis of strata in polar firn, *Journal of Glaciology*, *34*(118), 283–290.

Andrews, D., J. Holton, and C. Leovy (1987), *Middle atmosphere dynamics*, *International Geophysics Series*, vol. 40, Academic Press, Inc.

Andrews, D. G. (2000), *An introduction to atmospheric physics*, Cambridge University Press, Cambridge, UK; New York, NY.

Arcone, S., D. Lawson, and A. Delaney (1995), Short-pulse radar wavelet recovery and resolution of dielectric contrasts within englacial and basal ice of Matanuska Glacier, Alaska, USA, *Journal of Glaciology*, *41*(137), 68–86.

Arcone, S., V. Spikes, G. Hamilton, and P. Mayewski (2004), Stratigraphic continuity in 400 MHz short-pulse radar profiles of firn in West Antarctica, *Annals of Glaciology*, *39*, 195–200.

Arcone, S. A., V. B. Spikes, and G. S. Hamilton (2005), Stratigraphic variation within polar firn caused by differential accumulation and ice flow: interpretation of a 400 MHz short-pulse radar profile from West Antarctica, *Journal of Glaciology*, *51*(174), 407–422, doi:10.3189/172756505781829151.

Arthern, R. J., and D. J. Wingham (1998), The natural fluctuations of firn densification and their effect on the geodetic determination of ice sheet mass balance, *Climatic Change*, *40*(3), 605–624.

Arthern, R. J., D. G. Vaughan, A. M. Rankin, R. Mulvaney, and E. R. Thomas (2010), In situ measurements of Antarctic snow compaction compared with predictions of models, *Journal of Geophysical Research*, *115*(F3), F03011.

Bader, H. (1954), Sorge's law of densification of snow on high polar glaciers, *Journal of Glaciology*, *2*(15), 319–323.

Baldwin, M., and T. Dunkerton (2001), Stratospheric harbingers of anomalous weather regimes, *Science*, *294*(5542), 581–584.

Baldwin, M., L. Gray, T. Dunkerton, K. Hamilton, P. Haynes, W. Randel, J. Holton, M. Alexander, I. Hirota, T. Horinouchi, D. Jones, J. Kinnersley, C. Marquardt, K. Sato, and M. Takahashi (2001), The quasi-biennial oscillation, *Reviews of Geophysics*, *39*(2), 179–229, doi:10.1029/1999RG000073.

Bates, D., and P. Hays (1967), Atmospheric nitrous oxide, *Planetary and Space Science*, *15*(1), 189–197, doi:10.1016/0032-0633(67)90074-8.

Beck, C., and F. Schlögl (1993), *Thermodynamics of chaotic systems: an introduction*, *Cambridge nonlinear science series*, vol. 4, Cambridge University Press, Cambridge, UK.

Belina, F. A., B. Dafflon, J. Tronicke, and K. Holliger (2009), Enhancing the vertical resolution of surface georadar data, *Journal of Applied Geophysics*, *68*(1), 26–35, doi:10.1016/j.jappgeo.2008.08.011.

Bentley, C., J. Clough, K. Jezek, and S. Shabtaie (1979), Ice-thickness patterns and the dynamics of the Ross Ice Shelf, Antarctica, *Journal of Glaciology*, *24*, 287–294.

Bjornsson, H., Y. Gjessing, S. Hamran, J. Hagen, O. Liestol, F. Palsson, and B. Erlingsson (1996), The thermal regime of sub-polar glaciers mapped by multi-frequency radio-echo sounding, *Journal of Glaciology*, *42*(140), 23–32.

Bodeker, G., H. Struthers, and B. Connor (2002), Dynamical containment of Antarctic ozone depletion, *Geophysical Research Letters*, *29*(7), 1098, doi:10.1029/2001GL014206.

Bogorodsky, V. V., C. R. Bentley, and P. E. Gudmandsen (1985), *Radioglaciology*, D. Reidel Publishing Company, Norwell, Massachusetts.

Bracewell, R. (2003), *Fourier analysis and imaging*, Kluwer Academic/Plenum Publishers, New York, NY.

Charney, J., and P. Drazin (1961), Propagation of Planetary-Scale disturbances from lower into upper atmosphere, *Journal of Geophysical Research*, *66*(1), 83–109, doi:10.1029/JZ066i001p00083.

Cofield, R., and P. Stek (2006), Design and field-of-view calibration of 114-660-GHz optics of the Earth Observing System Microwave Limb Sounder, *IEEE Transactions on Geoscience and Remote Sensing*, *44*(5), 1166–1181, doi:10.1109/TGRS.2006.873234.

Davis, C., and A. Ferguson (2004), Elevation change of the Antarctic Ice Sheet, 1995-2000, from ERS-2 satellite radar altimetry, *IEEE Transactions on Geoscience and Remote Sensing*, *42*(11), 2437–2445, doi:10.1109/TGRS.2004.836789.

Davis, C., Y. Li, J. McConnell, M. Frey, and E. Hanna (2005), Snowfall-driven growth in East Antarctic Ice Sheet mitigates recent sea-level rise, *Science*, *308*(5730), 1898–1901, doi:10.1126/science.1110662.

de la Pena, S., P. Nienow, A. Shepherd, V. Helm, D. Mair, E. Hanna, P. Huybrechts, Q. Guo, R. Cullen, and D. Wingham (2010), Spatially extensive estimates of annual accumulation

in the dry snow zone of the Greenland Ice Sheet determined from radar altimetry, *Cryosphere*, *4*(4), 467–474, doi:10.5194/tc-4-467-2010.

d'Ovidio, F., E. Shuckburgh, and B. Legras (2009), Local mixing events in the upper troposphere and lower stratosphere. Part I: detection with the Lyapunov diffusivity, *Journal of the Atmospheric Sciences*, *66*(12), 3678–3694, doi:10.1175/2009JAS2982.1.

Drews, R., O. Eisen, I. Weikusat, S. Kipfstuhl, A. Lambrecht, D. Steinhage, F. Wilhelms, and H. Miller (2009), Layer disturbances and the radio-echo free zone in ice sheets, *The Cryosphere*, *3*(2), 195–203, doi:10.5194/tc-3-195-2009.

Drinkwater, M., D. Long, and A. Bingham (2001), Greenland snow accumulation estimates from satellite radar scatterometer data, *Journal of Geophysical Research. D. Atmospheres*, *106*, 33,935–33,950.

Dunbar, G., N. Bertler, and R. McKay (2009), Sediment flux through the McMurdo Ice Shelf in Windless Bight, Antarctica, *Global and Planetary Change*, *69*(3), 87–93.

Dunse, T. (2006), Measuring near-surface firn structure in the percolation zone of the Greenland Ice Sheet using Ground-Penetrating radar, Diploma thesis, University of Bremen, Bremen.

Dunse, T., O. Eisen, V. Helm, W. Rack, D. Steinhage, and V. Parry (2008), Characteristics and small-scale variability of GPR signals and their relation to snow accumulation in Greenland's percolation zone, *Journal of Glaciology*, *54*(185), 333–342.

Egorova, T., E. Rozanov, V. Zubov, E. Manzini, W. Schmutz, and T. Peter (2005), Chemistry-climate model SOCOL: a validation of the present-day climatology, *Atmospheric Chemistry and Physics*, *5*, 1557–1576.

Eisen, O., F. Wilhelms, U. Nixdorf, and H. Miller (2003), Revealing the nature of radar reflections in ice: DEP-based FDTD forward modeling, *Geophys. Res. Lett*, *30*(5), 1218–1221.

Eisen, O., U. Nixdorf, F. Wilhelms, and H. Miller (2004), Age estimates of isochronous reflection horizons by combining ice core, survey, and synthetic radar data, *Journal of Geophysical Research-Solid Earth*, *109*(B4), B04106, doi:10.1029/2003JB002858.

Eisen, O., M. Frezzotti, C. Genthon, E. Isaksson, O. Magand, M. R. van den Broeke, D. A. Dixon, A. Ekaykin, P. Holmlund, T. Kameda, L. Karlof, S. Kaspari, V. Y. Lipenkov, H. Oerter, S. Takahashi, and D. G. Vaughan (2008), Ground-based measurements of spatial and temporal variability of snow accumulation in East Antarctica, *Reviews of Geophysics*, *46*(1), RG2001, doi:10.1029/2006RG000218.

Eyring, V., N. Butchart, D. W. Waugh, H. Akiyoshi, J. Austin, S. Bekki, et al. (2006), Assessment of temperature, trace species, and ozone in chemistry-climate model simulations of the recent past, *Journal of Geophysical Research-Atmospheres*, *111*(D22), doi:10.1029/2006JD007327.

Fujita, S., H. Maeno, S. Uratsuka, T. Furukawa, S. Mae, Y. Fujii, and O. Watanabe (1999), Nature of radio echo layering in the Antarctic Ice Sheet detected by a two-frequency experiment, *Journal of Geophysical Research*, *104*(B6), 13,013–13,024, doi: 199910.1029/1999JB900034.

Garny, H., G. E. Bodeker, and M. Dameris (2007), Trends and variability in stratospheric mixing: 1979-2005, *Atmos. Chem. Phys.*, *7*(21), 5611–5624.

Grahn, J. (2012), Renyi entropy and finite Lyapunov exponents as metrics of transport and mixing in an idealised stratosphere, Master's thesis, Chalmers University of Technology, Gothenburg, Sweden.

Gray, L. J. (2010), Stratospheric equatorial dynamics, in *Stratosphere: Dynamics, Transport, and Chemistry*, edited by L. Polvani, A. Sobel, and D. Waugh, no. 190 in Geophysical Monograph Series, pp. 93–107, American Geophysical Union, Washington.

Hamilton, K. (1998), Dynamics of the tropical middle atmosphere: A tutorial review, *Atmosphere-Ocean*, *36*(4), 319–354, doi:10.1080/07055900.1998.9649616.

Harper, J. T., and J. H. Bradford (2003), Snow stratigraphy over a uniform depositional surface: spatial variability and measurement tools, *Cold Regions Science and Technology*, *37*(3), 289–298.

Harvey, V., M. Hitchman, R. Pierce, and T. Fairlie (1999), Tropical aerosol in the Aleutian High, *Journal of Geophysical Research-Atmospheres*, *104*(D6), 6281–6290, doi: 10.1029/1998JD200094.

Harvey, V., R. Pierce, T. Fairlie, and M. Hitchman (2002), A climatology of stratospheric polar vortices and anticyclones, *Journal of Geophysical Research-Atmospheres*, *107*(D20), 4442, doi:10.1029/2001JD001471.

Harvey, V. L., C. E. Randall, G. L. Manney, and C. S. Singleton (2008), Low-ozone pockets observed by EOS-MLS, *Journal of Geophysical Research-Atmospheres*, *113*(D17), D17112, doi:10.1029/2007JD009181.

Hawley, R. L., E. M. Morris, R. Cullen, U. Nixdorf, A. P. Shepherd, and D. J. Wingham (2006), ASIRAS airborne radar resolves internal annual layers in the dry-snow zone of Greenland, *Geophys. Res. Lett*, *33*(4), L04502.

Hawley, R. L., O. Brandt, E. M. Morris, J. Kohler, A. P. Shepherd, and D. J. Wingham (2008), Techniques for measuring high-resolution firn density profiles: case study from Kongsvegen, Svalbard, *Journal of Glaciology*, *54*(186), 463–468, doi: 10.3189/002214308785837020.

Haynes, P., and E. Shuckburgh (2000), Effective diffusivity as a diagnostic of atmospheric transport 1. Stratosphere, *Journal of Geophysical Research-Atmospheres*, *105*(D18), 22,777–22,794.

Heilig, A., O. Eisen, and M. Schneebeli (2010), Temporal observations of a seasonal snowpack using upward-looking GPR, *Hydrological Processes*, *24*(22), 3133–3145, doi: 10.1002/hyp.7749.

Heine, A. J. (1967), McMurdo Ice Shelf, Antarctica - a preliminary report, *New Zealand Journal of Geology and Geophysics*, *10*(2), 474–478.

Helm, V., W. Rack, R. Cullen, P. Nienow, D. Mair, V. Parry, and D. J. Wingham (2007), Winter accumulation in the percolation zone of Greenland measured by airborne radar altimeter, *Geophysical Research Letters*, *34*(6), L06501, doi:10.1029/2006GL029185.

Hoerhold, M. W., S. Kipfstuhl, F. Wilhelms, J. Freitag, and A. Frenzel (2011), The densification of layered polar firn, *Journal of Geophysical Research-Earth Surface*, *116*, F01001, doi:10.1029/2009JF001630.

Holton, J., and R. Lindzen (1972), An updated theory for the Quasi-Biennial cycle of the tropical stratosphere, *Journal of the Atmospheric Sciences*, *29*(6), 1076–1080, doi: 10.1175/1520-0469(1972)029<1076:AUTFTQ>2.0.CO;2.

Holton, J., and H. Tan (1980), The influence of the equatorial Quasi-Biennial oscillation on the global circulation at 50 mb, *Journal of the Atmospheric Sciences*, *37*(10), 2200–2208, doi:10.1175/1520-0469(1980)037<2200:TIOTEQ>2.0.CO;2.

Holton, J. R. (2004), *An Introduction to Dynamic Meteorology*, 4th ed., Elsevier Academic Press, Burlington, Massachusetts, USA.

Holton, J. R., P. H. Haynes, M. E. McIntyre, A. R. Douglass, R. B. Rood, and L. Pfister (1995), Stratosphere-Troposphere Exchange, *Reviews of Geophysics*, *33*(4), 403–439.

Hood, L., S. Rossi, and M. Beulen (1999), Trends in lower stratospheric zonal winds, Rossby wave breaking behavior, and column ozone at northern midlatitudes, *Journal of Geophysical Research-Atmospheres*, *104*(D20), 24,321–24,339, doi:10.1029/1999JD900401.

Hoskins, B., M. McIntyre, and A. Robertson (1985), On the use and significance of isentropic potential vorticity maps, *Quarterly Journal of the Royal Meteorological Society*, *111*(470), 877–946.

Irving, J., and R. Knight (2003), Removal of wavelet dispersion from ground-penetrating radar data, *Geophysics*, *68*(3), 960–970, doi:10.1190/1.1581068.

Irving, J., and R. Knight (2006), Numerical modeling of ground-penetrating radar in 2-D using MATLAB, *Computers & Geosciences*, *32*(9), 1247–1258, doi: 10.1016/j.cageo.2005.11.006.

Jenkins, A., H. F. J. Corr, K. W. Nicholls, C. L. Stewart, and C. S. M. Doake (2006), Interactions between ice and ocean observed with phase-sensitive radar near an Antarctic ice-shelf grounding line, *Journal of Glaciology*, *52*(178), 325–346, doi:10.3189/172756506781828502.

Jin, J., K. Semeniuk, S. Beagley, V. Fomichev, A. Jonsson, J. McConnell, J. Urban, D. Murtagh, G. Manney, C. Boone, et al. (2009), Comparison of CMAM simulations of carbon monoxide (CO), nitrous oxide (N2O), and methane (CH4) with observations from Odin/SMR, ACE-FTS, and Aura/MLS, *Atmospheric Chemistry and Physics*, *9*, 3233–3252.

Jiracek, G. R., and C. Bentley (1971), Velocity of electromagnetic waves in Antarctic ice, *Antarctic Research Series*, *16*, 199–208, doi:10.1029/AR016p0199.

Kapitsa, A. P., J. K. Ridley, G. d. Q. Robin, M. J. Siegert, and I. A. Zotikov (1996), A large deep freshwater lake beneath the ice of central East Antarctica, *Nature*, *381*(6584), 684–686, doi:10.1038/381684a0.

Knuth, K. H. (2006), Optimal Data-Based Binning for Histograms, arXiv:physics/0605197v1.

Knuth, K. H., A. Gotera, C. T. Curry, K. A. Huyser, K. R. Wheeler, and W. B. Rossow (2005), *Revealing Relationships among Relevant Climate Variables with Information Theory*, paper presented at Earth-Sun Systems Technology Conference, Earth Science Technology Office, NASA, Adelphi, Md.

Kovacs, A., A. Gow, and J. Cragin (1982a), The brine zone in the McMurdo Ice Shelf, *Annals of Glaciology*, *3*(1), 166–171.

Kovacs, A., A. Gow, J. Cragin, and R. Morey (1982b), The brine zone in the McMurdo Ice Shelf, *CRREL Report 82-39*, U.S. Army Cold Regions Research and Engineering Laboratory, Hanover, New Hampshire.

Kovacs, A., A. Gow, and R. Morey (1995), The in-situ dielectric-constant of polar firn revisited, *Cold Regions Science and Technology*, *23*(3), 245–256, doi:10.1016/0165-232X(94)00016-Q.

Kruetzmann, N. C., W. Rack, A. J. McDonald, and S. E. George (2011), Snow accumulation and compaction derived from GPR data near Ross Island, Antarctica, *Cryosphere*, *5*(2), 391–404, doi:10.5194/tc-5-391-2011.

Krützmann, N. C. (2008), Application of Complexity Measures to Stratospheric Dynamics: A thesis submitted in partial fulfilment of the requirements for a Masters Degree in Physics at the University of Canterbury, M.Sc., University of Canterbury.

Krützmann, N. C., A. J. McDonald, and S. E. George (2008), Identification of mixing barriers in chemistry-climate model simulations using Rényi entropy, *Geophysical Research Letters*, *35*(6), L06806, doi:10.1029/2007GL032829.

Lambert, A., W. Read, N. Livesey, M. Santee, G. Manney, L. Froidevaux, D. Wu, M. Schwartz, H. Pumphrey, C. Jimenez, et al. (2007), Validation of the Aura Microwave Limb Sounder middle atmosphere water vapor and nitrous oxide measurements, *Journal of Geophysical Research*, *112*, D24S36.

Lee, A. M., H. K. Roscoe, A. E. Jones, P. H. Haynes, E. F. Shuckburgh, M. W. Morrey, and H. C. Pumphrey (2001), The impact of the mixing properties within the Antarctic

stratospheric vortex on ozone loss in spring, *Journal of Geophysical Research-Atmospheres*, *106*(D3), 3203–3211.

Livesey, N., W. Read, L. Froidevaux, A. Lambert, G. Manney, H. C. Pumphrey, M. L. Santee, M. Schwartz, S. Wang, R. E. Cofeld, D. T. Cuddy, R. A. Fuller, R. Jarnot, J. H. Jiang, B. W. Knosp, P. C. Stek, P. A. Wagner, and D. Wu (2011), Earth Observing System (EOS) Microwave Limb Sounder (MLS) Version 3.3 Level 2 Data Quality and Description Document, *JPL technical report D-33509*, available from http://mls.jpl.nasa.gov/ under EOS Aura MLS, Documentation (last accessed on 24.08.2013).

Maeno, N. (1982), Densification rates of snow at polar glaciers, *Memoirs of National Institute of Polar Research. Special issue*, *24*, 204–211.

McCrae, I. R. (1984), A summary of glaciological measurements made between 1960 and 1984 on the McMurdo Ice Shelf, Antarctica: a report submitted to the Antarctic Division of D.S.I.R., *Tech. rep.*, Dept. of Theoretical and Applied Mechanics: University of Auckland, Auckland.

McIntyre, M. E., and T. N. Palmer (1984), The 'surf zone' in the stratosphere, *Journal of Atmospheric and Terrestrial Physics*, *46*(9), 825–849.

Miyazaki, K., and T. Iwasaki (2008), The gradient genesis of stratospheric trace species in the subtropics and around the polar vortex, *Journal of the Atmospheric Sciences*, *65*(2), 490–508, doi:10.1175/2007JAS2403.1.

Moore, J., and A. Grinsted (2006), Singular spectrum analysis and envelope detection: methods of enhancing the utility of ground-penetrating radar data, *Journal of Glaciology*, *52*(176), 159–163.

Morel, B., H. Bencherif, P. Keckhut, T. Portafaix, A. Hauchecorne, and S. Baldy (2005), Fine-scale study of a thick stratospheric ozone lamina at the edge of the southern subtropical barrier: 2. numerical simulations with coupled dynamics models, *Journal of Geophysical Research-Atmospheres*, *110*, D17101, doi:10.1029/2004JD005737.

Nakamura, N. (1996), Two-dimensional mixing, edge formation, and permeability diagnosed in an area coordinate, *Journal of the Atmospheric Sciences*, *53*(11), 1524–1537.

Nash, E., P. Newman, J. Rosenfield, and M. Schoeberl (1996), An objective determination of the polar vortex using Ertel's potential vorticity, *Journal of Geophysical Research-Atmospheres*, *101*(D5), 9471–9478, doi:10.1029/96JD00066.

Neu, J. L. (2000), Tropical transport and the seasonal variability of the subtropical "edges" in the stratosphere, Ph.D., Massachusetts Institute of Technology.

Neu, J. L., and R. A. Plumb (1999), Age of air in a "leaky pipe" model of stratospheric transport, *Journal of Geophysical Research*, *104*(D16), 19,243–19,255.

Neu, J. L., L. C. Sparling, and R. A. Plumb (2003), Variability of the subtropical "edges" in the stratosphere, *Journal of Geophysical Research-Atmospheres*, *108*(D15), 4482, doi:10.1029/2002JD002706.

Nguyen, A., and T. Herring (2005), Analysis of ICESat data using Kalman filter and kriging to study height changes in East Antarctica, *Geophysical Research Letters*, *32*, L23S03, doi:10.1029/2005GL024272.

Oswald, G., and S. Gogineni (2008), Recovery of subglacial water extent from Greenland radar survey data, *Journal of Glaciology*, *54*(184), 94–106.

Oswald, G. K. A., and G. D. Q. Robin (1973), Lakes beneath the Antarctic Ice Sheet, *Nature*, *245*(5423), 251–254, doi:10.1038/245251a0.

Palazzi, E., F. Fierli, G. Stiller, and J. Urban (2011), Probability density functions of long-lived tracer observations from satellite in the subtropical barrier region: data intercomparison, *Atmos. Chem. Phys*, *11*, 10,579–10,598.

Parry, V., P. Nienow, D. Mair, J. Scott, B. Hubbard, K. Steffen, and D. Wingham (2007), Investigations of meltwater refreezing and density variations in the snowpack and firn within the percolation zone of the Greenland Ice Sheet, *Annals of Glaciology*, *46*(1), 61–68.

Pendlebury, D., and T. Shepherd (2003), Planetary-wave-induced transport in the stratosphere, *Journal of the Atmospheric Sciences*, *60*(12), 1456–1470, doi:10.1175/1520-0469(2003)060<1456:PTITS>2.0.CO;2.

Peters, M., D. Blankenship, and D. Morse (2005), Analysis techniques for coherent airborne radar sounding: Application to West Antarctic ice streams, *J. Geophys. Res*, *110*(B6), B06303.

Pierce, R. B., W. L. Grose, J. M. Russell, and A. F. Tuck (1994), Evolution of Southern-Hemisphere Spring Air Masses Observed by HALOE, *Geophysical Research Letters*, *21*(3), 213–216.

Plewes, L. A., and B. Hubbard (2001), A review of the use of radio-echo sounding in glaciology, *Progress in Physical Geography*, *25*(2), 203–236, doi:10.1177/030913330102500203.

Plumb, R. A. (1984), The quasi-biennial oscillation, in *Dynamics of the Middle Atmosphere*, edited by J. R. Holton and T. Matsuno, pp. 217–251, Terra Scientific Publishing Company.

Plumb, R. A. (1996), A "tropical pipe" model of stratospheric transport, *Journal of Geophysical Research-Atmospheres*, *101*(D2), 3957–3972.

Plumb, R. A. (2002), Stratospheric transport, *Journal of the Meteorological Society of Japan*, *80*(4B), 793–809.

Plumb, R. A. (2010), Planetary waves and the extratropical winter stratosphere, in *Stratosphere: Dynamics, Transport, and Chemistry*, edited by L. Polvani, A. Sobel, and D. Waugh, no. 190 in Geophysical Monograph Series, pp. 23–42, American Geophysical Union, Washington.

Polvani, L., D. Waugh, and R. Plumb (1995), On the subtropical edge of the stratospheric surf zone, *Journal of the Atmospheric Sciences*, *52*(9), 1288–1309, doi:10.1175/1520-0469(1995)052<1288:OTSEOT>2.0.CO;2.

Portafaix, T., B. Morel, H. Bencherif, S. Baldy, S. Godin-Beekmann, and A. Hauchecorne (2003), Fine-scale study of a thick stratospheric ozone lamina at the edge of the southern subtropical barrier, *Journal of Geophysical Research-Atmospheres*, *108*(D6), 4196, doi: 10.1029/2002JD002741.

Press, W., S. Teukolsky, W. Vetterling, and B. Flannery (1997), *Numerical recipies in FORTRAN 77 - The Art of Scientific Computing*, no. 1 in Fortran Numerical Recipes, 2nd ed., Cambridge Univ Press.

Pukite, J., S. Kuhl, S. Dorner, and T. Wagner (2012), Detection of tropical stratospheric transport barriers from the long term NO2 data set measured by SCIAMACHY, in *EGU General Assembly 2012, Geophysical Research Abstracts*, vol. 14, EGU2012-9038.

Punge, H. J., P. Konopka, M. A. Giorgetta, and R. Mueller (2009), Effects of the quasi-biennial oscillation on low-latitude transport in the stratosphere derived from trajectory calculations, *Journal of Geophysical Research-Atmospheres*, *114*, D03102, doi: 10.1029/2008JD010518.

Randel, W., J. Gille, A. Roche, J. Kumer, J. Mergenthaler, J. Waters, E. Fishbein, and W. Lahoz (1993), Stratospheric transport from the tropics to middle latitudes by planetary-wave mixing, *Nature*, *365*(6446), 533–535, doi:10.1038/365533a0.

Randel, W. J., F. Wu, J. M. Russell, A. Roche, and J. W. Waters (1998), Seasonal cycles and QBO variations in stratospheric CH_4 and H_2O observed in UARS HALOE data, *Journal of the Atmospheric Sciences*, *55*(2), 163–185.

Rényi, A. (1961), On measures of entropy and information, in *Proceedings of the 4th Berkeley Symposium on Mathematics, Statistics and Probability 1960*, vol. 1, edited by F. Neyman, pp. 547–561, University of California Press, Berkeley.

Rial, F. I., H. Lorenzo, M. Pereira, and J. Armesto (2009), Waveform analysis of UWB GPR antennas, *Sensors*, *9*(3), 1454–1470, doi:10.3390/s90301454.

Rienecker, M. M., M. J. Suarez, R. Gelaro, R. Todling, J. Bacmeister, E. Liu, M. G. Bosilovich, et al. (2011), MERRA: NASA's Modern-Era Retrospective Analysis for Research and Applications, *Journal of Climate*, *24*(14), 3624–3648, doi:10.1175/JCLI-D-11-00015.1.

Riger-Kusk, M. (2011), Ice dynamics of the Darwin-Hatherton glacial system, Transantarctic Mountains, Antarctica, Ph.D., University of Canterbury.

Robin, G. D. Q., S. Evans, and J. T. Bailey (1969), Interpretation of radio echo sounding in polar ice sheets, *Philosophical Transactions of the Royal Society of London. Series A, Mathematical and Physical Sciences*, *265*(1166), 437–505.

Roscoe, H. K., W. Feng, M. P. Chipperfield, M. Trainic, and E. F. Shuckburgh (2012), The existence of the edge region of the Antarctic stratospheric vortex, *Journal of Geophysical Research*, *117*, D04301, doi:201210.1029/2011JD015940.

Rosenlof, K. H. (1995), Seasonal cycle of the residual mean meridional circulation in the stratosphere, *Journal of Geophysical Research-Atmospheres*, *100*(D3), 5173–5191, doi: 10.1029/94JD03122.

Rotschky, G., W. Rack, W. Dierking, and H. Oerter (2006), Retrieving snowpack properties and accumulation estimates from a combination of SAR and scatterometer measurements, *IEEE Transactions on Geoscience and Remote Sensing*, *44*(4), 943–956, doi: 10.1109/TGRS.2005.862524.

Ruzmaikin, A., J. Feynman, X. Jiang, and Y. L. Yung (2005), Extratropical signature of the quasi-biennial oscillation, *Journal of Geophysical Research*, *110*, D11111, doi: 200510.1029/2004JD005382.

Scagliola, M. (2013), CryoSat footprints (v. 1.2), *Aresys Technical Note: SAR-CRY2-TEN-6331*, Europan Space Agency.

Sensors and Software Inc. (2003), *EKKO_View Enhanced & EKKO_View Deluxe Users Guide*, Mississauga, Ontario, Canada.

Sensors and Software Inc. (2006), *pulseEKKO PRO - User's Guide*, Mississauga, Ontario, Canada.

Shepherd, T. G. (2000), The middle atmosphere, *Journal of Atmospheric and Solar-Terrestrial Physics*, *62*(17-18), 1587–1601, doi:10.1016/S1364-6826(00)00114-0.

Shepherd, T. G. (2003), Large-scale atmospheric dynamics for atmospheric chemists, *Chemical Reviews*, *103*(12), 4509–4531.

Siegert, M. J., and R. Hodgkins (2000), A stratigraphic link across 1100 km of the Antarctic Ice Sheet between the Vostok ice core site and Titan Dome (near South Pole), *Geophysical Research Letters*, *27*(14), P. 2133, doi:200010.1029/2000GL008479.

Sparling, L. C. (2000), Statistical perspectives on stratospheric transport, *Reviews of Geophysics*, *38*(3), 417–436.

Spikes, V., G. Hamilton, S. Arcone, S. Kaspari, and P. Mayewski (2004), Variability in accumulation rates from GPR profiling on the West Antarctic plateau, *Annals of Glaciology*, *39*, 238–244.

Steinhoff, D. F., D. H. Bromwich, M. Lambertson, S. L. Knuth, and M. A. Lazzara (2008), A dynamical investigation of the May 2004 McMurdo Antarctica severe wind event using AMPS, *Monthly Weather Review*, *136*(1), 7–26, doi:10.1175/2007MWR1999.1.

Stohl, A., P. Bonasoni, P. Cristofanelli, W. Collins, J. Feichter, A. Frank, et al. (2003), Stratosphere-troposphere exchange: A review, and what we have learned

from STACCATO, *Journal of Geophysical Research-Atmospheres*, *108*(D12), 8516, doi:10.1029/2002JD002490.

Struthers, H., G. E. Bodeker, J. Austin, S. Bekki, I. Cionni, M. Dameris, M. A. Giorgetta, V. Grewe, F. Lefevre, F. Lott, E. Manzini, T. Peter, E. Rozanov, and M. Schraner (2009), The simulation of the Antarctic ozone hole by chemistry-climate models, *Atmospheric Chemistry and Physics*, *9*(17), 6363–6376.

Sutton, R., H. Maclean, R. Swinbank, A. O'Neill, and F. Taylor (1994), High-resolution stratospheric tracer fields estimated from satellite-observations using Lagrangian trajectory calculations, *Journal of the Atmospheric Sciences*, *51*(20), 2995–3005, doi:10.1175/1520-0469(1994)051<2995:HRSTFE>2.0.CO;2.

Takahashi, S., and T. Kameda (2007), Instruments and methods snow density for measuring surface mass balance using the stake method, *Journal of Glaciology*, *53*(183), 677–680.

Taner, M., F. Koehler, and R. Sheriff (1979), Complex seismic trace analysis, *Geophysics*, *44*(6), 1041–1063, doi:10.1190/1.1440994.

Trepte, C. R., and M. H. Hitchman (1992), Tropical Stratospheric Circulation Deduced from Satellite Aerosol Data, *Nature*, *355*(6361), 626–628.

Trepte, C. R., R. E. Veiga, and M. P. McCormick (1993), The poleward dispersal of Mount Pinatubo volcanic aerosol, *Journal of Geophysical Research*, *98*(D10), 18,563–18,573, doi: 199310.1029/93JD01362.

Turner, G. (1994), Subsurface radar propagation deconvolution, *Geophysics*, *59*(2), 215–223, doi:10.1190/1.1443583.

Ulrych, T. J. (1999), The whiteness hypothesis: Reflectivity, inversion, chaos, and Enders, *Geophysics*, *64*(5), 1512–1523.

U.S. Government Printing Office (1976), *U.S. Standard Atmosphere, 1976*, Washington D.C.

van den Broeke, M. (2008), Depth and density of the Antarctic firn layer, *Arctic, Antarctic, and Alpine Research*, *40*(2), 432–438, doi:10.1657/1523-0430(07-021)[BROEKE]2.0.CO;2.

Vaughan, D. G., H. F. J. Corr, C. S. M. Doake, and E. D. Waddington (1999), Distortion of isochronous layers in ice revealed by ground-penetrating radar, *Nature*, *398*(6725), 323–326, doi:10.1038/18653.

Walden, A., and J. Hosken (1985), An investigation of the spectral properties of primary reflection coefficients, *Geophysical Prospecting*, *33*(3), 400–435, doi:10.1111/j.1365-2478.1985.tb00443.x.

Wallace, J. M., and P. V. Hobbs (2006), *Atmospheric science : an introductory survey*, 2nd ed., Academic Press, Burlington, Mass.

Waters, J. W., L. Froidevaux, R. S. Harwood, R. F. Jarnot, H. M. Pickett, W. G. Read, et al. (2006), The Earth Observing System Microwave Limb Sounder (EOS MLS) on the Aura satellite, *IEEE Transactions on Geoscience and Remote Sensing*, *44*(5), 1075–1092.

Waugh, D. (1993), Subtropical stratospheric mixing linked to disturbances in the polar vortices, *Nature*, *365*(6446), 535–537, doi:10.1038/365535a0.

Waugh, D. (1996), Seasonal variation of isentropic transport out of the tropical stratosphere, *Journal of Geophysical Research-Atmospheres*, *101*(D2), 4007–4023, doi:10.1029/95JD03160.

Waugh, D. W., and L. M. Polvani (2010), Stratospheric polar vortices, in *Stratosphere: Dynamics, Transport, and Chemistry*, edited by L. Polvani, A. Sobel, and D. Waugh, no. 190 in Geophysical Monograph Series, pp. 43–57, American Geophysical Union, Washington.

Waugh, D. W., and W. J. Randel (1999), Climatology of Arctic and Antarctic polar vortices using elliptical diagnostics, *Journal of the Atmospheric Sciences*, *56*(11), 1594–1613.

Wingham, D., A. Ridout, R. Scharroo, R. Arthern, and C. Shum (1998), Antarctic elevation change from 1992 to 1996, *Science*, *282*(5388), 456–458, doi:10.1126/science.282.5388.456.

Wingham, D. J., C. R. Francis, S. Baker, C. Bouzinac, D. Brockley, R. Cullen, P. de Chateau-Thierry, S. W. Laxon, U. Mallow, C. Mavrocordatos, et al. (2006), CryoSat: a mission to determine the fluctuations in Earth's land and marine ice fields, *Advances in Space Research*, *37*(4), 841–871.

World Meteorological Organization (1992), *International Meteorological Vocabulary (2nd ed.)*, Secretariat of the World Meteorological Organization, Geneva.

Xia, J., E. Franseen, R. Miller, and T. Weis (2004), Application of deterministic deconvolution of ground-penetrating radar data in a study of carbonate strata, *Journal of Applied Geophysics*, *56*(3), 213–229, doi:10.1016/j.jappgeo.2004.07.003.

Xiao, Q., Y. Kuo, Z. Ma, W. Huang, X. Huang, X. Zhang, D. M. Barker, J. Michalakes, and J. Dudhia (2008), Application of an adiabatic WRF adjoint to the investigation of the May 2004 McMurdo, Antarctica, severe wind event, *Monthly Weather Review*, *136*(10), 3696–3713, doi:10.1175/2008MWR2235.1.

Yang, G., B. J. Hoskins, and J. M. Slingo (2011), Equatorial waves in opposite QBO phases, *Journal of the Atmospheric Sciences*, *68*(4), 839–862, doi:10.1175/2010JAS3514.1.

Yilmaz, O. (1987), *Seismic Data Processing*, Society of Exploration Geophysicists, Tulsa, OK, USA.

Yilmaz, O. (2001), *Seismic Data Analysis: Processing, Inversion, and Interpretation of Seismic Data*, Society of Exploration Geophysicists, Tulsa, OK, USA.

Zwally, H. J., and J. Li (2002), Seasonal and interannual variations of firn densification and ice-sheet surface elevation at the Greenland summit, *Journal of Glaciology*, *48*(161), 199–207.

Appendix A

Animations of Domain Filled Maps of Nitrous Oxide (N_2O)

This thesis has an electronic supplement which can be accessed via the Research Repository of the University of Canterbury (http://ir.canterbury.ac.nz). The supplement consists of video files (.avi) with animations of the domain filled maps at 850 K for each of the eight years of EOS-MLS N_2O observations. The animations consist of four sub-plots for each day with the same layout as Figs. 3.15, 3.16, 3.17, 3.19, and 3.21. High-resolution daily global maps of N_2O include the EOS-MLS measurements from five preceding and subsequent days advected adiabatically to 12:00 UTC on the central day with a two-dimensional trajectory model and MERRA reanalysis winds. The potential vorticity (PV) contour plots are derived from MERRA data for the central day.[1] The colouring in the scatter plots of PV vs. N_2O volume mixing ratio is determined by the difference in PV between the initial and final position of each N_2O measurement after the advection process.

Table A.1 contains a list of the available files. Each .avi-file contains the domain filled maps for one of the years from 2004 to 2011. Days for which no MLS measurements were available are indicated in the third column of Table A.1. In most cases these data gaps are short and N_2O maps for the days without observations are created from the observations of surrounding days. In 2007 and 2011, large data gaps (> 10 days) in the observations did not allow domain filled maps to be created for every day of the year (these days are indicated in the fourth column of Table A.1). Accordingly, the animation for 2007 skips from 19.7. to 4.8.2007 and the animation for 2011 skips from 31.3. to 18.4.2011. The last column in Table A.1 indicates whether large-scale leaks of high-N_2O air from the tropical pipe to the southern hemisphere surf-zone are observed during austral winter in the respective year. As no MLS observations are available before 8.8.2004, it is unknown whether considerable leakage occurred earlier in the year. However, the relatively low levels of N_2O observed in the southern hemisphere surf-zone at the beginning of the observational period suggest that this was not the case.

[1] Occasional spots of increased PV observed at the highest latitudes in both hemispheres should be ignored as they are artefacts caused by interpolation issues near the poles. These errors only occur in the PV calculations and do not affect the trajectories for domain filling. No corresponding structures/errors are found in the domain filled N_2O maps.

Table A.1: Overview of the electronic supplement to this thesis. Each file contains a succession of images like Fig. 3.15 for every day of the respective year. The domain filled maps are derived from EOS-MLS observations of N_2O at 850 K advected adiabatically to 12:00 UTC of the central day with a two-dimensional trajectory model using MERRA reanalysis winds. Each daily map includes the N_2O observations of up to eleven days (five days before and after the central day). Large data gaps (> 10 days) in the N_2O observations for 2007 and 2011 result in sudden jumps in the animations for these years. The missing days are indicated in the comments column.

Year	Filename	Days without observations	Comments	Leak year
2004	N2O,SH,PV,scatterWithPVchangeAt850Kfor2004fromDay221.avi	1.1.-7.8., 9.8.-12.8., 9.9.	The first available observations of the EOS-MLS instrument are from 8.8.2004 (day 221). Two short data gaps are filled with advected data.	(no?)
2005	N2O,SH,PV,scatterWithPVchangeAt850Kfor2005.avi	none		yes
2006	N2O,SH,PV,scatterWithPVchangeAt850Kfor2006.avi	30.3.-3.4.	The short data gap is filled with advected data from preceding and subsequent days.	no
2007	N2O,SH,PV,scatterWithPVchangeAt850Kfor2007.avi	13.7.-8.8.	No domain filled maps between 18.7. and 3.8.	yes
2008	N2O,SH,PV,scatterWithPVchangeAt850Kfor2008.avi	none		no
2009	N2O,SH,PV,scatterWithPVchangeAt850Kfor2009.avi	none		yes
2010	N2O,SH,PV,scatterWithPVchangeAt850Kfor2010.avi	none		yes
2011	N2O,SH,PV,scatterWithPVchangeAt850Kfor2011.avi	27.3.-18.4., 26.11.-31.12.	No domain filled maps between 1.4. and 17.4.; observations after 25.11.2011 were not considered in this work.	yes